

Dipartimento di / Department of

MATERIALS SCIENCE

Dottorato di Ricerca in / PhD program in Materials Science and Nanotechnology Ciclo / Cycle XXXV

Curriculum in Materials Science

DEVELOPMENT OF HEART-ABUNDANT CHALCOGENIDE THIN FILMS FOR PHOTOVOLTAIC APPLICATION

Cognome / Surname FRIONI Nome / Name LUIGI

Matricola / Registration number 735930

Tutore / Tutor: SIMONA BINETTI

Cotutore / Co-tutor: STEFANO MARCHIONNA
(se presente / if there is one)

Supervisor:
(se presente / if there is one)

Coordinatore / Coordinator: MARCO BERNASCONI

ANNO ACCADEMICO / ACADEMIC YEAR 2021/2022

UNIVERSITY OF MILANO BICOCCA
DEPARTMENT OF MATERIALS SCIENCE



PhD School in Materials Science and Nanotechnology

Cycle XXXV

**DEVELOPMENT OF EARTH-ABUNDANT
CHALCOGENIDE THIN FILMS FOR
PHOTOVOLTAIC APPLICATIONS**

PhD thesis by

Luigi Frioni

Supervised by Prof Simona Binetti and Dr Stefano Marchionna

1. TABLE OF CONTENTS

1.	TABLE OF CONTENTS	2
2.	TABLE OF ABBREVIATIONS AND ACRONYMS	5
3.	ABSTRACT	7
4.	INTRODUCTION AND STATE OF THE ART	8
4.1.	CHALCOGENIDE TFS AS ABSORBER LAYERS FOR PV	8
4.2.	CZTS TF	11
4.2.1.	Material properties	11
4.2.1.1.	Crystalline structure.....	11
4.2.1.2.	Optoelectronic properties	12
4.2.1.3.	Defects and electrical properties.....	13
4.2.1.4.	Secondary phases	14
4.2.1.5.	CZTS band tailing: A particular problem	17
4.2.2.	CZTS deposition using sputtering technique.....	18
4.2.3.	Structure of CZTS-based SCs	21
4.2.3.1.	CZTS/CdS heterojunction.....	24
4.2.4.	PDTs' studies and application	25
4.2.4.1.	Post-sulphurisation thermal treatments	25
4.2.4.2.	Chemical treatments for the removal of secondary phases	26
4.2.4.3.	Quenching effect and order-disorder transition	26
4.3.	KESTERITE MONOGRAIN PRODUCTION	28
4.3.1.	Monograin growth process.....	28
4.4.	CFTS TF	31
4.4.1.	Material properties	31
4.4.1.1.	Crystalline structure and secondary phases.....	31
4.4.1.2.	Optoelectronic properties	37
4.4.1.3.	Fe oxidation state: XPS analysis.....	37
4.4.2.	Deposition methodology	39
4.4.3.	CFTS TF-based SCs.....	41
4.5.	CMTS TF	44
4.5.1.	Material properties	44

4.5.1.1.	Crystal structure and secondary phases.....	44
4.5.1.2.	Optoelectronic properties	46
4.5.2.	CMTS TF deposition and related PV devices	47
5.	FABRICATION AND CHARACTERISATION METHODS.....	49
5.1.	SPUTTERING MACHINE MO AND METALS' DEPOSITION.....	50
5.2.	SULPHURISATION PROCESS AND COOLING	51
5.3.	CdS DEPOSITION.....	52
5.4.	TCO DEPOSITION AND METAL GRID	53
5.5.	PDT.....	53
5.6.	MONOGRAIN PREPARATION	53
5.7.	CHARACTERISATION TOOLS.....	54
6.	RESULTS AND DISCUSSION.....	56
6.1.	CZTS TF	56
6.1.1.	TF deposition and series definition	56
6.1.2.	Material characterisation.....	57
6.1.2.1.	Morphological and compositional analysis	57
6.1.2.1.1.	First series: Varying the Cu content and the deposition order	58
6.1.2.1.2.	Second series: Varying the Argon flux and the sulphurisation temperature	59
6.1.2.2.	Crystallographic characterisation by XRD analysis	60
6.1.2.3.	Phase characterisation by Raman spectroscopy	62
6.1.3.	Cell finalisation and characterisation	64
6.1.3.1.	CdS deposition optimisation.....	65
6.1.3.2.	Characterisation of CZTS TF SCs.....	66
6.1.4.	Post-deposition treatment effects	69
6.1.4.1.	Chemical etching with HCl and thermal treatment: Effect on the material	69
6.1.4.2.	Chemical etching with HCl and thermal treatment: Effect on devices	71
6.1.5.	Defect mapping by impedance measure and $V_{OC}(T)$	73
6.1.5.1.	Impedance measure	73
6.1.5.1.1.	RT measures: Loss maps vs. V.....	73
6.1.5.1.2.	Low-temperature measures: Loss maps vs. T and $V_{OC}(T)$	75
6.1.6.	Conclusion	77
6.2.	CFTS TF	79
6.2.1.	TF deposition and series definition	79
6.2.2.	Material characterisation.....	81
6.2.2.1.	Morphological and compositional analysis	81
6.2.2.1.1.	First series of CFTS samples: The 'constant power' approach	82

6.2.2.1.2.	Second series of CFTS samples: ‘Constant current’ approach.....	84
6.2.2.1.3.	Second series: Cooling rate test.....	87
6.2.2.2.	Crystallographic characterisation by XRD analysis	88
6.2.2.2.1.	XRD data analysis: First and second series.....	89
6.2.2.3.	Phases’ characterisation by Raman spectroscopy.....	90
6.2.2.4.	Optoelectronic characterisation by UV–Vis spectroscopy	91
6.2.2.5.	Oxidation state characterisation using XPS analysis	93
6.2.3.	PV cells’ characterisation	94
6.2.4.	Monograin growth of CFTS	96
6.2.4.1.	Monograin powders and series definition	96
6.2.4.2.	Compositional and morphological characterisation by SEM/EDX	97
6.2.4.2.1.	First series: Investigating sulphurisation conditions	97
6.2.4.2.2.	Second series: Investigating various compositions.....	100
6.2.4.3.	XRD data analysis: First and second series	102
6.2.4.4.	Phases’ characterisation by Raman spectroscopy.....	103
6.2.5.	Conclusion	105
6.3.	CMTS TF	106
6.3.1.	TF deposition and series definition	106
6.3.2.	Material characterisation.....	107
6.3.2.1.	Compositional and morphological characterisation using SEM/EDX.....	107
6.3.2.1.1.	First series of CMTS samples: Varying composition	108
6.3.2.1.2.	Second series of CMTS samples: Varying the thickness	110
6.3.2.1.3.	Third series: Varying the precursors’ order	112
6.3.2.2.	Crystallographic characterisation by XRD analysis	114
6.3.2.3.	Raman characterisation.....	116
6.3.2.4.	UV–Vis characterisation by transmittance measure for E_g determination	119
6.3.2.5.	PL characterisation for E_g measures	120
6.3.2.6.	XPS analysis.....	123
6.3.3.	PV cell characterisation.....	124
6.3.3.1.	PV device characterisation: J–V curves and EQE curves	125
6.3.4.	Defect mapping: Impedance measure and $V_{oc}(T)$	127
6.3.4.1.	RT measures: Loss maps vs. V	127
6.3.4.2.	Low-temperature measures: Loss maps vs. T and $V_{oc}(T)$	129
6.3.5.	Conclusion	131
7.	CONCLUSION.....	133
8.	PUBLICATIONS	135
9.	REFERENCES.....	136
10.	ACKNOWLEDGEMENTS	142

2. TABLE OF ABBREVIATIONS AND ACRONYMS

ARC	Anti-reflective coating
AS	Admittance spectroscopy
AZO	Aluminium-doped zinc oxide
BE	Binding energy
CB	Conduction band
CBD	Chemical bath deposition
CBO	Conduction bands offset
CFTS	$\text{Cu}_2\text{FeSnS}_4$
CIGS	$\text{Cu}_2(\text{In,Ga})\text{Se}_2$
CIS	Cu_2InSe_2
CMTS	$\text{Cu}_2\text{MnSnS}_4$
CMTSe	$\text{Cu}_2\text{MnSnSe}_4$
CTE	Coefficient of thermal expansion
CZTS	$\text{Cu}_2\text{ZnSnS}_4$
CZTSSE	$\text{Cu}_2\text{ZnSn(S,Se)}_4$
DAP	Donor-acceptor pair
DC	Direct current
DSSC	Dye-sensitised solar cell
EDX	Energy dispersive X-ray
E_F	Fermi energy
E_g	Bandgap
EQE	External quantum efficiency

FF	Fill factor
ITO	Indium-doped tin oxide
J_{sc}	Short circuit current density
MGL	Monograin layer
PDT	Post-deposition treatment
PL	Photoluminescence
PV	Photovoltaic
PVSK	Perovskite
QDAP	Quasi donor-acceptor pair
RF	Radio frequency
RT	Room temperature
RTA	Rapid thermal annealing
SC	Solar cell
SEM	Scanning electron microscopy
SGL	Soda-lime glass
SILAR	Successive ionic layer adsorption and reaction
STM	Scanning tunnelling microscopy
T_c	Critical temperature
TCO	Transparent conductive layer
TF	Thin film
UV-Vis	UV-Visible
VB	Valence band
V_{oc}	Open circuit voltage
XPS	X-ray photoelectron spectroscopy
XRD	X-ray diffraction

3. ABSTRACT

Climate change and the consequent reduction of CO₂ emissions are shifting energy production from fossil sources to renewable ones. In this context, PV technologies play a key role in the new paradigm of energy production generation. The continuous pursuit of efficiency and low production costs is guiding research in the PV field from classical Si-based technologies with high performance but low production throughput to TF technologies, which demonstrate less efficiency but also more throughput potential. The use of chalcogenide materials as absorber, such as CdTe and CIGS, displays good performance on both the laboratory and industrial scales. The shift to Earth-abundant elements is a good strategy to promote the industrial appeal of these materials, avoiding the use of expensive or toxic elements.

The focus of this PhD thesis is the validation of a high-throughput production process for three Earth-abundant chalcogenides applied in TF PV technology: CZTS, CFTS and CMTS. The absorber layer was produced with a two-steps process: the deposition of metallic precursors on the substrate by magnetron sputtering, followed by sulphurisation in an oven with elemental sulphur. After the characterisation of the grown material, prototypal SCs were realised and characterised.

The results of the CZTS TF demonstrated the good performance of the production processes: the CZTS material obtained presented high quality, good homogeneity and the absence of secondary phases. The SCs attained with these TFs exhibited PV performance in line with the literature, with high V_{OC} and FF values, although the J_{SC} was limited. The application of two PDTs raised the efficiencies of the SCs, leading to a record CZTS-based SC with $\eta=4.5\%$, J_{SC}=15.1mA/cm², V_{OC}=561mV and FF=54%. Defectivity studies showed the presence of deep defect levels placed at the interface between the absorber material and the buffer layer, and the antisite Cu_{Zn}+Zn_{Cu} defects couple due to order-disorder transitions. Both defects strongly limit the efficiency of CZTS-based SC.

The work on CFTS has been more explorative: a wider compositional condition has been investigated to correlate the compositional ratios of CFTS samples with the presence of secondary phases. Three secondary phases have been detected: rhodostannite, chalcopyrite and iron sulphide. The application of two approaches in metal deposition ('constant power' and 'constant current') demonstrated the strong correlation between the uniformity of the material and the steadiness of the metals' flux during the deposition. The study of the oxidation state of the elements in the TF illustrated that Fe atoms are present both as Fe²⁺ and as Fe³⁺, unlike CZTS, where Zn is present only as Zn²⁺.

As for CFTS, the work on CMTS tested the correlation between TF composition and the presence of secondary phases. Two secondary phases have been observed: thiospinel and manganese sulphide. With pure CMTS samples, we obtained prototypal SC with discrete efficiencies. The application of the two PDTs studied for CZTS TF increased the final performance of these devices, leading to a record device of $\eta=0.89\%$ V_{OC}=430mV, J_{SC}=6.14mA/cm² and FF=33.69%. The V_{OC} value was, to the best of our knowledge, the highest reported in the literature. Defect studies conveyed the presence of V_{Cu} defects and the absence of the previous cited anti-site defects Cu_{Zn}+Zn_{Cu}, proving the absence of order-disorder transitions in this material. However, oxidation states studies have depicted the presence of MnO inside the obtained TF, which strongly affect the material's conduction properties.

4. INTRODUCTION AND STATE OF THE ART

In this section, we will illustrate and discuss the main features of chalcogenide TF SC, starting with a brief introduction to PV. Subsequently, an in-depth analysis is reported regarding the state of the art for all three materials studied in this PhD thesis (CZTS, CFTS and CMTS).

4.1. CHALCOGENIDE TFS AS ABSORBER LAYERS FOR PV

The improvement and broadening of renewable energy production is the main path chosen worldwide to cover humans' enormous energy consumption needs (**25,000TWh of total electricity consumption worldwide** [1]) together with reducing CO₂ emissions. In Europe, documents and treaties such as the 'European Green Deal', the 'Fit for 55 package', the 'Paris Agreement', the 'Horizon Europe' and the '2020 European Recovery Plan' placed climate neutrality by 2050 at the centre of Europe's socio-economic future. To decarbonise energy production, electricity is the main actor in this paradigm change, and solar and wind-based electricity production are key technologies to keep this change accessible, affordable, and sustainable. Solar energy production has been demonstrated to be environmentally and economically competitive, but more challenges must be overcome related to device innovation, manufacturing, device integration and circularity. Most of these challenges are reported in the European Energy Research Alliance Strategic Research and Innovation Agenda on PV and are organized into five topics, with a different objective for every challenge:

- **Challenge 1: PV modulus and SC performance enhancements and cost reduction.**
 - **Objective 1: PV modules with higher efficiencies and lower costs.**
 - **Objective 2: System design for lower Levelized Cost of Energy (LCoE) of various applications.**
 - **Objective 3: Digitalization of PV.**
- **Challenge 2: PV technologies' lifetime, reliability and sustainability.**
 - **Sustainable and Circular PV.**
 - **Reliable and bankable PV.**
- **Challenge 3: PV integration and application.**
 - **Objective 1: Physical integration of PV into the built environment.**
- **Challenge 4: Smart energy system integration for large-scale deployment.**
 - **Energy system integration.**
- **Challenge 5: Socio-economic aspects of PV energy transition.**
 - **Higher awareness of solar PV-related externalities and benefit.**
 - **Economic and sustainability benefits.**

Challenge 1 in Objective 1 defines road maps for obtaining new-generation solar devices and moduli, from Si-based to many TF technologies, such as PVSK and chalcogenide-based. The last demonstrates promising

properties and performance for **terawatt-scale production**: They show a suitable and tuneable band gap and high adsorption coefficient that permit the use of less material to obtain the absorber layer of a SC (realising TF devices). In addition, they are usually obtained as polycrystals and have lower process temperatures than traditional Si-based technology, lowering the final cost of the device.

CdTe-based and CIGS-based SC are the only two commercially available technologies employing chalcogenide materials: They both present very high performance at laboratory scale with record devices, respectively, with 22.1% [2] and $\eta=23.4\%$ [3]. The minimodules obtained with these two materials show efficiencies approaching 20% and long lifetime. Nonetheless, many factors limit these two materials' markets, such as scale-up differences (13-17% in commercial moduli), lower production volumes and higher risks factors. **The usage of rare elements** such as In and Ga [4] or **toxic elements** (Cd, Se) also lowers the commercial appeal of these materials. In this case, the employment of Earth-abundant elements in the absorber layer is crucial for reducing the final costs of the device. Metals such as Zn, Sn, Fe, Mn and chalcogenides in combinations such as S_xSe_{4-x} began to be substituted for these elements. These compounds, with the general formula $Cu_2M^IM^{II}(S_xSe_{4-x})$ ($M^I = Zn, Fe, Mn$ etc., $M^{II} = Sn, Ge$), displayed very promising performance, with record devices at a laboratory scale of $\eta=12.6\%$ for CZTSSe [5], but their application is still difficult in large devices and/or in high-throughput processes. An evaluation of the abundance of elements used in chalcogenide materials, together with their prices, is illustrated in Figure 1.

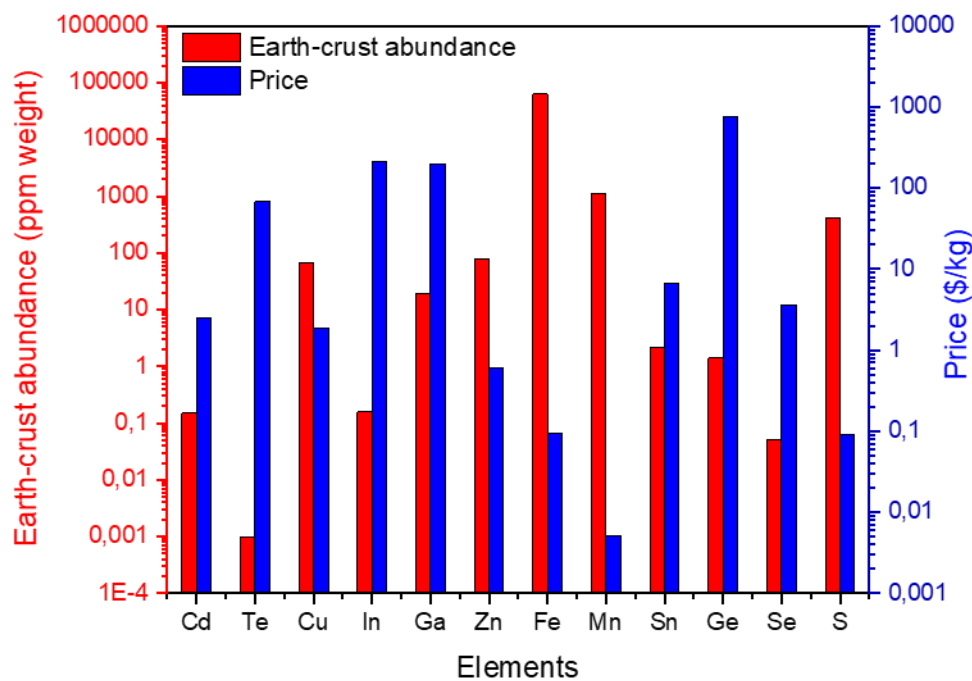


Figure 1: Evaluation of abundance in the Earth's crust [6] and the price [7] of elements involved in chalcogenide-based solar technologies.

These TF technologies are also very interesting due to their employment in **tandem devices** related to Challenge 1 to increase device performance. Two or more SCs are stacked mechanically or monolithically to absorb different fractions of the light spectrum and increase the total power produced by the single cells alone and/or reduce the area needed for the device. Many theoretical works have been published to demonstrate the applicability of this technology, especially in tandem with PVSK devices. Figure 2 reports a monolithic PVSK/CZTSSe tandem device with the J-V curves of the two separated SCs and of the tandem device, having an efficiency of 17% [8].

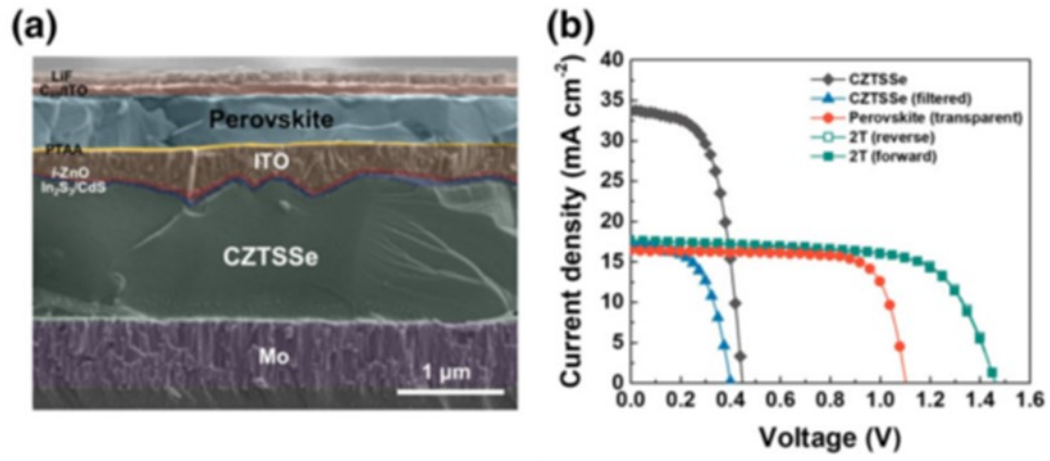


Figure 2: a) Structure of a PVSK/CZTSSe tandem SC and b) J-V curves of a CZTSSe device (filtered and unfiltered), of the PVSK device and of the tandem device (in forward and reverse scan) [8]

4.2. CZTS TF

In this section, we report the main properties of CZTS. We will discuss the material's main features, which are useful for the application of this material in PV devices. Chemical and physical properties, growth methods and the application of the CZTS TF as absorber layer will be discussed hereafter.

4.2.1. Material properties

In this section, we will discuss the chemical and physical properties of synthetic CZTS or natural compounds (e.g. mineral stannite). Only some properties are discussed, focusing on those important for the PV application of CZTS, as follows:

- Crystal structure: This feature can be studied using XRD to identify the formation of the CZTS phase and to check for the absence of possible secondary phases in the samples.
- Optoelectronic properties: These features can be studied using optical spectroscopy, such as UV-Vis and PL, mainly to measure the E_g and the behaviour of electrically active defects.

4.2.1.1. Crystalline structure

For chalcogenide materials with the general formula $\text{Cu}_2\text{M}^{(\text{II})}\text{M}^{(\text{IV})}\text{S}_4$, two possible tetragonal crystal structures were identified: kesterite (with space group I-4) and stannite (I-42m), displayed on the left and on the right of Figure 3. These two structures are very similar, with a different occupation of tetrahedral sites by cations. Kesterite and stannite structures are based on sphalerite (cubic ZnS). Starting with four formula units (Zn_4S_4), we obtained these structures by changing three divalent cations Zn^{2+} with two monovalent Cu^{1+} and one quadrivalent Sn^{4+} . From theoretic calculations, it has been demonstrated that kesterite is the configuration with the lowest free energy value for CZTS, so it should be the most stable structure [9].

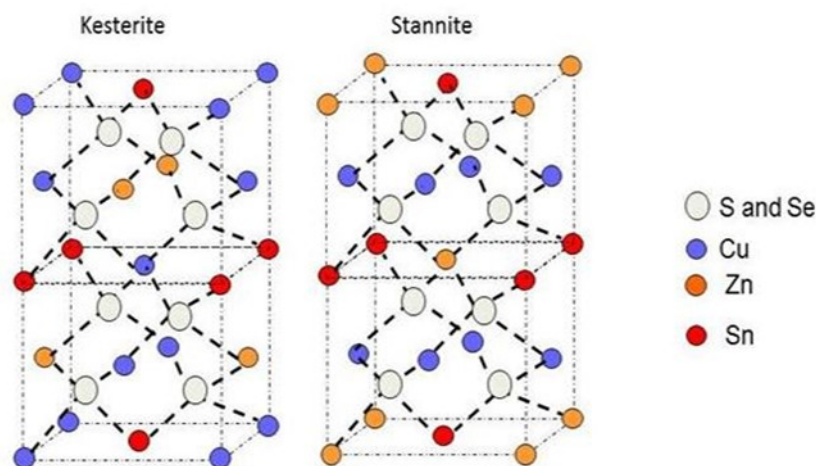


Figure 3: Representation of kesterite (left) and stannite (right) structure for CZTS.

It is possible to find in the literature that CZTS can undertake structural transitions from the 'ordered kesterite' to the 'disordered kesterite'; this transition is termed the 'order-disorder transition'. In this transient, cations with similar energies can switch positions. *Scragg et al.* [10, 11] studied this phenomenon

and described it with an ‘order parameter’ that portrays the occupation degree of cations’ sites. Its value is equal to 1 with a perfectly ‘ordered structure’ and 0 with a perfectly ‘disordered structure’. These kinds of phenomena are associated with a T_c , where the transition is complete for the material under consideration (in the case of the CZTS, $T_c=250^\circ\text{C}$).

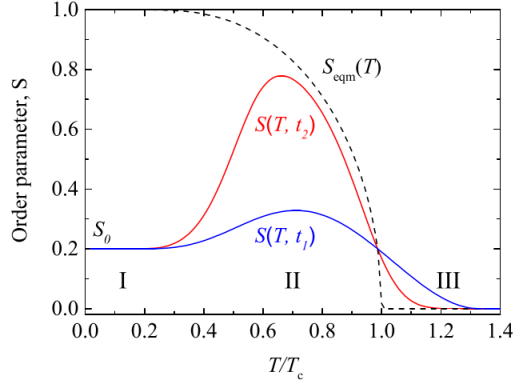


Figure 4: Trend of order parameters for order-disorder transitions, with T_c identified as the temperature at which the entire phase is disordered.

Interestingly, the stannite structure possesses the same symmetry group as ‘disordered kesterite’ [12]. It is not possible to distinguish the two differently ordered structures with XRD, but in any case, this characterisation tool can provide information to determine the approximate structure analysed. The tetrahedral distortion (defined as the ratio between the two crystal parameters, $c/2a$) can assume various values, depending on the structure analysed. It is near 1 in systems cooled down at very low cooling rates, as in ordered systems. This correlation is more valid for powder samples grown under equilibrium conditions than for TF samples, probably due to *internal strain*. For these samples, $c/2a$ is less than 1 [13].

4.2.1.2. Optoelectronic properties

Earth-abundant chalcogenide materials possess optoelectronic features ideal for single-junction PV applications. As Shockley-Queisser theory explains, a maximum efficiency of $\approx 33\%$ can be achieved with absorber materials having $E_g \approx 1.5\text{eV}$ [14]. CZTS is a semiconductor with a direct band gap around 1.5eV with an adsorption coefficient $\alpha > 10^4\text{cm}^{-1}$ [15] that permits the adsorption of more than 90% of light radiation with a material thickness equal to 1-2 μm [16].

Theoretical studies show that the E_g value of the CZTS diverges with the order state of the material, with a difference of 0.2eV between the two states (see Table 1). This disparity could lead to V_{oc} variation in the respective PV devices.

Table 1: Theoretical band gap value in eV for the two structures of CZTS

	<i>Chen et al.</i> [17]	<i>Paier et al.</i> [18]	<i>Person</i> [19]	<i>Botti et al.</i> [20]
Kesterite	1.50	1.49	1.56	1.64
Stannite (disordered kesterite)	1.38	1.30	1.42	1.33

These E_g values only partially describe the complexity of radiative transitions in this material. CZTS PL experiments demonstrate a recombination peak that *Krustok et al.* placed at lower values equaling to 1.2-1.3eV [21]. This effect is not described as a band-to-band transition, but as a DAP or QDAP recombination that occurs using empty intermediate states in the gap to recombine the charge pair, as represented in

Figure 5. This behaviour is usually attributed to defects typical of compensated materials, with both p-type and n-type doping [22]. More details on CZTS defects will be discussed in the next section.

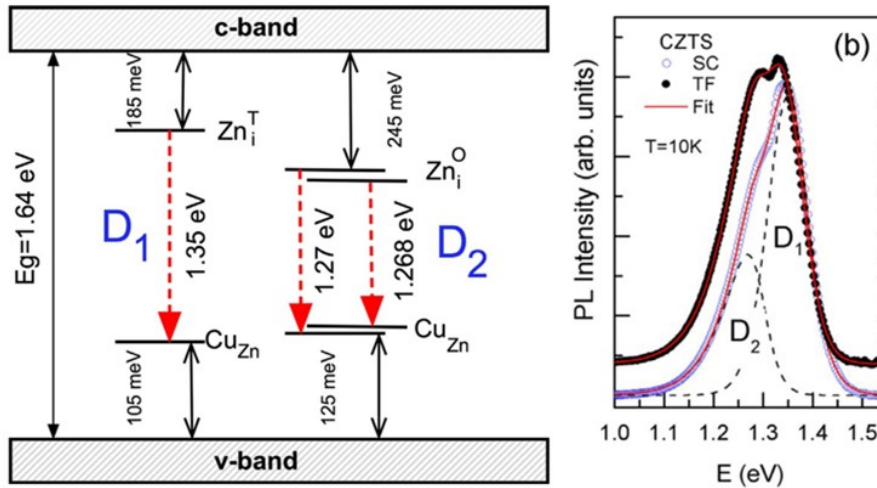


Figure 5: Donor-acceptor recombination peaks and the relative transition scheme of the levels [21].

4.2.1.3. Defects and electrical properties

In terms of electrical properties, CZTS is quite similar to CIGS. Point defects in CZTS induce the same doping behaviour, inducing a p-type doping profile with a carrier concentration equal to $10^{16} \sim 10^{17} \text{cm}^{-3}$, similar to CIGS [23]. According to theoretical calculations [9], three types of defects exist in CZTS: vacancies (V_{Cu} , V_{Zn} , V_{Sn} , V_S), anti-site defects (Cu_{Zn} , Zn_{Cu} , Cu_{Sn} , Sn_{Cu} , etc.) and interstitial defects (Cu_i , Zn_i , Sn_i , etc.). Some point defects induce p-type doping, such as V_{Cu} , V_{Zn} , Cu_{Zn} , etc., while others induce n-type doping, such as Zn_{Cu} , Sn_{Zn} , Cu_i . Finally, some of them are deep defects, such as V_S and Sn-related defects. A summary of CZTS point defects is provided in Figure 6.

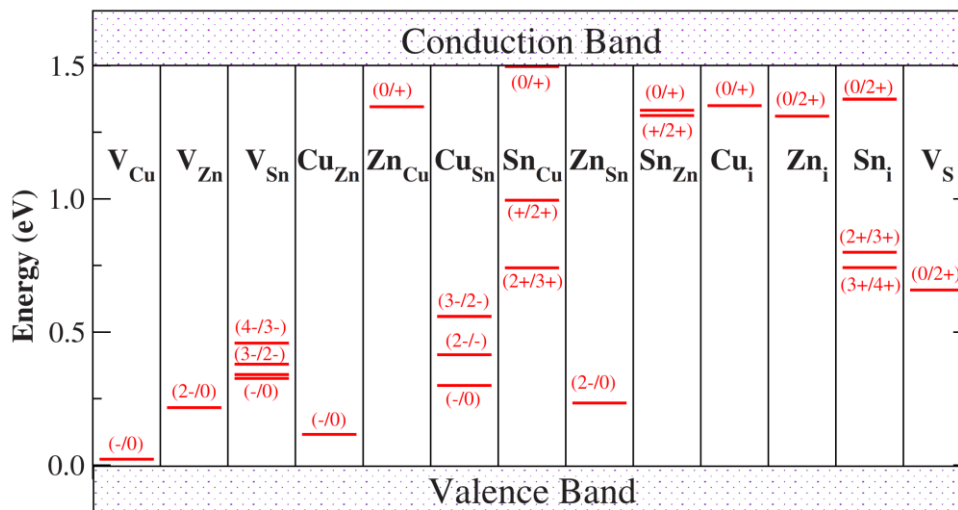


Figure 6: Defect position inside the CZTS band gap, reposted in [9].

The formation energy of all the p-type defects is lower than the n-type ones, so CZTS is always a p-type semiconductor. For example, V_{Cu} is a shallow defect that induces p-type conductivity, while V_{Sn} is a deep defect that induces n-type conductivity with low formation energy. This could be why, for a good PV application, the composition displayed is usually Cu-poor and Sn-rich: to promote the formation of V_{Cu} and

avoid the formation of V_{Sn} . The CZTS mobility is lower than $1 \text{ cm}^2/Vs$, exceedingly lower than CIGS, which limits the charge transport [24].

4.2.1.4. Secondary phases

The deposition of extremely pure CZTS TF is a key aspect for obtaining high efficiency kesterite-based SCs. However, doing so is challenging due to the rather narrow stoichiometric conditions in which this is possible. Theoretical studies on thermodynamic stability demonstrated that the pure CZTS phase region is much narrower than the results obtained for CIGS TF [25]. Figure 7 reports the stability region of the species in the metals' chemical potential space, where the stability region of pure CZTS material is highlighted in black. This narrow region explains the difficulties in avoiding the precipitation of detrimental secondary phases. For example, a Zn-poor sample will depict the formation of Cu_2SnS_3 , while a Zn-rich condition will promote the formation of ZnS in the material matrix.

This theoretical analysis is supported by works that utilise a ternary phase diagram for this material. *Olekseyuk et al.* [26] reported this phase diagram for CZTS material obtained at 400°C , as shown in Figure 8, where the pure-CZTS stability region is marked with an *. Moreover, it is clear that obtaining a pure CZTS phase is quite complex due to the limited stoichiometric tolerance for obtain this material, both for kinetic reasons, due to the unfinished reaction of intermediate phases, and thermodynamic reasons, such as low stoichiometric deposition control or the presence of volatile species, such as SnS. High-efficiency CZTS-based SCs have been obtained at high temperatures ($>550^\circ\text{C}$) with an excess of the two most volatile compounds in this material, S and SnS [27].

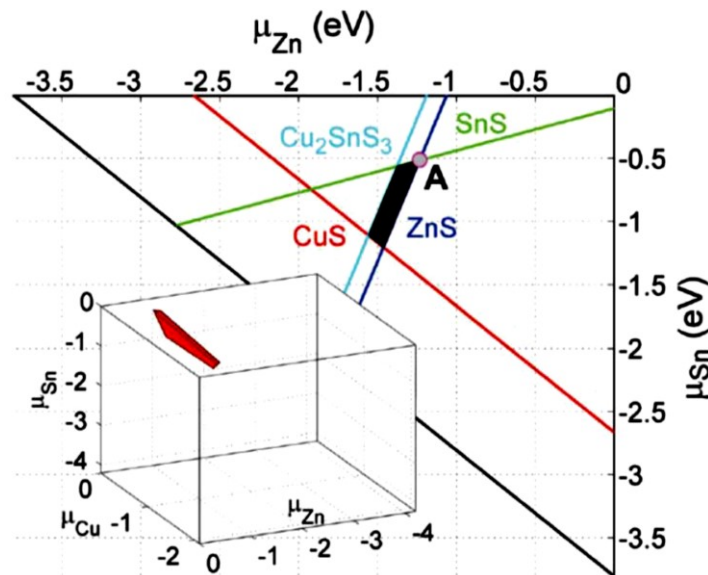


Figure 7: Stability study for pure-CZTS TF samples depending on the chemical potential of the three elements; the region where the CZTS phase is stable is marked in black [25].

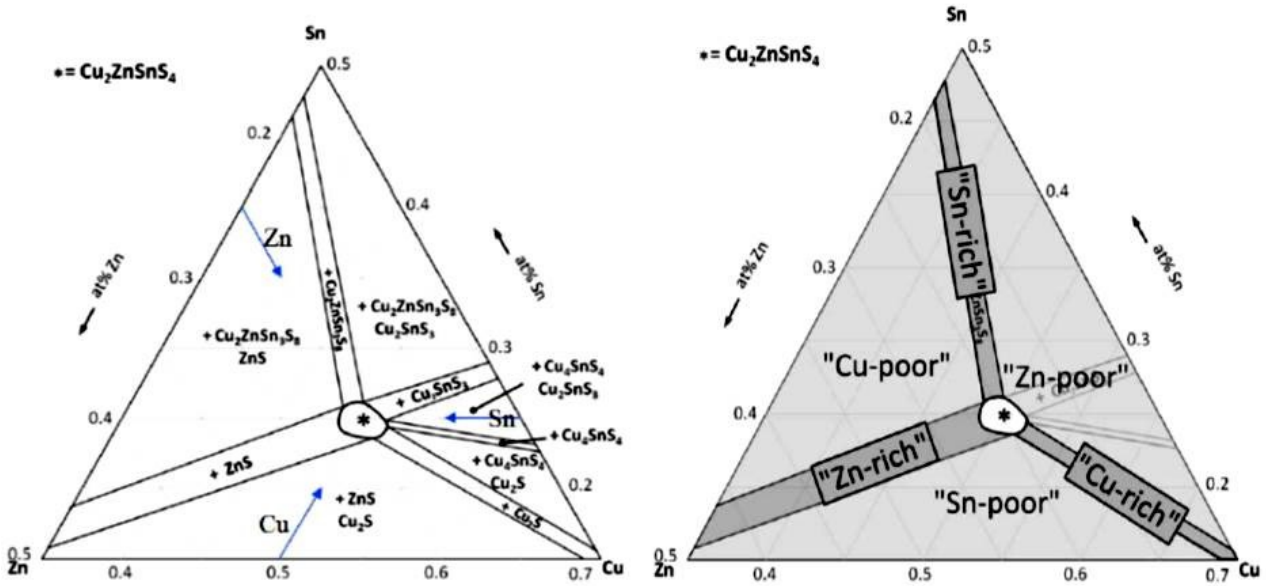


Figure 8: On the left is a ternary phase diagram that illustrates the stoichiometric condition for the formation of secondary phases together with CZTS, where the stability region of the pure-phase material is marked with an *. On the right, the definition of ‘M-rich’ or ‘M-poor’ (where M: Cu, Zn or Sn) regions that will be used to define the stoichiometric condition of our samples [26].

The effect of these materials inside the CZTS matrix can be mainly explained by the evaluation of the band gap of these materials. Table 2 presents the main secondary phases observed in CZTS samples for stoichiometric conditions, together with their band gap values [28]. All these materials demonstrate band gap values greater than CZTS. For example, phases such as Cu_2S that show metallic conduction will behave as conductive channels in and on the surface of the material, with short-circuit spots that lessen the current density of the final device. Meanwhile, the presence of low band gap semiconductors such as SnS and Cu_2SnS_3 introduce deep levels inside the band gap of the material that act as trap states for the charge carrier, lowering the V_{oc} . Finally, highly resistive materials, such as ZnS and SnS_2 , will increase the resistive behaviour of the material, lowering J_{sc} and FF [27]. These secondary phases can be identified with various techniques, such as Raman spectroscopy. Table 2 also depicts the main peak positions of these phases [29], which must be confronted with the main peaks of CZTS, as reported in Table 3 [30].

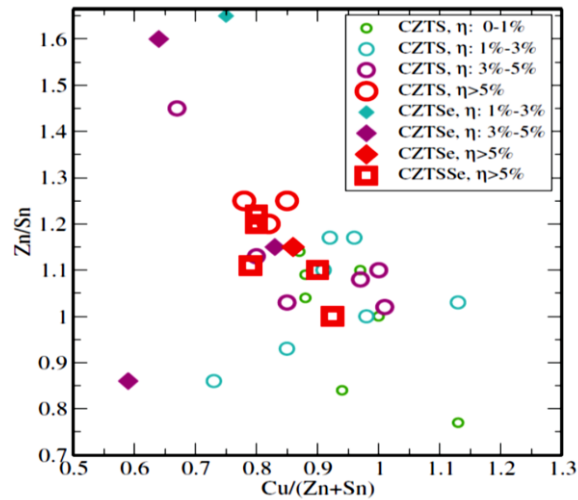
Table 2: Main secondary phases observed in CZTS-related experiments with their band gap value [28] and Raman shift [29].

Secondary phases	Band gap (eV)	Raman shift (cm-1) (and mode)						
CuS	---	19	65	142	267	475 (A)		
Cu_2S	1.2	-	-	-	-	-		
ZnS	3.7					219	273 (A1)	351 (A1)
SnS	1.0 indirect, 1.3 direct	96	163	189	220			
SnS_2	≈ 2.5					202 (Eg)	317 (A1g)	
Sn_2S_3	---	52	60	183	234	307		
Cu_2SnS_3	1.0					290 (A')	352 (A')	

Table 3: Raman shift and mode symmetry of CZTS, both in kesterite and stannite.

Symmetry	Kesterite		Stannite		Experimental data	
	This work		Symmetry	This work	Raman	IR
A	340.04		A ₁	334.08	338.00	
	284.30				277.12	287.00
	272.82		A ₂	263.11		
B (TO LO)	355.80	374.05	B ₁	291.12	368.00	316.00
	309.56	313.19		74.17		
	238.48	254.73	B ₂ (TO LO)	360.12	370.63	
	166.65	168.21		277.08	291.82	168.00
	98.82	98.83		149.69	150.91	
	86.70	87.51		95.85	95.86	86.00
E (TO LO)	351.55	366.35	E (TO LO)	346.01	364.87	351.00
	281.07	293.44		264.37	275.52	293.00
	250.26	257.85		235.41	246.58	252.00
	150.53	151.05		161.68	162.63	143.00
	105.93	106.00		97.34	97.38	
	83.64	83.65		78.39	78.73	68.00

To reduce the formation of these detrimental secondary phases and lessen the presence of deep defects in the CZTS material, most of the literature has observed that two conditions lead to high-efficiency CZTS-based SC: Cu-poor and Zn-rich conditions together with stoichiometric ratios $[Cu]/[Zn]+[Sn] \approx 0.8$ e $[Zn]/[Sn]=1.2-1.3$. Figure 9 reports the comparison between the PV efficiencies of different CZTS-based SC together with their relative stoichiometric ratios $[Cu]/[Zn]+[Sn]$ and $[Zn]/[Sn]$ [31].

**Figure 9: Comparison between stoichiometric conditions and relative PV efficiencies [31].**

Another effect due to compositional ratios to CZTS features was observed by *Sumitomo et al.* [32]. As illustrated in Figure 10, carriers' lifetime, calculated from time-resolved PL, decreases strongly for $[Cu]/[Sn]$ values close to 2 and for $[Zn]/[Sn]$ values less than 1. This reflects on the final SC performances, whereby the highest efficiency values are obtained on samples with longer lifetime. In this material, the conduction mechanism works through V_{Cu} states [33], meaning that conditions that limit the formation of these defects lower the p-type doping of the material and lower its final performance as PV absorber.

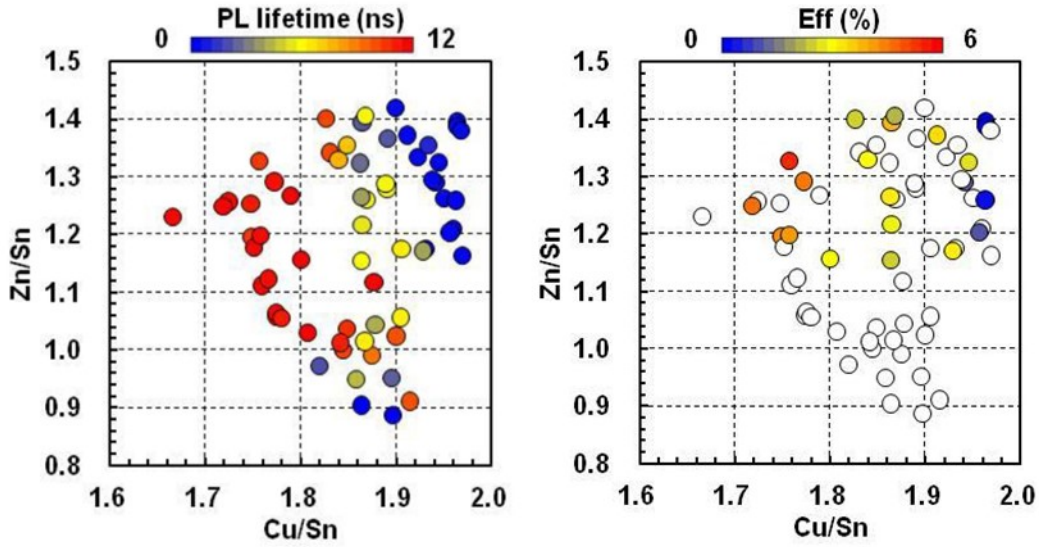


Figure 10: On the left, photogenerated carriers' lifetime trends correlated with $[Cu]/[Sn]$ and $[Zn]/[Sn]$ and were obtained from time-resolved PL. On the right, SC efficiencies trends were obtained from the same compositional ratios [32].

4.2.1.5. CZTS band tailing: A particular problem

Unlike other chalcogenide materials, CZTS conveys a particular feature in its band structure known as 'band tailing'. This phenomenon is caused by spatially localised variations of both the **effective band gap** of the material and/or **the electrostatic potential due to defects**, thus influencing V_{oc} . This model was developed by *Gokmen et al.* [34]. Starting from high-efficiency kesterite-based SCs, they demonstrated that the smoothing of the EQE edge at lower energy values and the higher width of the PL peak in lower-performance cells are correlated with band-tailing features. Figure 11 shows two mechanisms proposed in this work to explain the appearance of band tailing, describing the effect of the band gap and electrostatic potential fluctuations: on the left, the effect of band gap fluctuations, and on the right, the effect of electrostatic potential fluctuation.

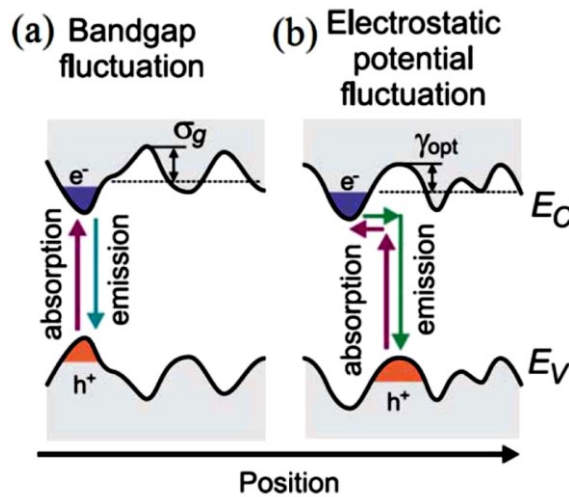


Figure 11: Schemes of band gap fluctuation and electrostatic potential fluctuation that generate band tailing features [28].

The first phenomenon is usually caused by compositional inhomogeneity, while the second is usually associated with the presence of charged point defects that alter the local potential, inducing misalignment between the two band gap edges. This effect is particularly present in CZTS and is attributed to the coupling

of two defects, Cu_{Zn}^- and Zn_{Cu}^+ , forming the DAP [$\text{Cu}_{\text{Zn}}^- + \text{Zn}_{\text{Cu}}^+$], defined as the main defect in disordered kesterites. The high concentration of these defects can be explained by the fact that Cu and Zn possess similar ionic radii, so the substitution of one of these cations with bigger ones, for example with Ba and Cd, should limit the occurrence of cation disorder in the crystalline structure of kesterite [35, 36].

4.2.2. CZTS deposition using sputtering technique

The high interest in realising high-quality CZTS (and CZTSSe) TF explains the range of techniques studied and implemented to obtain this material with suitable features for high-performance PV applications, with particular attention to the sustainability and high throughput of the process tested. The most efficient results in terms of efficiencies have been obtained with vacuum techniques, such as sputtering and co-evaporation techniques. However, many other techniques have succeeded in obtaining good compromises between a lower final PV efficiency and a lower production cost while maintaining a high productive value. From spray pyrolysis, electrodeposition, photochemical growth and monograin synthesis to inks and sol-gel depositions, several techniques have been tested. In addition, many studies have compared these techniques, for example the review of *D.B. Mitzi et al.* [37]. However, a comprehensive analysis of all these techniques can become quite complicated due to the extreme complexity of some techniques and the modifications beyond deposition methods introduced over the years, as follows:

- Compositional variation with cation substitution in the CZTS structure (e.g. Ba, Cd, Ge etc.).
- Thermal treatments are introduced at different moments in the production process.
- Acid treatments for secondary phases removal (e.g. HCl, KCN etc.).
- Implementation of extra layers to improve the final performance of the device.
- Chemical treatments for the diffusion of alkali ions, such as Na and K, are similar to those obtained for high-efficiency CIGS devices [38].

The simple analysis of final PV performance without an in-depth analysis of boundary conditions is insufficient for confronting distinct deposition techniques, since in every recent work, the optimisation of the absorber layer is connected to external optimisation, particularities that diversify the work from research groups. For this reason, we cite other techniques and will consider and analyse only techniques similar to the one used in this PhD thesis: **a two-steps deposition technique obtained with the sputtering deposition of a metallic multilayer and sulphurisation in a pure sulphur atmosphere**. In this kind of processes, the absorber layer is obtained from the vacuum deposition of the metals' precursors (in metallic or sulphide form) and a successive heat treatment at $T \approx 550^\circ\text{C}$ in the presence of sulphur and/or SnS (to compensate for the loss of volatile compounds). Consequently, this sort of process is quite interesting for industrial scale-up, since the sputtering deposition process is more scalable than other vacuum techniques and the quality of the material is superior to those obtained from wet chemistry [37].

Table 4 portrays the comparison between various deposition methodologies applying a two-steps process, together with the PV performance of SC based on the materials obtained with these methodologies [39]. Between them, the result obtained by *Chang Yan et al.* actually has the record efficiency for this material, $\eta \approx 11\%$ [40]. Comparing these data, it is clear that the process parameters that can be potentially optimised are numerous and become even more complex if we also consider the optimisation of the other layers. For the absorber layer deposition, we can affirm that the main optimisable parameters are as follow:

- Metal deposition order and deposition mode (co-sputtering vs. multilayer).
- Precursors' nature (pure metals or chalcogenides).
- Substrate temperature during metal precursors' deposition.
- Type of sulphur precursor (pure sulphur vs. H_2S)

- Temperature and duration of the sulphurisation process.
- Thickness of the absorber layer.
- Ramp-up and/or ramp-down of the heating process (e.g. application of the RTA or controlled cooling to diminish order-disorder effects).
- Initial compositional ratios of metallic precursors.

Table 4: Comparison between results for two-steps processes employing vacuum deposition techniques to obtain CZTS TF SC, including precursors' deposition temperature (T_S), sulphurisation temperature (T_A) and atmosphere used during the annealing (Atm), the precursors used, material for the buffer layer, PDT when applied, the antireflective coating layer used and the main SC parameters obtained [39].

Route (Year)	T_S [°C]	T_A [°C]	Atm.	Notes	Buffer Type	PDA	AR	E_g [eV]	η [%]	V_{OC} [mV]	J_{SC} [mA cm ⁻²]	FF[%]	A [cm ²]
Co-Sputt. (2008)	RT	580	H ₂ S, N ₂	2.2 μ m-CZTS: Cu, SnS, ZnS, soaked in DIW	CdS	No	No	/	6.8	610	17.9	62	0.15
Co-Evap. (2013)	~150	570	S ₂ , N ₂	600 nm-CZTS: Cu, Zn, Sn, S (hot plate; 5min)	CdS	No	MgF ₂	1.45	8.4	661	19.5	65.8	N.D.
Seq. Evap. (2013)	/	/	S	CZTS: Submodule (7 cells)	In ₂ S ₃ /CdS	/	Yes	/	9.2	708	21.6	60.1	14
Co-Sputt. (2013)	180	560	Ar, S	CZTS:Cu/Sn, Zn in H ₂ S reactive atm., KCN etched	CdS	/	No	/	7.9	667	19.6	60.0	/
Seq.Sputt. (2015)	RT	570	S	~500 nm-CZTS:Cu/SnS/ZnS/Mo	CdS	No	No	1.50	7.5	632	19.2	61.6	0.4
Monograin (2015)	/	740	S	CZTS:KCN etched	CdS	No	No	1.53	9.4 (EA)	713	21.24	62	0.04
Co-Sputt. (2016)	RT	560	S	~900 nm-CZTS:Cu/ZnS/SnS/Mo	Zn _{0.35} Cd _{0.65} S	No	No	1.50	9.2	748	19.5	63.2	0.4
Co-Sputt. (2016)	RT-250	250-510	N ₂ , H ₂ S	1 μ m-CZTS:SnS ₂ , ZnS, Cu	CdS	No	MgF ₂	1.4	8.6	625	21.2	65.1	0.5
Co-Sputt. (2017)	RT	580	S	CZTS:CuS,ZnS and SnS, ZTO ALD (145 °C)	(Zn,Sn)O	CZTS	MgF ₂	1.50	9.0	679	21.6	61.4	0.5
Co-Sputt. (2017)	RT	570	S	900 nm-CZTS:Cu,ZnS,SnS	CdS	On cell	Yes	1.5	7.9	642	19.3	64	0.1
PLD (2017)	RT	560	S,SnS	<450 nm- CZTS:2CuS:ZnS:SnS	CdS	No	MgF ₂	1.53	5.2	616	17.6	47.9	0.21
Monograin (2017)	/	740	S	CZTS:PA at 150 °C (4h), KCN etched	CdS	CZTS	No	1.55	9.1 (EA)	759	19	63	0.04
Co-Sputt. (2018)	RT	560	SnS, S	CZTS:Cu/ZnS/SnS/ Al ₂ O ₃ /Mo,	CdS	CZTS	Yes	1.5	11.0	731	21.74	69.3	0.234
PLD (2019)	/	/	/	CZTS Oxide target	/	/	/	/	5.4	673	15.2	53	0.09

Due to these results, the process chosen in this PhD thesis to deposit the absorber material presents a few advantages to minimise the complexity of the deposition process, to improve the future scale-up of the process and to increase its eco-sustainability, as follow:

- **Reduced target cost:** Pure metals' targets are far cheaper than the sulphurised ones: the difference can become quite wider, up to an order of magnitude, since the chalcogenide version is obtained using a *sintering* process (where elemental metal and chalcogenide react through a solid-solid reaction at high temperature and high pressure), unlike pure metal targets obtained from metallurgic processes. The sintering processes also possess intrinsic difficulty in the scale-up process of obtaining large targets, since the control of the process is difficult for larger dimensions. This explains the nonlinear trend of price with the target dimensions. The metal target can also be easily recycled, returning to the metallurgic process to produce new targets.
- **Faster deposition:** Using pure metal targets allow the use of a faster approach for sputtering deposition, the employing of DC generators, instead of the slower method that employs RF generators, which is necessary for low-conductivity compounds' targets, as sulphides. The RF-mediated deposition possesses a limited deposition ratio, from half to one-third of DC-mediated deposition, and the power generator's cost is lower (up to one order of magnitude less). The use of an RF generator limits the high throughput of the production process, both in production speed and costs. Moreover, the co-sputtering approach used in some experiments displayed in Table 4 necessitates the tilting of the sputtering sources to aim at the substrate, further limiting the deposition ratio. The deposition ratio of sputtering sources does not scale linearly with the target-substrate relative distance. It also depends on other factors, such as partial pressure of the inert gas that induce scattering in the material flux.
- **Lower maintenance and projecting costs:** Another particularity of the sulphides' target is the limited thickness due to the low thermal conductivity that would create temperature gradients during the

deposition, which could cause breaks in the target. This mainly lowers the working time of these targets, increasing the total costs of maintaining of the hypothetical industrial process. The usage of sulphides targets would also necessitate a more in-depth design for the production plant to reduce the machine's downtime while the target is changed and to optimise the cooling systems of the targets.

All of these advantages come together with a few disadvantages that limits the **final PV efficiency of the related SC**. As observed in Table 4, the best efficiency values were obtained on samples deposited from ZnS and SnS targets. A low difference was observed in changing the geometry of the deposition (multilayer vs. co-sputtering approach), and the best results were obtained with a multilayer approach. A few publications use a direct sulphurisation process on a pure metal multilayer, and the sulphurisation conditions change from work to work, from the precursor order to the usage of Sn pellets during the process [29, 41-43]. The only feature that all these works share is general compositional conditions using **Cu-poor/Zn-rich conditions**, as already observed. From these publications, we can observe the following:

- Using a multilayer with Zn in direct contact with the Mo substrate, with Cu and Sn on it (as illustrated in Figure 12), the sulphurisation process that starts from the above induces the formation of **voids** at the back contacting Mo in the final CZTS layer and an accumulation of **ZnS** at the front surface [42].
- The efficiency $\eta=5.5\%$ was obtained as the record efficiency by *A. Fairbrother et al.* using a similar approach to the one used in this PhD thesis [29]. The samples were obtained using a multi-layer approach with the structure (order of deposition) Mo/Sn/Cu/Zn. Our research group used the same structure as in a previous publication [41]. However, the lack of Sn during the sulphurisation process probably caused less efficiency ($\eta\approx 3.5\%$). This sequence was chosen for many reasons: to **limit Sn loss** due to volatile SnS during the sulphurisation process (placing this element furthest from the front surface) and to reduce ZnS formation during the main-phase reaction. This geometry was also studied by *H. Araki et al.*[43] between other metals' order, as presented in Table 5. It seems that this structure is not the best, but in this work, the efficiencies are overall quite low.

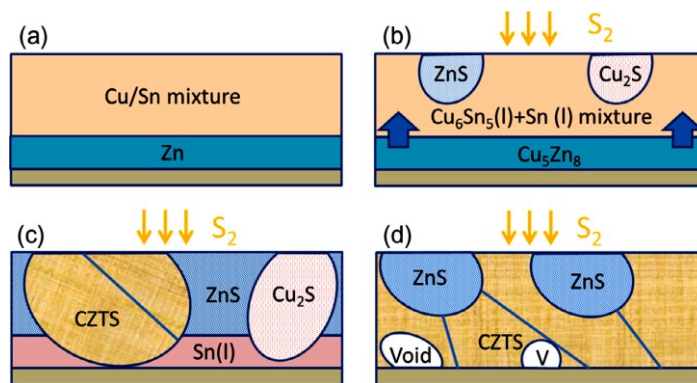


Figure 12: Schematic shown in [42] of the sulphurisation mechanism in a multi-layered sample with the structure Zn/Cu/Sn.

- CZTS formation undergoes the formation of a eutectic **between Cu₂S and SnS** (with composition ratios around 68%-32%) that is formed at 480°C [29]. The other secondary phases are no longer detectable (outside ZnS) after which the sample overcome the treatment at 550°C for 30min.
- The presence of **ZnS at the back contact** is identified as the main limitation for PV performance of the CZTS TF SCs obtained from pure metals' precursors. The high band gap of this material influences the charge transfer from the CZTS layer to the Mo substrate, limiting the current flow and thus the J_{sc} value.

Table 5: Study of the precursor order effect on the final SC results [43].

Stacking order	Group	Photovoltaic properties of cells				
		Area (cm ²)	V _{oc} (mV)	J _{sc} (mA/cm ²)	Fill factor	Efficiency (%)
Mo/Zn/Cu/Sn	A	0.132	478	9.78	0.38	1.79
Mo/Zn/Sn/Cu	A	0.135	406	6.44	0.43	1.12
Mo/Cu/Sn/Zn	A	0.120	377	5.43	0.38	0.77
Mo/Cu/Zn/Sn	B	0.166	24	2.60	0.27	0.01
Mo/Sn/Cu/Zn	B	0.126	495	5.81	0.45	1.29
Mo/Sn/Zn/Cu	C	0.150	166	2.54	0.25	0.11

4.2.3. Structure of CZTS-based SCs

After describing the deposition methods used to obtain the CZTS absorber layer, we provide in this Section a brief description of the realisation of kesterite-based SCs. This description will be useful for comprehending the technical solutions in the literature to improve the final PV performance of these devices, especially when applied to the device structure. As general information, the standard structure used for kesterite-based SC is the same as that developed for CIGS-based devices [44], and it will be taken for granted in the introduction of other innovative materials since the structure used is the same.

A sheet of SLG covered by a thin layer of Mo (0.5-1 μ m) is usually used as a substrate for the CZTS layer's deposition. This combination possesses the correct properties for use as a substrate in this process:

- **Compatibility with the environment:** The material must be compact enough to avoid desorption phenomena during the growth process in a vacuum and/or at 550°C.
- **Thermal stability:** The material must be inert, both physically and chemically, in the growth condition of the CZTS layer, so it cannot bend or melt at high temperature (500-600°C). CZTS can also be grown at lower temperatures, but the material's quality will be much lower than that of the high-temperature samples.
- **Optimal thermal expansion:** the substrate CTE must be comparable to the CTE of the CZTS ($\approx 12 \cdot 10^{-6} \text{ }^\circ\text{C}^{-1}$ at 25°C[45]), to minimise exfoliation and delamination problems during the various deposition processes. Table 6 reports the thermal features of the most-used substrates for CIGS. The SLG substrate CTE is close enough to the CZTS CTE but not the same, so using thermal processes that are too long could be detrimental for both the substrate and absorber layer.
- **Chemical stability:** The substrate must be chemically inert under the growth conditions of CZTS. In particular, the interaction with sulphur at high temperatures must be minimal to conserve the ohmic contact at the back of the absorber layer. Simultaneously, the substrate must block every strange element to be driven to the absorber layer when it is not requested (e.g. alkali metals from the glass to improve the crystallinity of the CZTS layer).
- **Humidity barrier:** The system must be protected from atmospheric agents to conserve the lifespan of the device. The Mo layer tends to oxidise if left untreated for too long in atmospheric conditions, especially in humid environments, so it must be protected.

Figure 13 presents a cross-sectional SEM image of a complete CZTS-based SC, together with the scheme of a system of SCs on the same substrate. This approach, called 'monolithic integration', is easier with the TF devices than with the classical SC obtained with Si. The isolation of different devices can be performed using *laser ablation* (P1 cut) and/or *mechanical ablation* (P2 and P3 cuts) that are alternated through the various steps of layers' deposition. This structure comprises the following:

Table 6: Thermal properties of some materials used for the deposition of CIGS; CTE and the maximum process temperature that the substrate can resist are reported; a) the T_{max} value depends on the process's duration and b) a polyimide covering a glass substrate [46].

Material	CTE (10^{-6} K^{-1})	T_{max} ($^{\circ}\text{C}$)	Notes
SLG	9 (20–300 $^{\circ}\text{C}$)	~600	Standard glass substrate, contains Na, K, etc.
Corning 7059	4.6	>600	Alkali-free glass
Cr steel	10–11	>600	Diffusion of Fe, Ni, Cr, etc.; low-cost substrate
Ti	8.6	>600	Low Ti diffusion, restricted Ti purity
Ni/Fe-alloys, e.g. Kovar*	5–11	>600	CTE can be well-matched
Al	23–24	600	Low cost, low weight, very high CTE
Kapton® E	17 (20–200 $^{\circ}\text{C}$)	<500*	Polyimide
Upilex® S	12–24 (20–400 $^{\circ}\text{C}$)	<500*	Polyimide
ETH-PI	3	<500*	Polyimide ^b
Mo	4.8–5.9 (20–600 $^{\circ}\text{C}$)	>600	Back contact
CuInSe ₂	11.2–11.4/7.9–8.6 (20 $^{\circ}\text{C}$)		\perp c-axis//c-axis
ZnO	4.75/2.9		\perp c-axis//c-axis
SiO ₂	1–9	>600	Insulation layer and/or diffusion barrier
Al ₂ O ₃	6–8	>600	Insulation layer and/or diffusion barrier

A thin layer of Mo (0.5–1 μm) was used as a substrate and electrical back contact. This Mo layer can be deposited at RT on SLG by sputtering or evaporation. The critical parameters are adhesion (as a function of the growth speed), resistivity ($\approx 10^{-5} \Omega\text{cm}$) and/or sheet resistance ($\leq 1 \Omega/\square$). Mo conveys limited reactivity to S vapours, but not zero, at CZTS reaction temperatures. The formation of a thin layer of MoS₂ is inevitable due to the high S partial pressure during the sulphurisation process (1–1000mbar). As a reference, the partial pressure of Se used for the CIGS reaction is $\approx 10^{-5}$ mbar. The structure of this thin layer is also quite controversial in the literature, since it depends on several external parameters, such as crystallographic orientation, thickness, and the doping level induced by growth conditions. The lamellar nature of MoS₂ expresses itself in strongly anisotropic behaviours, both in growth mechanisms and in physical and mechanical properties. Another aspect that depends on the MoS₂ orientation is the Na passage through this layer to reach the CZTS TF, identified as a factor in the increased crystallisation of this material. The complexity connected to the control of this layer's growth and properties has pushed research on this topic to use a strongly empirical approach to the optimisation of the effect of MoS₂ on the final device. Notably, if we reduce the S partial pressure to reduce the MoS₂ formation, there is the possibility of further reducing the total performance of devices. As found by *Scraag et al.* [47], when the S content at the back of CZTS layer is too low, the Mo will gather S from the material to form MoS₂, causing the degradation of CZTS and thus the reduction of overall performance. In most cases, thin layers of MoS₂ with thicknesses higher than 100nm are reported. The effect of this layer is still quite complex, but the overall effect is to form a back barrier for holes transport with a successive reduction of PV parameters (especially FF and V_{oc}). Nonetheless, during high performance, CZTS based SCs display MoS₂ layers with thickness between 100 and 500nm [45].

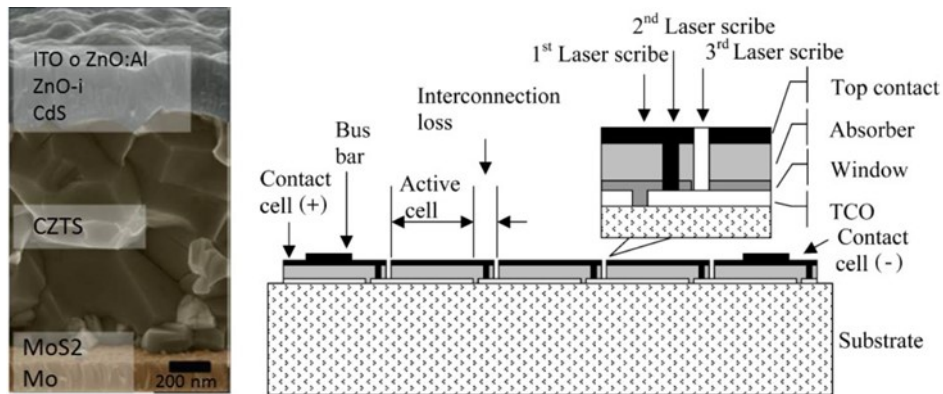


Figure 13: On the left, cross-sectional SEM image of a standard kesterite-based SC (this structure can be generalised for every material studied in this PhD thesis). On the right is the schematic of a monolithic integration process of devices built on the same substrate [48].

- The p-n junction with the naturally p-type doped CZTS is realised with a **thin layer of CdS** (with thickness $\approx 50\text{nm}$, also named BL). This TF is usually realised with the CBD technique, to obtain this material with n doping. CdS precipitates from the bath solution as an insoluble compound and grows on the surface of the CZTS material; the critical parameters of this growth are many, such as the precursor's salt concentration, temperature, solution pH, precursors' order etc.
- A **very thin layer of insulating i-ZnO** with high resistivity ($10\text{-}100\ \Omega\text{cm}$) is deposited on the CdS layer by the sputtering technique (pulsed DC or RF generated) to minimise the electrical shunts of the device. The purpose of this film is to cover all the holes left by the substandard deposition of CZTS and/or CdS and thus to limit the preferential paths for photogenerated carriers that these holes cause.
- The front contact, which the light must penetrate, is realised with a **TCO** layer a few hundreds of nanometres thick (depending on the specific transparency and resistivity of the material employed). The materials most used for this purpose are AZO and ITO. Due to the high price of In, AZO has become the most used TCO in these devices when developed on an industrial scale, despite the better electrical performance of ITO.

To realise laboratory-scale devices, a **metal grid** is usually deposited on the surface of TCO with the appropriate geometry for use as a real metal contact to perform cell characterisation. In a high-performance device, this grid is obtained with a sequence of metals, such as Ni($\approx 5\text{nm}$)/Al($\approx 200\text{-}300\text{nm}$)/Ni($\approx 5\text{nm}$), which is obtained by *e-beam evaporation*. In Figure 13, this metal grid is not shown because the scheme refers to an industrial procedure for PV modulus production.

Many variants on this structure have been tested in the literature to optimise the so-called *device finalisation* that collects all the layers from the buffer layer above. Many tests have been performed to change the TCO and the BL with different compounds to obtain CZTS devices with enhanced performance, also using particular deposition techniques to obtain high-quality layers with limited thickness, such as *Atomic Layer Deposition* (ALD) or *Successive Ionic Layer Adsorption and Reaction* (SILAR), which are much more difficult to scale-up at the industrial scale. C. Platzer-Björkman *et al.* provided a good recap on this topic [45]: Table 7 reports solutions to improve the final PV device, with the parameters of the SC obtained with these solutions.

Table 7: Recap of combinations of BL and TCO, BL deposition methods and relative PV cell parameters obtained in the literature; the ARC is reported when used [45].

Front contact	Thickness [nm]	BL deposition method	BL material	CZTS Eg (eV)	V _{oc} (mV)	FF (%)	J _{sc} (mA cm ⁻²)	η (%)	ARC
i-ZnO/ITO	60/240	CBD	CdS		708	65.1	21.8	10	Yes
i-ZnO/ITO	60/240	CBD	CdS		731	69.3	21.7	11	Yes
ZnO:B		CBD	Zn-based		593	50.2	19.6	5.8	No
ZnO:B		CBD	In-based		653	53	18.3	6.3	No
i-ZnO/ITO	60/200	SILAR	CdZnS	1.5	748	63.2	19.5	9.2	0.3–0.4
i-ZnO/ITO	60/200	CBD	CdS	1.5	665	57.4	20.4	7.8	0.3–0.4
i-ZnO/ITO		CBD	In ₂ S ₃	1.4	621	54.5	20	6.9	No
IZO/ITO	60/200		In ₂ S ₃ /CdS		714	52.7	17.6	6.6	0.3–0.4
IZO/ITO	60/200		CdS		641	53.7	15.9	5.5	0.3–0.4
i-ZnO/ZnO:Al	80/200	ALD	Zn _{1-x} Sn _x O _y	1.55	746	68	19.1	9.7	Yes
i-ZnO/ZnO:Al	80/200	CBD	CdS	1.55	715	64	16.4	7.5	No
i-ZnO/ZnO:Al	80/200	ALD	Zn _{1-x} Sn _x O _y	1.64	778	56.4	16.3	7.1	No
i-ZnO/ZnO:Al	80/200	CBD	CdS	1.64	809	61.2	17	8.4	Yes
i-ZnO/ITO	50/210	ALD	Zn _{1-x} Sn _x O _y	1.5	720	63.5	20.4	9.34	Yes
i-ZnO/ITO	50/210	CBD	CdS	1.5	652	64.2	16.5	9.9	No

4.2.3.1. CZTS/CdS heterojunction

A crucial aspect of a good-quality p-n junction is the band alignment of the two materials that constitute the junction. The two materials, the absorber layer (p-doped) and the BL (n-doped), possess different band gaps and different **electron affinity**. When these two materials are in touch, they exchange charge carriers to put their E_F level at the same value and locally bend their band structure. In heterostructure junctions (heterojunctions), the band's alignment exhibits a step in the passage between the two CBs, called **CBO**. This offset can rise with two conditions, called *spike-like* CBO and *cliff-like* CBO, both represented and described in Figure 14.

From theoretic calculations [49], a spike-like CBO is considered a favourable condition in heterojunctions. However, the positive CBO must be lower than 0.4eV to avoid blocking phenomena for the photogenerated electrons that travel from the absorber layer to the BL, increasing recombination at the interfaces through defects. It has been observed that a higher positive CBO is quite detrimental, especially for FF and J_{SC} . Conversely, a cliff-like CBO is not optimal, since under the illumination condition, this feature creates a strong barrier at the interface for the minority charge carriers generated in the BL (electrons) and in the absorbers (holes), respectively. Once they are blocked at the junction, they recombine through the interface's defect states. The presence of these defects strongly reduces the V_{OC} of the device.

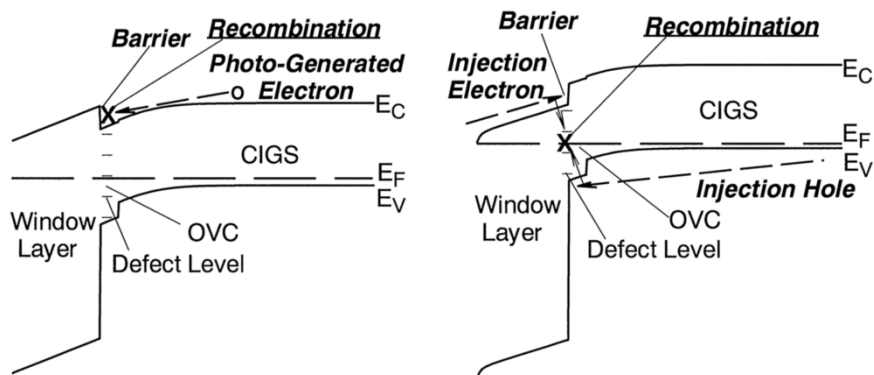


Figure 14: Band alignment scheme of the two band structures at the edge of the p-n junction for the heterojunction CIGS/CdS. Both spike-like and cliff-like CBOs are illustrated. At the interface are defect levels known as ordered vacancy compounds (OVC) [49].

Belonging to the same class of materials, CZTS SC are usually coupled with the same BL used for CIGS, a thin layer of CdS. Unlike what happens with CIGS, where the CIGS/CdS depict a CBO around +0.2/+0.3, in the literature, the sign and magnitude of CBO in the CZTS/CdS heterojunction is not well defined. The calculations convey a little negative CBO, leading to a cliff-like CBO, and experimentally, many values for CBO have been observed, both positive (+0.41eV[50]) and negative (-0.06eV[51], -0.33eV [52] e - 0.34eV[53]). The band alignment strongly depends on the interfacial quality of the junction, so the CBO also strongly depends on this feature. Surface passivation and/or a particular PDT could modify the behaviour of the p-n junction, leading to a different final CBO. Since the material's optimisation presents limits, many articles have investigated other solutions, trying to completely change the BL (also considering that a 'non-toxic' approach implies the substitution of CdS as BL). Some new solutions, such as Zn(O,S) and In_2S_3 [54], have been tested for BL with CZTS..

4.2.4. PDTs' studies and application

After the description of the material deposition and the discussion of the SC's project and realisation, we will now describe the kinds of PDTs studied in this PhD thesis and observed in the literature. Many PDTs have been tested on the CZTS-based SC in the literature, but we focused our attention on those that are more easily applicable to an industrial-scale production process to increase the final throughput of the full process. In particular, we focused on thermal treatments of the absorber materials (made at different stages of the device's realisation), chemical treatments of the absorber (to increase the quality of the absorber's surface before the realisation of the p-n junction and to reduce the secondary phase accumulations at the front surface) and the quenching treatment (where the CZTS TF is rapidly extracted from the furnace to freeze all the disorder phenomena already described in this Introduction).

4.2.4.1. Post-sulphurisation thermal treatments

Post-sulphurisation thermal treatments are a class of PDT that shows good results and correlations with the increase in the final CZTS-based SC performance, regardless of the CZTS deposition methods. As mentioned by *C. Platzer-Björkman et al.* [45], these processes consist of a thermal treatment at a temperature between 100°C and 400°C applied before the following steps of the production process: before the BL deposition, after the BL deposition and after the full device's realisation. Table 8 reports some PDT-related results, together with the PV parameters obtained before (in brackets) and after the treatment, while Figure 15 illustrates the effect of thermal PDT on a CZTS device that led to actual record efficiency [40].

Most of these treatments are performed after BL deposition since the effect of this treatment is multilevel. Together with the effects due to the order-disorder transition in the material, there are also cation migration effects at the interface, mainly due to the Cd motion from the CdS layer to CZTS and Zn from CZTS to CdS. This treatment also leads to a device with record efficiency [40]: In this case, a true chemical gradient for Cd and Zn has been observed between CZTS and CdS with the accumulation of Na and a depletion of Cu at the junction's interface. Interdiffusion led to formation at the interface of two mixed materials, $\text{Cu}_2\text{Cd}_x\text{Zn}_{1-x}\text{SnS}_4$ and $\text{Zn}_x\text{Cd}_{1-x}\text{S}$. This PDT improves the overall performance of these devices if performed both on the sole CZTS layer and on the formed heterojunction, but a higher increase in PV performance is obtained on the full p-n junction. For the full device treatment, the results are contradictory and depend on the starting device: SCs that show good PV performance will gain less (or even lose) PV efficiency compared to mediocre SCs that demonstrate a substantial increase in PV performance.

Table 8: Examples from the literature where a thermal PDT has been applied at various process steps on high-performance CZTS-based SC. Here are the devices' PV parameters before (in brackets) and after the PDT. For more in-depth details, see [45].

PDT application step	PDT parameters	V_{oc} (mV)	FF (%)	J_{sc} (mA cm ⁻²)	η (%)
CZTS	Laser dose: 34.5 J cm ⁻²	664 (674)	56 (56)	19.7 (18)	7.3 (6.7)
CZTS/CdS	Laser dose: 24.5 J cm ⁻²	536 (572)	60 (54)	17.4 (14.8)	5.6 (4.6)
CZTS/CdS	230°C	700 (720)	63 (43)	21.3 (16)	9.4 (5)
CZTS/CdS	270°C N ₂ 10min	730 (670)	65 (54)	21.7 (20.7)	11 (7.8)
CZTS/CdS/ZnO/ITO	270°C N ₂ 24h	702 (642)	43.1 (64)	16.3 (19.3)	4.9 (7.9)

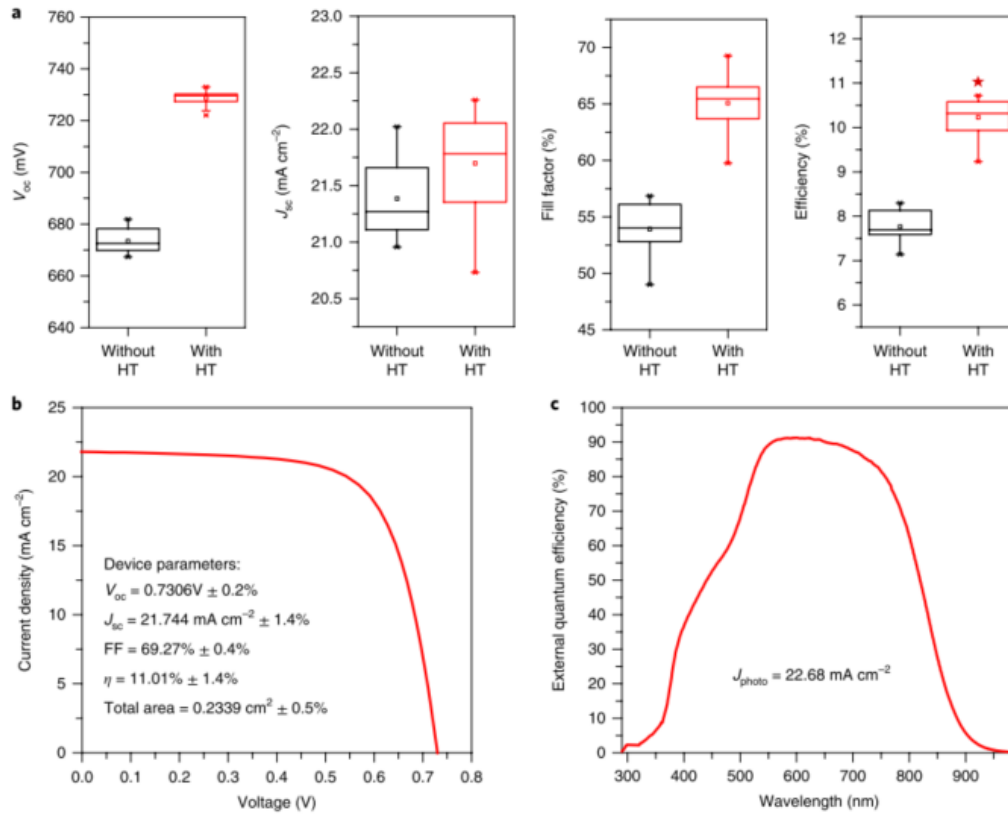


Figure 15: Above, the box plot describing the main PV parameters of the actual record CZTS-based SC (before and after the thermal treatment; below, the J-V curve (on the left) and EQE curve (on the right) of the record device after the thermal treatment [40].

4.2.4.2. Chemical treatments for the removal of secondary phases

Together with thermal treatments, a variety of chemical treatments have been tested to selectively remove secondary phases from the surface of CZTS materials to enhance the quality of the CZTS/CdS interface. Some examples of etching used in the literature are KCN for the selective removal of Cu_{2-x}S ; KMnO_4 , H_2SO_4 , Na_2S and HCl for ZnS and NH_3 to remove oxides. Other solutions, such as HBr and $(\text{NH}_4)_2\text{S}$, have been used for non-selective treatments on the surface of CZTS to remove a few atomic layers and prepare the surface of the material for CdS deposition.

In particular, the KCN treatment is widely used to etch the CZTS surface because both the main and secondary phases are removed from the surface, greatly improving its quality. The deep knowledge of this process, due to its application for CIGS TF SC, has further driven the wide usage of this treatment for CZTS [45], though the usage of this compound should be limited to a 'green' high throughput application due to its severe toxicity. An oxidative treatment with bromine creates an ultrathin layer of SnO_x that passivates the surface of the material, increasing the efficiency of the final device [39]. This also opens the application of ultrathin layers of dielectric materials to increase the performance of the CZTS/CdS interface.

4.2.4.3. Quenching effect and order-disorder transition

As described, cooling control is a crucial aspect for avoiding the phenomenon of exchange between Cu and Zn, which leads to an ordered (or disordered) crystalline structure [10]. We previously discussed the existence of a T_c (around 260°C) where this transition starts to happen. The rapid cooling of samples from

above this temperature, for example extracting the samples from the hot oven (higher than this temperature) to RT air, should *quench* the sample temperature, kinetically blocking the crystalline structure in the disordered state. This is reflected in the vibrational states of the material and depicts a difference in the relative height of the Raman spectrum between the quenched and the unquenched samples. Figure 16 conveys the comparison between Raman spectra (taken at two laser wavelengths) obtained by stoichiometric powders synthesised at 750°C and cooled with two regimes: a **very slow regime (VS)**, where the cooling is defined by the ramp set of the oven (10°C/h), and a **very fast regime (VF)**, where the still-hot samples are put in a cooling bath of ice and water [10].

The samples illustrate Raman spectra depending on the cooling ratio and laser wavelength. The disordered structure causes a general broadening of the peaks, and some disparities in relative height are visible. This variation in Raman spectra, together with the E_g variation already discussed, are the two main markers for the identification of the order grade of the material. Unfortunately, the laser used for Raman spectroscopy in this PhD thesis is the one at 663nm for CZTS, so no direct comparison with these spectra will be discussed. Nonetheless, a variation in these spectra has also been observed with the E_g value, so we will connect this variation to the order–disorder transition.

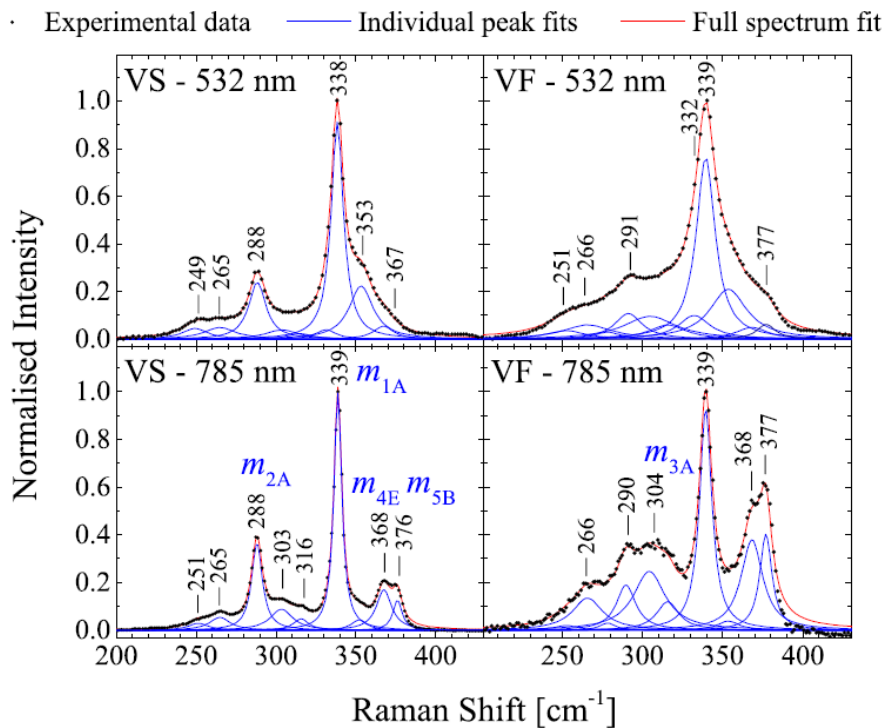


Figure 16: Raman spectra of stoichiometric CZTS powder samples obtained at 750°C and cooled with different ratios. The very slow regime (VS spectra) is obtained with a cooling trend of 10°C/h to induce the formation of ordered crystal structures, while the very fast regime (VF spectra) is obtained with a cooling trend that is difficult to define (hot samples put in a bath of ice and water) to induce the formation of disordered structures. The spectra are obtained with two laser wavelengths, 532nm and 785nm, and the peak deconvolution is displayed [10].

4.3. KESTERITE MONOGRAIN PRODUCTION

In this section, we will discuss the main properties of the technique for growing chalcogenide MGLs employed by the Laboratory of Photovoltaic Materials of Tallinn University of Technology (TalTech), where the researcher conducted a period abroad.

Monograin consists of a powder made of single-crystal grains or several single-crystal blocks grown into compact grains. The MGL SCs present a superstrate structure of graphite/MGL/CdS/i-ZnO/glass, where the MGL is a monolayer of powder grains of a determined size incorporated into an organic matrix, so the upper part of the grains remains uncovered. CdS was deposited by chemical bath deposition on the MGL or on the surface of the grains before MGL formation, followed by the RF sputtering of the i-ZnO and AZO layers. Finally, a metal grid was evaporated on the TCO, and the structure was glued onto a durable transparent substrate. For back contact, the bottom surface of the MGL was polished to expose monograins before applying the graphite contact. The research group began working to create and commercialise modules for CZTSSe MGL SCs in 2008 and has continued in collaboration with the TalTech spin-off company crystalsol OÜ.

4.3.1. Monograin growth process

The growth of monograin powders uses a **liquid inorganic salt**, also defined as molten flux or molten sand. Conducting reactions at a higher temperature than the melting point of the molten sand but lower than the melting point of the final product of the reaction acts as liquid media, where the reaction shows a lower process temperature and higher reaction speed. The start of this reaction can continue along two paths:

- The precursors completely dissolve in the molten media, where the nuclei of the reaction product are formed directly in the liquid phase.
- Low-solubility compounds react together, producing the nuclei of the product that grow more through Ostwald ripening [55].

In both cases, the growth of MG powders proceeds through liquid-to-solid crystallisation. The selection of the proper molten sand and the proper reaction temperature is crucial for the process. As for the ratio between precursors and molten flux volume, the liquid phase volume must be higher than the voids between the precursors' powders. To respect this condition, the ratio of solid volume V_s and liquid volume V_L usually is between 0.6 and 1. After synthesis, the powder must be washed with a suitable solvent to remove the molten sand before being dried and sieved to separate the grains by granulometry. Figure 17 depicts an example of an MGL-based SC structure, where the big monograins are clearly visible, and an SEM image of a sieved MG sample, where the dimensions of the single grains are quite similar.

Research started with CIS MG powders obtained in the 1990s [56] from various molten fluxes, such as Se, CuSe and a mixture of these compounds. Due to the difficulties of removing these compounds from the surface of the powders, other compounds have been tested, with KI being the most effective [57] due to its low hygroscopicity and low solubility in CIS. After CIS, researchers continued with CZTSe and CZTS [58, 59], and the use of other molten sand has been investigated, such as NaI and CdI₂ [60, 61].

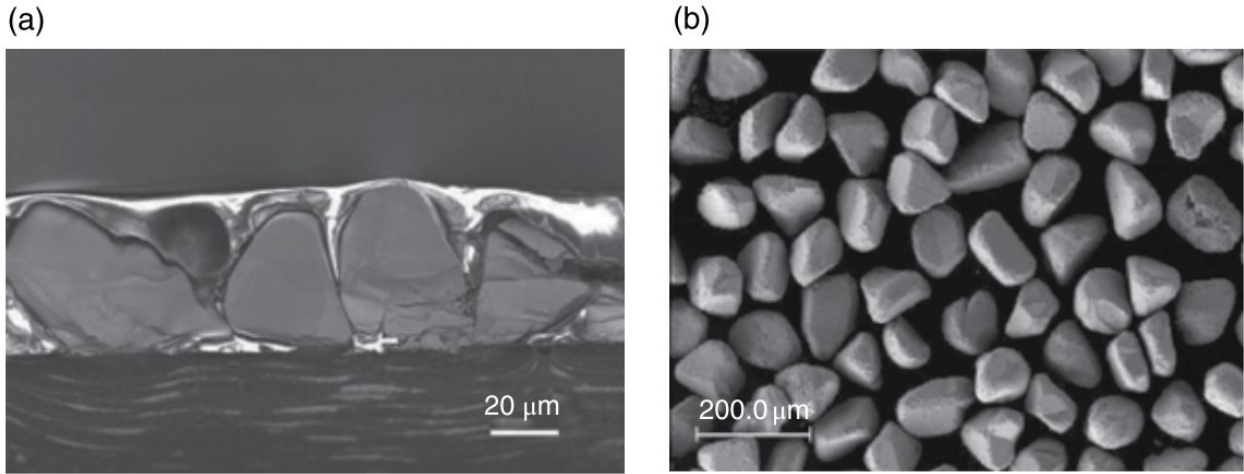


Figure 17: a) Cross-section SEM image of an MGL SC and b) SEM image of the CZTSSe MG sample obtained by KI molten flux [62].

In these samples, the correlation was examined between the composition of the precursor powder and the final composition of the kesterite material and secondary phase formation [63]. Figure 18 conveys the correlation between the compositional ratios of precursors and the compositional ratios of MG powders, respectively, in a Zn-rich condition (Figure 18-a) and in a Cu-constant condition (Figure 18-b). Figure 19 illustrates two cross-section images of samples with high Cu content under these two conditions.

In a Zn-rich condition, the increase of $[Cu]/[Zn]+[Sn]$ in precursors' powder caused a reduction of $[Zn]/[Sn]$ and the appearance of the $Cu_{1-x}S$ phase when $[Cu]/[Zn]+[Sn]>0.96$. Meanwhile, in a constant-Cu condition, switching from an Sn-rich to a Zn-rich condition caused the formation of ZnS inside the grains. All these observations agree with the work of *Oleksieuk et al.* [26], as mentioned.

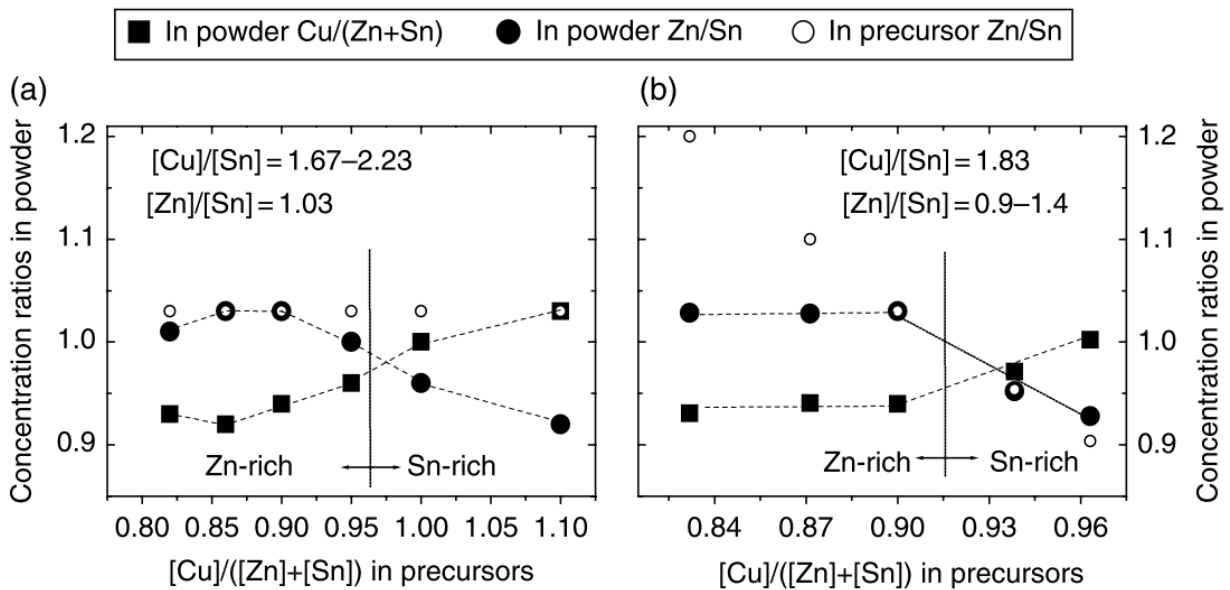


Figure 18: a) Compositional ratios of CZTS samples with different $[Cu]/[Zn]+[Sn]$ ratios in a Zn-rich condition and b) compositional ratios of CZTS samples with different $[Cu]/[Zn]+[Sn]$ ratios in a Zn-rich condition [63].

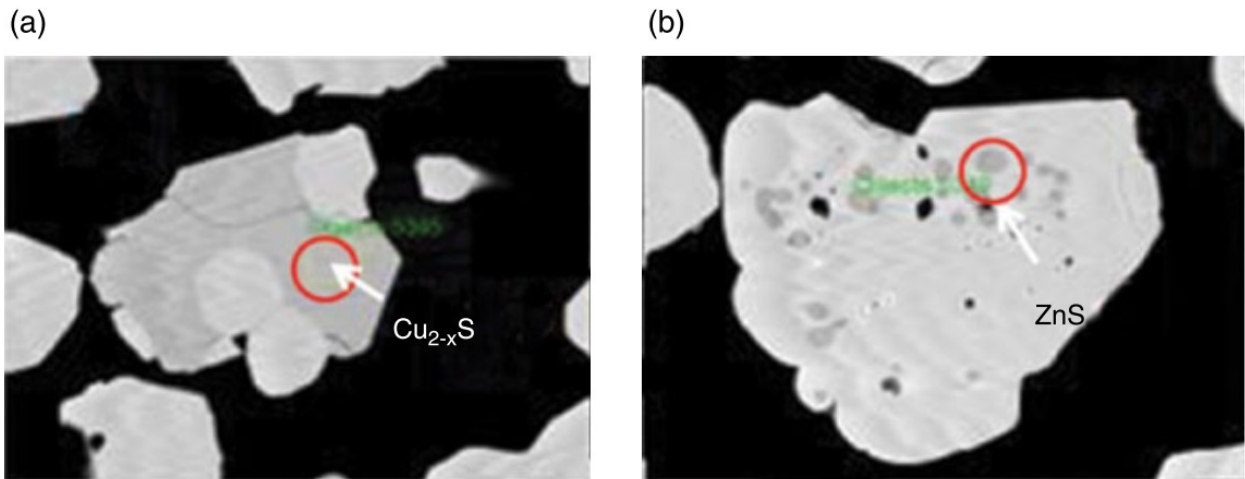


Figure 19: a) Cross-section SEM image of a CZTS MG sample in the Cu-rich condition with $[Cu]/[Zn]+[Sn]>0.96$ and b) cross-section SEM image of a CZTS MG sample in the Zn-rich condition with $[Cu]/[Zn]+[Sn]<0.91$ [63].

Many other PDT can be applied to these materials to increase the final efficiency of the MGL as an absorber layer, similar to chemical etching [64] or surface treatments at high temperatures in the presence of S and/or SnS [65]. All these optimisation processes can lead to a final PV device with a J–V curve similar to the one in Figure 20 [62].

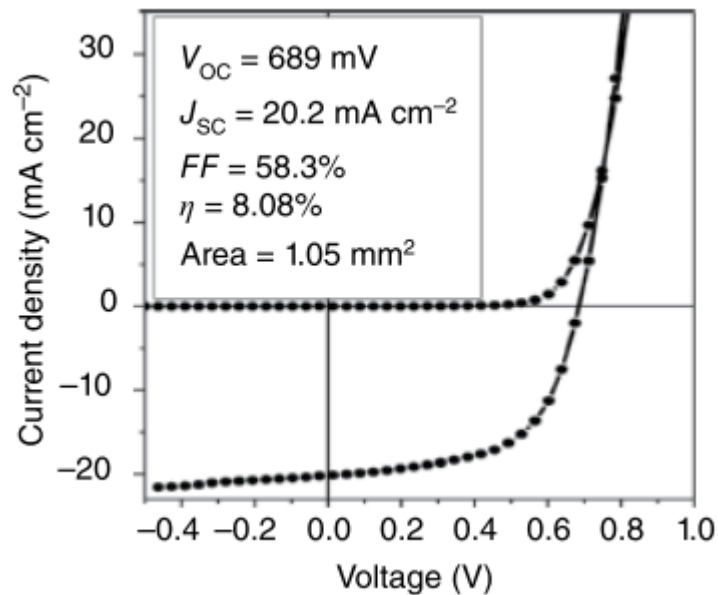


Figure 20: Performances of a single-grain CZTS-based SC [62].

4.4. CFTS TF

In this section, we will discuss the main properties of CFTS obtained around the world to define the state of the art for this material. As we have already done for CZTS, for CFTS, we will discuss the main features that are useful for this material application in PV devices, from material characterisation to the results obtained in the few works where an SC has been obtained. Features such as chemical and physical properties, growth methods and the application of the CFTS TF as an absorber layer will be discussed herein.

4.4.1. Material properties

The chemical and physical properties of CFTS analysed for this section have been gathered from the literature that discusses CFTS samples with natures that depart from TF, such as studies on nanoparticles and natural compounds (e.g. mineral stannite). Only a handful of parameters have been analysed, focusing on the ones that are important for the PV application of CFTS, as follows:

- Crystalline structure: This feature can be studied using XRD to identify in our samples the formation of the CFTS phase and to confirm the absence of possible secondary phases.
- Optoelectronic properties: These features can be studied using optical analysis, such as UV–Vis analysis and PL, mainly to understand the band gap energy (E_g) and the behaviour of electrically active defects.
- Secondary phase identification: Obtained by Raman spectroscopy and XRD analysis.
- Oxidation state of the elements that form our samples: Attained by XPS, used especially to study the different oxidation states of Fe (Fe^{2+}/Fe^{3+}).

CFTS can be found in nature as a mineral compound named stannite, in which Zn substitutes for part of the Fe cations, forming a pseudobinary system between CZTS (kesterite) and CFTS (stannite). There are several articles in the literature in which the parameters of the crystal structure are studied following the variation of the ratio $[Fe]/[Zn]$ in these systems.

4.4.1.1. Crystalline structure and secondary phases

The chemical composition of minerals that belong to the stannite group can be generalised in the brute formula $M1_2M2^{(II)}M3^{(IV)}S_4$ (with $M1=Cu, Ag \text{ o } In$; $M2=Fe, Cu, Zn, Cd, Mn \text{ o } Hg$ and $M3=Sn \text{ o } Ge$). The crystal structures of these minerals and their relative compounds are based on the structure of sphalerite (ZnS_{cub}). Three metallic cations ($M1, M2$ and $M3$) occupy iso-oriented tetrahedral positions inside a compact structure of sulphur atoms. A different order of occupation of these tetrahedrals leads to two similar but separated structures, stannite and kesterite, shown in Figure 21 [66] below, and the rarer velikite, identified only in Cu_2HgSnS_4 [67]. The two main structures, stannite and kesterite, demonstrate the symmetry group $(I-42m)$ e $(I4)$, respectively, two similar groups. The difference between these groups can be found in the divergent distribution of metallic cations in tetrahedral sites. Interestingly, stannite has the same symmetry group as the disordered phase of kesterite. The symmetry group of this structure is $(I4)$, and it results from an exchange in the positions between Cu and Zn cations while all the sites of the Fe cations are occupied by Cu. Particular types of cation exchange have been observed in the kesterite structure and are associated with the ‘order–disorder’ transitions activated by thermal processes at low

temperature, that is $\approx 250^\circ\text{C}$ [9, 10]. Consequently, CZTS can present order variations that can stimulate the presence of both crystal structures, even if the kesterite structure is connected to this material. However, for CFTS, the topic is more complex due to the presence of both synthetic and natural compounds, the stannite mineral, which is used for the crystal structure of this kind of chalcogenide. The synthetic compound can show different crystal structures due to the production process parameters, in particular depending on the thermal treatment temperature, where it is possible to observe cubic structures [67, 68] that can transform, reversibly or not, into tetrahedral structures depending on the disorder level of the site's occupation. Identifying these structures and studying the transitions between them are extremely complex due to the slow kinetic speed of these processes, which, with the timespan of geological events, leads to the result of natural tetragonal stannite. In the literature, we have found works studying the CFTS crystalline structure since the 1960s, and we can find this knowledge summarised in many articles [66-69]. For a better interpretation of XRD analysis on CFTS in this PhD thesis, the reader is referred to data from [67] and [68].

Many efforts have been made to identify the possible polymorphs into which CFST can organise, especially as a function of high-temperature thermal treatment. A temperature of around 570°C is interesting for the purpose of this PhD thesis, as this temperature is used to synthesise CZTS in the first part of this thesis. This maximum temperature is also limited to the mechanical properties of the soda lime glass substrate at that temperature when the glass starts to deform. The data available in the literature are unfortunately contradictory because many works do not depict enough information about the final composition of CFTS TF: This parameter is critical due to its connection to the crystal phase obtained in the final sample after thermal treatment. The structure of potential crystallographic configurations (polymorphs) and the relative content of these configurations in CFTS samples with stoichiometric conditions are topics to be further investigated, and the possibility of a structure's evolving to a cubic crystal structure is still unknown.

Most of the literature on crystal structures can be summarised with three phases observed in synthetic CFTS in the temperature range between 420°C and 820°C :

- **The cubic phase associated with $\text{Cu}_2\text{FeSnS}_{3.95}$** (cubic spatial group: I-43m, $10.837 < a < 10.85 \text{ \AA}$) is stable in the interval $420^\circ\text{C} < T < 500^\circ\text{C}$. Compounds that possess compositional range from $\text{Cu}_5\text{Fe}_{2.5}\text{Sn}_{2.5}\text{S}_{10}$ (=CFTS) to $\text{Cu}_{5.3}\text{Fe}_{2.3}\text{Sn}_{2.4}\text{S}_{9.8}$ ($=\text{Cu}_{2.16}\text{Fe}_{0.94}\text{Sn}_{0.98}\text{S}_4$), show this structure at temperatures equal to 500°C .
- **Stannite with a tetragonal structure** similar to chalcopyrite is stable for composition near $\text{Cu}_2(\text{Fe,Sn})_2\text{S}_{3.9}$ ($a=5.42 \text{ \AA}$, $c=10.70 \text{ \AA}$, $c/a=1.97$) for samples realised at a temperature equal to 600°C .
- **An intermediate phase** for compositions ranges from $\text{Cu}_{5.2}\text{Fe}_{2.3}\text{Sn}_{2.5}\text{S}_{10}$ to $\text{Cu}_{5.6}\text{Fe}_2\text{Sn}_{2.4}\text{S}_{9.7}$ with unknown cell symmetry, obtainable from the transformation of the cubic phase with thermal treatments at temperatures in the range of $580\text{--}600^\circ$.

From *Evstigneeva et al.* [67], notably, only two CFTS polymorphs can switch between each other, and this transition occurs around 565°C . These two polymorphs have been studied by *Ohtsuki et al.* [68], and they have been identified as cubic stannite 'at low symmetry' (*cubic 'low stannite'*, $a_0=10.838 \text{ \AA}$) and tetragonal stannite 'at high symmetry' (*tetragonal 'high' stannite*, $a_0=5.454 \text{ \AA}$, $c=10.735 \text{ \AA}$).

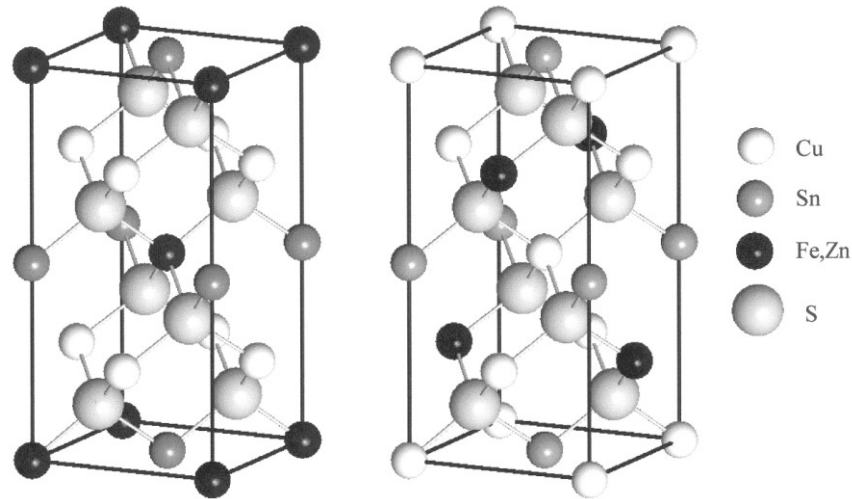


Figure 21: structure of stannite (left) and kesterite (right) for both CZTS and CFTS [69]

Ohtsuki *et al.* [68] synthesised CFTS crystals from sulphide compounds of the metallic precursors sealed in a quartz vial, with stoichiometric condition. The synthesis process has been performed with temperature from 350°C to 600°C and with a time span from 7 to 30 days. The target of the experiment was to evaluate the effects of very long treatments, simulating the natural process that creates the stannite mineral. These tests have been performed not only for CFTS but also for other formulations, like Stannioide ($\text{Cu}_8\text{Fe}_3\text{Sn}_2\text{S}_{12}$), Mawsonite ($\text{Cu}_6\text{Fe}_8\text{Sn}_8\text{S}_8$) e Rhodostannite ($\text{Cu}_2\text{FeSn}_3\text{S}_8$). For CFTS, the first part of the experiment has been performed with a treatment at 500°C with various treatment steps for a total of 30 days, alternating treatment phases with milling phases and sealing in new quartz vials. The obtained samples showed a cubic structure, which diffractogram shown peaks summarized in Figure 22 (left) corresponding to a theoretical cubic compound with cell parameter $a = 10.838(1)\text{Å}$ that are summarized in Figure 22 (right). The centre of Figure 22 summarizes the results on the samples growth at 600°C for 14 days that showing a tetragonal structure with cell parameters equal to $a = 5.454(1)\text{Å}$ e $c = 10.735(1)\text{Å}$.

In this work, together with the XRD analysis, are shown results about measures of *Differential Scan Calorimetry* (DSC) to study the phenomena around the transitions between these two crystal structures with temperature dependence; from these analyses it is noted that:

- For cubic sample, only one peak is present at 855°C, linked to coherent fusion of the material,
- No endothermic or exothermic process is visible at 565°C, temperature at which is confirmed the presence of the transition between cubic and tetragonal structures (by separate tests); authors suggest that the transition kinetic is too low to show any evidence in the DSC analysis,
- The cubic structure is stable from 350°C to 565°C.

Other analyses have been made on the sample that has been growth at 600°C, but they are not interesting for this PhD thesis, since the temperature selected for the thermal process used during the test is below 600°C due to substrate melting point.

d(obs.)	I/I ₀	d(calc.)	d(obs.)	I/I ₀	d(calc.)	hkl	d(obs.)	I/I ₀
5.416	20	5.419	5.370	6	5.368	002	5.365	3
3.833	10	3.832	5.297	4	-	-	-	-
3.128	100	3.129	3.859	6	3.856	110	3.848	3
2.7104	35	2.7094	3.132	100	3.132	112	3.131	100
2.4247	10	2.4233	2.7269	15	2.7269	020	2.7251	8
2.1973	6	2.2122	2.6860	6	2.6838	004	2.6856	5
1.9150	95	1.9158	2.4323	6	2.4311	022	2.4281	3
1.8071	4	1.8063	2.3054	2	-	-	-	-
1.7143	3	1.7136	2.2036	3	2.2028	114	2.2029	2
1.6347	75	1.6338	1.9287	35	1.9282	220	1.9266	25
1.5647	10	1.5643	1.9132	55	1.9128	024	1.9135	30
1.5033	2	1.5029	1.8131	2	1.8146	222	1.8124	1
1.4491	3	1.4482	1.7257	1	1.7246	130	1.7241	1
1.3552	20	1.3547	1.6426	35	1.6419	132	1.6411	20
1.3139	3	1.3142	1.6236	15	1.6230	116	1.6236	10
1.2769	2	1.2772	1.5664	7	1.5659	224	1.5653	3
1.2429	40	1.2432	1.4509	2	1.4509	134	1.4480	1
1.2117	10	1.2117	1.3639	7	1.3634	040	1.3617	3
1.1823	2	1.1825	1.3415	3	1.3419	008	1.3422	2
1.1554	1	1.1553	1.3210	1	1.3215	042	-	-
1.1058	45	1.1061	1.3119	1	1.3115	226	-	-
			1.2501	10	1.2501	332	1.2490	5
			1.2419	15	1.2417	136	1.2417	7
			1.2208	2	1.2195	240	1.2181	1
			1.2156	2	1.2156	044	-	-
			1.2039	2	1.2040	028	1.2065	1
			1.1588	1/2	1.1593	334	-	-
			1.1100	15	1.1102	244	1.1096	7
			1.1014	8	1.1014	228	1.1014	3

Figure 22: On the left, diffraction peak positions (expressed as the interplanar distance d_{obs}) determined from an XRD analysis of CFTS powders obtained with a thermal treatment at 500°C and the calculated values of a simulated cubical structure with the cell parameters $a=10.838(1)$ Å. In the centre, diffraction peak positions (expressed as interplanar distance d_{obs}) are determined from the XRD analyses of CFTS powders obtained with thermal treatments at 600°C. Together, the calculated tetragonal diffraction values of a simulated cell parameter $a=5.454(1)$ Å and $c=10.735(1)$ Å. On the right, diffraction peak positions (expressed as interplanar distance d_{obs}) for a natural stannite are taken as a reference with a tetragonal structure [68].

The cubic structure observed in samples treated under 565°C by *Ohtsuki et al.* has also been witnessed by *Evstigneeva et al.* for sample growth with the same technique, treating the samples at 400°C for 17 days. In this case, an alternative cubic structure was speculated, with the reticular parameter $a=5.4179(3)$ Å, a value half that observed by *Ohtsuki et al.* with symmetry group $P-43m$. This structure was defined as ‘isostannite’, where a partial disorder of the cation site’s occupation was observed. Fe and Sn are organised in the same cubic structure with the ratio $\text{Sn:Fe}=2:1$, while the body-centred positions are occupied by all the cations with the ratio $\text{Cu:Fe:Sn}=1.86:0.44:0.33$. *Evstigneeva et al.* pointed out that the complexity of the crystal structure’s organisation of CFTS arises from a lack of compositional studies together with XRD studies to limit the span of existence of different structures.

As for the crystallographic properties of other secondary phases that can be synthesised during CFTS growth as secondary and ternary compounds, we have discussed them in the CZTS section. Here, we merely report the phase diagram in the Cu-Fe-S system in Figure 23 to point out the higher complexity of this system compared to the Zn-related one, as reported by *Cabri* [70].

The exploration of the main and secondary phases was performed by XRD analysis and Raman spectroscopy, as performed for the CZTS samples. Figure 24 reports the XRD analysis of CFTS samples obtained using the sputtering technique in the literature [71-73] and the results obtained on samples synthesised by the SILAR technique [74], which holds the record CFTS-based PV device with an efficiency of 2.95%.

a-bn? = anomalous bornite
 an = anilite $Cu_{1.75}S$
 bbcv? = blaubleibender covellite $Cu_{1.1}S$
 bn = bornite Cu_5FeS_4
 cc = chalcocite Cu_2S
 cp = chalcopyrite $CuFeS_2$
 cv = covellite CuS
 cb = cubanite $CuFe_2S_3$
 di = digenite Cu_9S_5 , $(Cu, Fe)_7$
 dj = djurleite $Cu_{1.96}S$
 fk = fukuchilite Cu_3FeS_8
 gr = greigite Fe_3S_4
 hc = haycockite $Cu_4Fe_5S_8$
 h-po = hexagonal pyrrhotite Fe_9S_{10}
 id = idaite Cu_3FeS_4
 mk = mackinawite $Fe_{10}S_5$
 ma = marcasite FeS_2
 mh = mooihoeite $Cu_9Fe_9S_{16}$
 m-po = monoclinic pyrrhotite Fe_7S_8
 py = pyrite FeS_2
 sm = smythite Fe_3S_4 and $Fe_{3.3}S_4$
 tal = talnakhite $Cu_9Fe_8S_{16}$
 tr = troilite FeS
 ? probable new mineral Cu_5FeS_6
 ?? new mineral ? $Cu_{0.12}Fe_{0.94}S_1$
 □ Synthetic $Cu_3Fe_4S_6$

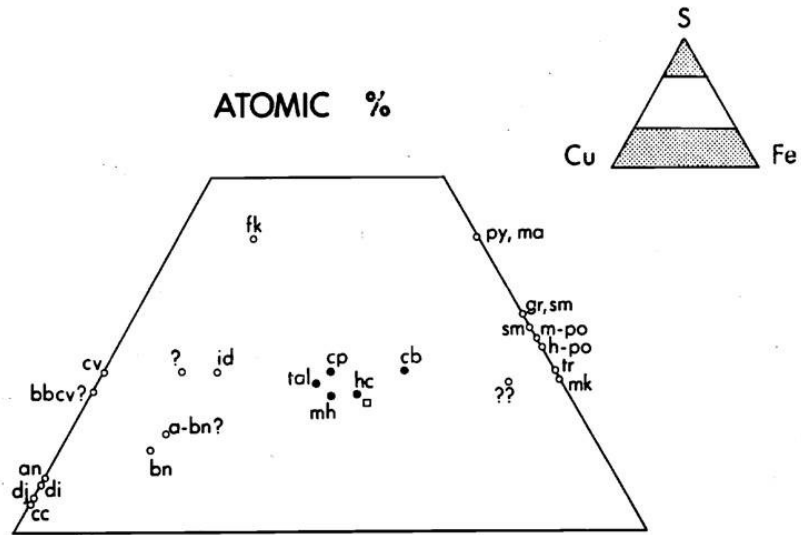


Figure 23: Part of the phase diagram of the Cu-Fe-S system (in the compositional range $25 \leq Cu \leq 60$, $35 \leq S \leq 70$ and $0 \leq Fe \leq 65$ [at.%) and the list of stable secondary phases [70].

From these images, we can observe that only a few reflections are visible, hindering the complete recognition of the main phase. We can connect this to the low dimension of crystallographic coherency due to the formation of small grains. The sample with the highest crystallinity was prepared by SILAR, which explains the higher PV performance in the correlated device. Another problem due to the low quality of the material is the impossibility of separating the tetragonal structure from the cubic structure. In most of the literature, the reasons for this issue refer to the tetragonal structure, as expected.

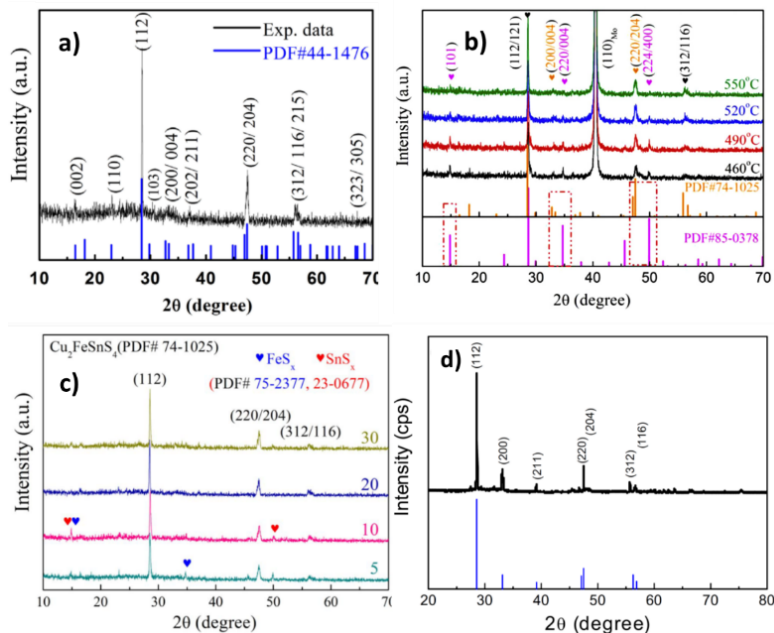


Figure 24: a), b) and c) XRD analysis of CFTS samples obtained using the sputtering technique [71-73]. d) XRD analysis of the CFTS sample obtained using the SILAR technique, which holds the record for CFTS SC efficiency [74].

From these images, we can observe that only a few reflections are visible, hindering the complete recognition of the main phase; we can connect this to the low dimension of crystallographic coherency due to small grain formation. The sample with the highest crystallinity was prepared by SILAR, which explains the higher PV performance in the correlated device. Another problem due to the low quality of the material is the impossibility of separating the tetragonal structure from the cubic structure. Most of the literature explains the reason for this issue as the tetragonal structure, as should be expected.

Figure 24-b) also illustrates the presence of a secondary phase visible in the XR diffractogram identified as Rhodostannite, which is identified due to a few reflections that do not belong to the main phase (this compound is identified with the code #85-0378 in the image).

As for CZTS, XRD analysis is usually coupled with Raman spectroscopy to identify phases with similar crystal structures or amorphous compounds. Table 10 and Table 11 report the Raman peaks observed in the relative spectrum with the nature of the sample and the deposition method. To further investigate this topic, we report in Figure 25 the Raman spectra of CFTS samples obtained by assorted techniques, that is, sputtering [73], SILAR [74] and microcrystal growth [75]. From these images, we can affirm the following:

- Only the main peak at 318cm^{-1} has been univocally identified for the CFTS phase in real samples. This is quite particular to this material (unlike CZTS, which depicts many peaks) and makes it easier to identify disparate peaks connected to disparate phases.
- No order–disorder transitions have been observed in the literature for this material, which corroborates the assumptions of this PhD thesis with what is described in the literature [13, 76, 77]

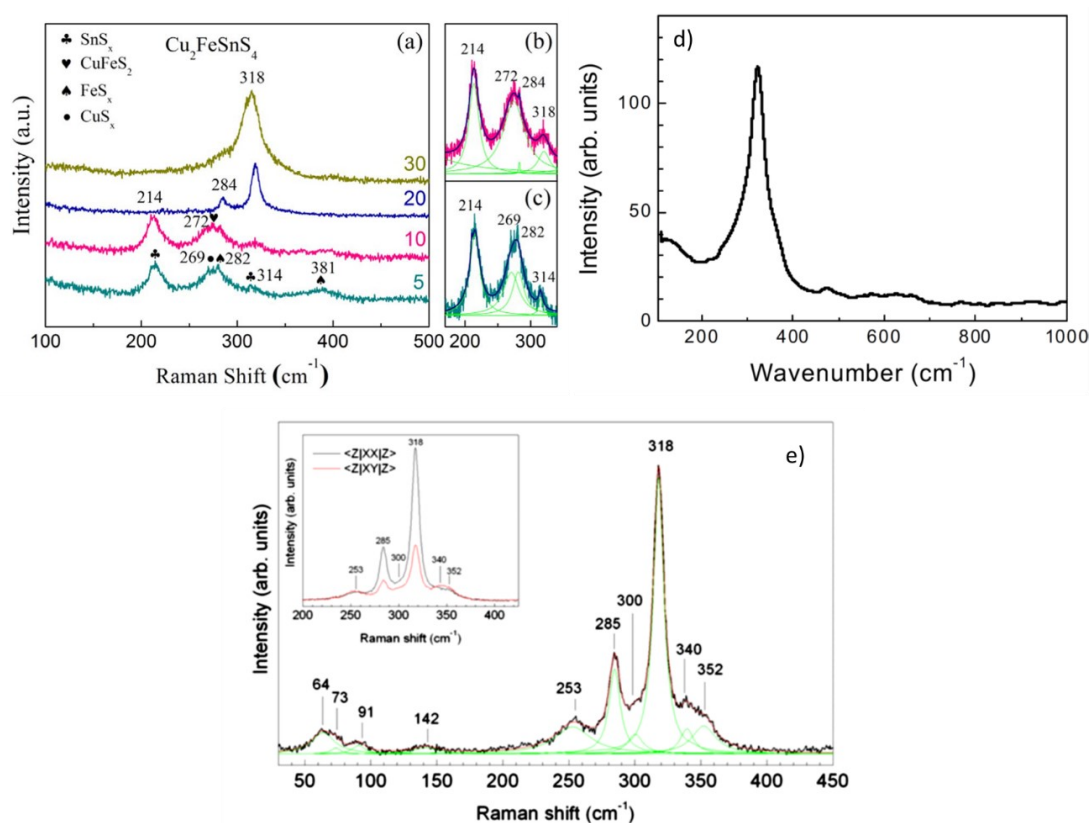


Figure 25: Comparison between Raman spectra of CFTS samples obtained using the sputtering technique a), b) and c) obtained at diverse sulphurisation process durations [73] using the SILAR technique (d) [74] and in microcrystal form [75].

4.4.1.2. Optoelectronic properties

The energy gap is particularly interesting for the application of a material as an absorber layer in PV devices. For CFTS, the E_g values found in the literature are dispersed in a wide range, strictly correlating with the deposition method used. Correspondingly, E_g values range from 1.22eV (*Guam et al.* [78]) in a CFTS obtained by 'hot injection' to 1.87eV (*Ghosh et al.* [79]) in a CFTS obtained by spin coating. A wide literature review of CFTS E_g values was conducted by *Vanalakar et al.* [80]. In this work, CFTS samples are classified into two main groups: NP and TF (a summary of the E_g of these materials is reported in Table 10 and Table 11).

In summary, it has been observed that:

- All samples presented tetragonal structures similar to stannite or kesterite.
- No cubic structure was observed in any sample in this work, so only E_g for tetragonal structures was reported.
- For sputtering techniques, only the work of *Meng et al.* [71] conveys an E_g value equal to 1.4eV.

As for the optoelectronic properties of the secondary phases that can arise during CFTS production, most have the CZTS case in common, such as Cu_xS , SnS, Cu_2SnS_3 etc. To these, we must add Fe-related compounds such as iron sulphides with a wide compositional range, the characterisation and study of which can be found in *Lennie et al.* [81]. In general, from the analysis of the secondary phases for the Cu-Fe-Sn-S system, the number of cases was exceedingly higher than for CZTS. These premises, with the analysis of possible CFTS crystal structures, make us believe that there are no easy analyses and interpretations of the results obtained for this material.

As for CZTS, the limitation of conductive secondary phase formation in our system is essential. Phases such as $Cu_{1-x}S$ (unique conductive compound in the CZTS secondary phase pool) and iron sulphides are detrimental to the behaviour of CFTS as an absorber layer in PV devices, and their formation must be prevented. Choosing the process parameters to obtain Cu-poor and Fe-poor compositions for CFTS could be a way to avoid these phases' formation, even though these conditions could lead to Sn-rich secondary phases, which are far less problematic.

4.4.1.3. Fe oxidation state: XPS analysis

In the specific case of CFTS, another analysis has been used in the literature to monitor the behaviour of the realised TFs: XPS characterisation. This technique investigates the BE of valence electrons and provides information about the chemical nature and environment of a chosen element in the material. For CZTS, this technique is not useful per se, since every element presents fixed oxidation states (Cu^{1+} , Zn^{2+} , Sn^{4+} and S^{2-}). However, for CFTS, this technique can expose problems related to Fe oxidation states (since the most stable oxidation state for Fe is 3+).

Figure 26 exemplifies the CFTS XPS spectrum obtained by *Chatterjee et al.* [74] on the material that demonstrated the best PV performances, together with an enlargement of this spectrum to illustrate the signals of the elements that constitute the chalcogenide material (relative to Cu 2p, Fe 2p, S 2p and Sn 3d orbitals). While a check of every one of these signals is relatively important, the most useful region is the one relative to the Fe signals. From the fitted peak position of the two Fe-associated peaks at BE values of 710.3eV and 724.0eV (for $Fe2p_{3/2}$ and $Fe2p_{1/2}$, respectively) the authors confirm the presence of Fe^{2+} in the

structure, comparing these values with the ones reported in other works in the literature, as displayed in Table 9 [82].

Table 9: BE position (in eV) of Fe-related XPS peaks (Fe2p_{1/2} and Fe2p_{3/2} with relative satellite peaks and Fe3p), together with their oxidation states and chemical environment [82].

Compound	Oxidation state	Fe2p				Fe3p
		Fe2p _{1/2}	Fe2p _{1/2} satellite	Fe2p _{3/2}	Fe2p _{3/2} satellite	
Fe	0	719.85	–	706.70	–	52.25
FeS ₂	+ II	720.05	–	707.15	–	53.30
FeO		723.35	729.15	709.85	715.50	??
FeCO ₃		724.20	728.50	710.50	715.00	55.00
FeSO ₄		724.30	728.90	711.00	715.30	55.40
Fe ₃ O ₄	8/3	723.70	–	710.60	–	??
FeOOH	+ III	723.80	732.40	710.20	718.70	55.60
Fe ₂ O ₃		724.40	732.70	710.95	719.00	55.55
Fe ₂ (SO ₄) ₃		726.65	732.30	713.25	718.95	57.35
Ferrihydrite		724.55	732.60	710.80	718.85	54.95

Trifiletti *et al.* [83] add new information about the Fe oxidation state in CFTS due to air exposure: Figure 27 demonstrates the spectra of samples of Cu₂(Fe_xZn_{1-x})SnS₄, with different x values, obtained in air or in an inert atmosphere (the condition obtained from the deposition of the material in a nitrogen-filled glovebox). The same figure contains an inset of these spectra in the Fe-related and O-related regions. The authors affirmed two statements: Fe atoms are present as Fe²⁺ and Fe³⁺ inside the material, unlike what happens for CZTS, where Zn is present just as Zn²⁺. In addition, the presence of O correlates to the formation of different compounds based on Fe, such as iron oxide and hydroxide. The presence of these compounds is lower in samples obtained in gloveboxes, demonstrating that this material can be easily contaminated by atmospheric oxygen, which is detrimental to PV performance.

These two examples depict the usefulness of the XPS technique in investigating the chemical properties of CFTS TF samples. Nevertheless, the limited access to this technique (due to the expensive characterisation device) and the difficulties in the detailed interpretation of the obtained spectra, especially in complex samples where the presence of many chemical species is observed, limit the wide usage of the XPS technique as a routine characterisation. Even so, a spot application of XPS characterisation on a few samples can be useful for understanding qualitative differences between production conditions.

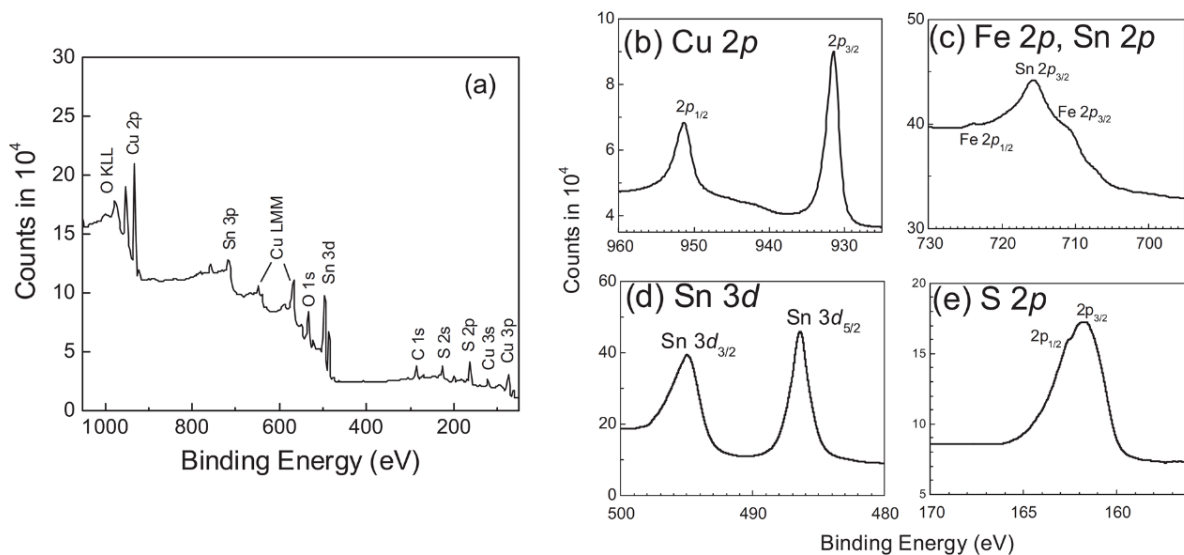


Figure 26: a) The total XPS profile of the XPS analysis of a sample obtained by SILAR, which holds the actual record for PV devices, together with the peaks relative to the single-element orbitals connected to the CFTS material, that is Cu2p, Fe2p together with Sn2p, Sn3d and S2p, respectively [74].

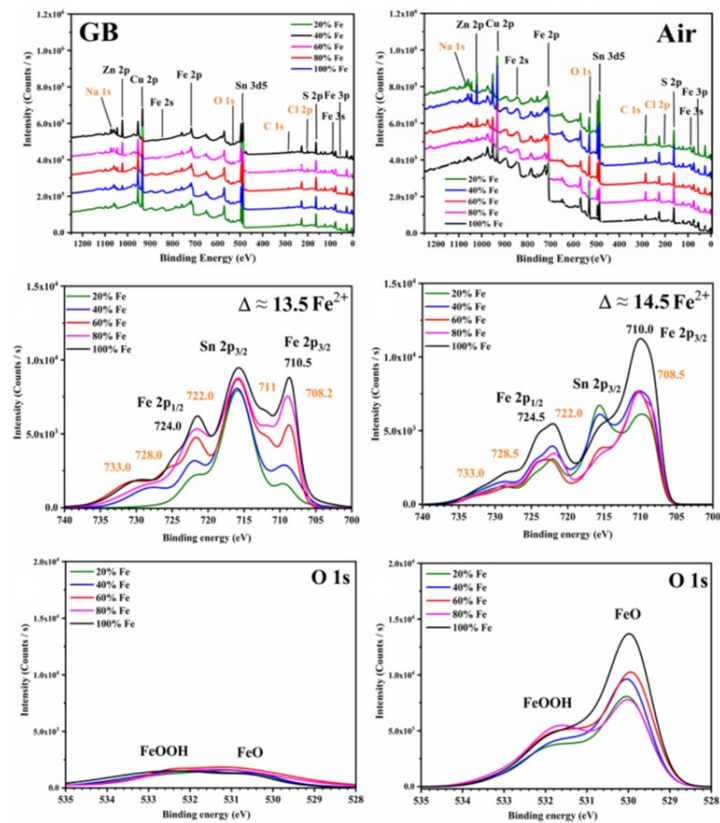


Figure 27: Above, the total profiles of XPS analysis of different $\text{Cu}_2(\text{Fe}_{1-x}\text{Zn}_x)\text{SnS}_4$ samples with different $[\text{Fe}]/([\text{Fe}]+[\text{Zn}]$ ratios; below, a study of the Fe-related and O-related regions of the same spectra. In every case, on the left are represented the spectra of samples obtained in an inert atmosphere – nitrogen in a glovebox (GB) – while on the right are represented the spectra of samples obtained in air [83].

4.4.2. Deposition methodology

Several methodologies have been used to obtain CFTS samples; most of them exploit wet processes to produce CFTS NP, such as the following:

- Hot injection techniques.
- Solvothermal and hydrothermal techniques.
- Solution synthesis.
- Microwave-assisted synthesis.
- Colloidal synthesis.
- Solid-state reactions.

Other publications illustrate techniques for CFTS TF production, such as the following:

- Sol-gel technique [84].
- Co-electrodeposition [85].
- Spray pyrolysis [86].

More detailed information, such as the precursors used and synthesis temperature, is summarised in Table 10 and Table 11: These tables present a complete view of the techniques used for CFTS synthesis, both in NP and TF forms. In particular, the approaches used for NP CFTS are very interesting because of their low price and industrial scalability. However, these approaches also have some critical aspects, for example:

- Toxic or expensive organic solvents are used.
- Impossibility of directly using NP to construct PV devices.

Table 10: Summary of techniques used to obtain CFTS NP, with information about the preparation and the band gap of the material [80].

Method	Size of particle (nm)	Precursor	Deposition Temperature (°C)	Deposition Time	Raman peak position (cm ⁻¹)	Band gap (eV)
Hot injection	13.2	1.5 mM Cu(acac) ₂ , 0.5 mM Fe(acac) ₃ , and 0.75 mM SnCl ₂ in oleylamine (OLA)	280	30 min	213, 276, 320, 392	1.28 eV
Hot injection	20	1 mM Cu(acac) ₂ , 0.5 mM Fe(acac) ₃ and 0.5 mM SnCl ₄ in 10 ml OLA, 0.25 ml 1-DDT and 1.75 ml t-DDT	210	30 min		1.5
Hot injection	7	0.5 mM Cu-(acac) ₂ , 0.25 mM Fe(acac) ₃ and 0.25 mM SnCl ₄ in 5 ml of 1-DDT and 10 ml of OLA	240	60 min	286, 318, 350	1.3
Micro-wave	Nano wire	0.1702 g CuCl ₂ , 0.1351 g FeCl ₃ , 0.1753 g SnCl ₄ , 0.1902 g NH ₂ CSNH ₂ , in 20 ml benzyl alcohol	180	15 min		1.71
Micro-wave		0.06 M Cu(NO ₃) ₂ , 0.03 M Fe(NO ₃) ₃ , 0.03 M SnCl ₂ , and 0.15 M H ₂ NCSNH ₂ in 50 ml EG	Room Temp.	120 min		1.52
Micro-wave	5	1.8 mM Cu(NO ₃) ₂ , 1 mM FeCl ₂ , 1 mM SnCl ₂ , 8 mM thioacetamide in 80 ml poly-EG	150	30 min		1.35
Micro-wave	300–400	1 mM CuCl ₂ , 0.5 mM FeCl ₃ , 0.5 mM SnCl ₄ , 2.4 mM ODA and 2.5 mM NH ₂ CSNH ₂ in 20 ml methyl orange	180	15 min		
Hydro-thermal	10–20	1 M NH ₂ CSNH ₂ , 2 M CuCl ₂ , 1 M FeSO ₄ and 1 M SnCl ₂	230–250	24–36 h		
Solvo-thermal	200	2 mM CuCl ₂ , 1 mM FeCl ₃ , 5 mM NH ₂ CSNH ₂ , and 1 mM SnCl ₂ dissolved in 80 ml DMF	250	24 h		1.28
Solvo-thermal	100	0.06 M Cu(NO ₃) ₂ , 0.03 M Fe(NO ₃) ₃ , 0.03 M SnCl ₂ , 0.15 M L-cystine in 40 ml EG	160	12 h	213, 320, 394	
Solvo-thermal	400–600	0.9 mM CuCl ₂ , 0.6 mM Fe ₂ Cl ₃ , 2.2 mM NH ₂ CSNH ₂ , and 0.5 mM SnCl ₂ in 0.2–0.8 g PVP and 20–50 ml EG	180–220	0.5–48 h	211, 280, 318, 392	1.33
Solvo-thermal	400–550	2 mM CuCl ₂ , (1-x) mM FeCl ₃ , x mM ZnCl ₂ and 1 mM SnCl ₄ , 4 mM NH ₂ CSNH ₂ and 0.64 g PVP in 40 ml EG	220	24 h	289, 318	1.2
Solvo-thermal	3–7	0.1 mM Cu(acac) ₂ , 0.05 mM FeSO ₄ , 0.05 mM SnCl ₄ , 0.25 mM NH ₂ CSNH ₂ and 1 mM 1-DDT, in 80 ml ethanol	180	16 h	320	1.66
Reflux	25	4 mM CuCl ₂ , 2 mM FeCl ₃ , 2 mM SnCl ₄ , and 8 mM CH ₄ N ₂ S in 15 ml triethylenetetramine (TETA) and 15 ml EG	200–250	3 h		1.32
reflux	70–240	4 mM CuCl ₂ , 2 mM FeCl ₃ , 2 mM SnCl ₄ , 8 mM CH ₄ N ₂ S in 30 ml TETA, EG and triethanolamine (TEA)	200–250	30 min–5 h		1.25

Table 11: Summary of techniques used to obtain CFTS TF, with information about the preparation and the band gap of the material [80].

Method	Precursor	Annealing Temperature (°C)	structure	SEM (Micrograph)	Raman peak position (cm ⁻¹)	Band gap (eV)
Spray pyrolysis	0.1 M CuCl ₂ , 0.1 M FeCl ₃ , 0.1 M SnCl ₂ and 1 M thiourea in DW	400, 500, 600		Compact film with large grains	285, 319, and 373	1.46–1.65
SILAR and CBD	For SILAR, 0.03 M SnCl ₂ , 0.06 M CuCl ₂ , 0.12 M Na ₂ S. For CBD, 1 M FeSO ₄ , 0.1 M EDTA	500	Stannite	Micro-grains and nano-rod (200–300 nm)	278, 319	1.22
Spray pyrolysis	Cu(acac) ₂ , Fe(acac) ₃ , SnCl ₂ and thiourea with molar ratios as 2:1:1:10 in equal amount of DMSO and ethanol	500–520 °C for 25 min in graphite box with S atmosphere	Stannite	Macro-grains	318, 253, 284, 353	1.37
Spray pyrolysis	0.1 M CuCl ₂ , 0.05 M FeCl ₃ , 0.05 M SnCl ₄ and 0.4 M thiourea in 50 ml distilled water	No post annealing	Stannite	Spherical particles around 20–40 nm in size		1.5
Spin coating	2 M CuCl ₂ , 1 M FeCl ₃ , 1 M SnCl ₂ and 12 M thiourea in methoxyethanol and a few drops of MEA	300	Kesterite	Porous like morphology	331	1.87
Electro- deposition	0.02 M CuSO ₄ , 0.01 M FeSO ₄ , 0.01 M SnSO ₄ , 0.02 M Na ₂ S ₂ O ₃ and 0.1 M Na ₂ C ₂ H ₂ O ₇	500, 550	Stannite	Not reported	284, 318	1.4
Sputtering	Sn, Fe and Cu targets	460–550 in sulfur atmosphere	Stannite	Not reported	285, 318, 324	
Sputtering	Sn, Fe and Cu targets	550 in sulfur atmosphere	Tetragonal	Large grains	72, 141, 252, 286, 301, 318, 340	1.4
Sputtering	Sn, Fe and Cu targets	550 in sulfur atmosphere		Compact and large grain	318	
PLD	Target made up of Cu ₂ S, ZnS, FeS and SnS ₂ powders	575	Stannite	Micro-grains	286, 319, 336,	1.33
SILAR	Cationic precursors consisted of 0.1 M SnCl ₂ , 0.1 M Fe(NO ₃) ₃ , 0.2 M CuSO ₄ in ethanol and anionic precursors consisted of 0.4 M Na ₂ S in ethanol	425	Stannite	Compact with some voids	150, 321, 473	

This approach shifts the issue of producing PV devices from material synthesis to NP aggregation in TF with suitable properties. One of the most critical issues in this field is limiting the creation of grain boundaries in the system, although this type of defect is associated with interfacial states that are recombination centres of photogenerated couples. NP aggregation can be a limiting factor in the optimisation of PV performance in chalcogenide-based PV devices.

Typically, NP processes for constructing PV devices are divided into four parts: NP synthesis, ink realisation where NP are finely dispersed, ink deposition on a chosen substrate and a thermal treatment to promote solvent evaporation and NP sintering. In this flow, the principal criticality in obtaining NP TF is the formation of cracks, low adhesion, obtaining TF with high porosity and low compactness, volume loss and the difficulty of coalescence between NP leading to inhomogeneous morphology.

From the analysis of the data contained in Table 11, we can observe the following:

- Only 10 publications show how to obtain CFTS as TF samples.
- In these 10 publications, only four use physical methods, and only three present the application of the sputtering technique, the same used in this PhD thesis.
- All these publications have been published by the same group [71-73].

- In these publications, sputtering deposition is performed with pure metallic targets for all metals, including Fe (this element, due to its ferroelectric nature, limits the usage of magnetron sources and forces the usage of RF sources to spark and sustain the plasma). The precursor's deposition was performed in a multilayer fashion with the order of the precursors Sn/Fe/Cu. These multilayer samples were then treated at high temperatures in the presence of sulphur using the parameters in Table 11.

The next section will discuss the set of characterisation tools used in the literature to analyse CFTS samples. This will give us the footprints to recognise CFTS in our samples, hypothetical secondary phases and information about devices.

4.4.3. CFTS TF-based SCs

Only two articles report PV devices based on CFTS TF: the work of *Meng et al.* [71] in 2015 and the work of *Chatterjee et al.* [74] in 2017. The latter holds the PV efficiency world record for these kinds of devices. *Meng et al.* reported results on CFTS TF samples obtained with a similar process to that used in this thesis: Metallic precursors are deposited using RF sputtering in multilayer geometry and then sulphurised at 550°C with sulphur vapours. The annealing was performed using RTA. In this work, the authors observed the formation of a single crystal phase recognised as CFTS (as shown in Figure 24) with an E_g value of 1.42eV. The device presented the same structure as a standard CZTS and an efficiency of 0.07% (Figure 28).

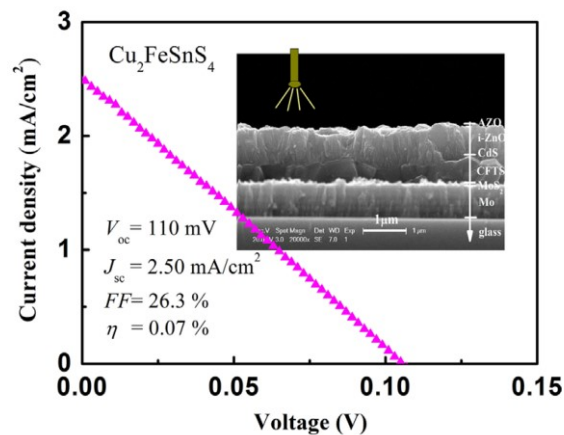


Figure 28: J–V curve and PV parameters of CFTS-based SC obtained by *Meng et al.* [71]. The inset shows a cross-sectional SEM image of the device.

Chatterjee et al. applied a different deposition technique, SILAR, to obtain the CFTS absorber layer. In this process, the precursors are deposited by dipping the substrate in a suitable solution for a fixed time, allowing the precursor molecules to organise on the substrate's surface. Subsequently, the sample was rinsed in deionised water and dried in air. This process is repeated for every precursor and for several layers, **without a final sulphurisation process**, in a 'rinse and repeat' approach. The many cycles required to obtain thick layers with this technique limit its application in high-throughput, high-area production. However, the high quality of the final layer is very useful for laboratory-scale studies. In the same work, the SILAR technique is also used to obtain different buffer layers (CdS, Bi_2S_3 and Ag_2S), to extend the application of this technique to the realisation of the full p–n junction. The choice of Bi_2S_3 and Ag_2S was made after the analysis of the band structure of these materials (represented in Figure 29). Using STM measures on the monolayer samples of these materials, it was possible to define the VB and CB energy positions from the E_F

value of these materials; with these values, the authors realised the band structure model displayed in Figure 29-b.

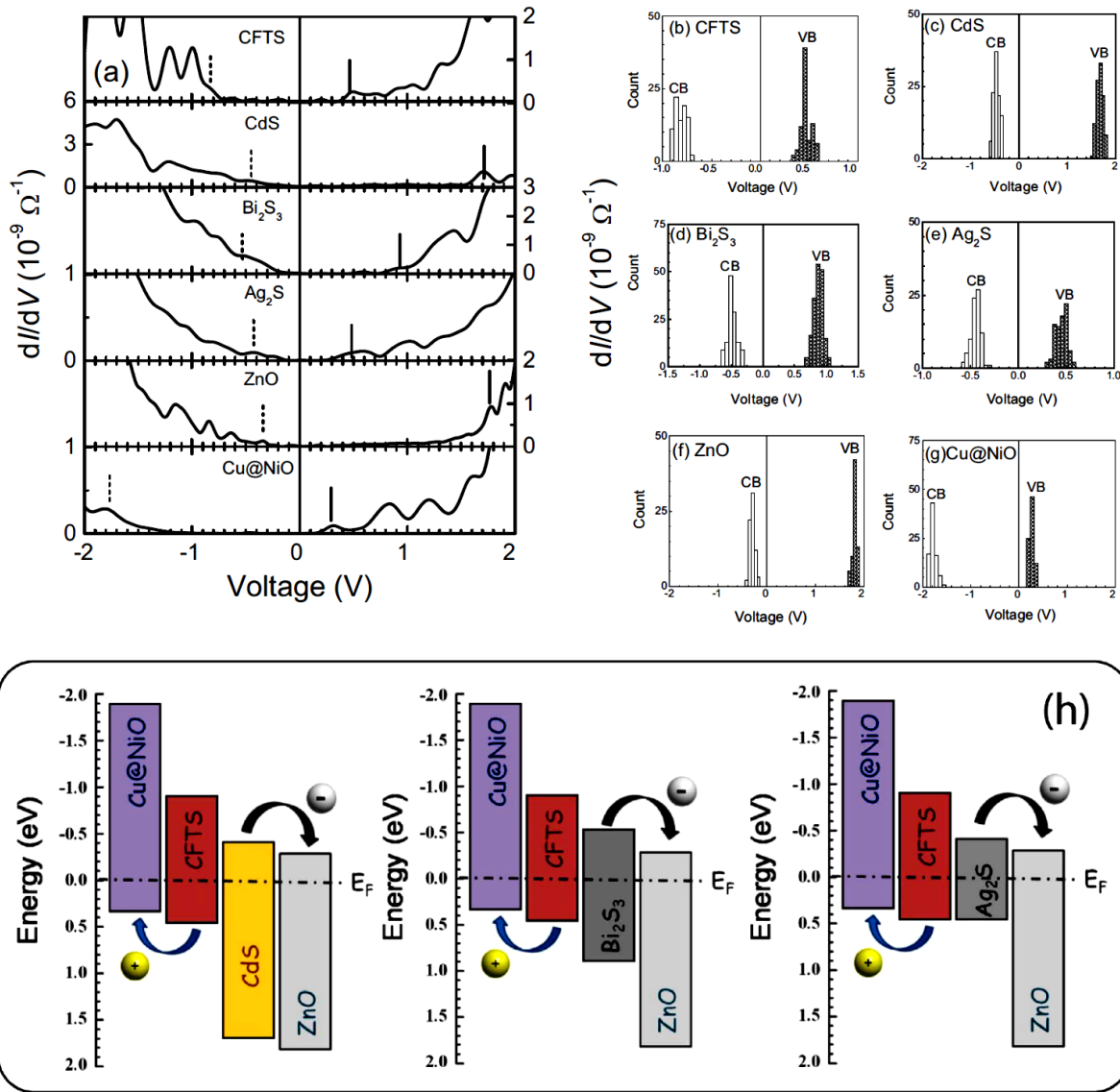


Figure 29: a) Differential conductance (dI/dV) obtained from STM measures on materials' monolayers attained using the SILAR technique (measures shown on other SC layers). (b–g) VB and CB limits' values, reported from the E_F level and measured in varying places on the same layer, are reported in histograms. (h) Disparate band structures for distinct SC structures (CFTS|CdS, CFTS| Bi_2S_3 and CFTS| Ag_2S), where the E_F value is placed at the same height to display the band alignment [74].

A higher difference between the CFTS VB and the BL CB leads to a higher V_{OC} in the final device, which the results of this series demonstrated: Table 12 highlights the difference between the two band edges in different structures with the main PV parameters of the related SC, while Figure 30 depicts the J–V curves of the related SC obtained with the three BL.

Table 12: Energy difference between CFTS VB and BL CB, together with the main SC parameters found in the three structures studied by Chatterjee et al. [74]. The statistical results from the 10 devices are displayed in brackets.

Active layer	Difference between VB of CFTS and CB of n-type material (eV)	Open-circuit voltage (V_{OC}) (V)	Short-circuit current density (J_{SC}) (mA/cm ²)	Fill factor (FF) (%)	Power conversion (%) efficiency (η)
CFTS Bi_2S_3	0.97	0.61 (0.58 ± 0.02)	9.3 (8.8 ± 0.37)	52 (48 ± 0.03)	2.95 (2.49 ± 0.29)
CFTS CdS	0.93	0.56 (0.53 ± 0.03)	6.5 (5.6 ± 0.87)	37 (33 ± 0.05)	1.37 (0.96 ± 0.21)
CFTS Ag_2S	0.90	0.40 (0.38 ± 0.02)	6.0 (5.7 ± 0.36)	32 (28 ± 0.02)	0.77 (0.61 ± 0.10)

The best results, both in V_{oc} value and efficiency, were derived by coupling the CFTS TF with the Bi_2S_3 BL, which represents the high energy difference between CFTS VB and BL CB. This leads to a record efficiency of **2.95%** for the p–n junction $CFTS|Bi_2S_3$, while a modest **1.37%** efficiency is obtained using the classical p–n junction $CFTS|CdS$.

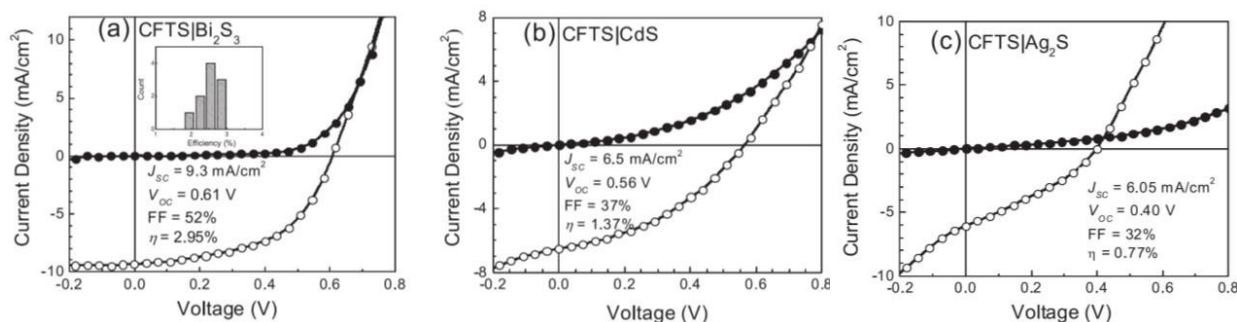


Figure 30: J–V curves of the three-best SCs obtained by Chatterjee et al [74], in dark conditions (black dots) and under illumination (white dots) for the three structures studied in the article. For the $CFTS|Bi_2S_3$ junction, in the inset, the efficiency distribution of 10 devices is displayed.

Even if not directly related to solid-state SC, this compound has also been tested as a counter electrode in DSSCs due to the high catalytic properties for the couple I/I^- usually used for this application. *Mokurala et al.* [87] tested the application of CFTS TF, comparing it with the more widely used Pt electrode and with another chalcogenide material (Cu_2CoSnS_4). Figure 31-a,b displays the J–V curves and the incident photon-to-current conversion efficiency (IPCE) curve, together with a comparison of a Pt counter electrode, conveying comparable results. The same application was studied by *Prabhakar et al.* [88], whose results are in Figure 31-c. In this case, the CFTS TF counter electrode showed higher performance than the Pt CE, with a final efficiency of 8% vs. the 7.5% efficiency obtained on Pt.

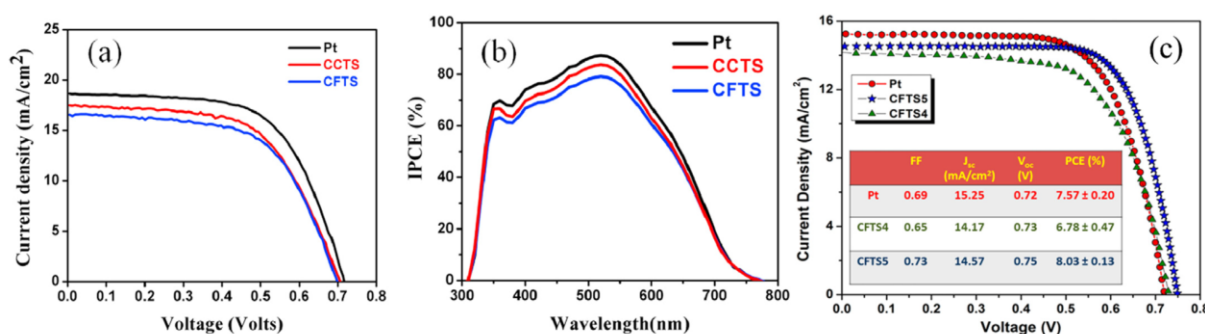


Figure 31: a-b) J–V curves and IPCE measured on DSSC realised with different counter electrodes studied by *Mokurala et al.* [87] depicting comparable results between the high-cost Pt electrode and the low-cost CFTS and CCTS TF electrodes, as well as c) J–V curves obtained by *Prabhakar et al.* [88] testing alternate annealing temperatures for CFTS TF.

To this exotic application, we can add the application of CFTS to hydrogen photocatalytic production. For example, *Gonge et al.* [89] obtained nanofibers of various chalcogenide materials by electrospinning, which showed promising results in hydrogen production.

4.5. CMTS TF

4.5.1. Material properties

In this section, the chemical and physical properties of CMTS will be discussed, not only from TF experiments but also from other samples in nature, such as nanoparticles and microcrystals. Unlike CFTS, which has a natural counterpart in stannite, Mn-based materials are not present in nature; their production is totally synthetic. Only the few most important properties will be described in this section that are the most useful for the interpretation of the data collected on the CMTS TF produced in this PhD thesis and for their application in PV devices. These properties are as follows:

- Crystalline structure: This feature can be studied using XRD to identify in our samples the formation of the CMTS phase and to confirm the absence of possible secondary phases.
- Optoelectronic properties: This parameter can be obtained from transmittance measurements using UV–Vis spectroscopy.
- Secondary phase identification, performed by Raman analysis coupled with XRD analysis.

Similar to the other chalcogenide materials analysed in this PhD thesis, CMTS can be synthesised utilising pure sulphur (obtaining CMTS), pure selenium (obtaining CMTSe) and mixed S/Se conditions (obtaining CMTSSe). A mixed binary system can also be developed wherein zinc partially substitutes for Mn to reach pure CZTS(/Se), realising a series with a grading composition. Numerous works in the literature with mixed Mn- and Zn-based compounds have been studied for PV applications. In this field, I mention the results of *Li et al.* [90], where the substitution of Zn with manganese (atomic 5%) in TFs CZTSSe TF deposited via the sol–gel method increases the final device’s efficiency from 7.7% to 8.9%. This result proves how the complex structure of these chalcogenides allows further improvement of the final device’s efficiency due to a deeper knowledge of their properties and how these properties can be modified using chemical modification (mixed compounds) and deposition techniques used to grow the TF.

4.5.1.1. Crystal structure and secondary phases

In the literature, some works [75, 91] state that the most stable crystal structure for this chalcogenide is kesterite (Figure 32, left), though most works demonstrate that this material organises itself in stannite structures (Figure 32, right). This statement is confirmed by neutron diffraction studies [92, 93], where the stannite symmetry group (I-42m) is better than the kesterite symmetry group (I-4) in fitting the experimental data. Other works do not choose a specific structure. Nevertheless, they analyse the tetragonal distortion parameter considering a synthetic process: A chalcogenide structure can be identified using the ratio between the crystal cell parameters of $c/2a$, defined as the tetragonal distortion parameter, where the kesterite structure conveys $c/2a \geq 1$ and the stannite structure presents $c/2a \leq 1$ [94, 95]. Theoretical analyses with different software (e.g. HSE06) contained in *Rudisch et al.* [96] identify the stannite structure as one able to minimise the system’s energy. Only in one work, where CMTS is synthesised in nanoparticles, is another crystal structure associated with this material: the wurtz-stannite structure [97].

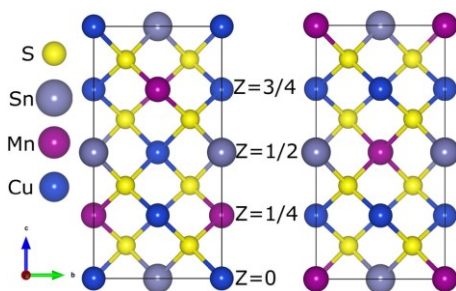


Figure 32: On the left, a kesterite structure; on the right, a stannite structure for CMTS.

As per the secondary phases that could form while synthesising the CMTS, excluding those already mentioned in the CZTS section based on Cu-Sn-S, compounds can also be found based on Mn and the other elements in chalcogenides. Table 13 discloses information from the literature about the compounds associated with the presence of Mn as binary or mixed sulphides. The presence of many quaternary phases inside the family of thiospinels is particularly intriguing and different from CZTS. These compounds, which illustrate a cubic crystalline structure, vary according to their composition. The most well-known one is the Sn-rich formulation ($\text{Cu}_{0.92}\text{Mn}_{0.5}\text{Sn}_{1.5}\text{S}_4$) [96, 98], while the other Mn-rich ($\text{Cu}_{0.5}\text{Mn}_{1.5}\text{SnS}_4$) and intermediate ($\text{Cu}_{0.5}\text{Mn}_{1.25}\text{Sn}_{1.25}\text{S}_4$) formulations are only observed in Harada [99]. The cubic structures are displayed in Figure 33 with the PDF-card code and the occupation fractions described with distinct colours on the same crystallographic. Clearly, every cationic site is occupied differently, from one or more elements to the distribution of cations in pure CMTS conveyed in Figure 32. No information on the Raman spectra of these compounds is available in the literature.

Table 13: Main secondary phases associated with the presence of Mn while preparing sulphide compounds with Cu and Sn. For every compound, the following are reported: i) Raman peak position, if available, ii) crystal structure and iii) electrical properties.

Secondary phase	Raman peaks [cm^{-1}]	Crystal structure	Electric properties	Reference
MnS	221,302,479,572	Cubic (Alabandite)	Insulating (Optic Eg: 2.8eV)	[100]
MnS₂	219,244,488	Cubic (Hauerite)	Semiconductor (Eg: 0.5eV)	[100]
Mn₂SnS₄	293,298,302	Ortorombic	Metallic [†]	[101]
Thiospinels				
Cu_{0.92}Mn_{0.5}Sn_{1.5}S₄	n.d.	Cubic (a=10.41(5)Å)	Semiconductor (Indirect Eg: 0.67eV) * (Direct Eg: 1.04eV) *	[96, 98]
Cu_{0.5}Mn_{1.5}SnS₄	n.d.	Cubic (a=10.44Å)	n.d.	[99]
Cu_{0.5}Mn_{1.25}Sn_{1.25}S₄	n.d.	Cubic (a=10.43Å)	n.d.	[99]

[†] The metallic behaviour of this compound has been estimated with respect to the Eg values simulated and represented in the database www.materialsproject.org.

* From a theoretical simulation with software from band structure analyses, where the minimum Eg (defined as indirect) and the second one are shown immediately after [96].

This fact is particularly detrimental, as the three thiospinels' structures are indistinguishable if studied by XRD, due to their similar crystalline structures and cell parameters. Only through compositional analyses (e.g. EDX analysis) associated with XRD measures is it possible to speculate the presence of these secondary phases inside the CMTS TF and recognise the right formulation. Their presence can be confirmed with XRD analysis due to the distinction between the crystallographic structure of CMTS (tetragonal) and the cubic structure of the other compounds. An example is shown in Figure 34 [96], where it is possible to separate

the presence of the CMTS phase from the presence of one of the three thiospinel phases that, due to the compositional analyses in the work, is associated with $\text{Cu}_{0.92}\text{Mn}_{0.5}\text{Sn}_{1.5}\text{S}_4$ ($\text{Cu}_2\text{MnSn}_3\text{S}_8$). In every other work, the only thiospinel recognised as a possible CMTS secondary phase is Sn-rich $\text{Cu}_{0.92}\text{Mn}_{0.5}\text{Sn}_{1.5}\text{S}_4$.

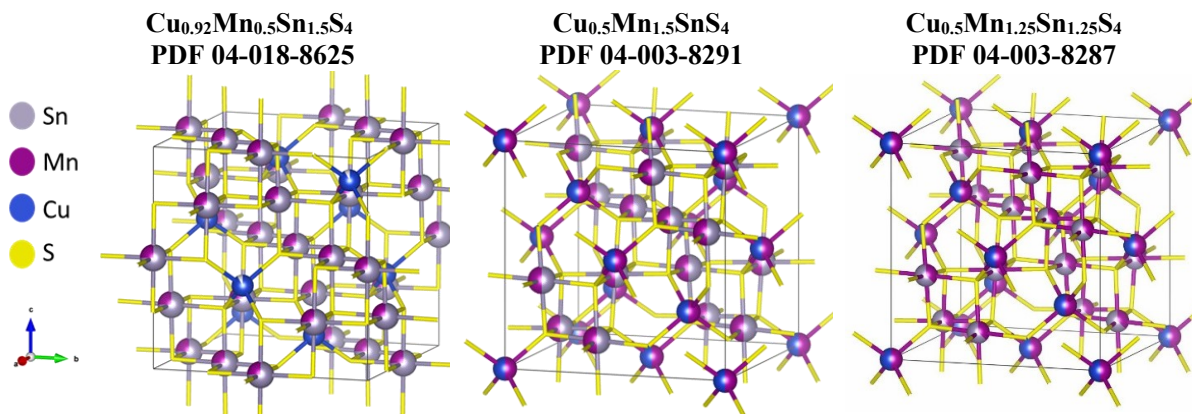


Figure 33: Thiospinel compounds that can be found as secondary phases in CMTS. Displayed are the following: i) chemical formulations, ii) PDF cards used to identify the XRD peaks of these compounds and iii) the schematisation of the crystalline structure of these compounds, where the colouring of the crystal site is proportional to the percentage of the occupation of the site for every cation. Images are elaborated on using Vesta software from the crystallographic data in the PDF cards.

Rudisch et al. [96] observed that the Sn-rich phase connected to CZTS ($\text{Cu}_2\text{ZnSn}_3\text{S}_8$) has been theorised in the phase diagram by *Olekseyuk et al.* [26] but that this phase formation is blocked due to the strong bond between CZTS and SnS_2 , as noted by *Pogue et al.* [102]. Figure 34 shows the XRD analysis and Raman spectra obtained by *Rudisch et al.* on the same CMTS samples, conveying the co-presence of the main CMTS phase in the stannite structure and the appearance of the Sn-rich thiospinel phase.

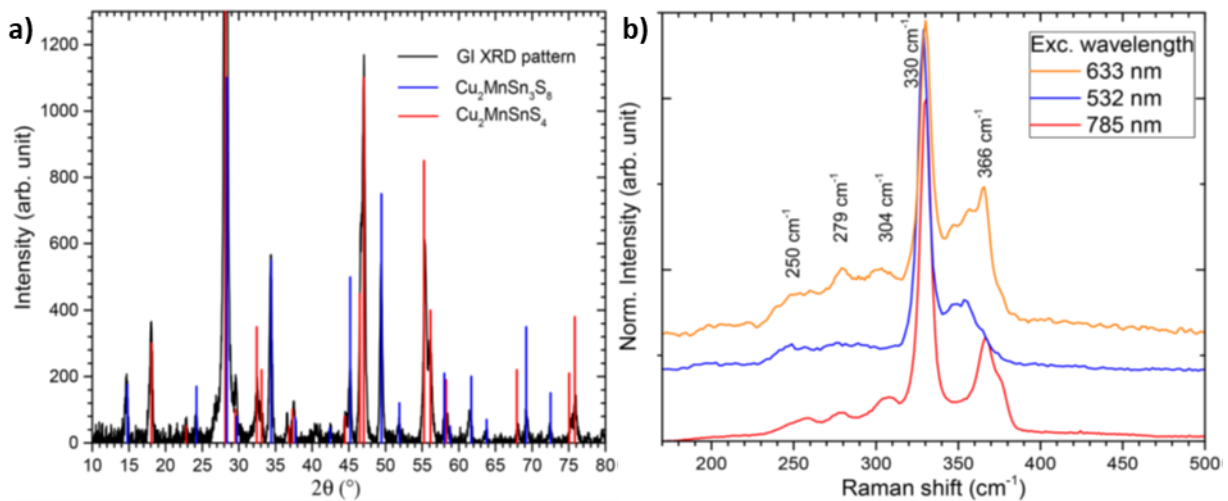


Figure 34: a) CMTS TF diffractogram deposited by co-sputtered precursors where the peaks of the CMTS and $\text{Cu}_2\text{MnSn}_3\text{S}_8$ phases are visible and b) the same CMTS TF Raman spectra obtained with excitation lasers, so some of these peaks should be assigned to $\text{Cu}_2\text{MnSn}_3\text{S}_8$ [96].

4.5.1.2. Optoelectronic properties

Optoelectronic properties are very important for a semiconductor-related application in PV technologies, as mentioned before for the other chalcogenide, especially Eg. For CMTS, the estimated values of Eg in the literature are scattered in a wide range and are strongly dependent on the deposition technique used to obtain the material and its nature (e.g. nanocrystals vs. TF). For example, *Rudisch et al.* [96] studied the Eg

of this material, varying its chemical composition (Figure 35): Using the Tauc elaboration [103] on transmittance measures, they determined that the E_g can vary from 1 to 1.6eV. These values corroborate the dispersion of E_g reported in other works [94, 104, 105].

Sample	Cu/Sn	Mn/Cu + Sn	Phases (XRD and Raman)
CMTS A	1.53	0.15	$\text{Cu}_2\text{SnS}_3/\text{Cu}_3\text{SnS}_4$, $\text{Cu}_2\text{MnSn}_3\text{S}_8$
CMTS B	1.42	0.28	$\text{Cu}_2\text{MnSnS}_4$, $\text{Cu}_2\text{MnSn}_3\text{S}_8$
CMTS C	1.79	0.43	$\text{Cu}_2\text{MnSnS}_4$, $\text{Cu}_2\text{MnSn}_3\text{S}_8$
CMTS D	1.50	0.47	$\text{Cu}_2\text{MnSnS}_4$, $\text{Cu}_2\text{MnSn}_3\text{S}_8$
CMTS E	2.39	0.79	$\text{Cu}_2\text{MnSnS}_4$, MnS
CMTS F	2.39	0.84	$\text{Cu}_2\text{MnSnS}_4$, MnS

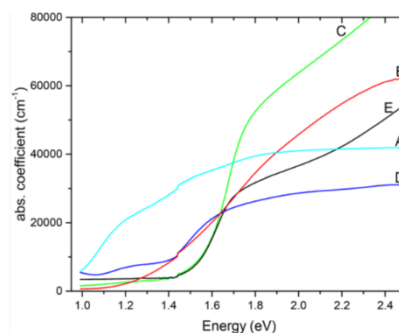


Figure 35: left) table with the samples used in [96], together with formulations and phases identified in the samples; right) absorbance spectra from the samples, where the determination of E_g is performed executing a linear regression in the linear region and finding the intercept of this regression with energy axis. See [103] for more details.

For the E_g of the Cu-Sn-S phases, see the CZTS section, while Table 13 reports the E_g for the Mn secondary phases. Accordingly, it can be observed that theoretical studies of E_g have only been performed concerning Sn-rich thiospinel [96]. From the study of the electronic density of states and the band structure of $\text{Cu}_{0.92}\text{Mn}_{0.5}\text{Sn}_{1.5}\text{S}_4$ ($\text{Cu}_2\text{MnSn}_3\text{S}_8$), it has been observed that this compound is a semiconductor with an indirect transition equal to 0.67eV and a direct E_g of 1eV. No information on the other two thiospinels has been provided.

4.5.2. CMTS TF deposition and related PV devices

It is possible to find synthetic techniques to produce CMTS in the literature, depending on the nature of the material. Starting from nanocrystals [97, 106], with low interest in the focus of this PhD thesis, we can focus on CMTS TF preparation techniques that can be divided between physical vacuum techniques and humid chemist techniques. Suresh Kumar [107] updated the situation concerning cation-substituted CZTS TF preparation to 2019, complete with other substitutions. The CMTS section is quite wide, and it is separated into the previous two topics, with an in-depth analysis of methods and results. For CMTS preparation, the most important techniques mentioned are as follows:

- Evaporation with an electronic beam (e-beam).
- Hot injection.
- Spray pyrolysis.
- Sol-gel.
- Solvothermal deposition.
- Dip coating (or SILAR).
- Electrodeposition.
- Co-sputtering.

Most of these processes have two steps. The metallic precursors are deposited first with, in some cases, a little chalcogen, followed by a second step consisting of a thermal treatment (TT) in the presence of chalcogen to form the CMTS phase. Significantly, the authors focused their analysis on solar device results, and TF characterisation is not always included in reviews. Table 14 summarises the efficiencies of the TF PV devices obtained using various techniques.

Table 14: Comparison of deposition techniques, process parameters and record PV device efficiency published for TF CMTS-based prototypal SCs.

Method	Precursor	Solvent	Absorber layer	η (%)	Year
Evaporation	Cu, Mn, Sn, S	NA	CMTS	0.33	2017
Evaporation	Cu, Mn, Sn, S	NA	CMTS	0.83	2017
Spray Pyrolysis	CuCl ₂ ·2H ₂ O MnCl ₂ ·4H ₂ O SnCl ₂ ·2H ₂ O Thiourea	Solution: DI water	CMTS	0.07	2016
Spray Pyrolysis	CuCl ₂ ·2H ₂ O MnCl ₂ ·4H ₂ O SnCl ₂ ·2H ₂ O Thiourea	Solution: DI water Na doping: NaCl	CMTS _{Se}	0.73	2016
Dip Coating	CuCl ₂ ·2H ₂ O Mn(CH ₃ COO) ₂ ·4H ₂ O SnCl ₂ ·2H ₂ O Thiourea	Solution: 2-methoxyethanol Stabilizer: acetyl-acetone	CMTS	0.38	2016
Sol-gel	CuCl ₂ ·2H ₂ O Mn(CH ₃ COO) ₂ ·4H ₂ O SnCl ₂ ·2H ₂ O Thiourea	Solution: 2-methoxyethanol Stabilizer: acetyl-acetone	CMTS	0.49	2015

A recent publication by Yu et al. [108] should be added to this list wherein the precursors are deposited by electrodeposition followed by a sulphurisation step with argon and sulphur vapour. The precursors were deposited as a dual layer with Cu and Sn, followed by a layer of manganese oxide (MnO). The study also analysed the effect of sulphurisation temperatures set between 500°C and 590°C.

The sample treated at 560°C for 20 minutes demonstrated the best PV parameters; see Figure 36. To date, the efficiency of this device, equal to 0.91%, has been the highest published for CMTS-based PV devices.

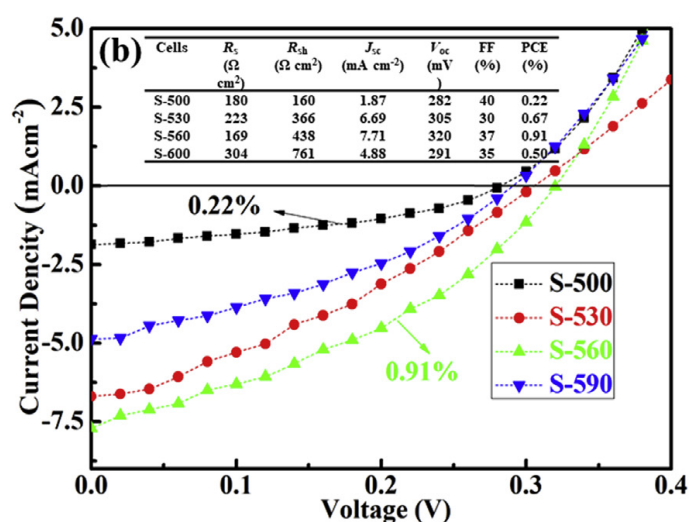


Figure 36: J–V curves of CMTS-based PV devices obtained by electrodeposition are listed according to their PV parameters [108].

As for the finalisation of PV devices, no work has been found concerning the assorted stacks of TCOs used to finalise CMTS-based devices. Unlike the literature on CFTS, only CdS has been tested to create the p–n junction; this led us to avoid investigating distinct buffer layers during this PhD thesis. Moreover, no works have been found in the literature about the synthesis of CMTS TFs by sputtering.

5. FABRICATION AND CHARACTERISATION METHODS

In this section, we briefly describe the techniques used for both the realisation of the chalcogenide TF samples and cell finalisation, showing the common parameters between the samples, the characterisation tools and the measure parameters used. As described in Section 4.2.3, to obtain chalcogenide-based SC, we followed the standard cell structure used for CIGS and CZTS. In particular, we realised:

- **Mo TF deposition using the magnetron sputtering technique** on an SLG substrate to realise back contact.
- **The metallic precursors deposition by the magnetron sputtering technique** on the substrate, from pure metals' targets, utilising a multilayer approach to realise the TF.
- **The sulphurisation process was conducted in a tubular oven**, placing the samples in a graphite box to contain the sulphur vapours needed for the process (source of vapours: pure sulphur powder).
- **After the cooling process, CdS BL deposition by CBD took place.** The application of PDTs happened before (for chemical PDT) or after (for thermal PDT) this material deposition.
- **Deposition of TCOs (i-ZnO and AZO) using magnetron sputtering deposition.**
- **The deposition of Al-grids using thermal evaporation.**

Knowing that using distinct substrates could lead to variations in the absorber material, we also grew the absorber layer on a bare SLG substrate to obtain transparent samples for the Tauc method to determine the optical E_g of the absorber layer. Physical deposition methods are less substrate-dependent than those obtained by chemical routes, so we assumed that the differences in the optical properties between opaque and transparent samples are minimal. The final shape of the TF SC is represented in Figure 37: 10 devices can be obtained on a single TF sample that measures $1.7 \times 3.0 \text{ cm}^2$. The characterisation of all these devices provides information on the homogeneity of the deposition processes.

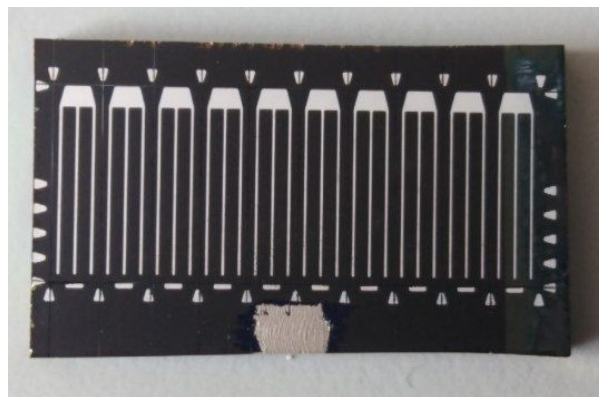


Figure 37: Photo of a chalcogenide-based SC array, where it is possible to see the 10 SCs separated by mechanical scratches. The total exposed area of the device is 0.3 cm^2 .

5.1. SPUTTERING MACHINE MO AND METALS' DEPOSITION

The deposition of the Mo layer on SLG and metals' multilayer on the substrate is realised using a confocal sputtering system (Kenosistec KS 300 C) and three magnetron sources with a 5-cm target diameter. The geometry of the system is bottom up, and the presence of three cathodes allows us to deposit the multilayer in one process, reducing deposition times. Metals are deposited from high-purity targets (pure Cu, pure Zn, pure Sn, mixed Cu:Fe 1:1 w/w% and pure Mn targets with 99.99% purity, 5cm diameter and 6mm thickness). The value of 6×10^{-3} Pa has been selected as the partial pressure of argon during the whole deposition process. No substrate heating was employed.

The target generators can be set in two configurations: 'constant power', where the generator controls electrical potential and current discharged on the target to keep the power consumed constant, and 'constant current', where the generator controls potential and power discharged on the target to keep the current constant. The first configuration is more suitable for target safety, since a constant power means a constant temperature for the target, limited degradation of the target due to rapid thermal change and the limited control of the material flux to the substrate, which is mainly determined by the current. The second configuration is more suitable for stoichiometric control since a constant current value means a constant material flux. However, varying the power discharged on the target could strongly affect the target's temperature. The 'constant power' approach has been used for every material obtained as TF, while the 'constant current' approach has been tested only on CFTS, since higher local stoichiometry inhomogeneity has been observed in this material.

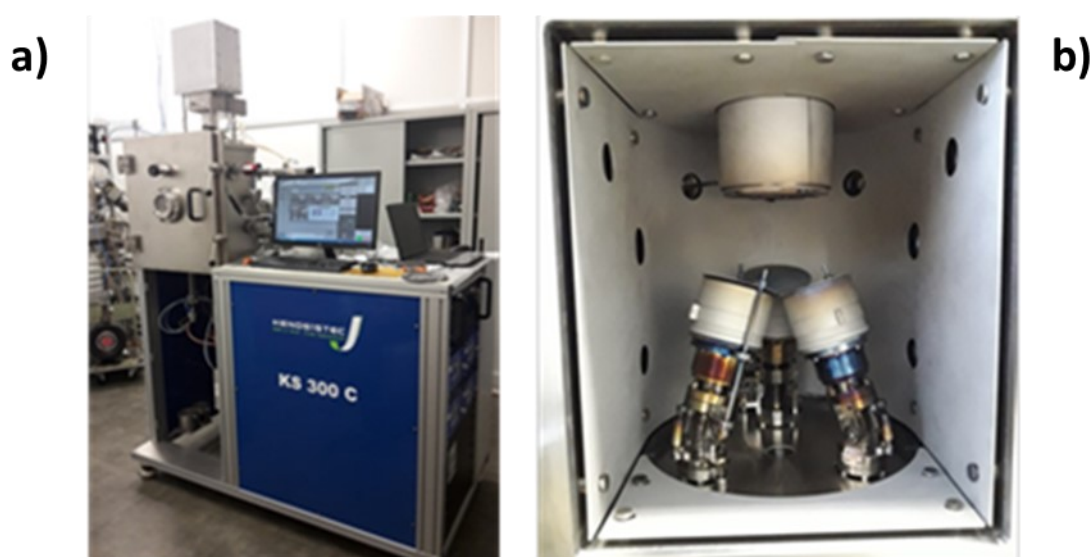


Figure 38: Photos of the Kenosistec KS 300 C sputtering system.

In Figure 16, we report the deposition parameters of the metals deposited by this sputtering machine, conveying only the constant parameters. The specific deposition times are presented in Section 6, excluding the standardised Mo deposition. The use of a Cu:Fe target for the deposition of Fe in CFTS samples was decided from tests made by the research group before the start of this PhD thesis: Indeed, a pure Fe target cannot be used in magnetron sputtering, since the target magnetises itself.

Table 15: Parameters for the deposition of metals, for both ‘constant power’ and ‘constant current’ approaches, as well as parameters for Mo deposition.

Metals	Parameters	
	Constant power (W)	Constant current (A)
Cu	50	124
Zn	25	---
Fe:Cu	120	94
Mn	45	---
Sn	20	43
Molybdenum	2 steps parameters	
	Step 1	Step 2
Power (W)	75	75
Deposition time (min)	20	60
Ar flux (sccm)	14	5.5

5.2. SULPHURISATION PROCESS AND COOLING

The metallic stacks were sulphurised in a graphite box containing 0.06g of sulphur. The box was moved in a quartz tube, which was placed in a tubular oven heated in Ar flow with a two-step temperature programme. After the process, the samples were cooled following specific ramps (for more details, see Table 16).

Figure 39 demonstrates the full setup used for the sulphurisation process. The graphite box is inserted inside a quartz tube sealed with a water-cooled steel flange and used to simplify the tube’s opening and closing operations. The quartz tube was then put inside the tubular oven and fluxed with Ar to expel the air atmosphere for 15 minutes. The tube is constantly inflated with Ar to purge the excess sulphur vapour from the tube. To quench these vapours, a set of chemical traps made from an oxygenated water (H₂O₂) solution and an NaOH solution were employed.



Figure 39: a) Photo of the sulphurisation setup; b) digital design of the graphite box and c) accommodation of a large kesterite sample (3.5x7 cm²) inside the box.

The two sulphurisation process sets were tested only on CZTS, while only the *Htemp* process was studied on CFTS and CMTS. For the cooling process, we used the natural one for every material, while the slow-cooling process was tested only on CFTS (to investigate the appearance of the cubic phase). The fast-cooling process was used only on CZTS (to investigate the order–disorder transition more deeply).

Table 16: Process parameters used for both the sulphurisation and cooling processes.

Sulfurization process	Parameters					
	Tmax 1 (°C)	Rmp 1(°C/h)	Duration 1 (min)	Tmax 2 (°C)	Rmp 2(°C/h)	Duration 2 (min)
Low temperature (Ltemp)	530	900	3	550	400	40
High temperature (Htemp)	550	900	3	570	400	40
Coolin process	Duration (min)			Cooling rate (°C/min)		
Slow cooling	1800			0,31		
Natural cooling	240			1,13		
Fast cooling	30			19		

5.3. CdS DEPOSITION

CdS deposition was performed by CBD in a setup displayed in Figure 40, using the recipe previously used and optimised by the research group to obtain a 50–70-nm-thick layer [109]. The kesterite samples are immersed in an aqueous solution of cadmium acetate ($\text{Cd}(\text{CH}_3\text{COO})_2$, 0.5 M), ammonia (NH_3 14.8 M) and ammonium chloride (NH_4Cl 2 M) right after the end of the sulphurisation process to avoid the formation of superficial oxides on the absorber layer. The solution was then put in a heat bath at 75°C. When the reaction solution also reaches this temperature, a solution of thiourea ($\text{SC}(\text{NH}_2)_2$, 0.5 M) is added to the reaction. At the end of the process, which lasts 11.5min, the samples are put in fresh deionised water and placed in an ultrasonic bath for 10min to remove the residual detached CdS crystals grown on the surface.

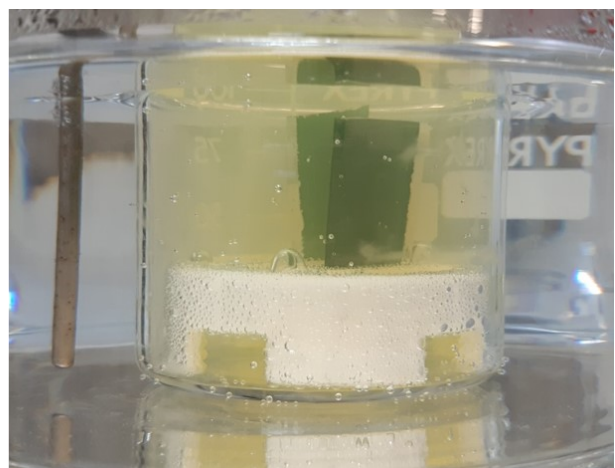
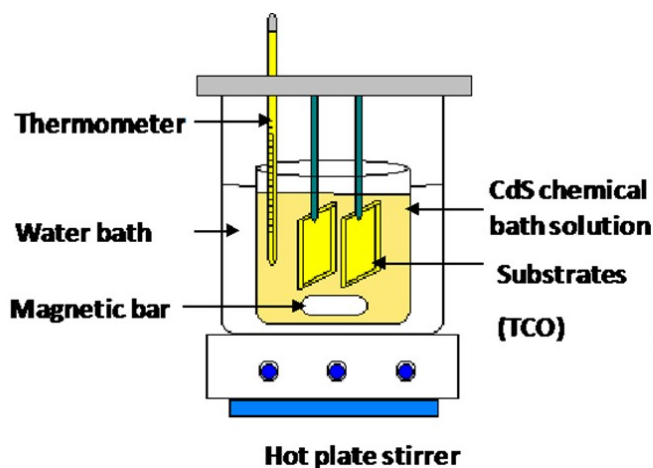


Figure 40: a) Setup used for the CdS CBD, where the becker containing the reaction environment is contained in a thermostatic bath [110]; b) Photo of the setup during a CdS CBD reaction, where two samples are processed.

5.4. TCO DEPOSITION AND METAL GRID

The deposition of TCO layers was performed using magnetron sputtering deposition with a multitarget sputtering machine. Both targets used are pure 5N and 20cm in diameter. The Al-grid deposition used thermal evaporation to obtain Al fingers shaped as shown in Figure 37, with thicknesses of $\approx 500\mu\text{m}$. The deposition parameters and the total transmittance measure of the TCO structure are in Figure 41.

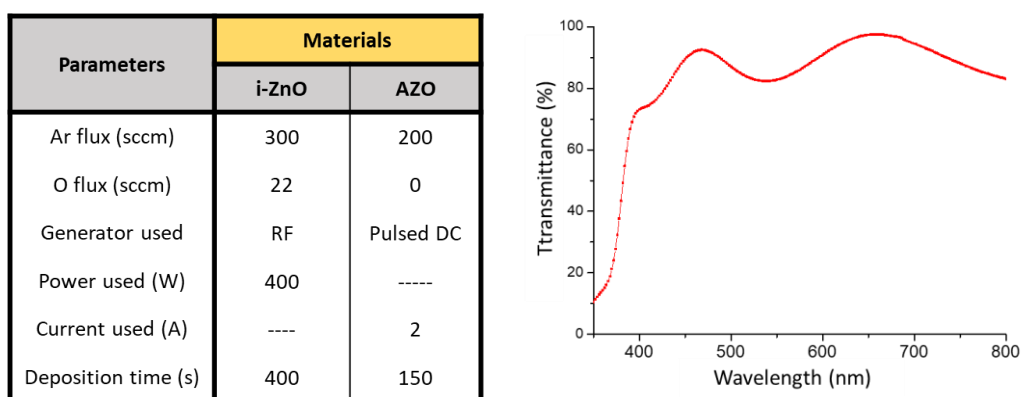


Figure 41: a) Deposition parameters of the TCO layers, obtained by sputtering; b) Transmittance measure of the transparent stack.

5.5. PDT

The thermal PDT was performed in two ways: at 260°C for 10 minutes in a tubular oven or on a thermostatic plate, depending on the production process step at which this PDT was applied (respectively, after the CdS deposition or after the full device realisation). The chemical PDT was performed using an HCl aqueous solution (3%vol) at 75°C , applied immediately after the chalcogenide sulphurisation process and before the CdS deposition for 10 min. Subsequently, the samples were rinsed in fresh deionised water and ultrasonicated for 10min.

For the ageing effect, samples were conserved in dark conditions at RT, with a relative humidity condition (RHC) between 25% and 55%.

5.6. MONOGRAIN PREPARATION

Monograin powders are prepared from separated powders for every precursor: Pure Cu (4N), Fe (4N), Sn(4N), S (5N) and KI (4N) powders are mixed at the proper ratios to obtain grains' final desired stoichiometry. The mix is performed manually by mortar and pestle until the precursors' powder is homogeneous. This powder is then placed into a long quartz ampule and connected to a rotative pump to be evacuated from the gas (down to 0.1Torr pressure). Before sealing, the ampule can be filled with inert gas (see Table 38). Once sealed, the ampoules were placed in an oven. The temperature setting depends on the molten flux used (in this case KI, which melts at 710°C), and the maximum temperature is reached in 12h. The duration of the process also depends on the presence of molten sand (136h for samples

containing KI and 304h for samples not containing KI). Once the sulphurisation process is complete, the ampules are removed from the oven and rapidly cooled at RT. Before the characterisation, the powders were washed by several steps in a sonication bath and deionised water to remove the molten sand remaining on the surface of the grains.

5.7. CHARACTERISATION TOOLS

To investigate the sample properties, several samples were produced. Except for the UV–Vis spectroscopic measurements of TF grown on SGL, all other characterisations were performed on Mo-coated SGL substrates.

Before the CdS buffer layer deposition, small portions of kesterite TFs were analysed via SEM (Tescan Mira3 FEG), both morphologically and compositionally, exploiting the EDX (Bruker Quantax Compact – electron acceleration=20keV). As the S and Mo main picks overlapped in the EDX spectra, the chalcogenide layers were partially scratched to remove small flakes from the Mo–back contact to be analysed by SEM/EDX, giving a reliable EDX evaluation of the amount of sulphur in chalcogenide TFs. Exploiting the random distribution of these freestanding flakes dispersed on the rest of the TF surface simultaneously, it is possible to conduct the following operations:

- Study the morphology of the interface between chalcogenide and Mo–back contact (face-down flakes).
- Check the grain structure along the section of the chalcogenide layer (orthogonally oriented flakes).
- Measure the EDX composition of flake bundles to increase the total thickness of the chalcogenide TF to minimise the Mo signal and have a reliable evaluation of the sulphuric percentage.

A quantitative evaluation of secondary phases was used for a relative comparison between samples. Then, the kesterite TFs were ground, and the powder was put on a misoriented Si holder to eliminate the Mo signal from the XRD patterns, obtained by using a Bruker D2 PHASER with a linear detector. XRD peak analysis and the identification of crystalline phases were performed using the PDF4 + database (ICDD).

The samples were further characterised by Raman spectroscopy with two devices. The first was a Jasco Ventuno μ -Raman, equipped with a Peltier-cooled charge-coupled device camera (operating temperature: -50°C) and an He–Ne laser (wavelength 632.8 nm, power density 6 kW/cm²) for the spectra taken with the red laser. The second was a Horiba LabRam HR800 spectrometer equipped with a 532-nm laser line for the spectra taken with the green laser. For UV–Vis transmittance measures, a Jasco V-570, range 250–2500nm, was used.

PV devices have been characterised with Solar Simulator I-V measures using a 500 W-Xe light source (ABET Technologies Sun 2000 class ABA Solar Simulator), which was calibrated to 1.5AM at 1,000W/m² by a reference Si cell photodiode (RR-103-O RERA SYSTEMS) provided with an IR cut-off filter (KG-5, Schott).

EQE measurements were also performed (SpeQuest quantum efficiency system equipped with an Omni 300 LOT ORIEL monochromator, single grating in a Czerny–Turner optical design and AC mode with a chopping frequency of 88 Hz).

PL data were collected using a single grating monochromator (Jarrell–Ash) in the 700–1,700 nm spectral range and a spectral resolution of 6.6 nm, using a standard lock-in technique with a short wavelength-enhanced InGaAs detector (maximum responsivity at 1,540 nm). A laser with an excitation wavelength $\lambda_{\text{xc}} =$

405 nm (Crystalaser) and a pump power of 90 mW was used. A cooling system consisting of a rotary pump, a turbomolecular pump and an He closed-circuit cryostat was used to perform PL measurements from 15 K to RT.

XPS measurements were taken with a Kratos Analytical AXIS Ultra DLD spectrometer equipped with an achromatic Mg K α /Al K α dual anode X-ray source and a monochromatic Al K α one. The monochromatic Al K α anode (1486.6 eV) was operated at 150 W and 15 kV. The 180° hemispherical energy analyser with an average radius of 165 mm was operated using a hybrid lens mode at a pass energy of 160 eV for the survey spectra and 20 eV for the region spectra. XPS spectra were recorded at a take-off angle of 90° from the surface of the sample holder using an aperture slot of 300×700 μm^2 . The samples were mounted on a stainless-steel sample bar (130×15 mm²). The relative atomic concentrations of the elements were determined from the appropriate integrated peak areas at the core level and the sensitivity factors provided by the original analysis (Kratos Version 2.2.10 software). Shirley background subtraction was used to calculate the relative atomic concentrations. No charge correction was applied to any energy scale, as the samples were sufficiently conductive.

AS data were collected using a Biologic SP-240 potentiostat with a four-probe configuration (amplitude of the superimposed AC potential 50mV, V_{bias} ranging from -1.5 to 2V with a step of 50mV, frequency ranging from 1MHz to 100Hz with six points per decade) for the RT measures and an Autolab PGSTAT302N bipotentiostat coupled with an He closed-circuit cryostat for the temperature-dependent measures. This cryostat has also been employed for $V_{\text{oc}}(T)$ measures.

6. RESULTS AND DISCUSSION

In this section, we discuss the results obtained during the work on the three previously illustrated materials. The data will be discussed in the same order mentioned in the introduction, starting with the results of the CZTS TF samples, which fixed the road map for the work on the two more innovative materials, CFTS and CMTS.

6.1. CZTS TF

6.1.1. TF deposition and series definition

Herein, we will discuss the results obtained from the realisation and study of CZTS TF samples. To begin, we describe the process parameters used to prepare these samples. After the first phase of machine calibrations, we realised that the samples varied many deposition parameters to investigate the effects of these changes on the material and on the PV performances of related PV devices. For a better explanation, we divided the samples prepared into series with the following characteristics:

- First series: Summarised in Table 17, this series contains test samples realised to investigate the relationship between the **precursors' deposition parameters and the final morphology and composition of the kesterite TF**. Two experiments were conducted: changing the Cu content in the stack without changing the order of the stack, itself, and changing the order of the precursors while keeping deposition times constant. For all samples, a Cu-poor, Zn-rich approach was used to limit the formation of the conductive phase as Cu_{2-x}S .

Table 17: First series of CZTS samples deposited with modifying metal deposition times.

# CZTS sample	Precursor sequence	Ar pressure (sccm)	Deposition time (s)		
			Sn	Cu	Zn
1	Sn/Cu/Zn	6,5	1750	736	450
2	Zn/Cu/Sn	6,5	1750	736	450
3	Sn/Cu/Zn	6,5	1750	600	450

- Second series: Summarised in Table 18, this series contains samples deposited following the same composition as sample #3 of the first series, since its final composition is closer to the composition of a high-PV performance CZTS-based device. In this series, we decided to modify **the pressure of the deposition chamber** to investigate the effect of this parameter on the morphology of pristine metallic stacks and sulphurised TF. At a higher pressure, the homogeneity of the stack should be higher.

Table 18: Second series of the CZTS samples deposited with the same stoichiometry of sample #3, modifying the sputtering chamber's pressure.

# CZTS sample	Precursor sequence	Ar pressure (sccm)	Deposition time (s)		
			Sn	Cu	Zn
4	Sn/Cu/Zn	5	1750	600	450
5	Sn/Cu/Zn	6,5	1750	600	450
6	Sn/Cu/Zn	8	1750	600	450

In these two series, **two sulphurisation temperatures** were tested. Samples obtained with different sulphurisation processes are identified with the two labels '*LTemp*' for samples obtained at 550°C and '*HTemp*' for samples taken at 570°C. A deeper description of these two approaches is reported in Table 19.

Table 19: Sulfurisation parameters tested on the samples of the two series.

Sulfurization process	Sulphurisation process parameters					
	Tmax1 (°C)	Rmp1(°C/h)	Duration (min)	Tmax1 (°C)	Rmp1(°C/h)	Duration (min)
Low temperature (Ltemp)	530	900	3	550	400	40
High temperature (Htemp)	550	900	3	570	400	40

- Third series: Summarised in Table 20, this series contains the samples obtained by applying **two PDTs**. **Keeping the** parameters of sample #6, we made a few replicas to test the influence of the application of the acidic treatment, the application of the thermal treatment and the application of both treatments.

Table 20: Third series of CZTS samples deposited with the same stoichiometry of sample #3 but applying different PDT.

# CZTS sample	Precursor sequence	Ar pressure (sccm)	Deposition time (s)			PDT
			Sn	Cu	Zn	
6	Sn/Cu/Zn	8	1750	600	450	none
7	Sn/Cu/Zn	8	1750	600	450	HCl
8	Sn/Cu/Zn	8	1750	600	450	HCl+TT

Every sample was deposited considering the ideal stoichiometry mentioned before ($[\text{Cu}]/[\text{Zn}]+[\text{Sn}]\sim 0.8$, $[\text{Zn}]/[\text{Sn}]=1.2\sim 1.3$ $[\text{Cu}]/[\text{Sn}]=1.65\sim 1.85$).

6.1.2. Material characterisation

6.1.2.1. Morphological and compositional analysis

In what follows, we will discuss the results of the SEM–EDX analysis of CZTS TF samples, separately describing the three series detailed before. The samples will be described and observed on every available surface. The sample preparation for SEM–EDX analysis depicted in Section 5.7 allows us to investigate the full material, as the FRONT, BACK and SECTION surfaces are available for observation.

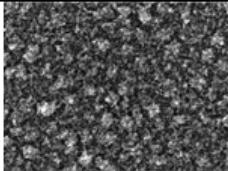
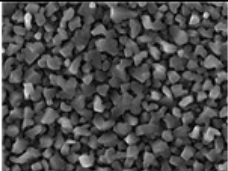
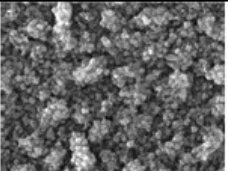
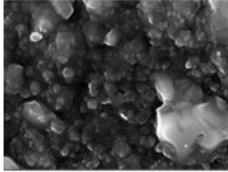
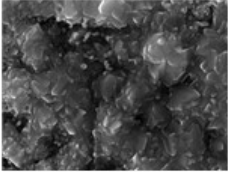
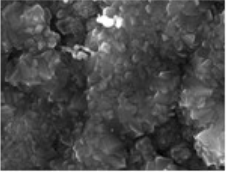
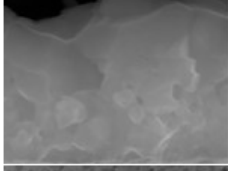
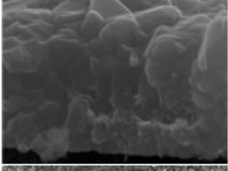
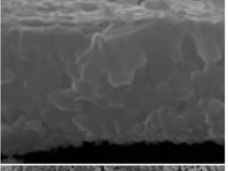
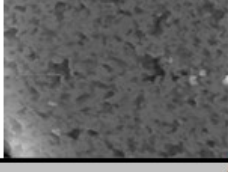
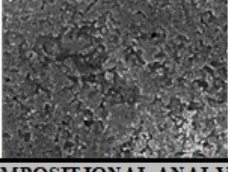
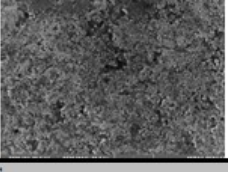
6.1.2.1.1. First series: Varying the Cu content and the deposition order

In the first series of samples, two deposition times for Cu deposition and two metal stacks were tested. These tests were conducted to investigate the impact of Cu content on the formation of Cu-based secondary phases and on the formation of voids with back contact with molybdenum, as tested by *Fairbrother et al.* [42]. See Figure 12. The samples obtained in this series were sulphurised using the LTemp procedure. At the end of the process, all samples illustrated good adhesion, confirmed after the deposition of the various layers to finalise the PV device.

Comparing the SEM images in Table 21, we can affirm the following:

- Metallic stack morphology **depends more on the precursors' order** (sample #1 vs. #2) than on the thickness of the Cu layer (sample #2 vs. #3).
- The samples' morphologies do not change between samples and **do not depict the formation of Cu_xS** on the front surface. Sample #3's morphology conveys less roughness than the other samples, which is confirmed with a cross-section of SEM images.
- From the cross-section images, a thickness of **1 μm** can be measured for all samples. This value is consistent with the value of 800nm measured in the literature for record CZTS PV devices [111].
- Every sample's back surface **demonstrates the typical formation of voids**: The dimension and distribution of these defects vary for every sample, presenting a higher dimension of voids in sample #2, in accordance with the literature [42].

Table 21: Comparison of results for the CZTS samples of the first series. Here are the SEM images reported of the FRONT and BACK surfaces as well as the cross-sections and compositional ratios obtained with EDX analysis.

		CZTS #1	CZTS #2	CZTS #3			
		SEM IMAGES		Metals			
FRONT							
Cross-section							
BACK							
		COMPOSITIONAL ANALYSIS					
		sulf	metals	sulf	metals	sulf	metals
Cu/Zn+Sn		0.9	1.0	0.9	1.0	0.8	0.8
Zn/Sn		1.2	1.4	1.1	1.1	1.2	1.3
Cu/Sn		2.1	2.4	1.8	2.1	1.8	1.8
S/Met		1.0	---	1.0	---	0.9	---

The EDX analysis of both the pristine metal stack (blue data in Table 21) and the post-sulphurisation TF (black data in Table 21) reveals the following:

- Samples #1 and #2 show a compositional ratio $[Cu]/[Zn]+[Sn]$ **slightly higher than 0.8**; this value was corrected in sample #3, decreasing the Cu content. This confirms the viability of sputtering deposition for this application, wherein fine control of stoichiometry is needed.
- Only in sample #1 is a strong difference in stoichiometry observed between the metal stack and the sulphurised TF, while for a lower Cu content, stoichiometry **ratios are not significantly different before and after the sulphurisation process**. This demonstrates that in our process, no significant Sn loss is observed in high-performance stoichiometry conditions. Consequently, there is no need to implement the presence of Sn or SnS in the sulphurisation chamber.
- **The order of precursors scarcely influences the final composition of the film**; observing the data obtained for samples #1 and #2, $[Cu]/[Sn]$ depicts the higher difference between these samples, mainly due to disparate diffusion gradients of Sn and Zn, depending on their position in the stack during sulphurisation.
- Sample #3 reveals the best compositional ratios for PV device applications ($[Cu]/[Zn]+[Sn] \approx 0.8$, $[Zn]/[Sn] \approx 1.2-1.3$ e $[Cu]/[Sn] \approx 1.65-1.8$). Accordingly, we chose this metal stack deposition parameter to obtain the samples for the next two series.

6.1.2.1.2. Second series: Varying the Argon flux and the sulphurisation temperature

With the second series of CZTS samples, we investigated the effect of Ar flux during the metals' deposition and the effect of higher temperatures during the sulphurisation process. From the parameters of sample #3 of the first series, we deposited samples using lower (5sccm) and higher (8sccm) Ar flux settings during the deposition of the metal stack. This study aims to understand the connection between the energy that the metal atoms possess when they reach the substrate and the morphology of both a pristine metal stack and sulphurised TF, since the metal atoms impact Argon plasma more frequently when the flux is higher due to the higher number of Ar atoms inside the chamber and lose more energy before reaching the substrate.

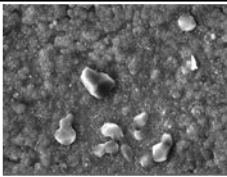
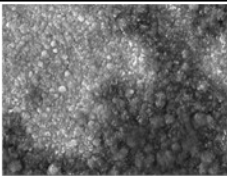
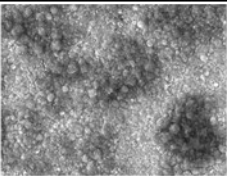
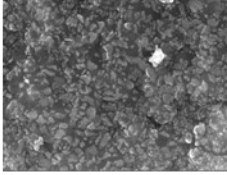
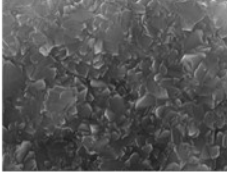
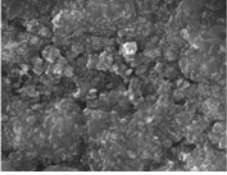
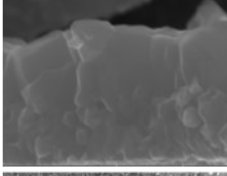
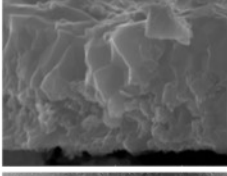
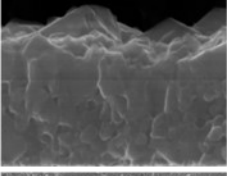
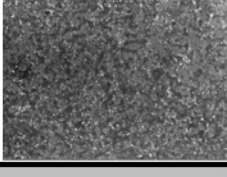

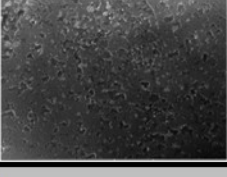
Simultaneously, we wanted to study the effect of a higher temperature during the final step of the sulphurisation process, realising the samples labelled '*HTemp*'. The comparison of SEM images in Table 22 demonstrate the following:

- The FRONT surface morphology of these samples conveys that **the Ar flux has an impact on superficial secondary phases**: In the 5sccm samples, bits of Cu_xS are visible on the front surface, while in the 6.5 and 8 sccm samples, wide precipitates of ZnS are visible.
- Zones without ZnS, 6.5 and 8sccm samples present the best surface morphology, with compact and crystalline grains.
- Even in this case, the mean thickness is **1 μm** , in line with the literature [40].
- The **dimension of the voids** at the back interface was lower than that observed for the first series' samples.

The EDX analysis of the samples of Table 22 have been performed both on the FRONT (black value) and the BACK (blue value) surfaces to spot differences. From the comparisons of these values, it can be affirmed that:

- For sample #5, there are **no significant differences in the stoichiometric ratios** between the samples sulphurised at various temperatures (*HTemp* vs. *LTemp*).
- Increasing the Ar flux, stoichiometric ratios tend to approximate the ideal ones for PV application, especially $[Zn]/[Sn]$ and $[Cu]/[Sn]$, and to become similar between the FRONT and BACK surfaces. The $[Cu]/[Zn]+[Sn]$ ratio remains constant for all AR flux settings, showing that the samples remained Cu-poor, even if sample #4 illustrates the presence of Cu_xS on its front surface.
- In sample #6, **no compositional gradients between the FRONT and BACK surfaces are visible**; the compositional homogeneity permits the minimisation of randomised differences in band structure in the absorber layer (negatively influencing the final PV behaviour of the layer).

Table 22: Comparison of results for the CZTS samples of the second series; SEM images are reported for the FRONT and BACK surfaces and cross-sections and the compositional ratios obtained by EDX analysis.

		CZTS #4	CZTS #5	CZTS #6			
SEM IMAGES	Metals						
	FRONT						
	Cross-section						
	BACK						
COMPOSITIONAL ANALYSIS							
		FRONT	BACK	FRONT	BACK	FRONT	BACK
Cu/Zn+Sn		0.8	0.8	0.8	0.8	0.7	0.7
Zn/Sn		1.5	1.4	1.1	1.1	1.4	1.7
Cu/Sn		2.0	1.9	1.8	1.6	1.7	1.9
S/Met		1.0	1.0	1.0	0.9	1.0	1.1

6.1.2.2. Crystallographic characterisation by XRD analysis

For all samples contained in the first series, XRD analysis represented the kesterite structure as the main crystal phase (Database PDF4+ 04-023-6314). From the Rietveld fitting of the pattern of these samples, we calculated the cell parameters $a = 5.414 \text{ \AA}$ e $c = 10.856 \text{ \AA}$. With these values, the $c/2a$ ratio was 1,002, demonstrating the appearance of a kesterite structure, unlike a stannite structure, which reveals $c/2a$ ratios of 0.98 [13].

Figure 42 conveys a diffractogram of sample #3 as an example for the samples of the first series. In this figure, the raw data, the fitting curve, the residue curve and the peaks of the kesterite phase are visible. The kesterite structure is the only one visible, and there are no traces of the secondary phases or parasitic compounds (e.g. MoS_2 at the back surface, which possesses a highly visible peak at $2\theta \approx 33.8^\circ$).

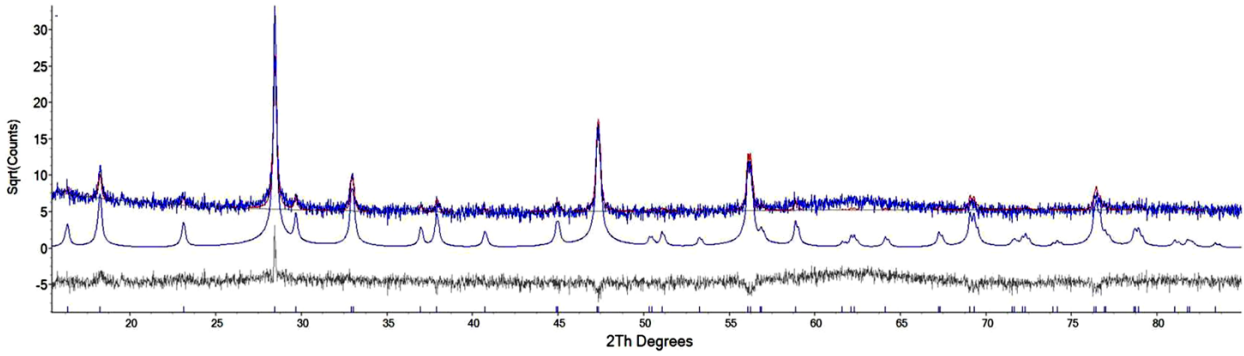


Figure 42: From above, a diffractogram of CZTS #3, a fitting curve obtained from Rietveld refinement, a residue curve and a peak position for a kesterite structure.

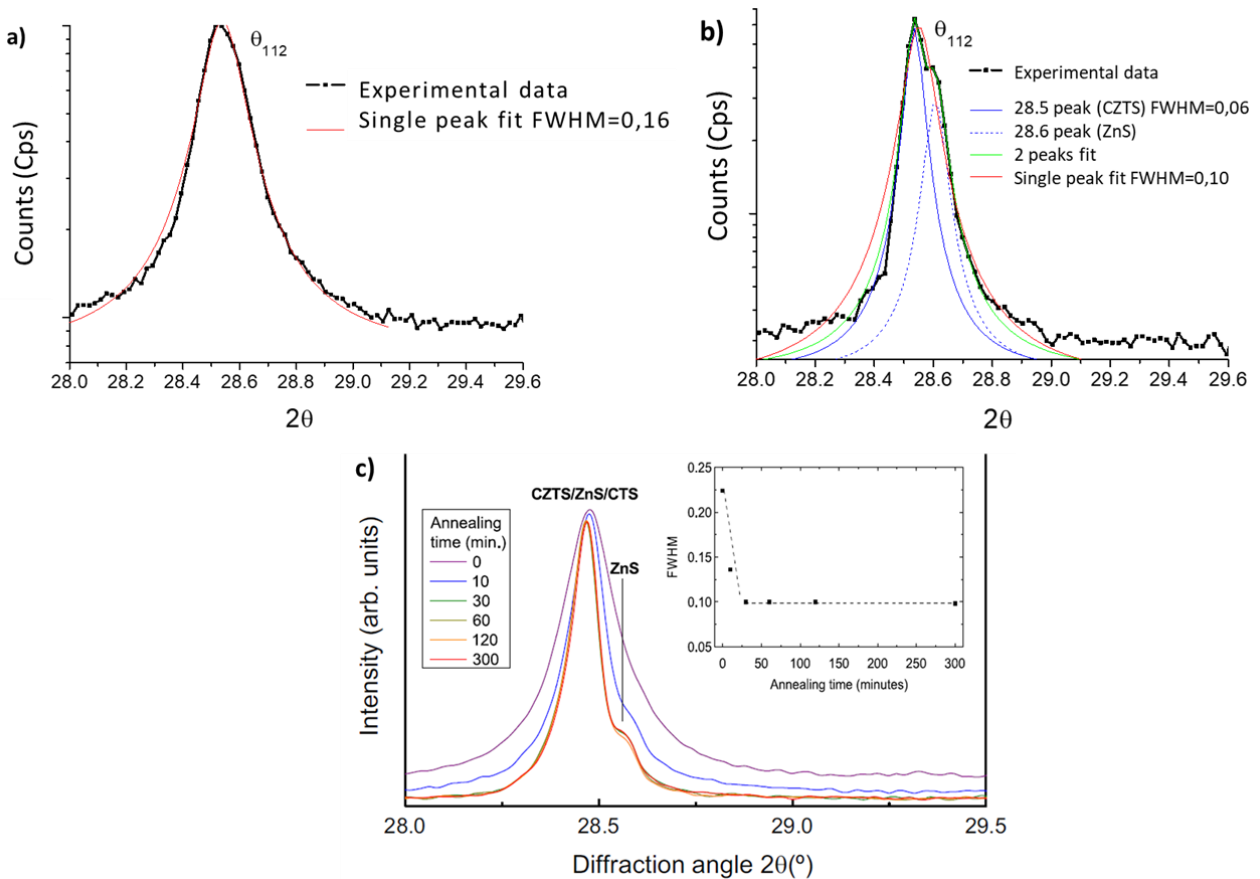


Figure 43: a) Main diffraction peak (black) and single peak fit (red) of a CZTS sample obtained at 550°C; b) main diffraction peak (black), single peak fit (red) and double peak fit (blue, dotted blue and green) of a CZTS sample obtained at 570°C and c) literature reference for CZTS samples sulphurised at 550° for different timespans [29].

For the samples of the second series, XRD analysis confirmed the presence of a kesterite crystal structure as the main phase. Consequently, a few observations on the fine analysis of the main peak [112] of CZTS for samples grown at different temperatures can be made:

- For *LTemp* samples, the main peak can be fitted with a **single peak distribution centred on 28.5°** (Figure 43-a), which is typical of CZTS structures.
- For *HTemp* samples, the main peak can be fitted with a **double peak distribution**: Figure 43(b) shows the two deconvolutions, a single peak approach (red) and a double peak approach (blue continuous and

dotted, green). For both approaches, the FWHM of the 28.5° peak was lower than that obtained for the *LTemp* sample, implying higher crystallinity in the material with a higher sulphurisation temperature.

- The double peak can be associated with the **presence of ZnS** (Database PDF4+ 04-003-6961), which has been observed in the literature: Figure 43-c [29] depicts the results of the XRD analysis of samples sulphurised at 550° for different times. Increasing the process time, the main peak becomes sharper, and the appearance of a second peak associated with ZnS is visible.
- No secondary peak was clearly visible in the *LTemp* sample. However, in the *HTemp* sample with a process time of 40min, a similar behaviour to the literature is visible. This phenomenon can be associated with a lower temperature in the chamber for geometric reasons (the temperature inside the graphite box is slightly different from the one set due to the spacing from the heating element inside the oven). A potential difference of 20°C was estimated (before this test) between the set temperature and the process temperature inside the box, which was confirmed by this test.
- The FWHM value obtained in Figure 43(b) with the single peak approach (0.10) corresponds with the minimum value measured in the literature for sulphurisation times higher than 30min. See Figure 43(c). This allowed us to state that we reached the highest possible dimension for crystalline domains in CZTS. The different heights of the ZnS peak can be attributed to the higher Zn content, which slightly changed the stoichiometry of the samples.

Even if the formation of ZnS on the surface is detrimental to PV performance, we decided not to overcome the ZnS formation by compositional adjustment, since the TF bulk composition and crystallinity corroborated the literature for PV applications but with **the application of an acidic PDT** (this topic will be described in greater detail in the following section).

In conclusion, an **Ar flux of 8sccm** inside the sputtering machine during the deposition of the metal stack and a sulphurisation process conducted at **570°C for 40min** have been identified as optimal parameters for CZTS TF. Several samples were grown with these parameters to prove the homogeneity and reproducibility of the production process. Specifically, samples with dimensions of 3.5x7cm² presented **high compositional homogeneity**. A slight thickness reduction (10%) was observed between the centre and the side of these large samples, as expected, considering the limitations of the sputtering technique, especially the low difference in dimension between targets and samples and the distance between them. Figure 44 provides photos of one of these large samples after the sulphurisation process and after CdS deposition.

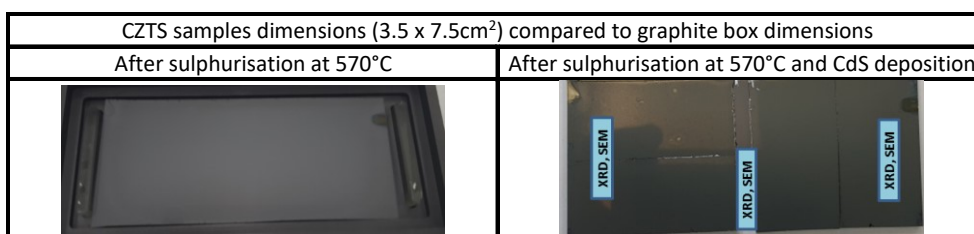


Figure 44: Image of a CZTS sample with the maximum possible dimension (3.5x7cm²) to fit in the graphite box. On the left, the sample after the sulphurisation process is still inside the box; on the right, the same sample is cut into different portions after CdS deposition. The areas of the sample used for characterisation are reported in blue.

6.1.2.3. Phase characterisation by Raman spectroscopy

To support the information obtained from the XRD analysis, all the samples were characterised with Raman spectroscopy. This analysis was used to better identify the potential presence of detrimental secondary phases with a content too low to be observed with XRD and to comprehend the correlations between

cooling processes on the CZTS material and the occurrence of order–disorder transitions, as observed in the literature [10]. For every sample, we collected Raman spectra similar to the one on the left of Figure 16: From the fitting processes of these spectra, we obtained the deconvolution of the single peaks that form the spectra to search for the same resonance observed by *Scraag et al.* [10]. Unlike their work, we acquired these spectra with only the red laser ($\lambda=663\text{nm}$). From the spectra of our samples, displayed in Figure 45, we can affirm the following:

- The deconvoluted peaks are in the same position in Table 3 and in Figure 16 (the only peak missing is the one placed at 375cm^{-1}).
- Observing the peak position of the secondary phases noted in Table 2, **no secondary phases were clearly identified**. The only potentially present compound is Cu_2SnS_3 (CTS), which peaks at 290cm^{-1} and 351cm^{-1} . The quantification of this compound is still very low (if present), as no evidence of CTS presence in the XRD diffractograms has been observed. Other secondary phases with peaks visible in the deconvolutions are Cu_xS (263cm^{-1}) and ZnS (351cm^{-1}). The other peaks of these compounds are not visible, however, so we can exclude the presence of these compounds from our samples.

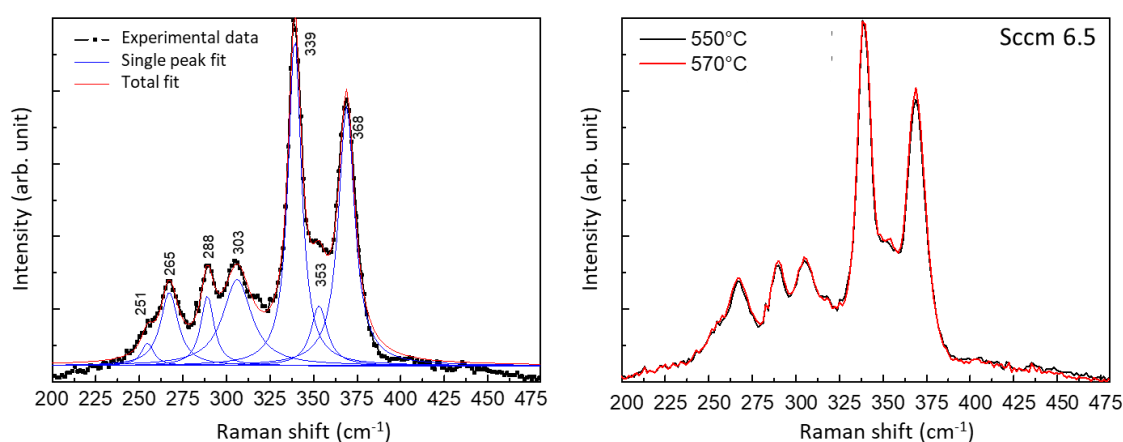


Figure 45: On the left is an example of the Raman spectrum of samples of the two series. The deconvolution of the spectrum depicts the peaks reported in the literature [10]; on the right is a comparison of the Raman spectra of samples obtained under LTemp and Htemp conditions. Sample 5 presents an example, conveying no difference in the material using two sulphurisation temperatures.

- Comparing the two Raman spectra of samples sulphurised at different temperatures, no **distinction is visible** (Figure 45, on the right); the same situation has been observed for samples grown with different Ar flux (Figure 46, on the right) and using a different Mo substrate (Figure 46, on the left), highlighting the versatility of the technique.

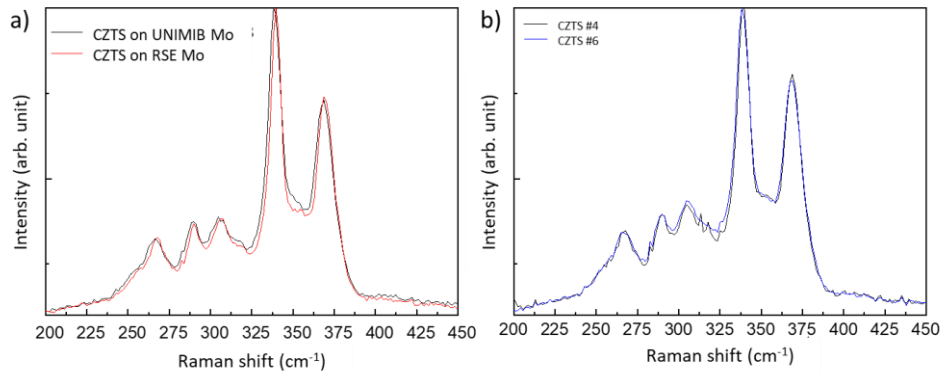


Figure 46: On the left, a comparison between two samples grown with the same procedure but on two substrates (an SLG/Mo substrate grown in the machine placed in RSE and an SLG/Mo substrate grown in the machine placed in UNIMIB); on the right, a comparison between samples grown with disparate Ar fluxes in the sputtering chamber.

- Comparing these spectra with the ones in Figure 16, a **difference in relative heights between the main peak at 339cm⁻¹ and the secondary peak at 368cm⁻¹** is observed. Comparing these spectra, one might conclude that the cooling process used in our samples could be labelled ‘fast’, but this assertion contradicts the literature. Correspondingly, we realised a sample whose cooling process was a great deal faster than the one described previously. We extracted the quartz tube from the furnace immediately after finishing the sulphurisation process; the Raman spectra of this sample are represented in Figure 47. We can observe that the secondary peak at 368cm⁻¹ has a lower height in the quenched sample, while it should be the opposite. This effect can be attributed to the switch from an ordered crystal structure obtained with slow cooling to a disordered crystal structure obtained with fast cooling, as described in the literature [10]. Figure 16 could be due to the distinct lasers used for the analysis ($\lambda_R=663\text{nm}$ vs. $\lambda_{IR}=785\text{nm}$). This effect will be discussed later, when we introduce the effect of thermal treatment on our samples.

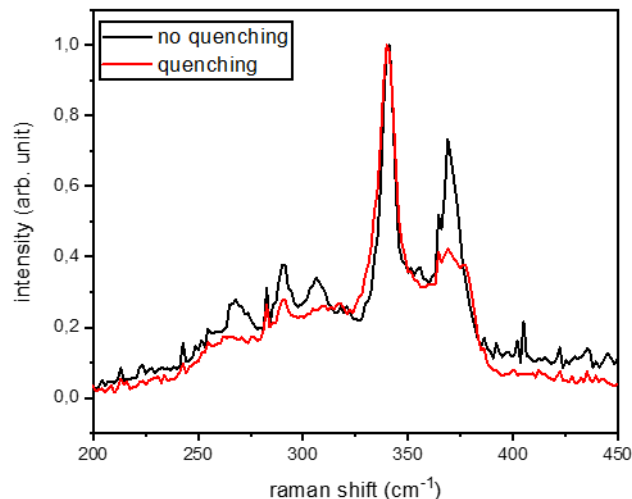


Figure 47: Comparison of two samples obtained from the same metal stack that undergo the same sulphurisation process but are cooled differently, with (red) or without (black) a quenching process.

6.1.3. Cell finalisation and characterisation

From the TF samples attained in the previous section, prototypal SCs were made by applying the experimental methods described in Section 5. The first step of the optimisation of the CdS deposition

method was performed to standardise this process for future applications on innovative chalcogenide materials (CFTS and CMTS). Next, the obtained SC was characterised with the tools already described: A statistical study is reported to assert the reproducibility and homogeneity of CZTS sputtering deposition and the reliability of the full finalisation process.



6.1.3.1. CdS deposition optimisation

During the first phase of device optimisation, we optimised the CdS deposition, since the growth of this layer is strongly dependent on the nature of the layer below. Based on the aforementioned procedure, we focused the optimisation of this deposition on three parameters:

- Chemical bath temperature.
- Deposition time.
- Hydration of the precursor salts used.

This last parameter was investigated because, after a few preliminary deposition tests at UNIMIB labs, the process was translated to RSE labs to reduce the exposure time to the atmospheric agents of the bare samples. We started using the reagents as they were stored, but the final layers obtained were too thin. This behaviour has been connected to an overhydration of the salts that distort the dosing during the process. This hypothesis was confirmed after a **dehydration process** (in a stove at a temperature of 60°C for 12h), especially for the cadmium acetate that lessened the weight about 20% after the heat process. Table 23 demonstrates the results of this optimisation phase. As displayed, heating the bath's temperature increases the final thickness of the layer, and using anhydrous salts locks in the thickness obtained independently during the process, probably due to a limiting growth mechanism. We decided to use anhydrous salts in our process, since it is very difficult to monitor the natural hydration of these compounds.

Table 23: Recap of the process parameters used to optimise CdS deposition. These tests were performed on the SLG substrate, and the thickness was measured using a profilometer.

Bath temperature	Salts condition	Deposition time [s]	CdS layer colour	thickness [nm]
75°C	As stored	690		15-25
		810		30-40
	Dried at 60°C for 12h	690		60-75
		810		65-80
78°C	As stored	690		35-45
		810		65-75

After a few tests in SCs, the parameters we have chosen as optimal for this screening are as follows:

- $T_{\text{bath}}=75^{\circ}\text{C}$.
- Anhydrous precursor salts.
- $t_{\text{process}}=690\text{s}$.

To monitor CdS growth during deposition on the CZTS samples (and CFTS and CMTS samples afterward), we introduced SLG substrates to the CBD reactor together with the samples. Figure 48 reveals CdS layers deposited on the SLG substrates used to monitor CdS deposition when we performed it on CZTS samples. Very little variation in the thickness of these layers has been observed, depending on the Cu content of the CZTS layer to cover. On a qualitative level, it has been observed that the precipitation of CdS in the CBD reactor happens longer when the compositional ratio [Cu]/[Sn] of the CZTS increases from 1.8 to 2. The abundance of Cu on the surface of the CZTS layer seems to slow the process, growing thinner layers with the same process parameters.

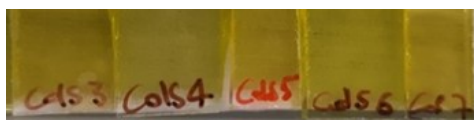


Figure 48: Comparison of CdS layers deposited on the SLG substrate during the CBD process with CZTS samples.

6.1.3.2. Characterisation of CZTS TF SCs

In the TF solar devices' finalisation tests and following characterisation, we used samples obtained from the parameters described previously (replicas of sample #6). We decided to test more samples made in the same way to check the homogeneity inside the same sample and the reproducibility between samples. With these parameters, we obtained homogeneous samples with reduced void appearance at the BACK interface and with stoichiometric ratios feasible for PV applications. Table 24 reports information about the CZTS TF deposited for the finalisation tests, together with the CdS deposition conditions already mentioned in the previous section. This first sample set did not contain a PDT test, since we needed a benchmark for our process before the application of these treatments. These replicas differ due to the sulphurisation temperature used and the hydration condition of the CdS precursor salts, as described in previous sections.

We report the use of hydrated salts for CdS deposition as a unicum, since the results on the CdS deposition tests mentioned above have already depicted its limits. Consequently, outside sample #1, we decided to test only the usage of anhydrous salts to enrich the statistical study of the performances of CZTS-based SC. No tests were conducted regarding the deposition parameters of the TCO and metal grid, as already optimised in the previous works of the research group.

Table 24: Deposition parameters for CZTS TF and CdS depositions for the finalisation and characterisation tests.

#	Max sulfurization temperature (°C)	CdS salt condition
6-1	550	As stored
6-2	550	Dried
6-3	550	Dried
6-4	570	Dried
6-5	570	Dried
6-6	570	Dried

From every 3.5x3.5cm², we managed to obtain about 8–9 SC per sample, as shown in Figure 37-a) with a mean dimension of 0.15cm². Figure 49 reports the main cell parameters (η , FF, Voc and Jsc) obtained from

these samples, calculated from the I-V curves. The data distribution was shown using a *box plot* representation: The data are grouped and shown by percentiles labelled as the 25th (lower line of the box), the 75th (higher line in the box), the 95th (vertical line above the box) and the fifth (vertical line under the box). Moreover, the two extreme values are reported as over and under all markers.

Figure 50 conveys the I-V curves under dark and illuminated conditions (1sun = 1,000W/m²) for the record cells obtained from the samples in Table 24 and for the same cell we report in Figure 51. On the left is the normalised EQE curve, and on the right is the EQE curve elaboration for a Tauc elaboration to obtain the Eg value, evaluating Y=0 of the curve $E \cdot \ln(1-EQE)^2$ vs. E, where E is the incident photon energy in eV [37].

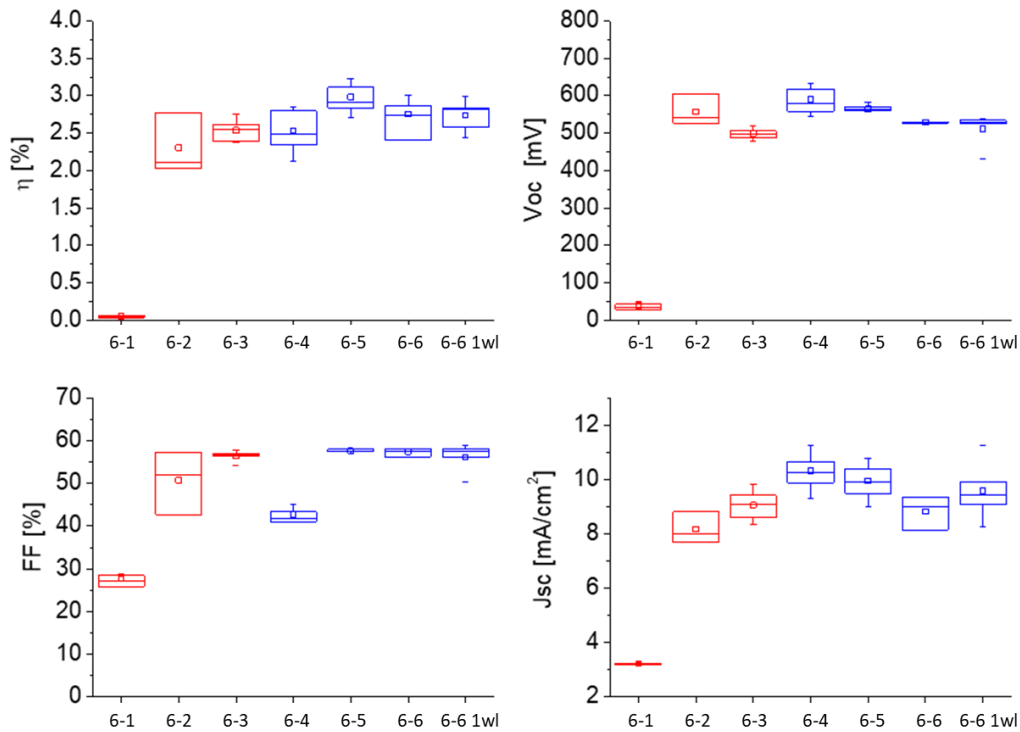


Figure 49: Statistical analysis of the main PV parameters from the samples in Table 24. The *box plots* demonstrate the median value (central line), the average value (square in the centre) and the following percentiles: 25th (lower line of the box), 75th (higher line in the box), 95th (vertical line above the box) and fifth (vertical line under the box). In addition, the two extreme values are reported as over and under all markers. For sample #6, the parameters are reported from a measurement taken a week after the first measurement was reported.

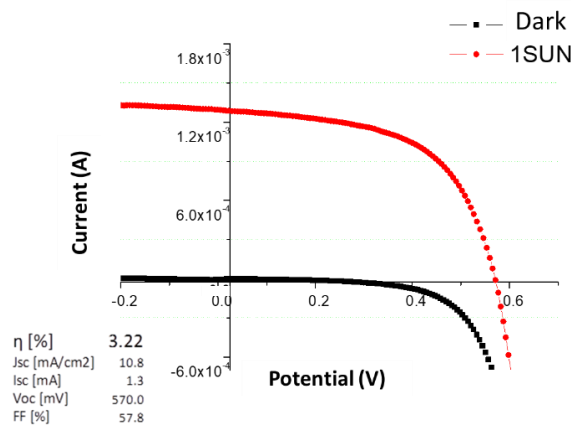


Figure 50: I-V curves in dark (black) and illuminated conditions for the record sample of Table 24.

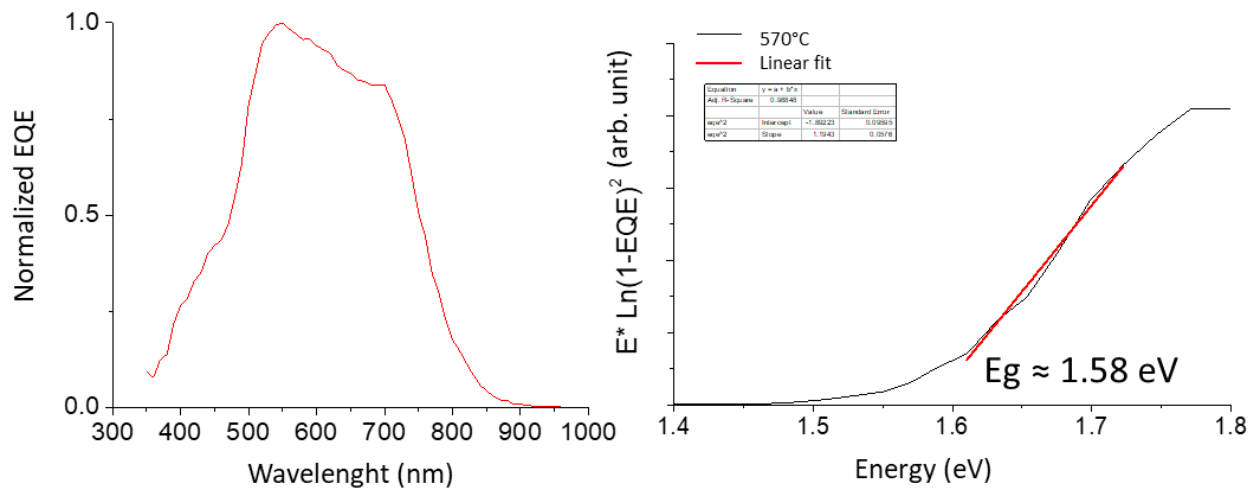


Figure 51: On the left, an EQE curve of the record cell displayed in Figure 50; on the right is an EQE curve elaboration to attain the E_g value, evaluating $Y=0$ of the curve $E \cdot \ln(1-EQE)^2$ vs. E , where E is the incident photon energy in eV [37].

From the complete data analysis derived from this characterisation, we can conclude the following:

- **The quality and thickness of CdS are key features** for the final performance of these solar devices; the layer obtained from anhydrous salts showed better performance, with uniform SC parameters whose magnitude depends on the CZTS layer's qualities.
- **The E_g value obtained from the EQE measures is comparable to that reported in the literature.** The value is in the higher portion of the range usually considered optimal for CZTS-based SCs (1.45–1.65eV) [112]. This high value is usually connected to a highly ordered structure, meaning that, for this material, the cooling process used to attain these samples can be considered 'slow'.
- Observing samples sulphurised at the same temperature, we can observe a **very low dispersion of the data** obtained from the SCs inside the same sample and few variations between samples. This aspect proves the high grade of the homogeneity and the reproducibility of the sputtering technique for quite large samples, much lower than other techniques.
- The **high FF values obtained** (around 60%) are comparable to those in the literature, demonstrating the high value of optimising these SCs.
- Slightly **better performances were achieved from samples with higher sulphurisation temperatures.** The best cell obtained possess an efficiency $\approx 3.2\%$, a value higher than similar samples in the literature [43] for CZTS TF SC similar to our approach (see Table 5), but inferior to the efficiencies found ($\approx 5\%$) in CZTS sulphurised with Sn in the chamber to limit the Sn loss from the TF [29].
- EQE measures represented as from the best devices displayed **loss phenomena in the low-energy region** (with a little step down after the highest peak at around 550 nm). This kind of phenomenon could be due to deep defects inside the CZTS layer or at the interfaces between this layer and the CdS layer above or the MoS₂ layer below. Moreover, the presence of *voids* could be another source of energy loss for charge carriers. Another cause could be the presence of the secondary phases, as ZnS and CTS could lead to this situation.
- The high V_{oc} values measured (550–650 mV) are comparable to the results obtained in the literature (see Table 4). **The main parameter lower than the literature is the J_{sc} .** Since the area below the EQE curve represents the complete current value of the device, any limitation already mentioned in the EQE curve loss can also be applied to the limited value of the current density.

- For Sample #6, a new measurement was performed after a week; it depicts PV parameters in line with or slightly higher than the first measure. **This positive ‘ageing’ effect** is known in the kesterite field, and its nature is still under discussion. Measurements obtained after a longer period reveal similar behaviour, making us believe that this ageing process is complete after a week.

6.1.4. Post-deposition treatment effects

From the results obtained from the characterisation tests and displayed in the previous section, experiments have been conducted to apply two post-deposition treatments (PDTs) to our production processes to further enhance the PV performance of our solar devices (see the section above):

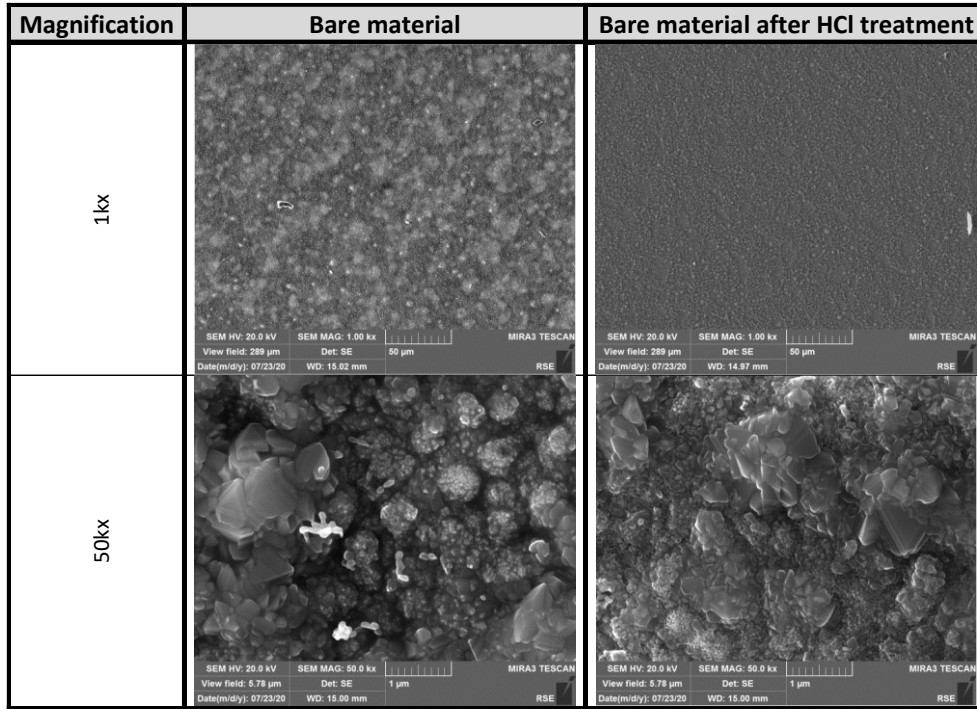
- **Chemical etching with diluted HCl (5% v/v) at 75°C for five minutes:** This process should eliminate the surface secondary phases observed in the SEM-EDX characterisation, such as ZnS. This process was performed after the sulphurisation process and before CdS deposition; the process should augment the quality of the interface between CZTS and CdS and form a better p–n junction.
- **A thermal treatment at 260°C for 10min in air on samples after the deposition of CdS** to ameliorate the interdiffusion of ions at the interface of the p–n junction and improve its quality. The samples were extracted from the oven and cooled in air without any control.

These two processes were preferred over many processes in the literature to boost the PV performances of CZTS TF SC, as they are easily implementable in a hypothetical industrial scale-up scenario. In the next section, we discuss the effects of these two processes.

6.1.4.1. Chemical etching with HCl and thermal treatment: Effect on the material

Table 25 compares the morphologies from SEM imaging of a sample before and after the chemical etch treatment with HCl. The presence of ZnS islands on the surface visible before treatment at low magnification disappeared after treatment. Comparing the high magnification images, it is clear that the small bits **of secondary phase visible in other samples are also removed by the treatment**. Altogether, the chemical etch’s main effect is to remove the front surface’s secondary phase formation observed previously, leaving the pure CZTS surface ready for CdS deposition. A partial texturisation effect can also be seen.

Table 25: SEM images at assorted magnifications of CZTS TF before and after the chemical etching treatment.



In Figure 52, the Raman spectra of samples #7 and #8 before and after the PDT are compared: on the left, the comparison before and after the chemical etch and, in the centre, before and after the thermal treatment. On the right of this figure is represented the multipeak deconvolution of the spectrum obtained after the thermal treatment. While no macroscopic distinction is visible between the Raman spectra before and after the chemical treatment, it is clear that the thermal treatment induces a **variation in the height of the secondary peak at 368cm^{-1}** in a similar way to the quenching process in the previous section (see Figure 47). This implies that quenching from a very high temperature and thermally treating the sample above the order–disorder process T_c with a fast-cooling process have the same effect: putting the CZTS layer in a disordered structure at a high temperature and making it kinetically impossible to transit to the ordered state at low temperatures, abruptly decreasing the sample temperature.

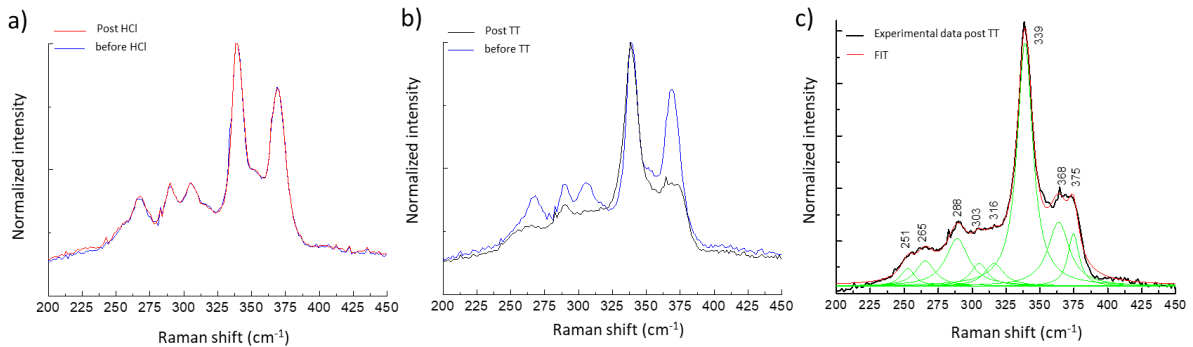


Figure 52: Comparison of the Raman spectra of samples before and after the two PDTs: a) before and after the chemical etch, b) before and after the thermal treatment and c) the peak deconvolution of the Raman spectra of a sample after the thermal treatment.

6.1.4.2. Chemical etching with HCl and thermal treatment: Effect on devices

Figure 53 presents the PV parameters of the CZTS-based SC, in which the two post-PDTs are illustrated in this section. The two processes were applied sequentially: a first study where only the chemical etch after sulphurisation was applied and a second study where both treatments were applied. Again, the samples are replicas of sample #6, which was arrived at with the optimised procedure mentioned in the previous section. The parameters were compared using the *box plot* approach already used in an earlier section. The samples were measured again after a week, marked as *1w*, to monitor the ageing process, as witnessed in previous SC series.

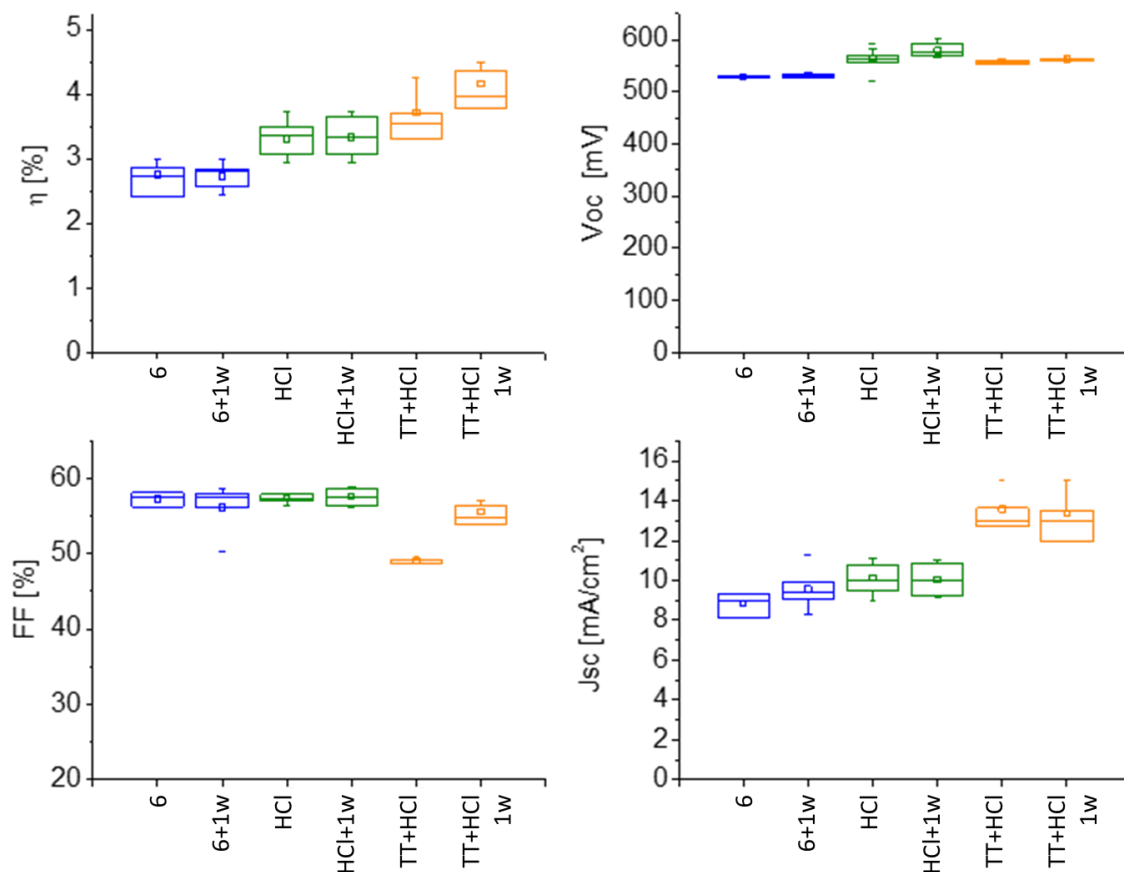


Figure 53: Statistical analysis of the main PV parameters of cells obtained progressively by applying the PDTs mentioned in this section. The *box plots* depict the median value (central line), the average value (square in the centre) and the following percentiles: 25th (lower line of the box), 75th (higher line in the box), 95th (vertical line above the box) and fifth (vertical line under the box). In addition, the two extreme values are reported as over and under all markers. For every sample, the parameters were reported from a measurement taken a week after the first measurement was reported.

Figure 54 conveys the results of the EQE measures on these samples. On the left is a comparison of the EQE curves obtained from the two samples. One with and the other without the application of both PDT is displayed, while on the right is the EQE curve elaboration for a T_{auc} elaboration to obtain the E_g value, evaluating $Y=0$ of the curve $E \cdot \ln(1-EQE)^2$ vs. E , where E is the incident photon energy in eV [37]. The evaluation of E_g is comparable to the high-efficiency CZTS SC in the literature and connected to a highly disordered material. This confirms the assumption in previous sections, where the variation of the CZTS secondary Raman peak at 368cm^{-1} was connected to the transition from ordered to disordered phases.

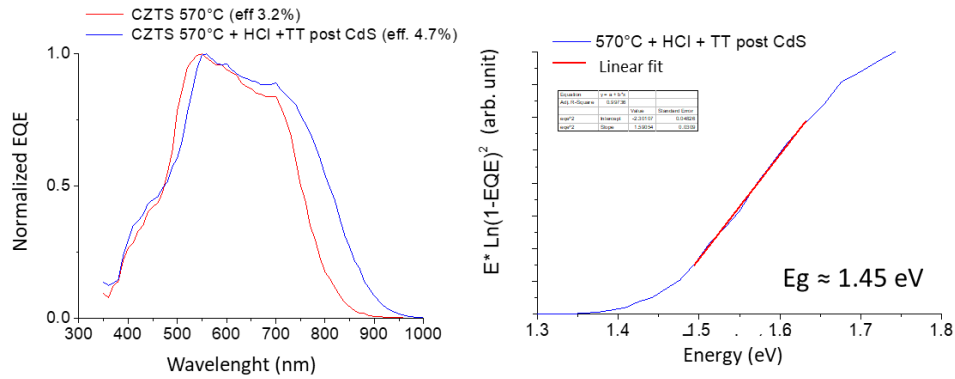


Figure 54: On the left, a comparison of the EQE curves of devices with (blue curve) or without (red curve) the application of both PDT; on the right, an EQE curve elaboration to obtain an E_g value, evaluating $Y=0$ of the curve $E \cdot \ln(1-EQE)^2$ vs. E , where E is the incident photon energy in eV [37].

From this analysis, we can affirm that both PDTs increases the final performance of CZTS-based SC, in particular:

- **Chemical treatment mainly affects the increase in V_{OC}** , a parameter usually connected to the energy of the charge carrier, implying a diminishing or loss of phenomena. Due to the localised effect of this treatment, we can affirm that these lost phenomena are correlated to the presence of secondary phases on the surface of the CZTS TF before treatment, thereby increasing the quality of the p-n junction. **The thermal treatment has a positive influence on the J_{SC}** , parameter usually connected to photon collection: The EQE measure reveals a decrease of the E_g after thermal treatment and an increase of the area below the curve. These factors explain the thermal increase in J_{SC} .
- **The FF loss observed on the first measure after the thermal treatment is gradually restored during the ageing period:** After a week, the value is like those of other samples ($\approx 60\%$). In the literature, this ageing effect has already been recorded for samples that undergo similar thermal treatment [112], but the origin of this phenomenon is still under discussion. Our samples portray ageing-related parameters that are higher than those in the literature. More tests were conducted, **changing the temperature of the treatment or the phase of the production process when we applied the thermal treatment. We changed** the treatment's temperature from 200°C to 275°C and applied the treatment after the total finalisation of the cell. In a departure from the literature [45], **all these treatments worsened the SC performance of the treated samples.** This demonstrates that the effect of a thermal treatment is very complex and can change many properties of the final device.
- **The combination of the two treatments increased the final efficiency of the SC.** For the best cell, we obtained a record efficiency $\eta=4.5\%$, with $J_{SC}=15.1\text{mA}/\text{cm}^2$, $V_{OC}=561\text{mV}$ and $FF=54\%$.

6.1.5. Defect mapping by impedance measure and $V_{oc}(T)$

6.1.5.1. Impedance measure

To attain a refined understanding of the defects' presence and nature in the CZTS TF, impedance measurements were recorded on specific samples. This kind of measurement can be conducted under different temperature conditions, depending on the information we want to obtain. Two approaches have been applied:

- RT measures: From this kind of measure, we can understand which surface of the final device acts as a non-ohmic contact. By performing these measures at different bias voltages, we can build so-called *loss maps* to understand the distribution of defects inside the device and their approximative activation energy (E_a). Last, we used the Mott–Schottky approach to calculate the flat band potential (V_{FB}) and the concentration of acceptor states at the edge of the VB.
- Temperature-dependent measures: From these kinds of measures, we can build a different *loss map* to correlate the peak frequency of (dC/df) with the temperature and calculate the E_a from an Arrhenius plot.

6.1.5.1.1. RT measures: Loss maps vs. V

We used the impedance technique at RT to investigate the position of the defect states in our devices. The variance of the capacitance versus bias voltage (V_{BIAS}) and frequency (f) represent the effect of nonlinearities in the device as resistances and defects [113]. Figure 55 presents the loss maps of two similar samples (untreated on the left, thermally treated on the right) from room-temperature impedance measures depending on V_{BIAS} and on f , plotted with data obtained from *Brammertz et al. [113]*. Figure 56 depicts the Mott–Schottky elaborations calculated from raw impedance data obtained experimentally [114] to calculate the flat-band potential (V_{FB}) and the density of acceptor states (N_a).

From the loss maps in Figure 55, we can affirm the following:

- The *loss map* derived from the untreated sample has made two main contributions: In agreement with [113], the contribution at high frequencies can be associated with a high series resistance, while the region that starts from a low frequency with a V_{bias} between 0V and 0.5V that rises to 100kHz can be associated with a defect placed at the surface with the activation energy at $E_{a1} \approx 0.5eV$. This defect is considered a *deep defect*; the exact attribution of these levels to a particular defect is quite complex but can be associated with many Sn-related defects. The presence of these defects strongly limits the V_{oc} of the final device.
- The *loss map* from the treated sample shows very similar results in terms of contribution number, but quite different results concerning contribution positions. The series resistance contribution is positioned higher, assessing a lower value of series resistance, while the interface contribution is thinner, assessing a reduction in defect concentration. This confirms the curing effect of the thermal treatment on the surface defect's concentration.

- No effect is visible due to shallow defects (as Cu_{Zn}) since the energy of these defects is too low to produce effects at RT (as explained by *Brammertz* [113]). This kind of study was performed on temperature-dependent impedance measures, as discussed later in this section.

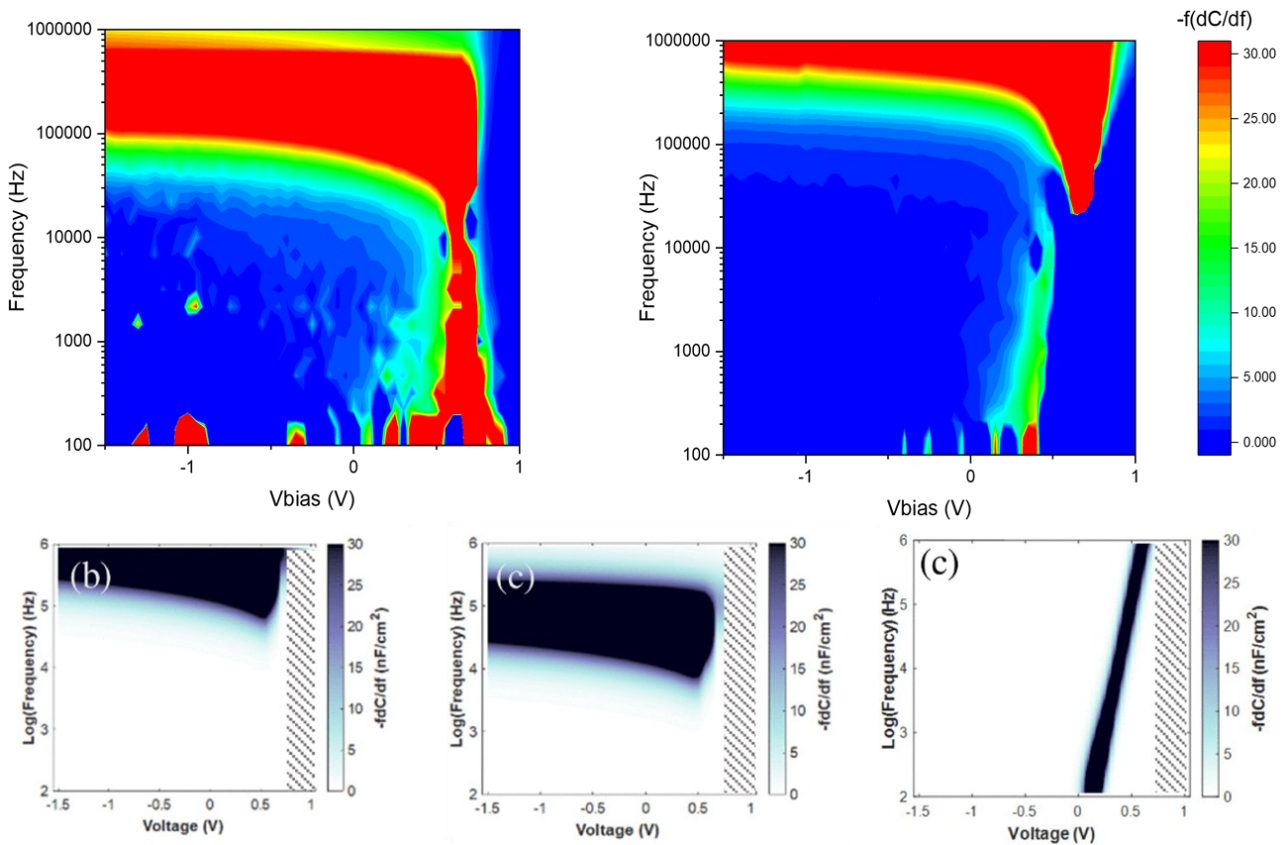


Figure 55: On top, the loss maps of untreated (left) and treated (right) CZTS SCs, where the high regions represent capacitance variation due to non-linearities. Below, for comparison, the loss maps of CZTS-CdS SC are reported in [113], where the evolution of defects' distribution is followed by the duration of thermal treatment at 200°C.

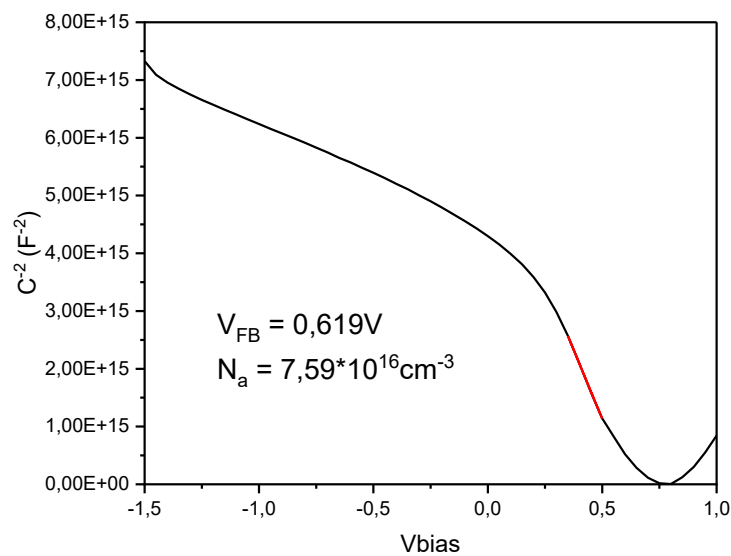


Figure 56: Mott-Schottky elaboration of the data from the record CZTS SC, collected from raw impedance data. The V_{FB} and N_a values are 0.619V and $7.59 \cdot 10^{16} \text{cm}^{-3}$.

From Figure 56, we can extract the following conclusions:

- The negative slope in the step region confirms the p-type behaviour of the CZTS semiconductor [115].
- The value of $V_{FB} = 0.619V$ is in line with the literature and represents the maximum V_{OC} value that this device can reach, demonstrating the high value of optimisation reached in this work.
- The value of $N_a = 7.59 \times 10^{16}$ accords with the acceptor density of high-performance CZTS SC, and it is the typical defect density of a doped semiconductor suitable for SC applications. The nature of these shallow defects was investigated due to temperature-dependent measures.

6.1.5.1.2. Low-temperature measures: Loss maps vs. T and $V_{OC}(T)$

A very similar work to the one made for the loss maps f vs. V can be made with a loss map f vs. T to assess defects with lower activation energy (from 0.2V below). To do this, temperature-dependent impedance measurements were taken on our CZTS record device using the same formulae used in the previous section. The top of Figure 57 portrays the loss map f vs. T derived from temperature-dependent impedance measures on the record CZTS device and the related Arrhenius plot. Below is a literature review from *M. Grossberg et al.* [116], who conducted the same elaboration.

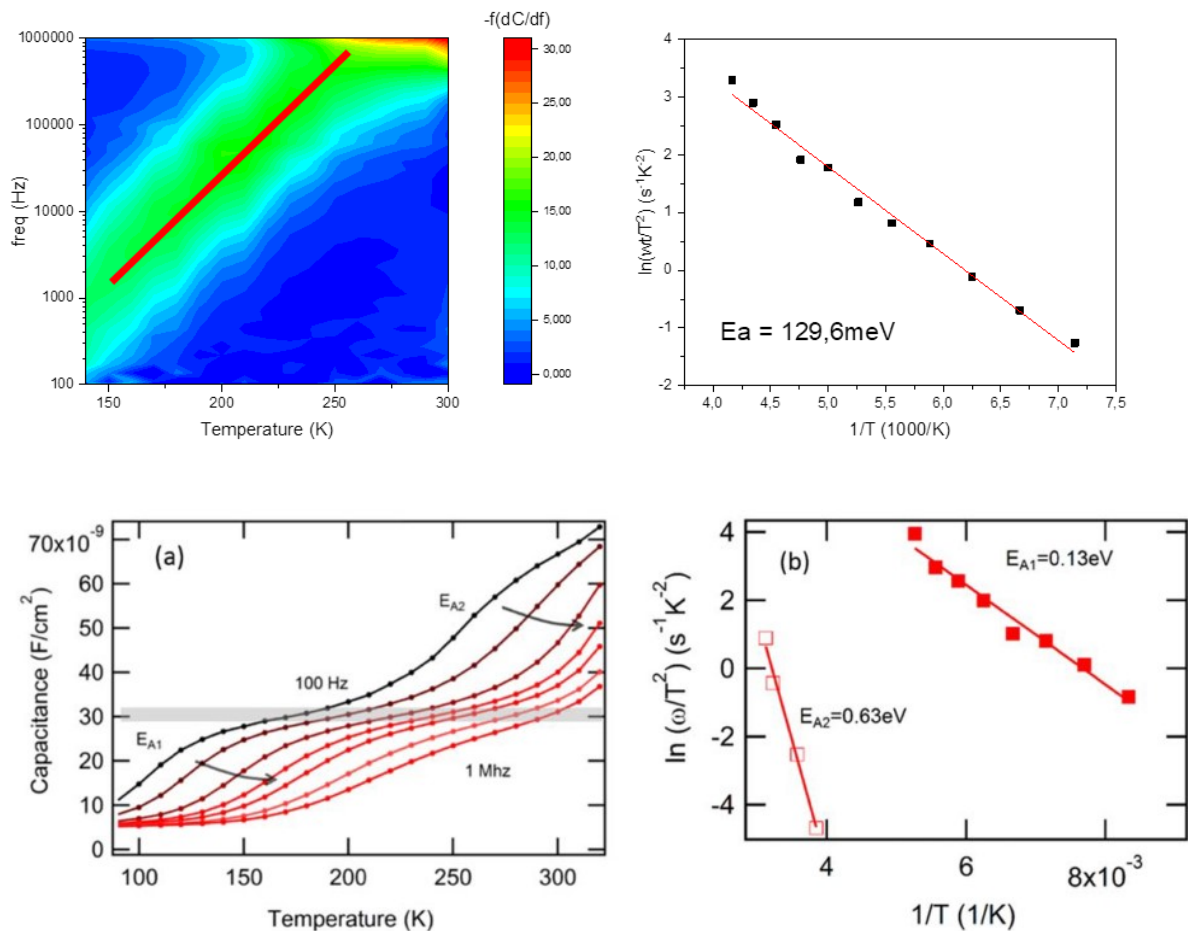


Figure 57: On top, an experimental loss map of record CZTS SC, where in red is marked the movement of the $-f(dC/df)$ function vs. f and T . It is useful to calculate the Arrhenius plot of this defect (left) and the Arrhenius plot of the defect spotted on the loss map, which conveys an E_a value of 129.6meV (right). Below, C vs. T at different frequency trends and the Arrhenius plot derived from it, as reported by *M. Grossberg et al.* [116].

From Figure 57, we observe the following:

- In our analysis, **only one peak is visible in the loss map, which starts to appear at $T \approx 250\text{K}$** and moves in frequency down to 150K. Another contribution could be present at a higher temperature (red region of the loss map), but the very low variation in the position of this contribution and its appearance at such a high temperature make correct detection difficult.
- **Our data are limited to a specific temperature range:** under 140K, the impedance data are not accurate, unlike the cited literature, where the analysis is performed down to 100K. This could hide other contributions visible at lower temperatures.
- From the loss map's Arrhenius plot, we can figure an **E_a value of 129.6meV**. This value is compatible with the presence of the Cu_{Zn} defect, which confirms the presence of the Cu_{Zn} defect as the dominant acceptor defect in our material.

To complete the low-temperature characterisation, together with the temperature-dependent impedance measures, temperature-dependent I-V curves were also measured. This measure should provide information about the ideality factor of the SC and insight into the behaviour of defects inside the CZTS layer. The V_{OC} vs. T trend is revealed in Figure 58 with the interpolated value of V_{OC} at 0K and the slope of the linear fit.

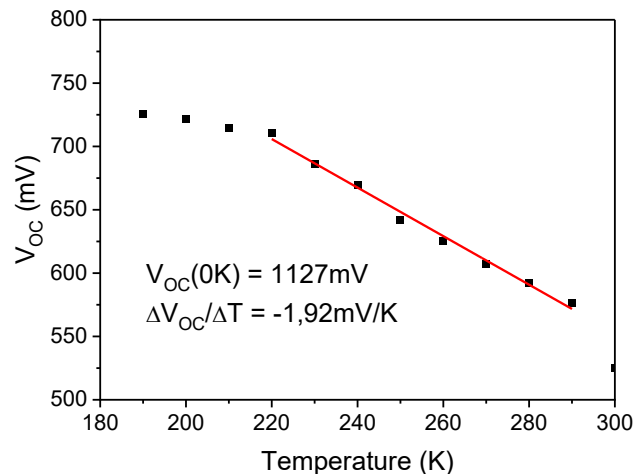


Figure 58: The V_{OC} vs. T measure with the value of V_{OC} at 0K attained by interpolation.

From this study, we can conclude the following:

- **The value of V_{OC} at 0K describes the main recombination of photogenerated carrier pairs.** The value reported is lower than E_g calculated by EQE measures, and this means that the main recombination path in our device is through the interface [117]. This V_{OC} at the 0K value corresponds with the effective E_g measure from CZTS layers containing Cu_{Zn} defects, where acceptor defects pair up with donor defects, forming QDAP [118]. With the information from temperature-dependent impedance, we built a qualitative model for band structure in CZTS samples after thermal treatment, as shown in Figure 59. Inside the optical band gap obtained from EQE measurements, we can find an acceptor defect associated with the defect Cu_{Zn} and a donor defect associated with the donor defect Zn_{Cu} .
- The slope value corroborates values obtained in the literature [119], demonstrating that the ideality factor and, hence, the quality of our p-n junction is in line with the literature.

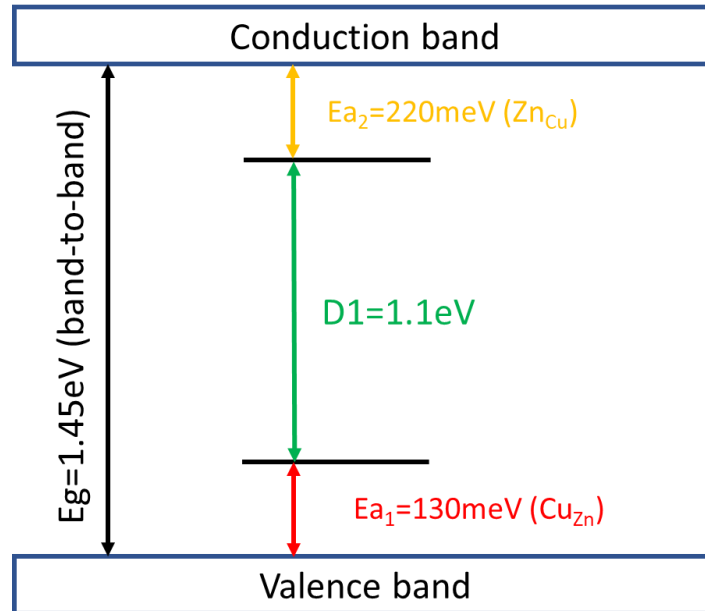


Figure 59: Qualitative model for the band structure of thermally treated CZTS samples. Inside the optical band gap of the material (1.45eV), an acceptor state is placed at 130meV (associated with the Cu_{Zn} anti-site defect) and a donor state at 220meV (associated with M_1 or anti-site Zn_{Cu} defects [118]).

To conclude the defect study, we can affirm that the loss map at the RT sample depicts the presence of a defect with $E_{\text{act}} \approx 0.5 \text{ eV}$ at the CZTS/CdS interface; these features drastically decrease in the treated sample, leading to an increase in J_{SC} in the final device. A temperature-dependent loss map revealed the presence of defects at $E_a = 0.130 \text{ meV}$, which is typical of a Cu_{Zn} defect. Other defects at lower E_a are not visible, especially in the temperature-dependent loss map, but their presence cannot be excluded due to the aforementioned measurement limits. Finally, the V_{OC} at the 0K extrapolation discloses that the main recombination in our device happens through interface defects, where the anti-site couple $\text{Cu}_{\text{Zn}}\text{-Zn}_{\text{Cu}}$ is the shorter recombination path.

6.1.6. Conclusion

We obtained good-quality CZTS TF samples in accordance with the literature on the application of this chalcogenide in PV devices, validating the two-step technique used in this PhD thesis to produce this class of materials. We optimised both processes' parameters, the deposition of metallic precursors on the Mo/SLG substrate and the sulphurisation process, to reach compositional ratios suitable for PV application ($[\text{Cu}]/([\text{Zn}]+[\text{Sn}])=0.8$, $[\text{Zn}]/[\text{Sn}]=1.2$, $[\text{Cu}]/[\text{Sn}]=1.8$). After preliminary experiments, we worked on two series of samples: a first series of samples where we optimised the Cu content to reduce the metallic behaviour of the TF and a second series of samples where we adjusted the Ar pressure inside the sputtering chamber and the sulphurisation temperature. The samples were characterised with tools suitable for this field. We used SEM-EDX, XRD and Raman analyses to monitor the composition and morphology of these samples, spotting the presence of a ZnS secondary phase in samples garnered at higher temperatures. The Ar pressure decreases the average energy of the plasma, leading to a more homogeneous metal deposition. XRD and Raman analyses confirmed the long-range homogeneity of these samples. With these parameters optimised, we derived a standard PV efficiency of around 3% with PV parameters, in line with the literature's results when similar procedures were used. The EQE measures performed on these devices presented curves in line with the literature, from which we collected E_g values of $\approx 1.55 \text{ eV}$ for CZTS. This value accords with E_g values connected to highly ordered CZTS layers, as described in the introduction.

A second step of the optimisation process has been the application of two PDT, an acid treatment with diluted HCl to remove the ZnS residues from the surface of CZTS material and a thermal treatment applied on the p–n junction CZTS/CdS to cure the interfacial defects between these two materials. Using SEM imaging, we observed the disappearance of the ZnS phase from the surface after the acid treatment, followed by an overall increase in PV performance, especially V_{OC} , while we observed the double effect of the thermal treatment on the samples. The first effect enables the CZTS to transition from an ordered to a disordered crystal structure. This structure relays higher PV performances, due mainly to the decrease of the E_g ($\approx 0.1\text{eV}$, down to 1.45eV) that mainly increases J_{SC} , as observed by EQE. The second is a quite complex effect on defects' states on the interfaces: The room-temperature loss maps gleaned from impedance measures convey the decrease of defects' contribution to the CZTS/CdS layer after the application of the thermal treatment, with persistent deep defects with $E_a \approx 0.15\text{eV}$ at the interface. The thermal loss map confirms the presence of this defect after treatment and is linkable to the presence of the Cu_{Zn} defect. The presence of Cu_{Zn} defects, which implies the presence of Zn_{Cu} defects, still limits the maximum V_{OC} that we can gain from the device. Taking all these effects together, we obtain a general increase of the final PV performances after the application of both PDT, with a record device that demonstrates remarkable PV parameters ($\eta=4.5\%$, with $J_{SC}=15.1\text{mA/cm}^2$, $V_{OC}=561\text{mV}$ and $FF=54\%$) in line with other works in the literature where similar approaches were applied.

6.2. CFTS TF

Based on the knowledge that we had matured on CZTS, we started working on the deposition of CFTS TF. In this case, we decided to prepare two sample series to study the effect of process parameters on the properties of CFTS TF. In this section, the CFTS sample series will be described and discussed with the process parameters of the experiments. In this case, a few tricks were applied to the deposition of chalcogenide TF, which diverges from our process for CZTS:

- To deposit Fe, a **mixed target made of Fe and Cu in a 1:1 composition** (atomic ratio) was used as an Fe source instead of a pure Fe target to overcome the problem of ferroelectricity in the magnetron source. Preliminary tests on the deposition of this material led to TF samples with a final 3:2 composition of Cu/Fe (60%:40%). This behaviour could be linked to inhomogeneity in the target or the effect of varying *extraction rates* from the target, in which the two elements possess the same energy as Argon ions in the plasma. Despite the presence of Cu in the target, which limits the high coercion field that Fe induces on the static field of the magnetron source, the deposition must be performed using an RF **generator**, since it is impossible to spark and sustain the plasma with a DC generator.
- The Cu/Fe ratio deposited directly from the Cu/Fe target permits control of the composition of the final CFTS since the theoretical relative content Cu/Fe equals 2:1. The usage of a separate pure Cu target allows the complete exploration of the phase diagram in the region **2>Cu/Fe>1.5**.
- As for the thermal treatment, the only variation compared to the CZTS process is the application of a very slow controlled cooling process (18°C/h) to evaluate its effect on possible variations in the crystal structure of the final chalcogenide.

6.2.1. TF deposition and series definition

In this section, we will discuss the results obtained from the realisation and study of CFTS TF samples. To begin, we describe the process parameters used to prepare these samples. After the first phase of machine calibration, we obtained samples varying in many deposition parameters to investigate the effects of these changes on the material and on the PV performances of related PV devices. For a better explanation, we divided the samples prepared in a 'series' with these qualities:

- First series: As summarised in Table 26, these samples were synthesised by setting the sputtering generators in constant 'power' mode. This setting is the standard choice for working with the magnetron sputtering technique for metallic targets. This was the same approach we used to arrive at all the CZTS samples. The samples in this series were synthesised with different focuses, as follows:
 - Couples #7–#8 and #10–#12 for the sputtering deposition reproducibility test.
 - Samples #11–#14–#15: The effect of the precursor deposition order on the morphologic control at the Mo interface (void formation) and superficial secondary phase formation.

In detail, this sample's objectives are as follows:

- **Qualitative evaluation of the control** of the two-step process proposed in this PhD thesis applied to CFTS samples and a comparison of the results with CZTS. Critical aspects of the process could be the usage of a Cu:Fe mixed target instead of pure targets and the application of an RF source generator.

- Investigation of a section of the CFTS phase diagram with composition limits from the stoichiometry to the composition ratios already confirmed (in the literature) for CZTS PV application, **Cu/Fe+Sn ≈0.75 -0.9, Fe/Sn≈1.1-1.3 e Cu/Sn≈1.8-2.**
- Study the effect of **precursors' ordering** in multilayer deposition by sputtering with constant deposition times.

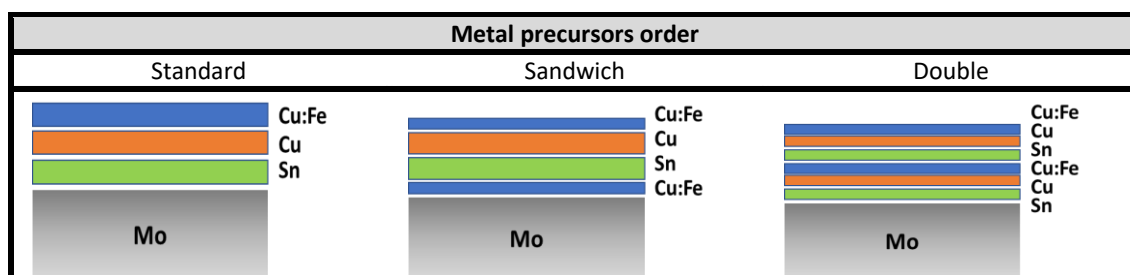
Table 26: Process parameters of CFTS samples (first series).

# CFTS	Precursors order	Deposition time [s]		
		Sn	Cu	Cu:Fe
7	Mo/Sn/Cu/Cu:Fe Standard sequence	1400	185	1320
8		1400	185	1320
9		1400	185	1400
10		1400	175	1470
11		1250	150	1600
12		1400	170	1470
14	Cu:Fe/Sn/Cu/Cu:Fe "Sandwich" sequence	1250	150	800+800
15	Sn/Cu/Cu:Fe/Sn/Cu/Cu:Fe "Double" sequence	625+625	75+75	800+800
16	Mo/Sn/Cu/Cu:Fe Standard sequence	1410	40	1710

In detail, for the last aim, different deposition orders were tested (Table 27), defined as follows:

- **Standard:** The same sequence is used for the best CZTS sample deposition, where Sn is the first element deposited at the interface with Mo. In this way, Sn is not directly exposed to S flux during thermal treatment. This should limit the formation of Sn sulphides, highly volatile compounds, during the first moments of treatment, avoiding Sn loss and variations in Sn content in the samples. This sequence should induce the formation of *voids* at the Mo interface.
- **Sandwich:** The Cu:Fe deposition is conducted in two cycles, one at the start and one at the end of the deposition process, limiting Sn contact with Mo and, thus, limiting the formation of *voids*.
- **Double:** The standard structure is replicated twice, but with halved deposition times to keep the element quantity constant. This structure should mimic a possible co-sputtering process in which the elements are deposited together simultaneously.

Table 27: Three structures used in this section for CFTS deposition.



- Second series: Summarised in Table 28, these samples were deposited after completing the characterisation of CFTS TF for the first series. These samples were synthesised by setting the sputtering generators in 'constant current' mode. We decided to test this feature to confirm the stability of material flux during the deposition obtained for 'constant power' samples. The focus of these samples was as follows:

- Samples #18–#19–#20: Deeper study of the **Cu concentration** and its consequences for physical chemist features, as secondary phases and Eg.
- Samples #20–#21: Deeper study of the **Fe concentration** and its consequences for physical chemist features, as secondary phases and Eg.
- Samples #20–#22–#23: Completing the study regarding the effect of **precursor orders** on the morphology of the CFTS layer at the Mo interface (*voids'* formation) and the effect of Fe isolation from the environment to limit the presence of Fe⁺³.
- Sample #17: This sample has been deposited to forcibly obtain a **high content of the Sn-rich phase of CFTS, rhodostannite**.

Table 28: Process parameters of CFTS samples (second series).

# CFTS	Precursors order	Deposition tims [s]		
		Sn	Cu	Cu:Fe
17	Sn/Cu/Cu:Fe	1704	48	1020
18		1704	48	2066
19		1704	70	2066
20		1704	115	2066
21		1704	115	2210
22	Cu/Sn/Cu:Fe	115	1704	2066
23	Cu:Fe/Sn/Cu	2066	1704	115

The process parameters for the deposition of this series are identical to those used for the first series. However, a different approach has been applied to this series: Instead of utilising the ‘constant power’ employed in the previous section, we decided to apply a ‘constant current approach’ due to the theoretically higher reproducibility that this approach possesses compared to the former approach.

Some samples that belonged to the second series, specifically some of those deposited varying the precursor order, were processed with two sulphurisation processes in which the only different parameter was the cooling rate after the thermal treatment. This step usually follows the natural cooling of the oven, set to RT at the end of the process (the approach also used for CZTS). The test was performed setting a lower cooling rate (18°C/h) so the samples cooled from 570°C to RT in approximately 30h. With this process, we wanted to study a temperature transition similar to the natural one, slow and steady, to observe secondary phases connected to slow processes and witness the transition between cubic and tetragonal structures, as verified by *Ohtsuki et al.* [68] with microcrystals grown with extremely slow processes.

6.2.2. Material characterisation

6.2.2.1. Morphological and compositional analysis

Herein, we discuss the results gained from SEM-EDX analyses of the two series of CFTS TF samples. The sample preparation for SEM-EDX analysis described in the ‘Fabrication and Characterisation’ section allows us to investigate the entirety of the material, as the FRONT, BACK and SECTION surfaces are available for observation. The compositional study will be wider than that performed for CZTS since the study of the relationship between composition and morphology is more in-depth.

6.2.2.1.1. First series of CFTS samples: The ‘constant power’ approach

Table 29 summarises the results of the compositional analysis of the samples within the first series. The reported values are the mean value calculated by 10 EDX analyses on the surface of samples with an area of 5*3mm². In the table, the S value is not reposted due to the difficulty of evaluating it together with Mo in the EDX analysis, since the peaks of these two elements overlap. All samples are considered to possess a ratio [metals]/[S]<1, since we work in the S-excess condition. In Figure 60, the same compositional data are organised in a ternary phase diagram, where the axes correspond to the relative metals’ atomic concentration. For clarity in the diagram, a purple dot signifies the compositional point of the stoichiometric CFTS (Cu:Fe:Sn = 2:1:1), and the intersection of three blue arrows marks the compositional point of the best-performing CZTS compositions. In Figure 60, below, the compositional ratios are compared, studying the dependence of [Cu]/[Sn] and [Fe]/[Sn] respecting [Cu]/[Fe]+[Sn]. Light blue highlights the best-performing CZTS compositions.

Both Table 29 and Figure 60 reveal where on the sample these data are collected: FRONT compositions are data taken from the free surface in the sample, while BACK compositions are data collected from the interface between CFTS and Mo. These data were collected by removing the material from the substrate in scales and analysing both faces. The focus of this study is to verify whether compositional gradients are present following the TF depth.

From these EDX data analyses, we can observe the following:

- All samples convey compositional values that belong inside the range **between the perfect stoichiometry point of CFTS and the best compositional range of CZTS**.
- We observed **no trends** in the variation of compositions **between the FRONT and BACK** measurements, especially for samples with a standard deposition order. The variation between the FRONT and BACK measurements is lower than the EDX sensitivity, which portrays the perfect interdiffusion of all the elements in the multilayered structure during thermal treatment.
- Almost every sample has **Cu-poor composition** ([Cu]<50%), an ideal condition for limiting the formation of Cu_{2-x}S.
- Every sample was far from CZTS’s best performance point.

Table 29: Process parameters, FRONT and BACK compositions and relative compositional ratios of CFTS TF belonging to the first series.

# CFTS	Deposition time (s)			FRONT composition						BACK composition					
				Atomic %			Compositional ratio			Atomic %			Compositional ratio		
	Sn	Cu	Cu:Fe	Cu	Fe	Sn	Cu/Fe+Sn	Fe/Sn	Cu/Sn	Cu	Fe	Sn	Cu/Fe+Sn	Fe/Sn	Cu/Sn
7	1400	185	1320	49	24	27	0,96	0,91	1,83	48	24	28	0,92	0,85	1,69
8	1400	185	1320	48	25	28	0,91	0,89	1,71	46	24	30	0,85	0,81	1,54
9	1400	185	1400	47	26	27	0,88	0,99	1,76	48	25	27	0,91	0,94	1,76
10	1400	175	1470	48	26	26	0,94	1,00	1,88	49	27	25	0,94	1,10	1,98
11	1250	150	1600	51	29	20	1,03	1,43	2,50	51	29	21	1,03	1,38	2,45
12	1400	170	1470	48	27	26	0,91	1,04	1,86	47	27	26	0,88	1,03	1,79
14	1250	150	800+800	47	27	25	0,90	1,09	1,87	47	27	26	0,89	1,06	1,84
15	625+625	75+75	800+800	48	26	25	0,94	1,05	1,92	49	26	25	0,96	1,06	1,97
16	1410	40	1710	45	31	24	0,81	1,33	1,89	45	30	25	0,83	1,23	1,85

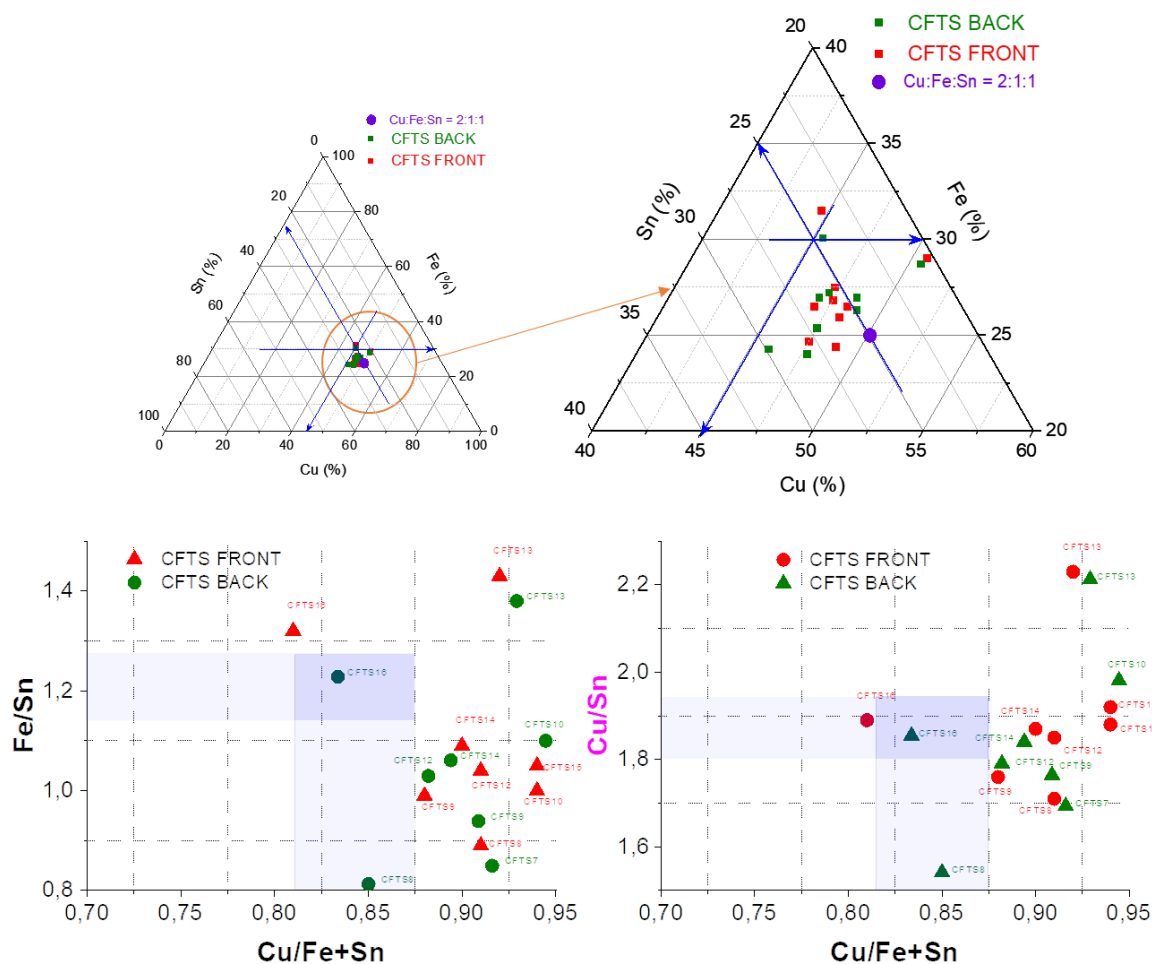
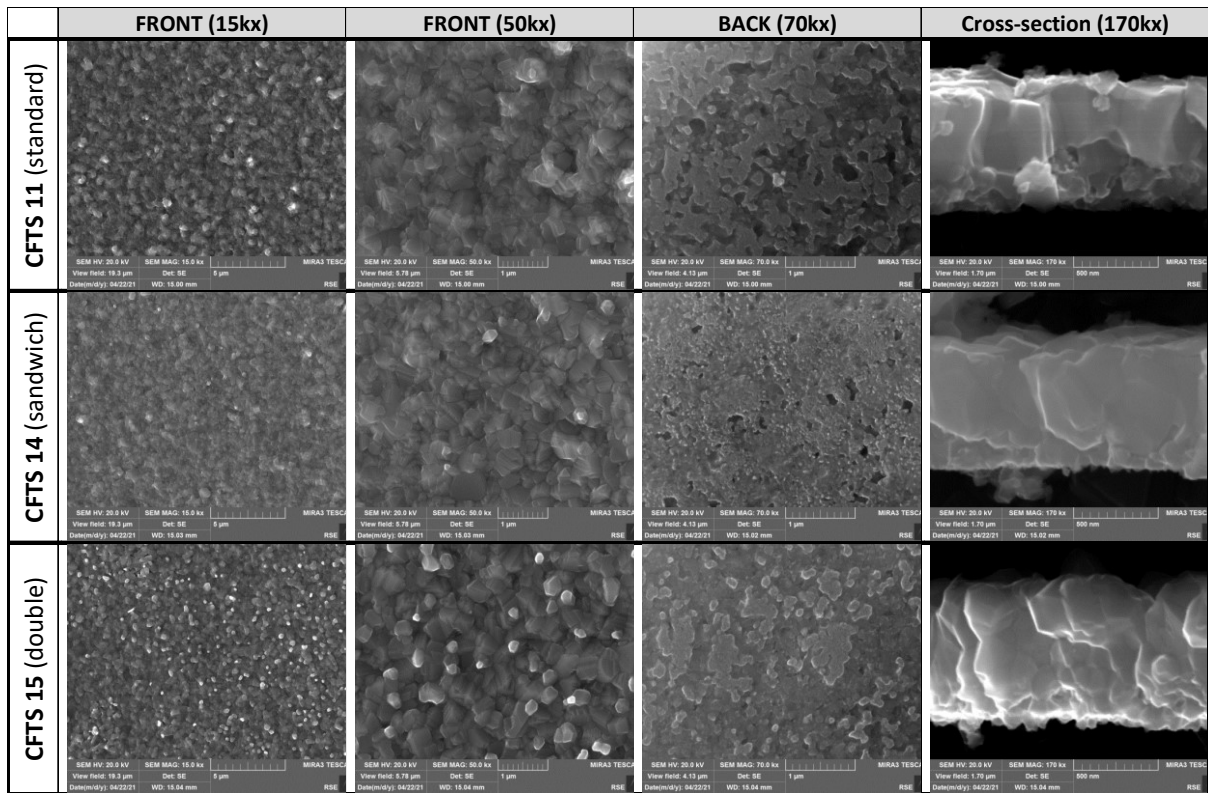


Figure 60: Above, the dispersion of composition points of CFTS TF belonging to the first series inside a ternary phase diagram for metals (Cu-Fe-Sn); below, the dispersion of compositional ratios [Cu]/[Sn] (right) or [Fe]/[Sn] (left) vs. [Cu]/[Fe]+[Sn]. In the same image, the range of compositional ratios corresponds to those of the best PV-performing CZTS. For every sample, two series of data were reported. Red dots report FRONT data, and green dots report BACK data.

Table 30 summarises a morphological study of the samples with different precursors' orders presented in Table 26, with both FRONT and BACK images. From the proposed images, we can observe that CFTS TF shows compact and homogeneous FRONT surfaces and large compact grains (from cross-section images). The BACK surface conveys classic *voids'* distributions that are already observable in CZTS samples. The order of precursors does not seem to affect these *voids'* concentrations, but it does seem to affect the distribution of these defects. The TF depicts very good adhesion to the Mo substrate, despite the presence of voids, since no detachment phenomena have been observed during the characterisation or the finalisation processes or after further thermal treatments (to be described later).

Table 30: SEM images at diverse magnifications of the FRONT and BACK surfaces and a cross-section for samples #11–#14–#15, describing the variations in precursor order in the first series.



6.2.2.1.2. Second series of CFTS samples: ‘Constant current’ approach

Table 31 summarises the results of the compositional analysis of the samples of the second series. Data were collected and summarised the same way we conducted the first series. Consequently, both as a purpose and as revealed information, ternary diagrams and compositional ratios were provided for this series in comparison graphs. See Figure 4-3. Every sample in this series was characterised both as the precursors’ multilayer (black dots) as well as FRONT (red dots) and BACK (green dots) surfaces after the sulphurisation process. Sample #17 was realised with the purpose of studying Sn-rich samples for secondary phase formation.

From the EDX analysis, we can state the following:

- The deposition control of precursors in ‘constant current’ mode permitted us to gather CFTS samples with compositions arranged in a **very limited range** around the target compositions. For this series, the target composition was considered the best for CZTS best final devices (cf. the point where arrows cross in Figure 61).
- All samples take place in the ‘optimal’ [Fe]/[Sn] region, while a progression in the values of [Cu]/[Sn] exists. Accordingly, only samples #20–#21–#22–#23 also possess the ‘optimal’ [Cu]/[Sn] ratio.
- All samples gathered by changing the order of precursors revealed similar **compositions**, considering the EDX measure’s sensitivity, confirming the good reproducibility of the process.
- **No compositional gradient was observed between** the FRONT and BACK surfaces.

Table 31: Process parameters, FRONT and BACK compositions and relative compositional ratios of the CFTS TF belonging to the second series.

# CFTS	Deposition time [s]			FRONT composition						BACK composition					
				Atomic %			Compositional ratios			Atomic %			Compositional ratios		
	Sn	Cu	Cu:Fe	Cu	Fe	Sn	Cu/Fe+Sn	Fe/Sn	Cu/Sn	Cu	Fe	Sn	Cu/Fe+Sn	Fe/Sn	Cu/Sn
17	1704	48	1020	35,5	23,5	41,0	0,55	0,57	0,87	35,5	23,5	41,0			
18	1704	48	2066	41,3	33,1	25,6	0,70	1,29	1,61	41,7	31,4	26,9	0,72	1,17	1,55
19	1704	70	2066	42,6	31,0	26,4	0,74	1,18	1,62	43,1	29,8	27,1	0,76	1,10	1,59
20	1704	115	2066	44,9	29,9	25,2	0,82	1,19	1,78	45,2	28,5	26,4	0,82	1,08	1,71
21	1704	115	2210	45,7	30,1	24,2	0,84	1,25	1,89	45,5	30,4	24,1	0,84	1,27	1,90
22	115	1704	2066	44,4	30,6	25,0	0,80	1,22	1,77	45,1	29,7	25,2	0,82	1,18	1,79
23	2066	1704	115	45,8	28,9	25,3	0,85	1,14	1,81	46,3	28,8	24,9	0,86	1,16	1,86

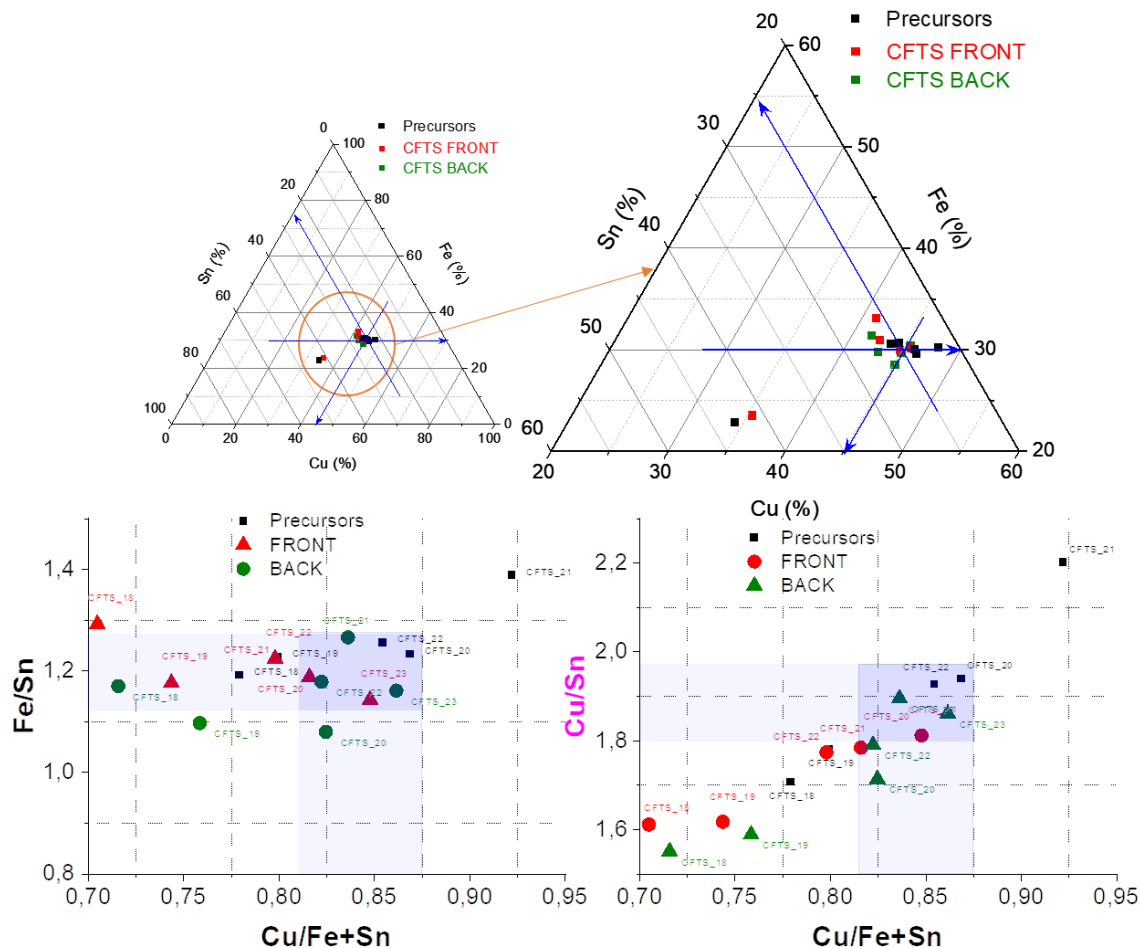


Figure 61: Above, the dispersion of composition points of the CFTS TF belonging to the second series inside a ternary phase diagram for metals (Cu-Fe-Sn); below, the dispersion of compositional ratios $[Cu]/[Sn]$ (right) or $[Fe]/[Sn]$ (left) vs. $[Cu]/[Fe]+[Sn]$. The same image reports the compositional ratios' range corresponding to those of the best PV-performing CZTS. For every sample, three series of data are reported: Black dots signify reported multilayer precursors' data, red dots supply FRONT data, and green dots provide BACK data.

- Every sample is **Cu-poor ([Cu]<50%) and Fe-rich ([Fe]>25%)**, an intermediate condition enabling the limiting of the formation of Cu_{2-x}S but not the formation of Fe-based conductive secondary phases (as Fe_{1-x}S).

Table 32 reports the SEM images of samples #18–#19–#20 following the variation of Cu content, while the SEM images taken of samples #20–#22–#23, which were grown with varying precursors' order, are conveyed in Table 33.

From Table 32, we can observe that the only disparity in these samples is the higher compactness and lower roughness increasing the Cu content. Meanwhile, Table 33 conveys more information:

- Observing the samples at high magnification (FRONT 30k image), the compactness of the film increases with the number of samples, verifying that the order of precursors affects the FRONT surface.

Table 32: SEM imaging of the FRONT surface of precursors' multilayer and FRONT and BACK surface of the post-sulphurisation treatment of samples #18–#19–#20 with different magnifications, following increased Cu content.

# CFTS	Before sulphurisation	After sulphurisation		
	Metallic precursors	FRONT		BACK
	30kx	1kX	30kX	30kx
18				
19				
20				

Table 33: SEM imaging of the FRONT surface of precursors' multilayers and FRONT and BACK surfaces of the post-sulphurisation treatment of samples #20–#22–#23 with distinct magnifications, following different precursors' order.

# CFTS	Before sulphurisation	After sulphurisation		
	Metallic precursors	FRONT		BACK
	30kx	1kX	30kX	30kX
20				
22				
23				
	Secondary phases incorporated in the TF (30kx) →		Cross-section (70kx)→	

6.2.2.1.3. Second series: Cooling rate test

Table 34 exemplifies the SEM images of the FRONT surfaces of samples #20 and #22, treated with the classical cooling process and with the slow cooling process (cf. Table 16 for details of the cooling process).

The slow cooling seems to slightly affect the growth of CFTS grains in the TF matrix but cause the formation of larger grains with similar stoichiometry to the rest of the TF. The nature of these grains will be discussed in the XRD and Raman analyses in the following sections.

Table 34: SEM images of the FRONT surface of samples #20 and #22, with diverse cooling processes.

#CFTS	FRONT		
	Natural cooling	Slow cooling	
	15kx	15kx	30kx
20			
22			

6.2.2.2. Crystallographic characterisation by XRD analysis

For all samples, XRD measures were performed by removing part of the TF from the substrates SLG/Mo and dispersing the obtained powder on a mis-oriented silicon sample holder. Correspondingly, no effects of the holder would be visible in the diffractograms, thereby enhancing the material signals.

Comparing the obtained measures with the data in the database (PDF4+ from ICDD), we identified the following crystalline phases inside our samples:

- **Synthetic tetragonal stannite** Database PDF4+ 00-035-1351
- **Chalcopyrite (CuFeS₂)** Database PDF4+ 00-037-0471
- **Iron sulphide (Fe_{0.87}S)** Database PDF4+ 04-006-4096
- **Rhodostannite (Cu₂FeSn₃S₈)** Database PDF4+ 01-085-0378
- **Synthetic cubic stannite** Database PDF4+ 01-070-8038

The last one, synthetic cubic stannite, was observed only in the slow-cooling process (a test performed for samples of the second series). Figure 62 displays an example of an XRD diffractogram (sample #20) with the visual representation of all the reported phases as a PDF card. Unfortunately, detrimental issues are related to every one of the secondary phases presented, as follows:

- Iron sulphides possess **metallic conduction**, such as copper sulphides.
- Chalcopyrite is an n-type semiconductor, unlike p-type CFTS. The p-type behaviour of CFTS has been demonstrated as coupling in PV devices with n-type CdS [74].
- There are no valid data about rhodostannite in the literature, although there is speculation that it should behave in similar ways as CFTS.

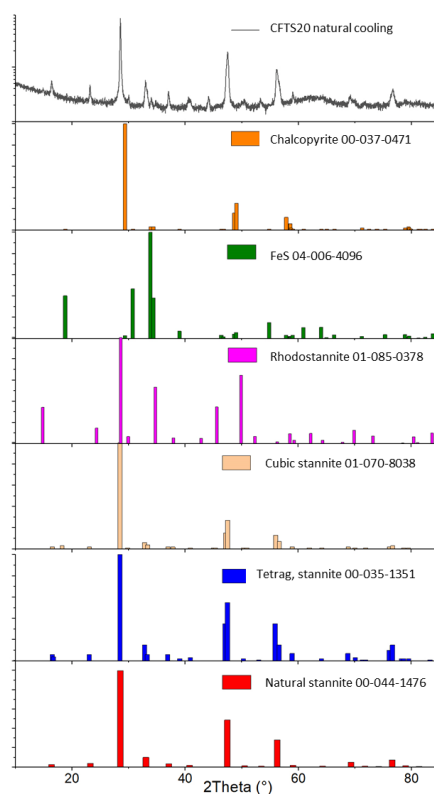


Figure 62: Example of a CFTS diffractogram taken for CFTS sample #20 and the PDF cards of secondary phases used to identify the secondary phases in the samples.

6.2.2.2.1. XRD data analysis: First and second series

Table 35 and Table 36 summarise the results of the peaks' identification and the quantification of the phases inside the samples of the first and second series, respectively.

Comparing the results, we can affirm the following:

- Samples realised to study the process's reproducibility in the 'constant power' configuration in the first series (sample couples #7–8 and #10–#12) **do not convey similar phase content**, as the discrepancy of these values are far from each other, even with the uncertainty of Rietveld refinement values.
- Almost every sample contains **rhodostannite**, which is typical of samples that present an Sn-rich composition; this is confirmed by the compositional ratios of samples of the first series, where $[Cu]/[Sn] \approx 1.8$.
- Sample #10 shows the highest purity, as the tetragonal stannite content is around 99%.
- The 'constant current' approach for samples of the second series demonstrated a **higher value of reproducibility**, as samples with similar deposition times (but a different stack order; see samples #20–#22–#23) revealed similar phase content.
- Increasing Cu content (samples #18–#19–#20), **rhodostannite content** (Sn-rich phase) decreased, though iron sulphide content also increased, giving higher metallic behaviour to the TF.
- Increasing the $[Cu:Fe]$ content, the system drifted from **iron sulphide formation** (sample #20) to **chalcopyrite formation** (sample #21).

Table 35: Comparison of process parameters and phase contents calculated by Rietveld refinement for the first series' samples.

# CFTS	Deposition time (s)			Crystalline phases % weight.			
				Natural cooling			
	Sn	Cu	Cu:Fe	Stannite	Chalcopyrite	Fe _{0.87} S	Rhodostannite
7	1400	185	1320	74,0			26,0
8	1400	185	1320	60,3			39,7
9	1400	185	1400	74,0			26,0
10	1400	175	1470	99,2		0,8	
11	1250	150	1600	90,0	10,0		
12	1400	170	1470	81,7			18,3
14	1250	150	800+800	83,0			17,0
15	625+625	75+75	800+800	86,0			14,0
16	1410	40	1710	75,9		5,6	18,5

Table 36 also depicts the results of the slow cooling experiment performed on twin samples from the samples #20 to #23. From the analysis of the two experiments, no difference in phase content was witnessed, except a little Sn content loss, probably due to the formation of volatile compounds at high temperatures. Instead, we report a **crystal phase transition from tetragonal stannite, obtained with a regular cooling process, to a cubic stannite structure, obtained with a slow cooling process**. The change in crystalline structure is detectable from the altered shape of some peaks of the stannite, which shifts from a duplet of peaks in the tetragonal structure to a singlet peak in the cubic structure (see Figure 63). This behaviour can be attributed to the fact that the slow cooling permitted CFTS samples to stay around 565°C (the temperature where the transition from a tetragonal to a cubic structure happens). This process mimics the one performed by *Ohtsuki et al.* [68], where the samples grew at this temperature for 1.5 days.

Table 36: Comparison between process parameters and phase contents calculated by Rietveld refinement for second series' samples, with the results of the slow cooling experiments.

# CFTS	Deposition time [s]			Crystalline phases % weight.							
				Natural cooling				Slow cooling (18°C/h)			
	Sn	Cu	Cu:Fe	Stannite	Chalcopyrite	Fe _{0.87} S	Rhodo stannite	Stannite	Chalcopyrite	Fe _{0.87} S	Rhodo stannite
17	1704	48	1020	32,5			67,5				
18	1704	48	2066	76,2		6,7	17,1				
19	1704	70	2066	83,0		5,5	11,5				
20	1704	115	2066	94,7		5,3		95,7		4,31	
21	1704	115	2210	82,0	18,0			85,5	13,8	0,7	
22	115	1704	2066	95,9		4,1		95		5	
23	2066	1704	115	96,3		3,7		91	4,7	4,3	

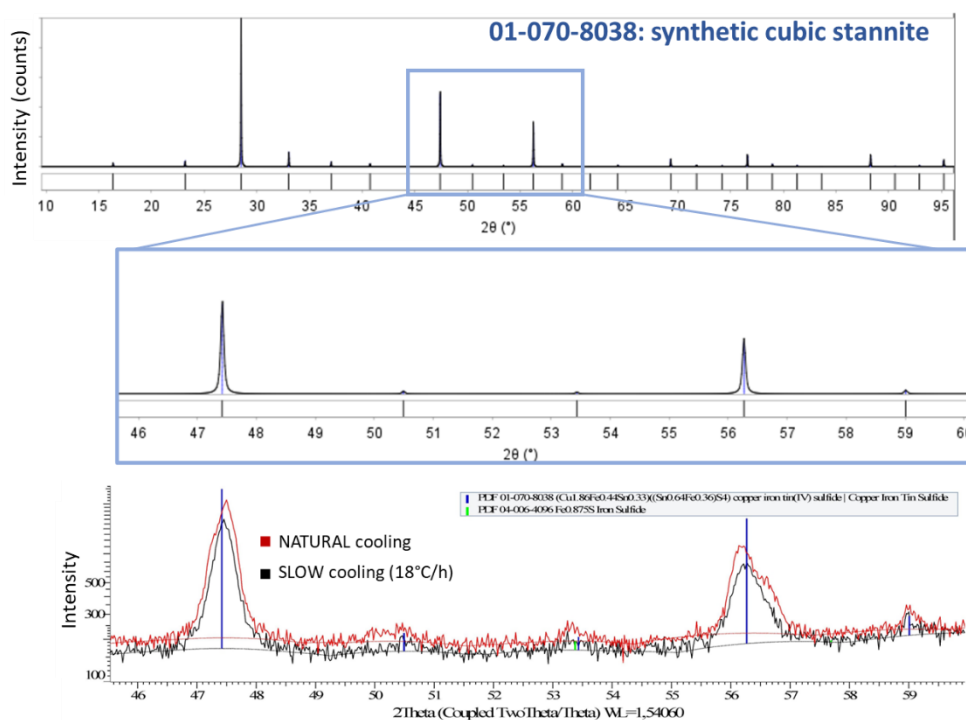


Figure 63: Comparison between diffractograms of naturally cooled (red) and slowly cooled (black) CFTS sample #20; the inset demonstrates the 2-theta range between 46° and 60°, where the peaks of tetragonal and cubic stannite diverge.

6.2.2.3. Phases' characterisation by Raman spectroscopy

To support the conclusions of the XRD analysis on the secondary phases for CFTS samples, Raman spectroscopy measures were performed on these samples. The measurements taken for this PhD thesis were performed using a Jasco Ventuno micro-Raman apparatus at RT in a backscattered configuration. The apparatus is equipped with a Peltier-cooled sensor (working temperature: -50°C) and an He-Ne laser ($\lambda=632.8\text{nm}$). The appropriate laser was used to obtain the best signal-noise ratio and to avoid modifying the spectra due to heating. In particular, a 20x objective was chosen, setting the scanned area diameter= $12\eta\text{m}^2$ and incident laser power= 0.8mW . With this setup, the depth of penetration through the sample of the laser was 200nm, calculated by the laser's wavelength and the CFTS theoretical adsorption coefficient $\approx 1\text{-}2\times 10^5\text{cm}^{-1}$.

Only a peak at 318 cm^{-1} in the range between 50 and 400 cm^{-1} can be attributed to the CFTS compound, as represented in Figure 25. In every analysis of CFTS samples, this peak is always present, and it is identified as the principal peak of the CFTS phase [76]. Variations in the experimental spectra are found in samples containing secondary phases, as revealed in Figure 64, where the Raman spectra of samples #17 and #21 are reported as examples containing rhodostannite and chalcopyrite, respectively. In samples where the rhodostannite phase is present, a peak placed at 355 cm^{-1} appears, and where the chalcopyrite is present, a peak placed at 298 cm^{-1} appears. As for the Raman measures of bare rhodostannite, the main peak of this material completely overlapped with the CFTS's main peak, while the secondary peak was visible.

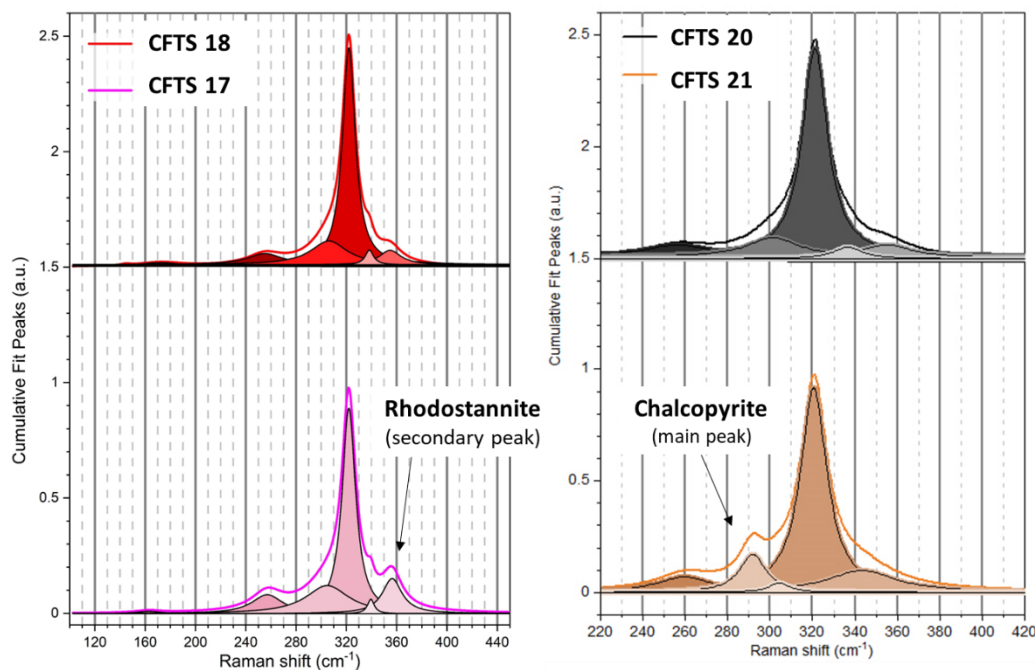


Figure 64: (Left) comparison between the Raman spectra (and the relative deconvolution) of samples #18 (red) and #17 (pink) to depict the effect of rhodostannite's presence in the sample; (right) a comparison between Raman spectra (and the relative deconvolution) of samples #18 (red) and #17 (pink) to illustrate the effect of chalcopyrite's presence in the sample.

Raman analysis confirmed the information collected from the XRD analysis, revealing the presence of secondary phases in these samples, but the Raman spectra did not detect the FeS secondary phases.

6.2.2.4. Optoelectronic characterisation by UV–Vis spectroscopy

We also collected profilometry measurements on CFTS samples to determine the thickness of our TF, which is useful as a parameter for obtaining the EG value from UV/Vis transmittance measures on samples grown on a transparent substrate. This approach follows the procedure defined by Tauc [103].

Figure 65 shows the results of the transmittance and reflectance measures of two samples (samples #21 and #23): From these data, we created the two graphs named the *Tauc plot* (Figure 65, below) from which we obtained the Eg values 1.43 eV and 1.13 eV , respectively, for samples #21 and #23.

These two samples have been chosen as an example, since they possess the two limits for the definition of the Eg value range for CFTS. The low Eg value for sample #21 can be associated with the presence of chalcopyrite inside the sample due to this material's low Eg found in the literature, that is 0.55 eV , [120].

Limited variations around 1.4eV have been measured for the rest of the samples, with no dependence on secondary phase content. This value, which is optimal for TF PV devices, perfectly agrees with the E_g values reported in the literature for CFTS grown with TF methods.

Table 37: Values of E_g calculated by the Tauc method for CFTS samples with the process parameters, the phase content calculated by Rietveld refinement and the active layer thickness measured by profilometry.

#CFTS	Deposition time (s)			Crystalline phases % weight				Band gap [eV]	Thickness [nm]
				Natural cooling					
	Sn	Cu	Cu:Fe	Stannite	Chalcopyrite	Fe _{0.87} S	Rhodostannite		
17	1704	48	1020	32,5			67,5	1.43	900 ±70
18	1704	48	2066	76,2		6,7	17,1	1.38	1200 ±25
19	1704	70	2066	83,0		5,5	11,5	1.35	800 ±87
20	1704	115	2066	94,7		5,3		1.39	1200 ±30
21	1704	115	2210	82,0	18,0			1.13	1100 ±52
22	115	1704	2066	95,9		4,1		1.41	1000 ±32
23	2066	1704	115	96,3		3,7		1.43	1000 ± 43

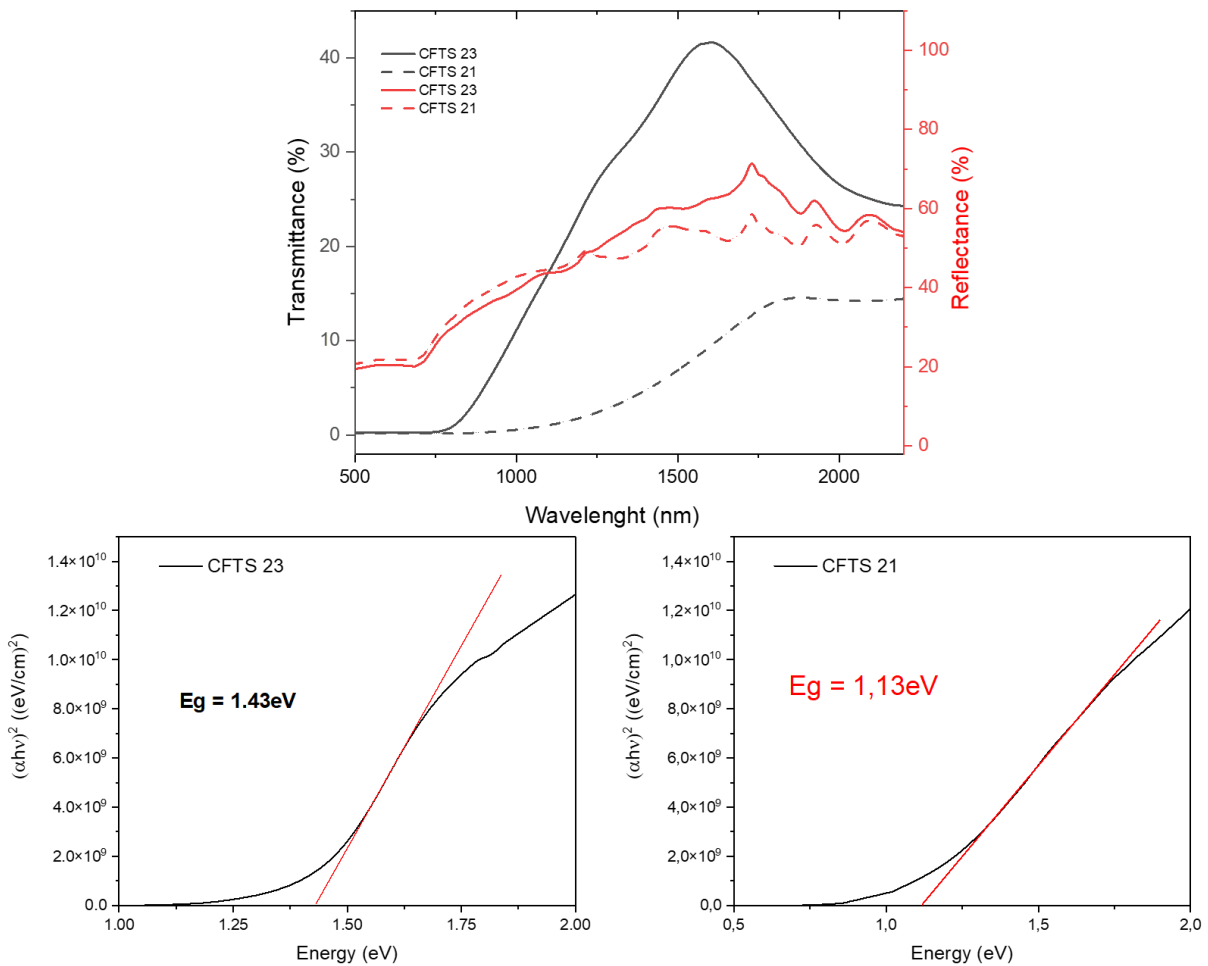


Figure 65: (Above) comparison of transmittance measure (black) and reflectance measure (red) of samples #21 and #23; (below) Tauc elaboration for these two samples to determine their E_g by linear regression.

The E_g value for sample #17, where rhodostannite is the main phase, is quite interesting, since even in this sample, the calculated E_g is around 1.4eV and, thus, similar to a sample with high stannite content.

6.2.2.5. Oxidation state characterisation using XPS analysis

XPS measurements were carried out to determine the oxidation state of the elements in the CFTS TF. The objective of the study is to define the oxidation state of all the elements comprising the material, especially Fe, which could be +2 or +3, unlike Zn (the oxidation state of which is +2) in CZTS. The analysis was performed on TF realised on the SLG substrate, both on the surface and after three *plasma etching* sequences, to first clean the surface and then investigate the chemical nature of the elements in deeper regions of the TF, since XPS is a surface-sensitive characterisation technique. In this case, this sequence is determined by the time of the process, 120s, 480s and 1,200s, respectively. For this study, the 120s step returns the best results, since we managed to eliminate foreign compounds and elements and did not convey the elements connected to the substrate.

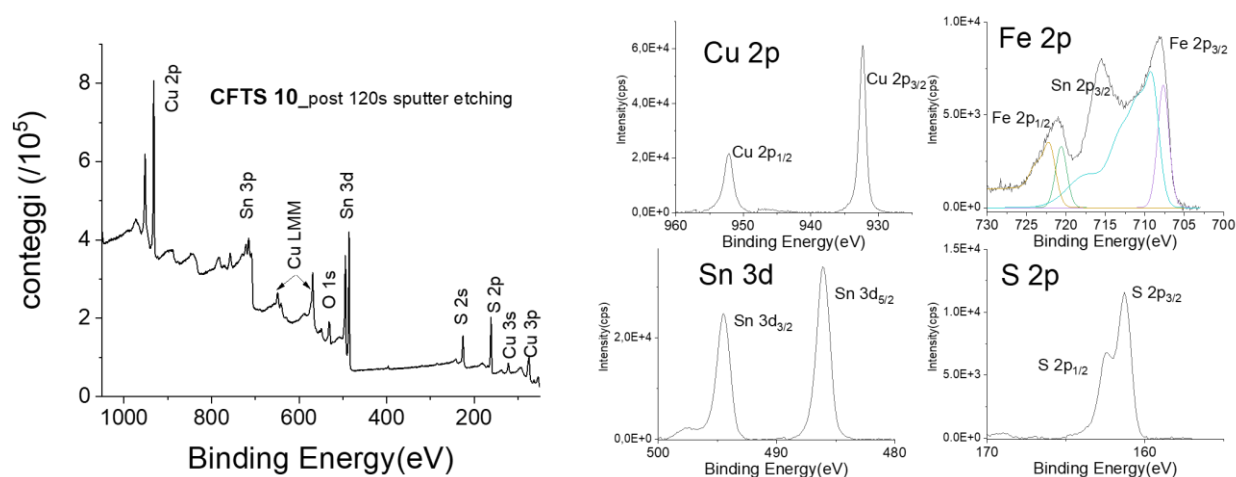


Figure 66: (Left) total XPS spectrum of CFTS sample #10 after a 120s plasma etch process, which demonstrates the peaks of every element contained in the TF; (right) regions of the spectra corresponding to the elements of interest for CFTS (Cu 2p, Fe 2p, Sn 3d and S 2p).

Considering what we described in Section 4.4.1.3, in Figure 66 (left), the results of the XPS analysis of CFTS sample #10's surface after 120s of *plasma etching* are displayed (sample #10 was chosen since it has the higher phase purity defined by *Rietveld refinement* on XRD data). Figure 66 (right) shows the magnification of the regions of interest of Cu, Fe, Sn and S in the XPS spectrum, as reported by *Chatterjee et al.* [74]. The spectra are comparable with the literature, presenting the correct oxidation states for Cu (+1), Sn (+4) and S (-2), but very much differing for Fe. The profile observed for this element can be described as the sum of various contributions of Fe species, both Fe^{2+} and Fe^{3+} , as revealed in Table 9. The observed profile is similar to that of *Trifiletti et al.* [83] for CFTS samples deposited outside the glovebox and in direct contact with air (oxygen, O). The presence of Fe^{3+} in our TF does not imply the presence of oxygen in the sample. No traces of O have been observed in the bulk of the material, so we can say that all the O contained in the TF has been substituted by S during the high-temperature sulphurisation process. Nevertheless, once Fe atoms turn from Fe^{2+} to Fe^{3+} , they cannot return to the desired oxidation state. This could lead to trap states inside the material, degrading the photo collection in the final device.

6.2.3. PV cells' characterisation

From all the CFTS samples obtained for this PhD thesis, we developed a prototypical PV device to complete the study of CFTS application SCs. The finalisation process used on CFTS TF is the same as described for the CZTS samples (see Section 5).

Even for CFTS, we chose to use a thin layer of CdS as an n-type material to couple to p-type CFTS to form the p–n junction. Although other materials have been investigated as ideal *buffer layers for CFTS*, for example bismuth selenide, or Bi₂Se₃ [74], this compound offers the possibility of directly comparing the final device performances of CFTS devices with the CZTS ones, since they have the same *buffer layer*.

During the study, we applied the same post-deposition treatments (PDT) tested on the CZTS device on the new CFTS cells: the application of an acidic treatment with diluted HCl before CdS deposition and a thermal treatment after the deposition of the *buffer layer*. As represented, these treatments had a beneficial effect on CZTS PV device performance (see the CZTS section).

The application of an acidic treatment to CFTS should remove the iron sulphides' formation on the surface of our samples, since these compounds are soluble in this acid as zinc sulphides. As for the thermal treatment, we did not observe a delamination process, despite the presence of *voids* between the CFTS layer and the SLG/Mo substrate, or the appearance of an order–disorder transition (as observed for CZTS).

No PV performance was witnessed in these devices. The relative J–V curves obtained under illumination were typical of short-circuited devices, as shown in Figure 67 (black graph). To exclude the possibility that the presence of conductive macrodefects would result in this behaviour, we tried to gradually reduce the active area of the device from 0.3cm² to 0.15cm², without any positive effect. Accordingly, the reasons for this behaviour must be examined elsewhere.

The only variation from this ohmic behaviour was garnered with samples that have received the thermal PDT. As revealed in Figure 67 (red), a little rectification of the J–V curve in dark conditions is visible in the samples after the PDT, but is insufficient to obtain PV performances under the light. The absence of a photogenerated current in the treated samples could originate in shunt macro-defects composed of conductive phases (see the previous section) not only on the surface but also in the bulk of the material. These kinds of defects should be investigated further, especially:

- Defects' nature: What are the composition and dimensions of these phases? Are these defects a feature of the CFTS material, itself, or are they caused by the deposition process?
- Their impact on PV performance: There is a concentration threshold where these defects are no longer active. What is the electrical behaviour of these phases?

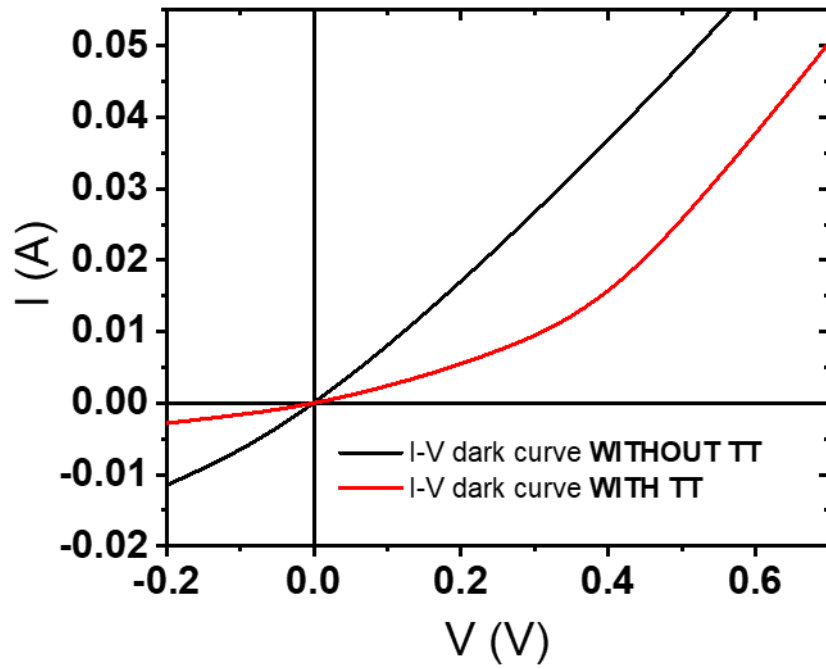


Figure 67: J-V curves under the dark condition of CFTS PV devices (#10, for example) with and without the application of the PDT after the deposition of CdS.

6.2.4. Monograin growth of CFTS

In this section, the results of realising the CFTS monograin samples will be analysed. These samples were created starting with the results from the CFTS TF samples of the first series before the optimisation took place for the TF's second series.

6.2.4.1. Monograin powders and series definition

To better comprehend the results of this technique, two series of experiments took place: a first series of samples made with the same quantity of metallic powder precursors sulphurised with varying process conditions and a second series where the best sulphurisation conditions were applied on diverse metal contents.

- First series of monograin samples: Summarised in Table 38, this series contains samples crafted from the same precursor content. The precursor content was calculated from the final samples of the TF's first series, testing typical sulphurisation procedures and changing **the process temperature and the presence of molten sand** to enhance the final crystallinity.

Table 38: List of CFTS monograin samples deposited for the first series, assessing sulphurisation process parameters.

#CFTS	Precursor content				Sulfurization temperature (°C)	Molten salt (KI) (g)	Atmosphere (Torr)
	Cu (g)	Fe (g)	Sn (g)	S (g)			
1	0,279	0,131	0,289	0,32	570	0	Vacuum
2	0,281	0,133	0,288	0,316	570	0	Ar 760torr
3	0,280	0,131	0,283	0,318	570	0	Ar 100torr
4	0,281	0,132	0,284	0,317	740	0	Vacuum
5	0,28	0,131	0,289	0,316	740	0	Ar 760torr
6	0,278	0,132	0,29	0,319	740	0	Ar 100torr
7	0,28	0,134	0,286	0,3	740	1,006	Vacuum
8	0,278	0,134	0,289	0,317	740	0,998	Ar 760torr
9	0,278	0,132	0,29	0,316	740	1,013	Ar 100torr

- Second series of monograin samples: As summarised in Table 39, this series contains samples made with the optimal sulphurisation conditions deduced by the previous series and **explores new metallic contents** to create a preliminary composition map, as obtained with TF samples.

Table 39: List of CFTS monograin samples deposited for the first series, investigating changes in the powder's composition.

#CFTS	Precursor content				Sulfurization temperature (°C)	Molten salt (KI) (g)	Atmosphere (Torr)
	Cu (g)	Fe (g)	Sn (g)	S (g)			
10	0,265	0,126	0,318	0,321	740	1,01	Vacuum
11	0,259	0,124	0,313	0,328	740	1,01	Vacuum
12	0,255	0,122	0,308	0,335	740	1,01	Vacuum
13	0,25	0,12	0,286	0,317	740	1,01	Vacuum
14	0,279	0,132	0,315	0,33	740	1,01	Vacuum

6.2.4.2. Compositional and morphological characterisation by SEM/EDX

In this section, we will discuss the results of morphological and compositional analyses of CFTS MG samples, as discussed for CFTS TF samples, with a focus on the distinctions between these samples and the previous samples. An in-depth analysis will be discussed concerning the outstanding homogeneity inside the same powder sample and between powders with similar preparation processes.

6.2.4.2.1. First series: Investigating sulphurisation conditions

Table 41 summarises the results of the compositional analysis of the MG samples of the first series. The reported values were derived from several measurements of different grains in the same powder sample. In this case, we also report the metal content of grain regions or full grains that we identify as ‘rhodostannite’ measures, observing the elements’ contents. Every sample reveals a very similar S content ($S \approx 50\%$ for kesterite measures, $S \approx 60\%$ for rhodostannite measures). Nevertheless, the compositional ratios are compared in Figure 68 below, displaying the dependence of $[Cu]/[Sn]$ and $[Fe]/[Sn]$ regarding $[Cu]/[Fe]+[Sn]$. Light blue highlights the best-performing CZTS compositions.

Both Table 40 and Figure 68 report where on the sample these data were collected: Surface compositions are data taken from the external surface of the grains. Bulk compositions are data collected from the inside of the grains (obtained after sanding the sample), and rhodostannite compositions are taken from bulk measures of grains with compositions diverging from the CFTS grains.

Table 40: Sulfurisation parameters, surface and bulk composition and relative compositional ratios of CFTS MG of the first series.

#CFTS	Sulfurization temperature (°C)	Molten salt (KI) (g)	Atmosphere (Torr)	Surface composition						Bulk composition						Rhodostannite composition					
				Element content			Element ratio			Element content			Element ratio			Element content			Element ratio		
				Cu	Fe	Sn	Cu/Fe+Sn	Fe/Sn	Cu/Sn	Cu	Fe	Sn	Cu/Fe+Sn	Fe/Sn	Cu/Sn	Cu	Fe	Sn	Cu/Fe+Sn	Fe/Sn	Cu/Sn
1	570	0	Vacuum	56	19	25	1,25	0,76	2,21	55	20	25	1,23	0,79	2,21						
2	570	0	Ar 760torr	53	22	25	1,11	0,90	2,10	52	23	25	1,09	0,94	2,11	32	18	50	0,47	0,35	0,64
3	570	0	Ar 100torr	57	18	25	1,34	0,73	2,32	57	18	25	1,33	0,70	2,26	33	18	49	0,49	0,37	0,67
4	740	0	Vacuum	51	26	23	1,02	1,15	2,19	50	27	23	1,00	1,19	2,19	29	23	48	0,42	0,48	0,62
5	740	0	Ar 760torr	50	26	23	1,00	1,13	2,13	50	27	23	1,01	1,20	2,22	31	23	46	0,44	0,50	0,66
6	740	0	Ar 100torr	51	26	23	1,03	1,10	2,17	50	27	23	1,02	1,15	2,19	30	22	47	0,44	0,47	0,64
7	740	1,006	Vacuum	49	26	25	0,95	1,07	1,96	49	27	24	0,96	1,09	2,00						
8	740	0,998	Ar 760torr	51	25	24	1,04	1,04	2,11	50	25	24	1,02	1,04	2,08						
9	740	1,013	Ar 100torr	49	27	24	0,97	1,13	2,07	49	27	24	0,96	1,15	2,07						

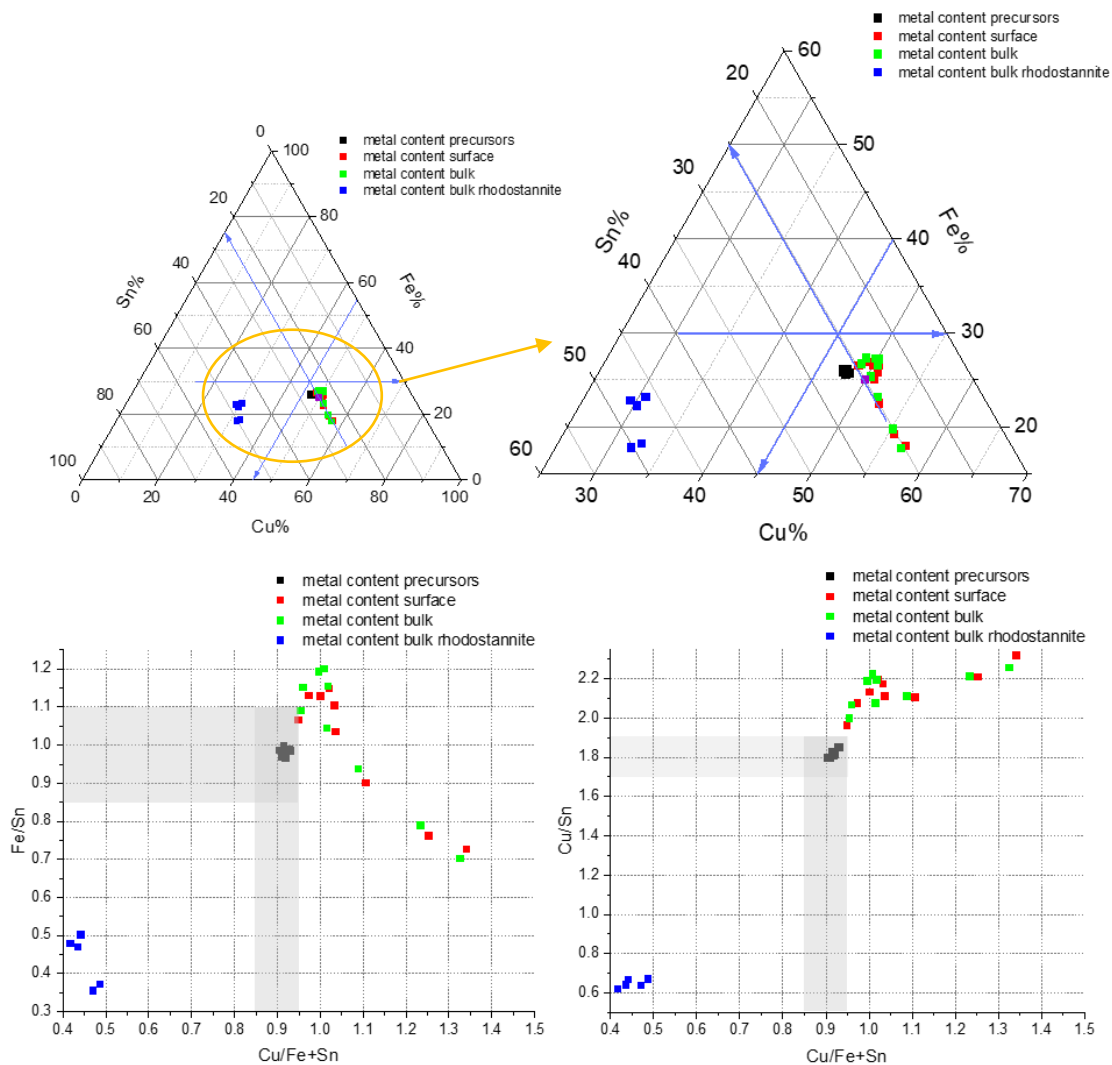


Figure 68: Above, the dispersion of the composition points of CFTS MG belonging to the first series inside a ternary phase diagram for metals (Cu-Fe-Sn); below, the dispersion of compositional ratios [Cu]/[Sn] (right) or [Fe]/[Sn] (left) vs. [Cu]/[Fe]+[Sn]. For every sample, four series of data were reported. Black dots relay powder precursors' data. Red dots reveal surface data, green dots convey bulk data, and blue dots report rhodostannite phase data.

From this analysis, we can affirm the following:

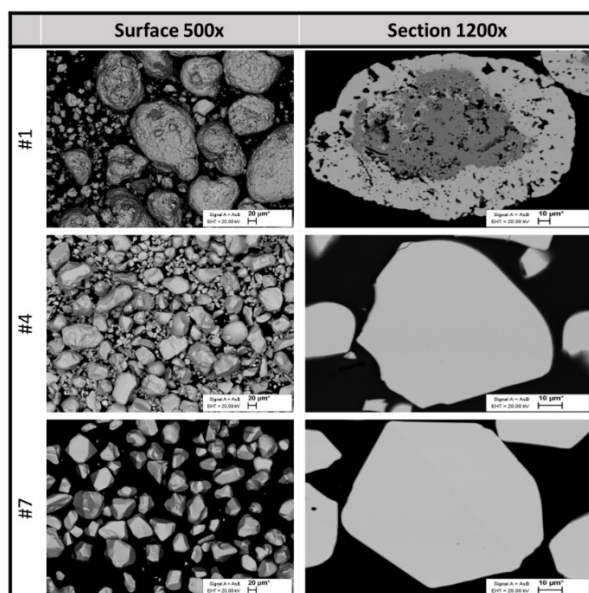
- Every sample (excluding samples #1–#2–#3 for reasons clarified later) demonstrates the formation of a **stoichiometric CFTS phase** with the general composition $\text{Cu}:\text{Fe}:\text{Sn} \approx 2:1:1$.
- The distinction in the distribution of metal between surface and bulk compositions corresponds with **the technique's experimental error**, depicting high homogeneity inside the grains and between grains in the same powder, since the growth of these powders is mainly thermodynamically driven due to the process time.
- The environment has little effect on the metal's distribution. No significant differences between metallic contents can be noted from samples obtained **at the same temperature in different atmospheres**.
- **Temperature has a strong effect on the composition of the powder:** Low-temperature powders display lower iron content than high temperatures, explained by the segregation of Fe-rich phases.
- Slightly higher Sn content in sample growth in the **copresence of KI**: A faster growth mechanism due to the presence of molten sand in the sulphurisation reaction can explain higher tin content, since this element has less time in the gas phase in the reaction vial.

- **No presence of KI was detected** in the samples prepared with this salt on the surface or in bulk. The surface accumulation of this compound was completely removed with the washing procedure, and no KI was incorporated inside the grains, confirming KI's behaviour as a molten medium for CFTS formation.
- Comparing the precursors' composition with the post-sulphurisation data, a deviation can be observed: the main phase (with a composition close to stoichiometric CFTS) illustrates a lower **Sn content** than the precursor powders due to the Sn-rich phase present in these samples and recognised as **rhodostannite** ($\text{Cu}_2\text{FeSn}_3\text{S}_8$). The dimensions of a single grain permit the observation and characterisation of large portions of this secondary phase, thereby facilitating the characterisation.
- The dispersion of the post-sulphurisation data was higher than that from the precursors' powder, mainly due to the presence of secondary phases in the final powder. However, the **standard deviation of the data taken in the same powder was lower than the experimental error of the machine**. Accordingly, we can state that the high homogeneity of the grains of the same powder, but the exact correlation of the stoichiometry with the metal content of the precursor powders must be better understood.

In Table 41, we report on the SEM images taken for MG samples #1, #4 and #7 to exemplify the rest of the samples, since no evident differences were observed on samples made in diverse environmental conditions. This series presents the effect of various temperatures (#1 vs. #4) and the effect of KI insertion in the reaction vial (#4 vs. #7). From these images, we can conclude the following:

- The low-temperature samples demonstrated different features than the high-temperature samples. The grains are **bigger and less idiomorphic**, and they depict a **core-shell structure in which a core of FeS_2 material is enclosed by an Fe-poor CFTS shell**. This could be explained by thermodynamically driven FeS_2 precipitation, since this effect is visible in every low-temperature sample, excluding the possibility of insufficient powder preparation for precursors.
- The two high-temperature samples show **slightly different geometry**, with the powder prepared with KI conveying more crystal facets despite the lower sulphurisation time.
- Lower small-grain formation has been observed in KI-treated samples, confirming the growth mechanism described in the literature. The nucleation **rate is lower than the growth rate when we pass from solid–solid reactions to liquid–solid reactions**.

Table 41: Comparison of the three sulphurisation conditions.



6.2.4.2.2. Second series: Investigating various compositions

After the analysis of the first series, we decided to fix the sulphurisation parameters as follows:

- Environmental conditions: Vacuum from air.
- Process temperature: 740°C.
- Usage of KI as a molten flux.

With these settings, we obtained the samples of the second series: In Table 42 and Figure 69, the results are summarised of the compositional analysis of these MG samples. Again, the samples depict a very similar S content ($S \approx 50\%$ for kesterite measures, $S \approx 60\%$ for rhodostannite measures). In Figure 68 below, the compositional ratios are compared regarding the dependence of $[Cu]/[Sn]$ and $[Fe]/[Sn]$ respecting $[Cu]/[Fe]+[Sn]$. Light blue highlights the best-performing CZTS compositions.

Table 42: Precursors' quantity, surface and bulk compositions and relative compositional ratios of CFTS MG belonging to the second series.

#CFTS	Precursor content				Surface composition						Bulk composition						Rhodostannite composition					
	Cu (g)	Fe (g)	Sn (g)	S (g)	Element content			Element ratio			Element content			Element ratio			Element content			Element ratio		
					Cu	Fe	Sn	Cu/Fe+Sn	Fe/Sn	Cu/Sn	Cu	Fe	Sn	Cu/Fe+Sn	Fe/Sn	Cu/Sn	Cu	Fe	Sn	Cu/Fe+Sn	Fe/Sn	Cu/Sn
10	0,265	0,126	0,318	0,321	51	26	23	1,03	1,10	2,17	50	27	23	1,01	1,15	2,18	31	22	47	0,45	0,46	0,65
11	0,259	0,124	0,313	0,328	51	25	24	1,04	1,07	2,17	51	26	23	1,04	1,10	2,18	31	22	47	0,46	0,46	0,67
12	0,255	0,122	0,308	0,335	51	25	24	1,03	1,07	2,14	51	26	23	1,04	1,16	2,25	33	22	46	0,48	0,47	0,71
13	0,25	0,12	0,286	0,317	50	27	23	1,01	1,16	2,18	51	26	23	1,04	1,17	2,25	32	23	45	0,47	0,50	0,70
14	0,279	0,132	0,315	0,33	50	26	24	1,02	1,08	2,12	51	26	23	1,05	1,14	2,25	31	21	47	0,46	0,45	0,66

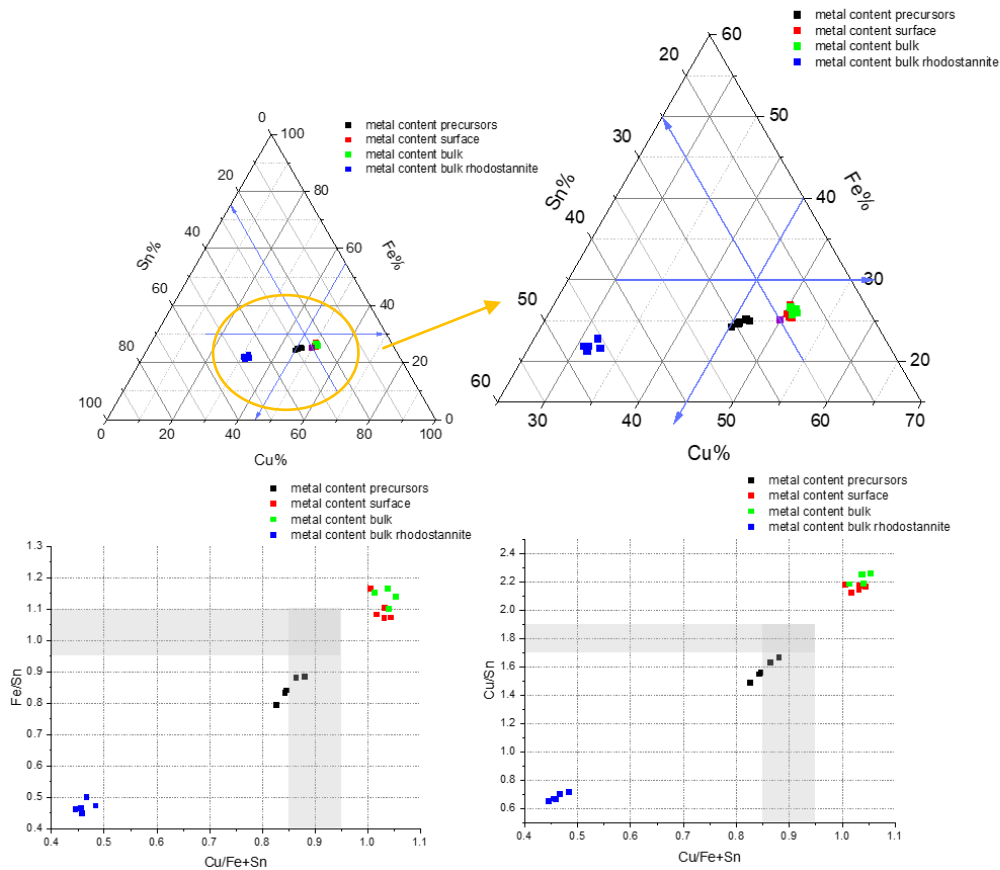
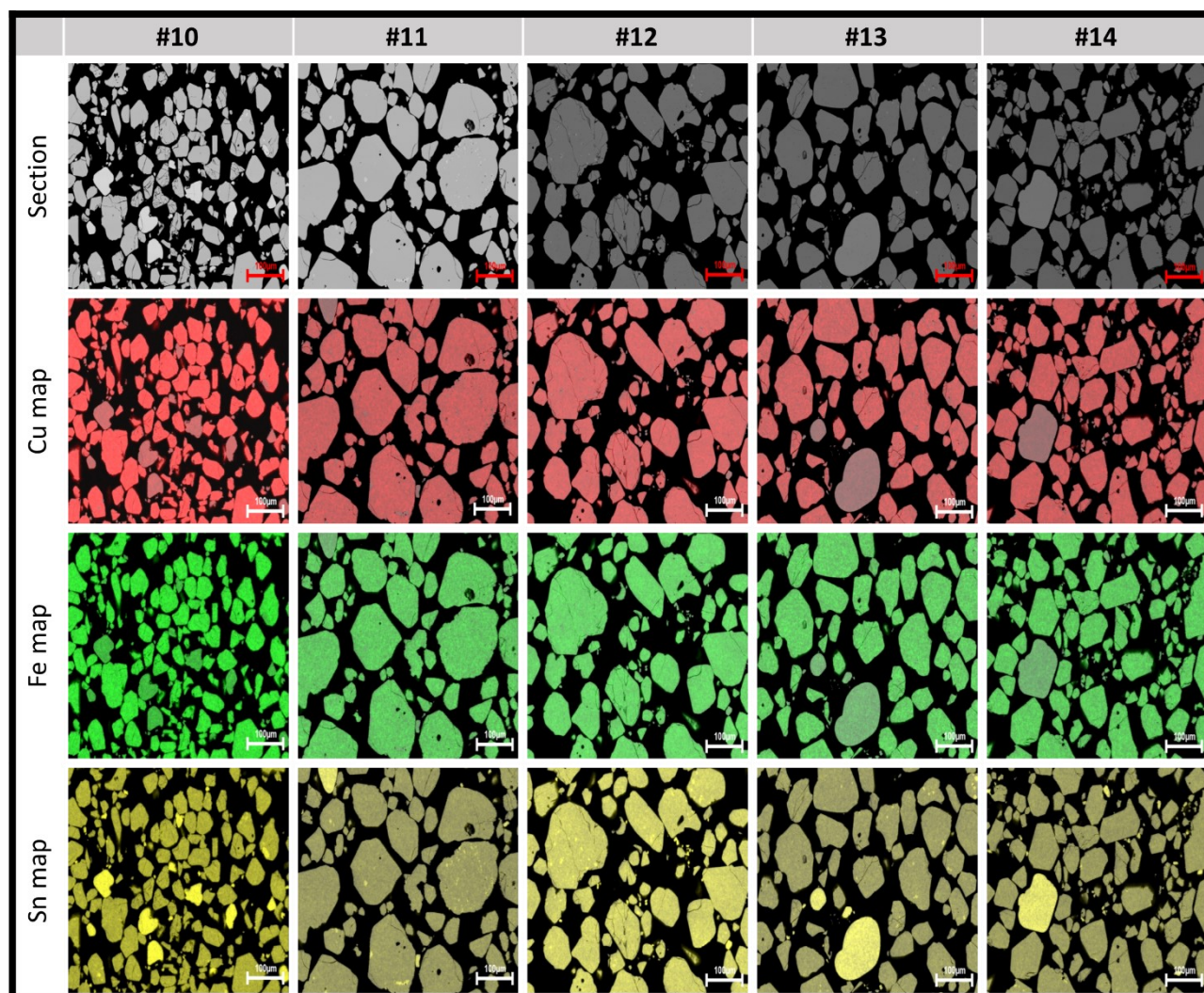


Figure 69: Above, the dispersion of the composition points of CFTS MG belonging to the second series inside a ternary phase diagram for metals (Cu-Fe-Sn); below, the dispersion of compositional ratios $[Cu]/[Sn]$ (right) or $[Fe]/[Sn]$ (left) vs. $[Cu]/[Fe]+[Sn]$. For every sample, four series of data are reported. Black dots relay powder precursors' data, red dots reveal surface data, green dots convey bulk data, and blue dots report rhodostannite phase data.

From this analysis, we can posit the following:

- **All the statements are still valid** concerning general stoichiometry, data dispersion inside the same powder and between surface and bulk measures, and KI removal made for the first series' samples.
- Post-sulphurisation measures differ more from the precursors' values than the first series' samples and corroborate the values obtained previously. This fact depicts that the CFTS thermodynamically stable composition is **Cu:Fe:Sn \approx 2:1:1**. This could lead to the practical difficulty of obtaining non-stoichiometric CFTS, which is theoretically more suitable for PV application due to the formation of V_{Cu} as observed in CZTS. This could also explain why TF SCs do not demonstrate any PV performance, since mobility through defects is the main conduction mechanism in this kind of material.
- **No evident trend** between post-treated samples can be observed; apparently, the different metal content in the precursors' powder does not affect the final composition of the main CFTS phase. This could be explained by the insensitivity of the process to lower compositional changes or higher secondary phase content, a topic to be discussed in section 6.2.4.3.
- The rhodostannite-like phase is still visible.

Table 43: Comparison of SEM images of CFTS MG samples of the second series, with compositional maps of varying elements.



In Table 43, we report on the SEM images of the samples in this series, together with the compositional maps obtained from EDX. These images were taken with magnifications equalling 500x to detail more grains and to better investigate the phases' distribution. From these images, we find the following:

- The grains' geometry is **comparable** with the high-temperature one of the first series' samples, showing the dependency of the morphology of the powder on the sulphurisation parameters.
- The main phase of the grain is still **stoichiometric CFTS**, with the coexistence of inclusions or even full grains with a completely different morphology (with a round shape) of the **Sn-rich secondary phase, which depicts the same composition as the rhodostannite** phase observed before, relating the stoichiometric composition to the formation of the rhodostannite phase.

6.2.4.3. XRD data analysis: First and second series

Table 44 and Table 45 summarise the results for the peak identification and quantification of the phases inside our samples, respectively, regarding the first and second series.

Comparing the results, we can state the following:

- The samples obtained in Ar at atmospheric pressures show the highest rhodostannite secondary phase content, while the low-pressure Ar conditions presented the lowest rhodostannite content.
- At higher temperatures, the formation of a stannite structure increases, conveying that the CFTS's main phase is more stable with greater temperatures. This shows how the temperature used for TF sample production could be too low to obtain a pure-phase CFTS layer (for compositions similar to the first series' TF samples).
- In samples #1, #2 and #3, no trace of pyrite was visible in the XRD analysis. This behaviour could be explained by two reasons: (i) the X-ray is too weak to penetrate the CFTS shell visible in the SEM images (with a thickness of several microns) and to reach the FeS₂ layer, or (ii) the amorphous nature of these pyrite cores makes it invisible to XRD analysis, with no peaks relatable to a pyrite structure.
- Using diverse metal contents did not make a difference in the material's final composition, but it depicted a remarkable difference in phase content. Reducing the Sn content also reduced the formation of the Sn-rich rhodostannite phase, lowering the S content and limiting the formation of Sn-rich, **S-rich** Cu₂FeSn₃S₈.

Table 44: Comparison of process parameters and phase contents calculated by Rietveld refinement for CFTS MG first series samples.

#CFTS	Sulfurization temperature (°C)	Molten salt (KI) (g)	Atmosphere (Torr)	Phase quantification through Rietveld method	
				Stannite	Rhodostannite
1	570	0	Vacuum	87,22	12,78
2	570	0	Ar 760torr	79,94	20,06
3	570	0	Ar 100torr	91,80	8,20
4	740	0	Vacuum	91,9	8,1
5	740	0	Ar 760torr	77,3	12,2
6	740	0	Ar 100torr	98,4	1,6
7	740	1,006	Vacuum		
8	740	0,998	Ar 760torr		
9	740	1,013	Ar 100torr		

Table 45: Comparison between process parameters and phase contents calculated by Rietveld refinement for CFTS MG second series samples.

#CFTS	Precursor content				Phase quantification through Rietveld method	
	Cu (g)	Fe (g)	Sn (g)	S (g)	Stannite	Rhodostannite
10	0,265	0,126	0,318	0,321	80,8	19,2
11	0,259	0,124	0,313	0,328	87,4	12,6
12	0,255	0,122	0,308	0,335	87,7	12,3
13	0,25	0,12	0,286	0,317	89,2	10,8
14	0,279	0,132	0,315	0,33	86,8	13,2

6.2.4.4. Phases' characterisation by Raman spectroscopy

To support the conclusions of the XRD analysis on the secondary phases for CFTS samples, these samples were measured by Raman spectroscopy. These analyses were attained with a green laser Raman device, so we can directly connect these data to the work of *Fontané et al.* [76], but the discussion of distinctive peaks remains coherent with the previous discussion of TF samples.

Figure 70 depicts the experimental Raman spectra of samples #3 and #4 as examples of low-temperature and high-temperature samples. On the left is displayed a comparison of 'core region' measures and the 'shell region' measures typical of low-temperature samples (#1-2-3). On the right is the comparison between the 'pure CFTS' measure between a low-temperature sample and a high-temperature sample (from #4 to #14). The fitting is also reported for a single-peak approach of the different samples and the fitting of *Fontané et al.* [76].

From this analysis, we can conclude that:

- The main component of the powder is **CFTS**: We can recognise in every spectrum the presence of peaks placed at 253, 285, 318, 340 and 355cm⁻¹, connected to the vibrational states of CFTS as represented by *Fontané et al.*

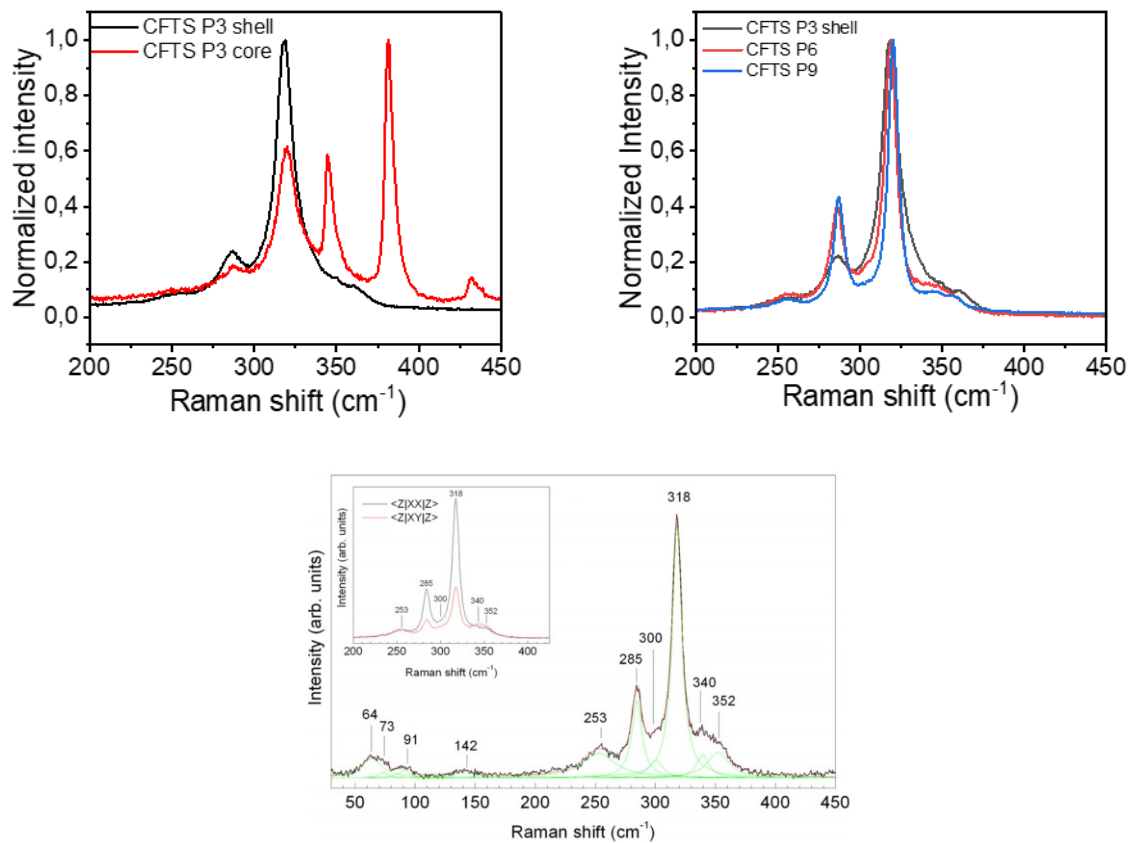


Figure 70: Comparison between Raman spectra of different measures; on the left, a comparison of the shell and the core regions of sample #3 of the first series, where the contributions at 344, 381 and over 431cm⁻¹ connect to the presence of a pyrite phase (together with the lower CFTS contribution similar to that in the shell region). On the right, disparities in the Raman spectra between samples (#3 in the shell for low-temperature samples, #6 for high-temperature samples and #9 for high-temperature samples treated with KI) and the other samples. The progressive blue shift of the CFTS-related peaks is associated with progressively higher crystallinity.

- We can confirm the presence of **pyrite in the 'core region'** of low-temperature samples with the contribution of the 'pure CFTS' phase due to the presence of three extra peaks at 344, 381 and over 431cm⁻¹. This phase, which was invisible for the XRD measurement of the pristine powder, became visible on EDX analysis and Raman spectra due to the varying natures of the samples analysed. (For SEM-EDX and Raman analysis, we used powders incorporated into epoxy resin and then lapped, while for XRD analysis, we solely used a powder due to the dimension of the incorporated sample). The x-ray penetration of dense materials is on the order of 20µm (comparable to the thickness of the 'shell region'), and this penetration lessens for materials containing transition metals (such as Cu, for example) that are highly adsorbent for radiation. Hence, **pyrite is not visible in XRD analysis, but it is visible in Raman spectroscopy, with measures performed directly on the phase.**
- The comparison between the pure-CFTS samples depicts differences between them: A **progressive blue shift** (≈2cm⁻¹/step) can be seen passing from low temperatures to high temperatures with KI samples. A blue shift of Raman peaks can be attributed to the higher crystallinity of the phase; this surely happens between the low-temperature and high-temperature samples, as described in the XRD section.
- A **sharpening of the main peak** is verifiable between samples; this behaviour can be associated with an increase in crystallinity, heightening the sulphurisation temperature.

6.2.5. Conclusion

We obtained CFTS TF samples, starting with the knowledge we developed in previous work about CZTS TF samples and SC. We decided to work on a wider compositional range than that used for CZTS, since very little information about the correlation between the composition of the material and the insurgence of secondary phases is present in the literature. After preliminary experiments, we worked on two approaches to obtain CFTS TF using sputtering: a 'constant power' approach, where sputtering electric generators perform the deposition of the material keeping the electrical power constant during the process, and a 'constant current' approach, where generators perform the deposition of material keeping the current constant during the process. These samples have been fully characterised using every technique already used for CZTS characterisation, with the addition of new tools: We used SEM-EDX, XRD and Raman analysis to monitor the morphology and composition of the TF, correlating the compositional ratios to the formation of secondary phases as rhodostannite in Sn-rich samples, chalcopyrite in Fe-rich samples and $\text{Fe}_{0.87}\text{S}$ in intermediate conditions. The influence of rhodostannite on the final behaviour of the TF is not clear, but chalcopyrite and $\text{Fe}_{0.87}\text{S}$ are conductive phases and should be avoided inside the film. Band gap measurements were calculated using UV-Vis measurements. Most obtained CFTS TF convey a band gap around 1.4eV with a lower value of 1.13eV gathered from samples containing chalcopyrite. Quite high purity was achieved with samples using the 'constant current' approach, up to 99% content of the pure CFTS phase. These samples were also characterised by XPS to monitor the oxidation state of the elements contained in the TF. While all the other elements presented an oxidation state equal to the nominal one (Cu^{1+} , Sn^{+4} , S^{-2}), the peaks observed in the Fe region disclosed the copresence of Fe^{2+} and Fe^{3+} , when this element should be only Fe^{2+} . The presence of a higher oxidation state completely changes the electrical behaviour of the whole TF, introducing n-type conductivity; this could be the reason behind the complete absence of PV performances in the CFTS TF-based SCs realised with these layers. A bland increase in p-n junction quality was attained after the application of the same thermal PDT tested for CZTS but not enough to obtain effective PV efficiency. Lowering this Fe^{3+} content should be the focus of future work on the CFTS TF derived by sputtering, with a consequent increase in the PV performances of CFTS-based SC.

From these results, we created CFTS samples using another synthesis technique: applying the MG production process (used in the literature to obtain CZTS and CZTSe). We analysed them using the same techniques used for TF, achieving promising results. The final composition of the powders was more homogeneous than TF inside the same sample, making large crystals ($>150\mu\text{m}$). The main secondary phase detected in these samples was rhodostannite, according to the results obtained for the TF samples' first series, where this phase was the main secondary phase detected. The presence of pyrite was verified by SEM-EDX and Raman spectroscopy on samples achieved at lower temperatures, showing the thermodynamic stability of this compound at a temperature usually employed to create TF samples. The final purity of these samples was $\approx 85\text{--}90\%$, in accordance with TF results, but this purity grade was still insufficient for obtaining a working PV device. Future efforts could further enhance the purity of the powder.

6.3. CMTS TF

6.3.1. TF deposition and series definition

In this section, we will discuss the results obtained from the realisation and study of CMTS TF samples. To begin, I will describe the process parameters used to prepare these samples. After the first phase of machine calibrations, we realised that samples varied the deposition time of every metal precursor. For a better explanation, we divided the various samples prepared into ‘series’ with these peculiarities:

- First series: As summarised in Table 46, this series contains the samples deposited, changing the **deposition time of precursors** and keeping the stack order constant, similar to that already used for record CZTS in this PhD thesis (substituting Zn with Mn). In this series, we studied the correlation between material properties (and the final PV device) with different metals’ content, with special attention to Mn content. We always deposited precursors, trying to obtain Cu-poor conditions to avoid Cu_{2-x}S formation with the composition ratios $[\text{Cu}]/([\text{Mn}]+[\text{Sn}])$ and $[\text{Mn}]/[\text{Sn}]$ near 1.

Table 46: First series of CMTS samples deposited with the standard stack order Mo/Sn/Cu/Mn.

# CMTS	Precursors sequence	Deposition time [s]		
		Sn	Cu	Mn
2	Sn/Cu/Mn	1450	550	1400
4		1450	510	920
5		1450	510	1200
10		2100	710	1200

- Second series: As summarised in Table 47, this series contains samples deposited following the same composition as sample #4 of the first series, where we found the lowest content of secondary phases, linearly **increasing the deposition times used for sample #4**. In this series, we studied the effect of increasing the TF thickness on the CMTS material and final PV devices and indirectly tested the reproducibility of the process, since the increase in deposition times should not vary the respective ratios of the metal’s content.

Table 47: Second series of CMTS samples deposited with the same stoichiometry as sample #4 and longer deposition times.

#CMTS	Precursors sequence	Deposition time [s]		
		Sn	Cu	Mn
4	Sn/Cu/Mn	1450	510	920
6		1640	585	1060
7		1830	660	1200
8		2070	760	1380

- Third series: As summarised in Table 48, the samples contained in this series are a preliminary test of the application of the **co-sputtering procedure** to obtain the precursor layer. Taking sample #8 of the second series as a reference, we tried to deposit all metal precursors simultaneously, a procedure enabled by three independent sources and powered by three independent DC generators in the machine used for this PhD thesis. With this test, we tried to assess the effect of the precursor order in the stack, especially for the interaction of Sn directly contacting the Mo substrate, which causes void

formation. (See the CZTS section for more information.) We also tried to apply this approach to the CFTS samples. However, in this case, we tried to apply a process never used for the alternative chalcogenide, such as CFTS or CMTS, but already studied for CZTS with positive feedback. As shown in Table 48, the deposition times of metal precursors in this series are the same as in sample #8; this implies that the metals are not deposited together for the entire process, since they start at once. In this scenario, samples are again organised into three layers: a first layer directly in contact with the Mo substrate that contains all metals, a second layer containing only Mn and Sn and a pure Sn layer.

Table 48: Third series of CMT samples with deposition times based on sample #8 for co-sputtering samples.

#CMTS	Precursors sequence	Deposition time [s]		
		Sn	Cu	Mn
8	Sn/Cu/Mn	2070	760	1380
9	Sn/Cu/Mn Co-sputtering	2070	760	1380
11		2100	755	1465

Additionally, for samples #4, #5, #6, #7 and #10, we performed **tests on the sulphurisation process**, both with the **standard protocol** already discussed for CZTS and with three-step sulphurisation, adding a mid-step at 150°C for 30min to the standard protocol. This step was already tested in a previous work on CMTS [105, 121] to study the interdiffusion process of metal precursors at low temperature to limit the formation of voids and to mimic the same approach applied on third-series samples with the co-sputtering process.

On sample #8, we tested a **rapid cooling process** after sulphurisation to study an order–disorder transition, as we did for CZTS samples. The quartz tube where the sulphurisation process takes place was removed from the furnace when the system was at 320°C, the temperature at which the disordered structure should still be stable for CMTS [96], and placed in the air. The cooling rate was estimated at 4°C/min.

6.3.2. Material characterisation

6.3.2.1. Compositional and morphological characterisation using SEM/EDX

In this section, the results of the compositional and morphological data are revealed and discussed. The samples are grouped into the series represented in the earlier section. The compositions for first series samples, where highly variable compositions are visible, are displayed in Figure 71, which depicts the ternary phase diagram of metals' precursors. The samples centre on a small section of the full diagram, with the composition between the stoichiometry condition for CMTS (purple dot, Cu:Mn:Sn=2:1:1) and the theoretical 'best-performance' stoichiometry point for CZTS (crossed blue arrows).

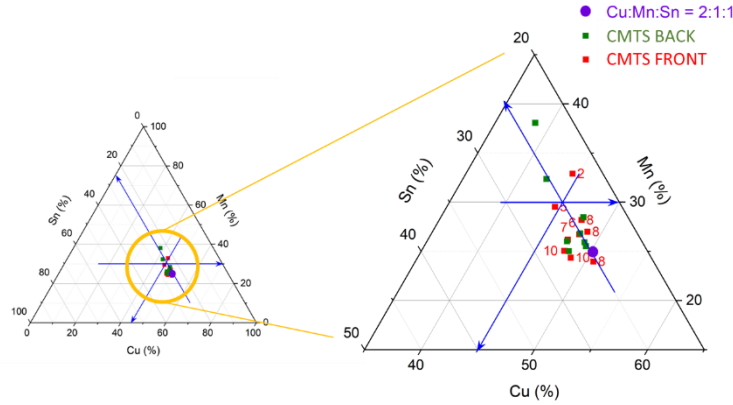


Figure 71: Ternary phase diagram of atomic metal content obtained by EDX for every CMTS TF sample realised in this PhD thesis. Red dots report compositions obtained from FRONT analyses; green dots convey compositions from BACK analyses.

6.3.2.1.1. First series of CMTS samples: Varying composition

Divided by acquisition place, that is, FRONT, and BACK data, Table 49 reports the compositional measures garnered from the EDX analysis of the first series of CMTS samples with the compositional ratios calculated from these data. In Table 50, the morphologic images are reported instead of samples of the same series from the FRONT and BACK surfaces and the cross-section.

From the EDX data, we can affirm the following:

- The good correlation between the metals' deposition time and the final composition of the samples, (already obtained for CZTS), as the final composition is in line with the initial condition set for the sample (e.g. CMTS sample #2 is effectively Mn-rich and Sn-poor; see Table 46).
- Every formulation depicts a Cu-poor condition ($[Cu] < 50\%$), which is ideal for avoiding $Cu_{2-x}S$ formation.
- Formulations can be grouped into two sub-series, depending on the $[Cu]/([Mn]+[Sn])$ ratio: a couple of samples #2 and #5, with a ratio value ≈ 0.8 , and a couple of samples #4 and #10, with a ratio value ≈ 0.9 .
- For samples #2 and #5, we noticed increased Mn content in the BACK measures.
- Sample #4 is the closest to the stoichiometric point.
- Sample #5 is the closest to the 'best CZTS performance' point.

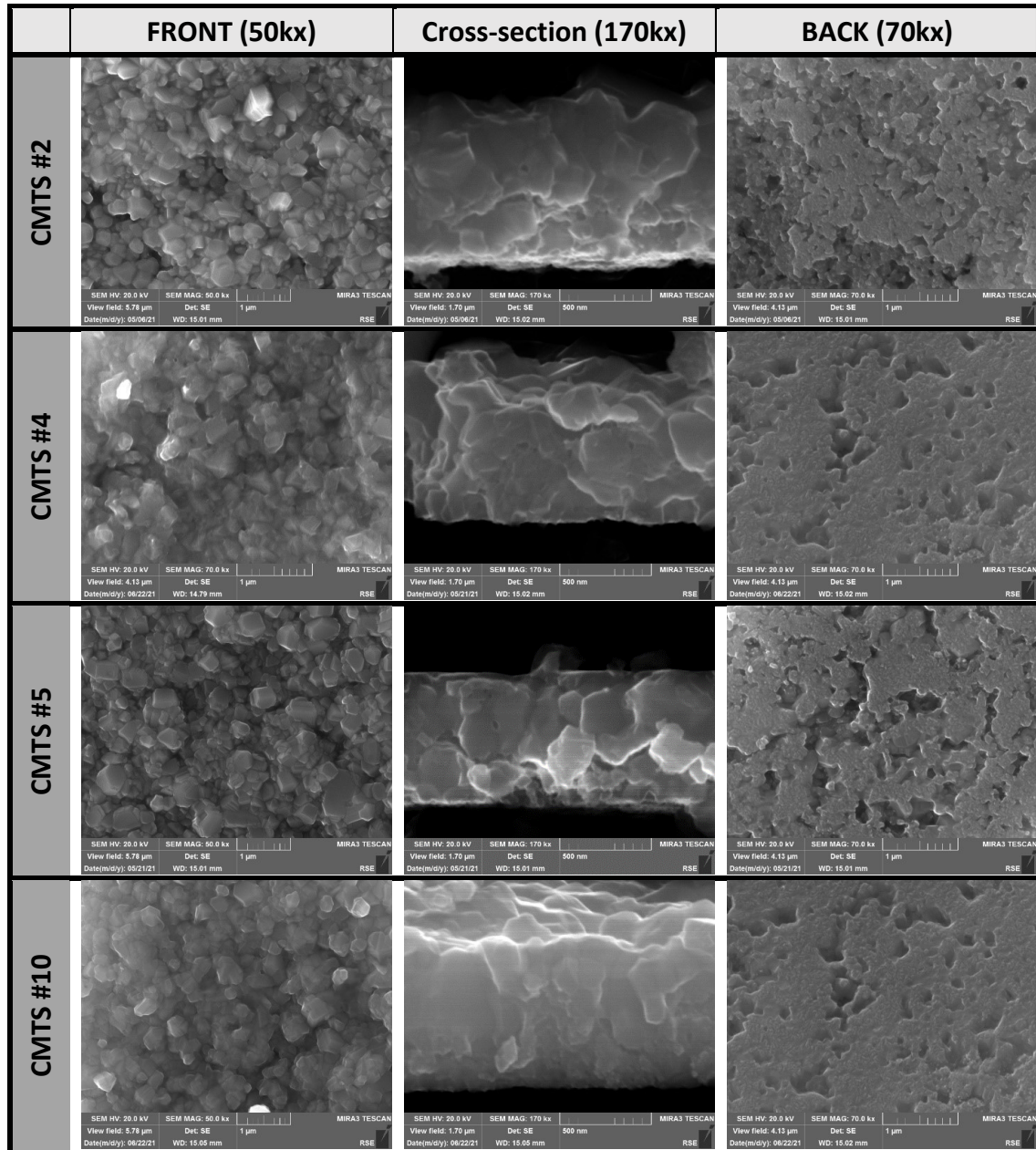
Table 49: Comparison of metals' deposition times, contents and compositional ratios of CFTS TF samples from the first series.

#CMTS	Deposition time [s]			FRONT composition						Back composition					
				Atomic %			Compositional ratios			Atomic %			Compositional ratios		
	Sn	Cu	Mn	Cu	Mn	Sn	Cu/Mn+Sn	Mn/Sn	Cu/Sn	Cu	Mn	Sn	Cu/Mn+Sn	Mn/Sn	Cu/Sn
2	1450	550	1400	44.4	32.9	22.7	0.80	1.47	1.98	38.5	38.1	23.4	0.63	1.63	1.65
4	1450	510	920	47.2	27.0	25.8	0.89	1.05	1.83						
5	1450	510	1200	44.6	29.5	25.9	0.81	1.14	1.72	42.4	32.4	25.2	0.74	1.28	1.68
10	2100	710	1200	47.6	25.1	27.3	0.91	0.92	1.75	49.3	25.5	25.2	0.97	1.02	1.96

As for morphologic analysis, we can state the following:

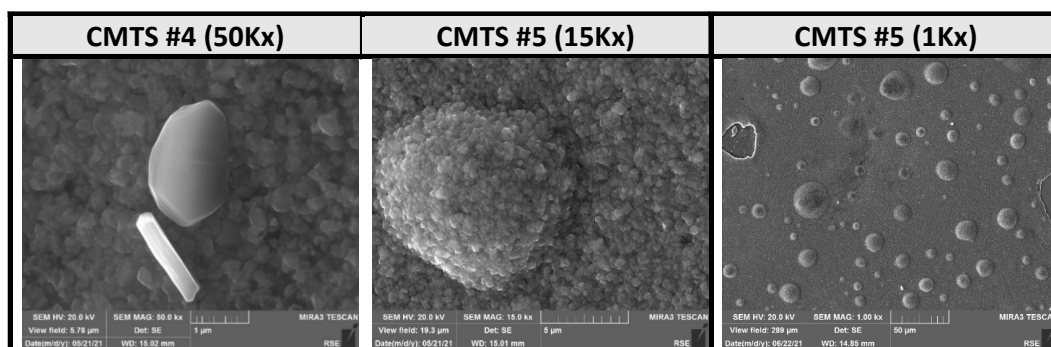
- Every TF conveys good homogeneity, compactness and large crystal formations.
- No secondary phases. Segregation is visible on the FRONT surface.
- Every TF demonstrates the formation of voids on the BACK surface, as observed for the CZTS and CFTS samples. Samples #4 and #10 present a lower void concentration, and their dimensions are limited.

Table 50: Comparison of FRONT, BACK and cross-sectional morphologies of samples from the first series.



As mentioned, for some of these samples, we tested the effect of a third temperature step in the sulphurisation process (as a first step, 150°C for 30min). Table 51 provides images of the FRONT surfaces of these samples. This alloying process causes macrodefects on the front surface that differ for every sample. For sample #4, for example it is possible to spot the lamellae of a different secondary phase that is traceable to a compound rich in Cu and Sn (similar to Cu_2SnS_3 , *Mohite*). Unfortunately, the limited dimensions of these formations and the limits of XRD for distinguishing similar crystal structures made the unequivocal characterisation of these defects impossible. In other samples, the formation of bubbles on the FRONT surface was visible, similar to sample #5, with wide regions of the samples affected by these defects. The low compactness of these structures left holes in the material, lowering the continuity of TF. Correspondingly, we ceased this study of other CMTS samples.

Table 51: SEM images of defects found on samples from the first series sulphurised with an extra step at 150°C for 30min.



6.3.2.1.2. Second series of CMTS samples: Varying the thickness

Table 52 shows data concerning the compositional analysis, coupled with precursor deposition times, for both the FRONT and BACK surfaces of samples belonging to the second series of CMTS samples. Table 53 conveys the SEM images taken for the FRONT surface and the cross-section of standard samples from the second series (samples #6–#7–#8), and Table 54 depicts the SEM images of the variants of sample #8.

From these data, we can affirm the following:

- Samples obtained with a linear increase in all deposition times shared the **same final composition** (inside experimental uncertainty).
- Variations in the [Mn]/[Sn] ratio between samples could be connected to **Sn loss** during the sulphurisation process or to experimental uncertainty in the deposition of Sn during the sputtering process (due to the low power used to deposit this metal in the specific case).
- Being Cu-rich, such as sample #4 in the first series, all these samples **do not convey remarkable differences** between their FRONT and BACK surfaces.
- Every sample revealed compositional ratios near the stoichiometric condition, with a small Sn excess and an even smaller Cu deficit. This reduces the formation of conductive phases, such as Cu_{1-x}S .
- The HCl treatment of sample #8, obtained with a ‘fast-cooling process’, possesses **very different compositional ratios**, switching from an **Mn-rich** condition to an **Sn-rich** condition. The reasons behind this phenomenon will be discussed in more detail later with morphological and XRD analyses.

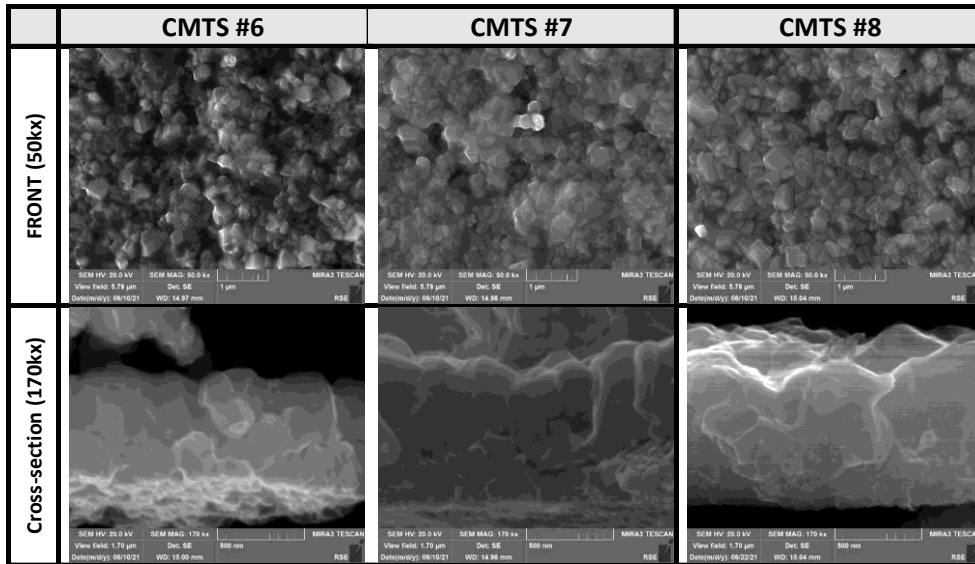
On a morphological level, we can affirm the following:

- Every sample showed very **good homogeneity, good compactness and a strong multi-crystalline nature**.
- No obvious presence of **the secondary phases was detected** on the FRONT surface.
- As in first series samples, these samples also presented the formation of voids on the BACK surface.
- The cross-section images show the progressive increase of the film’s thickness, which follows the increase in deposition times (#4≈600nm, #6≈670nm, #7≈820nm and #8≈800nm).

Table 52: Comparison of deposition times, compositional ratios for both the FRONT and BACK surfaces for the CMTS sample belonging to the second series, with two variants for sample #8, treated with rapid cooling with or without the acidic treatment.

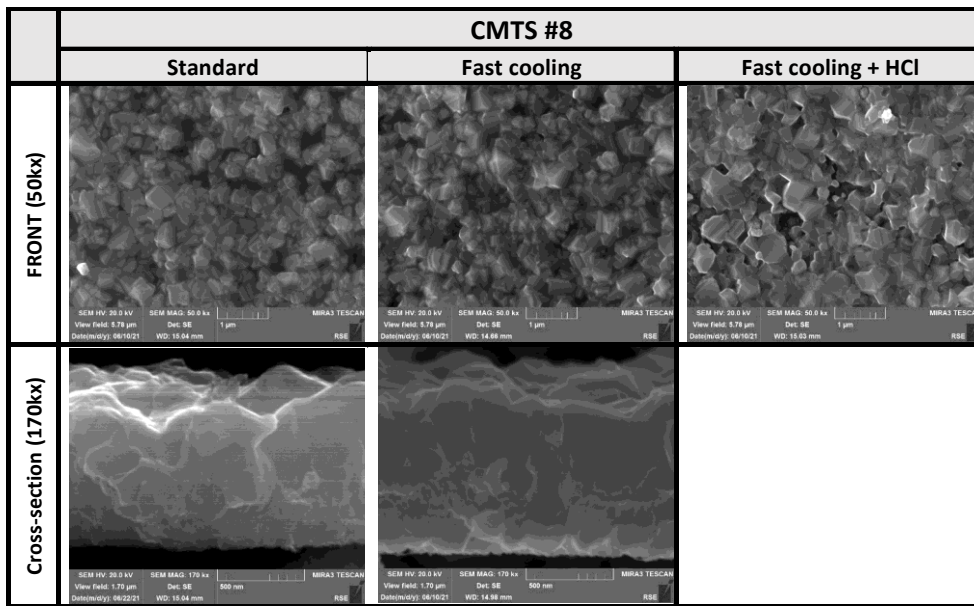
# CMTS	FRONT composition						BACK composition					
	Atomic %			Compositional ratios			Atomic %			Compositional ratios		
	Cu	Mn	Sn	Cu/Mn+Sn	Mn/Sn	Cu/Sn	Cu	Mn	Sn	Cu/Mn+Sn	Mn/Sn	Cu/Sn
4	47.2	27.0	25.8	0.89	1.05	1.83						
6	48.1	26.7	25.2	0.93	1.06	1.91	47.6	28.5	23.9	0.91	1.19	1.99
7	47.4	26.2	26.5	0.90	0.99	1.79	47.4	26.0	26.6	0.90	0.99	1.80
8	47.6	28.2	24.2	0.91	1.17	1.97	49.0	25.9	25.1	0.96	1.03	1.95
#8 variants												
8+ fast cooling	48.7	27.0	24.3	0.95	1.11	2.00	48.1	26.8	25.1	0.93	1.07	1.92
8+ fast cool. + HCl	50.7	24.0	25.3	1.03	0.95	2.01						

Table 53: Morphological comparison of the FRONT surface and cross-section of the CMTS sample in the second series.



As described before, two cooling procedures were applied to samples from sample #8: the classical cooling process, where the sample cools with the oven, and a ‘**rapid cooling**’ process, where the quartz ampule is removed from the oven at 320°C to reproduce what we obtained with CZTS. Table 54 reveals a comparison between the front surface and the cross-section images of these two samples’ series, together with an SEM image of the FRONT surface of the ‘rapid-cooling’ sample after standard HCl treatment. This process is the same as that used for CZTS samples to remove superficial secondary phases and increase the surface quality before the deposition of the CdS buffer layer. No differences were observed between the two samples with the two cooling processes, while the surface of the HCl-treated sample displayed grains with well-defined edges. This fact, observed in other samples where we applied this HCl treatment, can be explained by the removal of superficial secondary phases with the successive exposure of the bare CMTS surface. This hypothesis will be discussed more in the XRD data discussion later.

Table 54: Morphological comparison of the FRONT surface and the cross-section of variations in sample #8, with a fast-cooling process after the acidic treatment.



6.3.2.1.3. Third series: Varying the precursors' order

In Table 55, the data are displayed regarding the compositional analysis, coupled with precursor deposition times for both the FRONT and BACK surfaces of samples belonging to the third series of the CMTS sample. In Table 56, the SEM images of the FRONT and BACK surfaces with cross-section images of the same samples are represented. Table 57 provides insight into an exfoliation phenomenon observed in sample #9.

EDX analyses of these samples depict remarkable differences between the two processes:

- The cosputtering technique returns different **compositional properties** with respect to the classical multilayer approach; see sample #8 vs. #9. Using the same deposition times, the two samples diverge strongly in their metal content, conveying a strong decrease of the [Mn]/[Sn] ratio.
- This **difference decreases** if we compare the compositions of **BACK surfaces, indicating that** the main difference in deposition conditions happens in the final stage of the deposition.
- Sample #9 reveals a Cu content near the stoichiometry limit (50%) that is too high to avoid the formation of detrimental secondary phases.
- Sample #11, which is obtained by co-sputtering and modifying the deposition times to obtain a similar composition to sample #8, reveals good accordance with the record sample.

As for morphological analyses, the SEM images displayed the following:

- **No secondary phase segregation was visible** on the FRONT surface of the samples.
- On the FRONT surface of sample #11, **grains with different dimensions and shapes are visible**, but no difference in composition is detected in this region.

Table 55: Comparison of deposition times, metal content and compositional ratios for the CMTS TF of the third series.

# CMTS	FRONT composition						BACK composition					
	Atomic %			Compositional ratios			Atomic %			Compositional ratios		
	Cu	Mn	Sn	Cu/Mn+Sn	Mn/Sn	Cu/Sn	Cu	Mn	Sn	Cu/Mn+Sn	Mn/Sn	Cu/Sn
8	47.6	28.2	24.2	0.91	1.17	1.97	49.0	25.9	25.1	0.96	1.03	1.95
9	49.8	23.9	26.3	0.99	0.91	1.90	49.1	23.4	27.5	0.97	0.86	1.80
11	47.9	27.1	25.1	0.92	1.08	1.91	47.8	27.6	24.6	0.92	1.13	1.95

- Table 57 conveys that sample #9 demonstrates a double-layer structure (orange arrow); when removed, one of the two layers remains attached to the Mo substrate. This feature is also observed in sample #11, with lower magnitude.
- Due to this separation, the BACK surface morphology in these samples cannot be analysed, so it is quite difficult to observe and analyse the formation of voids.

Table 56: Comparison between the FRONT and BACK of samples inside the CMTS TF third series.

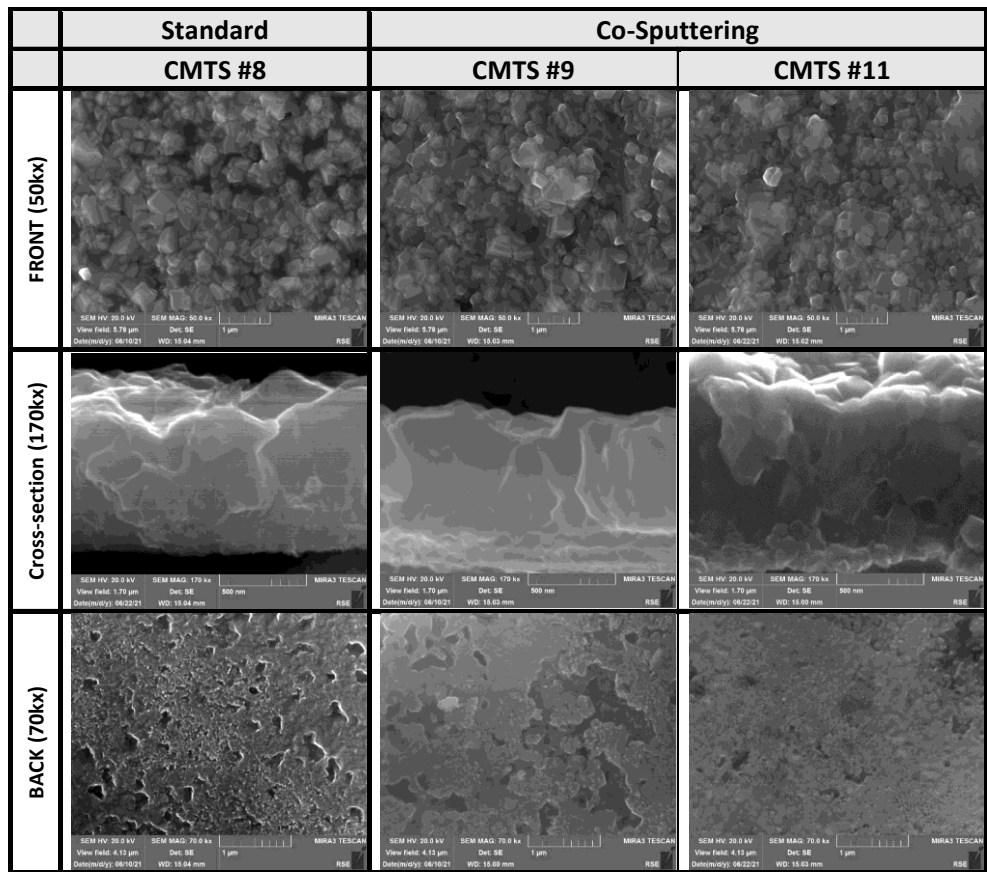
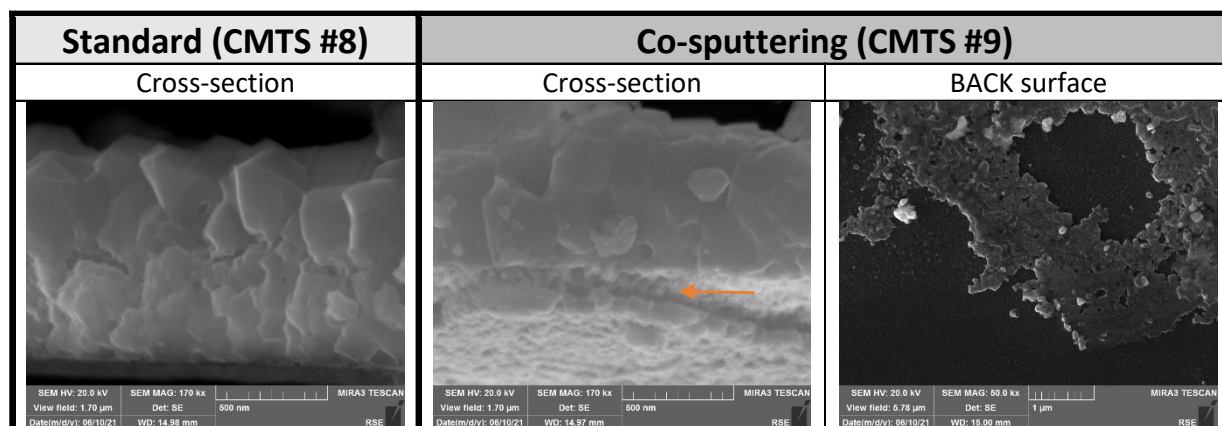


Table 57: Details of the BACK surface of sample #9, attained by cosputtering. Sample #8 was taken using the same deposition times in a multilayer configuration. Sample #9 also reports the surface of the Mo substrate after the removal of the CMTS material, showing the part of the material that remains attached on the substrate.



6.3.2.2. Crystallographic characterisation by XRD analysis

For all the analysed samples, XRD measures were performed removing part of the TF from the substrates SLG/Mo and dispersing the thus-obtained powder on a misoriented silicon sample holder, so any effect of the holder would be visible in the diffractograms, enhancing the material's signals.

Comparing the obtained measures with data from a dedicated database (PDF4+ from ICDD), we identified a set of three crystal phases inside our samples:

- **Synthetic CMTS stannite** Database PDF4+ 04-012-0329
- **Thiospinel (CuMn₃Sn₂S₈)** Database PDF4+ 04-003-8291
- **Alabandite (MnS)** Database PDF4+ 00-006-0518

For every set of samples, the compositions and phases' weight content from the Rietveld refinement of these crystal phases are reported in Table 58. For the secondary phases detected, we can add the following:

- Many of these compounds possess common diffraction peaks; for example, the three thiospinels revealed in Figure 33 and MnS (in the alabandite structure) show cubic structures with similar cell dimensions.
- The thiospinel diffractograms display peaks at $2\theta=24.2^\circ$, 45.2° and 49° , which MnS does not show.
- Since the diffractograms of the three thiospinel structures are the same, **it is not possible to recognise a specific thiospinel from the others without compositional analysis**. Nonetheless, in this study, we have shown that our samples possess Mn-rich compositions, so the presence of Mn-rich **thiospinel CuMn₃Sn₂S₈ is probable**. Analyses with a synchrotron light could identify with higher accuracy which phases we are dealing with.
- Only in sample #9 is an uncommon formation of the Sn-rich sulphide phase observed.

Table 58: Comparison between process parameters and phase contents calculated by Rietveld refinement for all the obtained CMTS TF samples, organised by series.

# CMTS	Deposition time [s]			Crystalline phase % weight				Eg	thickness
				CMTS	Thio-spinel CuMn ₃ Sn ₂ S ₈	MnS <i>alabandite</i>	Tin sulphide		
	Sn	Cu	Mn	[04-012-0329]	[04-003-8291]	[00-006-0518]	[00-014-0619]	[eV]	[nm]
Serie 1									
2	1450	550	1400	90		10		1.6	650
4	1450	510	920	95	4	1		1.59	600
5	1450	510	1200	85	9	6		1.57	710
10	2100	710	1200	93	6	1		--	830
Serie 2									
6	1640	585	1060	93	5	2		1.58	670
7	1830	660	1200	87	9	4		1.57	820
8	2070	760	1380	95	4	1		1.59	980
Serie 2									
9	2070	760	1380	85	9		6	1.45	900
11	2100	755	1465	90	9	1			920

From these observations, we can conclude that the Rietveld refinement of the samples in this section demonstrates the following:

- Every deposited sample represented the predominance of a **CMTS phase** with a stannite structure (with the PDF4+ code 04-012-0329).
- Following the compositional ratio [Mn]/[Sn] in the first series samples, it is shown that a higher **Mn content is followed by the formation of MnS**, while with **lower ratios, the formation of the thiospinel phase is higher**. Figure 72 reveals the diffraction pattern of samples inside first series, together with the markers of the crystallographic phases detected in every sample.
- Sample #4 illustrates the **highest purity in the first series of samples**, so we chose the composition of this sample to obtain the samples of second series.

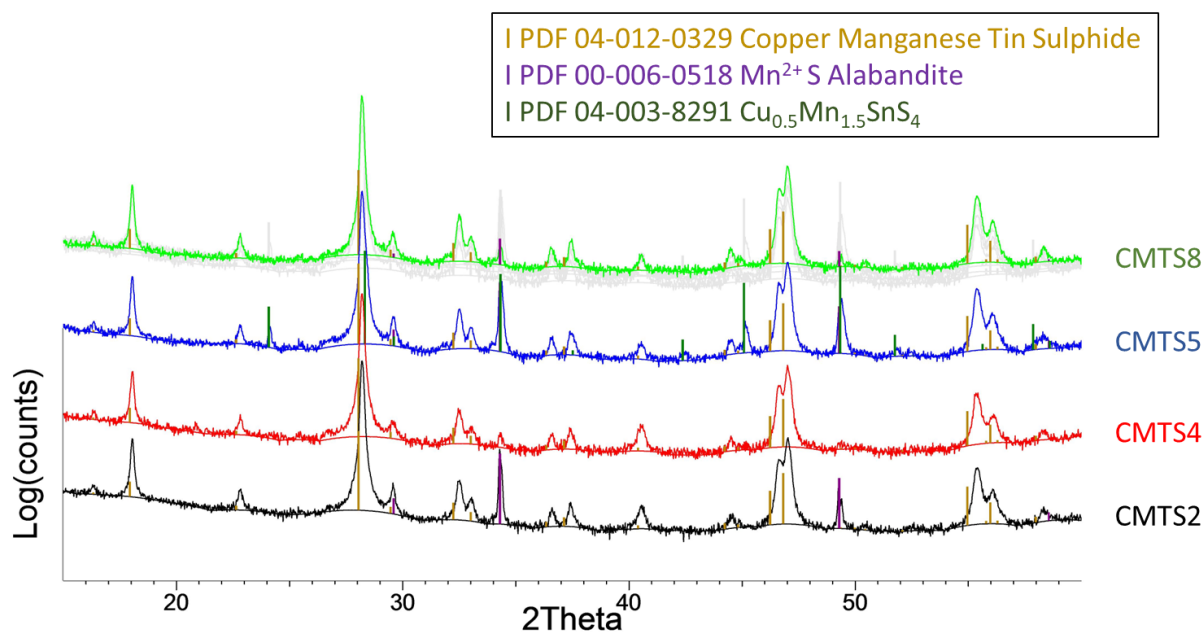


Figure 72: Comparison of XRD patterns for the first series' samples, conveying the rise of different peaks (red markers = CMTS phase, blue markers = MnS, green markers = CuMn₃Sn₂S₈).

- Leaving aside sample #7, samples inside the second series depicts high **main phase content**, presenting that the longer deposition process does not affect the final composition and phase formation.
- As for the effect of HCl treatment, Figure 73 reports the diffractograms of sample #8 before and after the HCl treatment. This treatment is useful for **removing secondary phases from the surface (thiospinel and/or MnS)**, and it will be used to explain better PV performance in correlated PV devices.

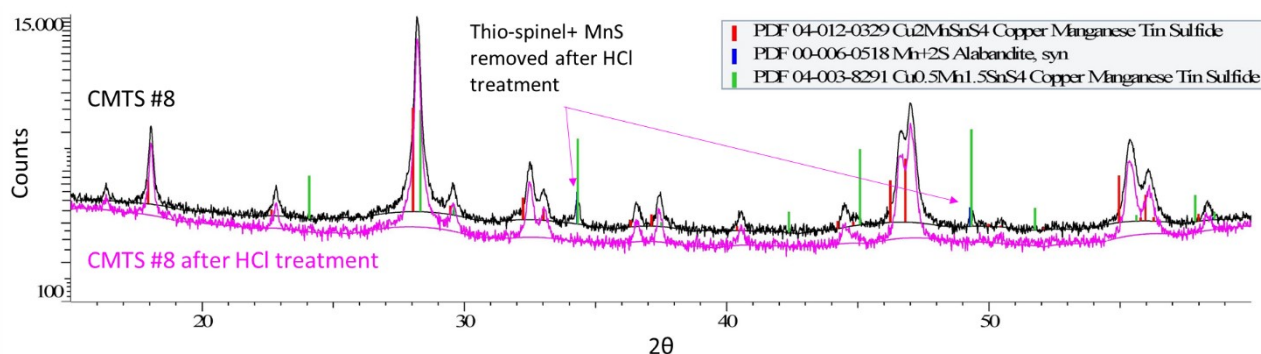


Figure 73: Comparison of the diffraction patterns of sample #8 before (black graph) and after (pink graph) the HCl treatment. The arrows point to peaks that disappear after treatment, connected with the removal of MnS and $\text{CuMn}_3\text{Sn}_2\text{S}_8$.

- Sample #9 is the only one that demonstrates the formation of binary phases of Sn sulphides (see Figure 74). The limited height of these peaks and the high patterns' similarities between compounds hinder the exact phase attribution from merely the XRD analysis. This will be clarified with the Raman analysis results of these samples, which will be displayed later in the manuscript. This sample could have suffered problems related to **inhomogeneity in element distribution due to the co-sputtering process**, which could also be the reason behind the double-layer structure observed in SEM images. This effect is lower on sample #11. It is also obtained by co-sputtering but with a correction in composition to obtain a metal content more similar to sample #8.

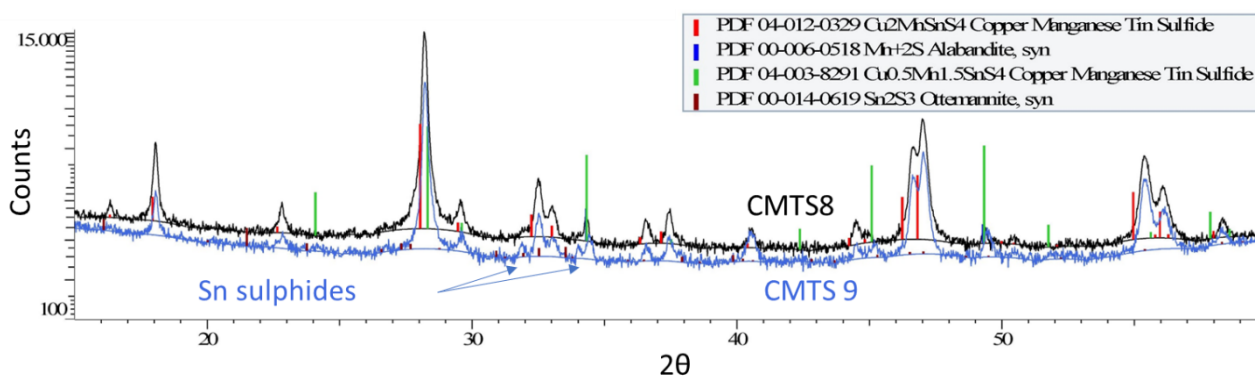


Figure 74: Comparison between the patterns of sample #8 ('pure') and sample #9 to discern the effect of the application of the co-sputtering approach. The arrows indicate peaks correlated with Sn-rich chalcogenides with an unknown composition.

6.3.2.3. Raman characterisation

Raman characterisation was carried out to reinforce the XRD analysis of the CMTS samples represented above. Figure 75, Figure 76 and Figure 77 show comparisons between the Raman spectra of different samples. Unfortunately, the absence of detailed research in the Raman literature about thiospinel phases prevents fine recognition of these phases with this technique, but other considerations can be made:

Comparing the results of the Raman spectra of the samples from the first series (see Figure 75), **every sample conveys the same peak position revealed in the literature for this chalcogenide** (see It is possible

to find synthetic techniques to produce CMTS in the literature, depending on the nature of the material. Starting from nanocrystals [97, 106], with low interest in the focus of this PhD thesis, we can focus on CMTS TF preparation techniques that can be divided between physical vacuum techniques and humid chemist techniques. Suresh Kumar [107] updated the situation concerning cation-substituted CZTS TF preparation to 2019, complete with other substitutions. The CMTS section is quite wide, and it is separated into the previous two topics, with an in-depth analysis of methods and results. For CMTS preparation, the most important techniques mentioned are as follows:

- Evaporation with an electronic beam (e-beam).
- Hot injection.
- Spray pyrolysis.
- Sol-gel.
- Solvothermal deposition.
- Dip coating (or SILAR).
- Electrodeposition.
- Co-sputtering.

Most of these processes have two steps. The metallic precursors are deposited first with, in some cases, a little chalcogen, followed by a second step consisting of a thermal treatment (TT) in the presence of chalcogen to form the CMTS phase. Significantly, the authors focused their analysis on solar device results, and TF characterisation is not always included in reviews. Table 14 summarises the efficiencies of the TF PV devices obtained using various techniques.

Table 14). The same situation can be observed for samples of second series (see Figure 76 on the left). A deviation from this behaviour can be observed in sample #5 (containing the thiospinel phase), where the higher contribution of the peak at 366cm^{-1} and a new peak at 350cm^{-1} can be observed. This difference is described in the literature [96] with **the presence of a thiospinel phase**.

- On sample #8, the Raman characterisation was performed with two laser sources, one with $\lambda=633\text{nm}$ used also for CZTS and CFTS, and one with $\lambda=532\text{nm}$ to check for the presence of differences due to varying material penetration, as realised by *Rudisch et al.* [96] and at the centre of Figure 76. **The main difference between the two spectra is limited to the region around 350cm^{-1} , which is associated with the presence of the thiospinel phase.** With the higher penetration wavelength (633nm), the thiospinel signal is higher than with the low penetration wavelength (532nm). As a qualitative observation, this could be connected to a lower thiospinel presence on the surface than in the bulk of the sample due to the HCl treatment applied to the sample.

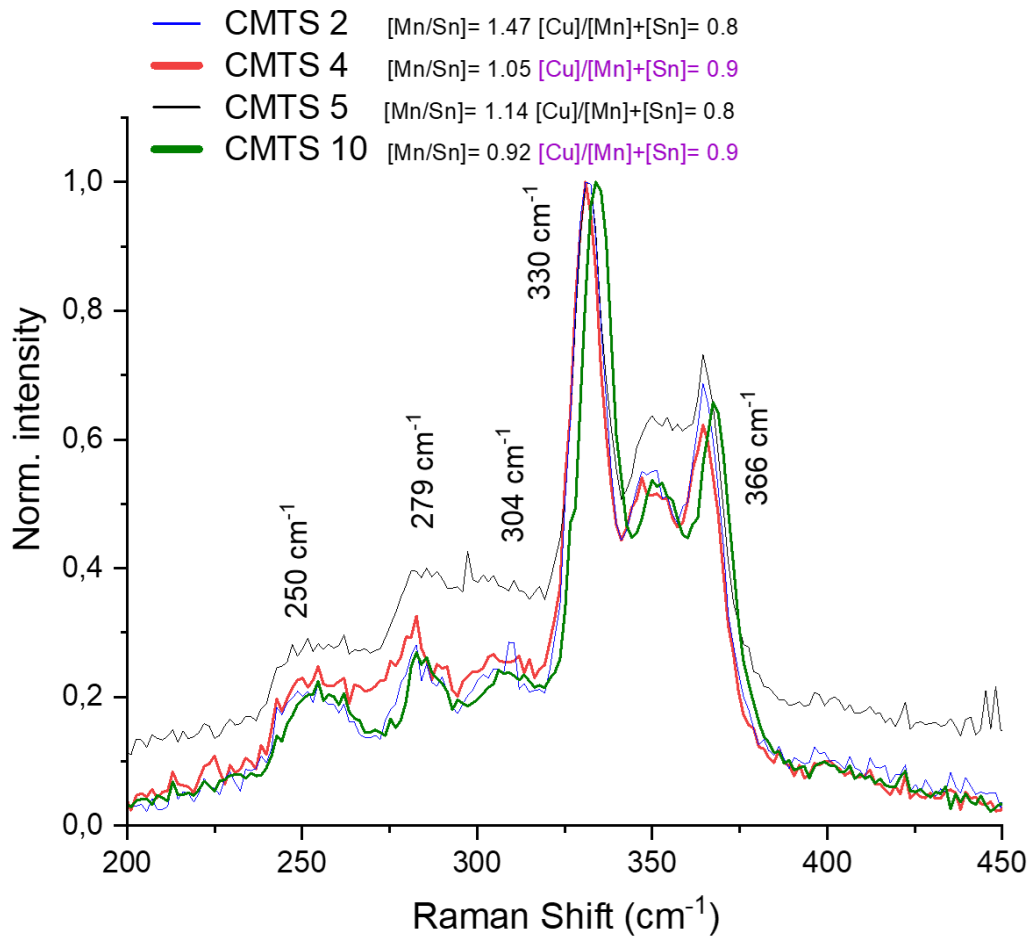


Figure 75: Comparison of the Raman spectra of samples from the first series.

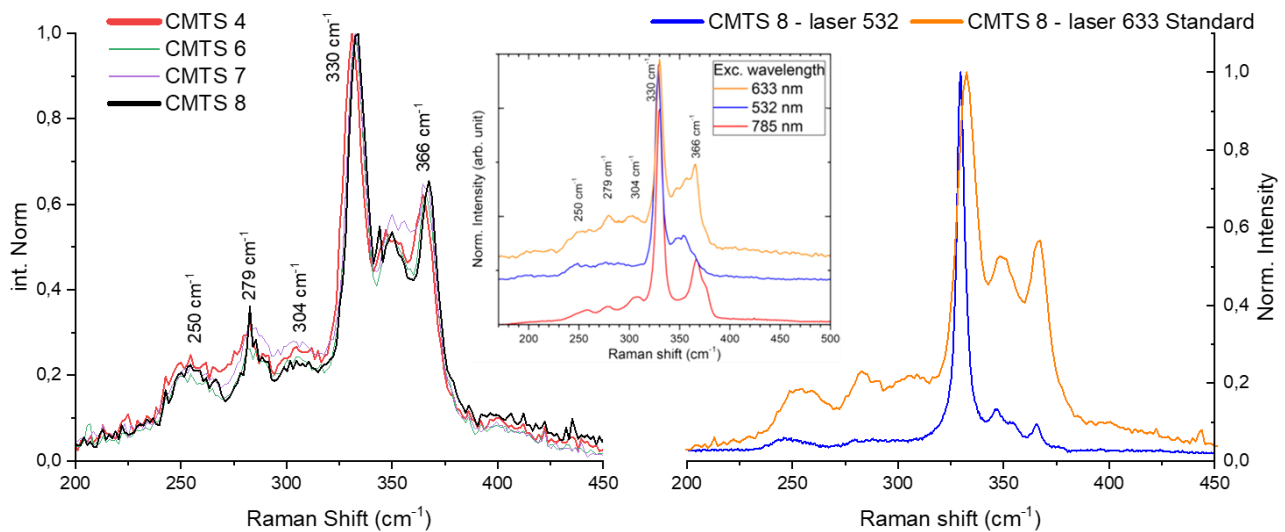


Figure 76: On the left, comparison between Raman spectra of samples from the second series; on the right, comparison between the Raman spectra of sample #8 taken with different laser wavelengths (blue graph: $\lambda=532\text{nm}$, yellow graph: $\lambda=633\text{nm}$) to be consistent with the literature (displayed in the centre [96]).

- Figure 77 on the left represents the Raman spectra of sample #8 replicas that underwent different cooling processes (regular cooling with the oven, rapid cooling and CZTS-like thermal PDT). In CZTS, this kind of cooling process forced an order–disorder transition visible in the E_g and Raman spectrum variations. **In this case, no evidence of this transition is visible**, which could be linked to the absence of this transition in the material, as supposed in the introduction.
- In sample #9, Raman spectra confirmed the presence of a superficial **Sn-rich chalcogenide phase**, connected to the presence of a peak at 319cm^{-1} (see Figure 77 on the right). From the literature [122], this peak can be linked to the presence of various Sn-based secondary phases (as SnS_2 e Cu_3SnS_4) that are compatible with what we observed in XRD analysis.

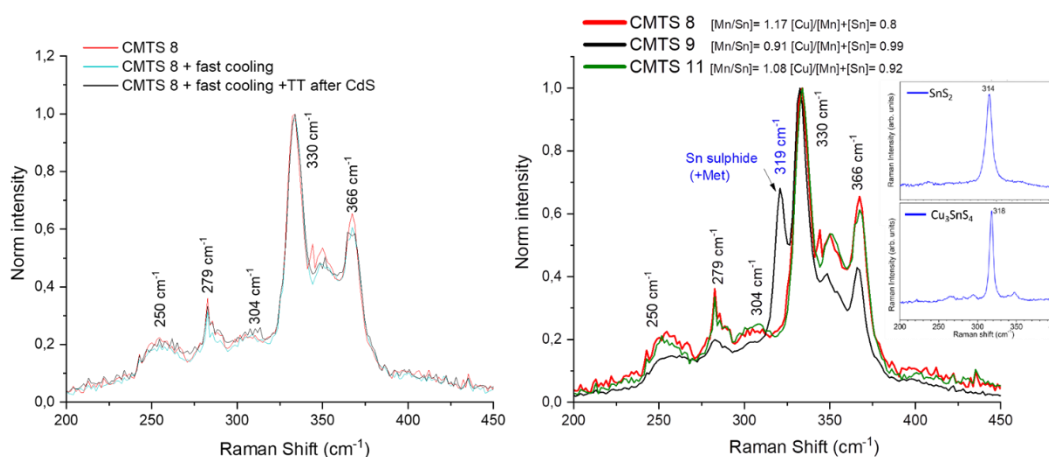


Figure 77: On the left, comparison between sample #8 replicas obtained with different thermal protocols (red: standard process, green: rapid cooling after the sulphurisation process, blue: rapid cooling after the sulphurisation process + thermal PDT after CdS deposition); on the right, comparison between samples from the co-sputtering approach, with a measurement from sample #9 that demonstrates a peak at 319cm^{-1} connected to the presence of Sn-based phases, where the inset depicts the literature spectra of these phases [122].

6.3.2.4. UV–Vis characterisation by transmittance measure for E_g determination

For all the samples taken for this material, we also produced an exact replica of their growth on a bare-SLG substrate, as obtained for CFTS samples, to perform transmittance measures and attain E_g values from the Tauc plot. Table 59 depicts the phase content of all the CMTS samples with the E_g calculated from the Tauc method and the film thickness calculated from the cross-sectional SEM images. Figure 78 conveys the comparison between the two Tauc plots, as an example of the ones from the other samples. This comparison between the band gap's values relates the following:

- Almost every sample of CMTS TF shows a value for the band gap around 1.6eV, near the value reported in the literature.
- The presence of MnS does not influence the final E_g of the material, since its own band gap is reported as 2.8eV in the literature.
- Sample #9 shows the lowest value of E_g of every series, which could be linked to the **presence of the Sn-rich secondary phase** seen in XRD and Raman analysis.

Table 59: Comparison of CMTS TF samples extracted on a transparent substrate with the phase content from Rietveld refinement, the Eg value from Tauc plots and the thickness from cross-sectional SEM images.

# CMTS	Deposition time [s]			Crystalline phase % weight				Eg	thickness
				CMTS	Thio-spinel CuMn ₃ Sn ₂ S ₈	MnS <i>alabandite</i>	Tin sulphide		
	Sn	Cu	Mn	[04-012-0329]	[04-003-8291]	[00-006-0518]	[00-014-0619]	[eV]	[nm]
Serie 1									
2	1450	550	1400	90		10		1.6	650
4	1450	510	920	95	4	1		1.59	600
5	1450	510	1200	85	9	6		1.57	710
10	2100	710	1200	93	6	1		--	830
Serie 2									
6	1640	585	1060	93	5	2		1.58	670
7	1830	660	1200	87	9	4		1.57	820
8	2070	760	1380	95	4	1		1.59	980
Serie 2									
9	2070	760	1380	85	9		6	1.45	900
11	2100	755	1465	90	9	1			920

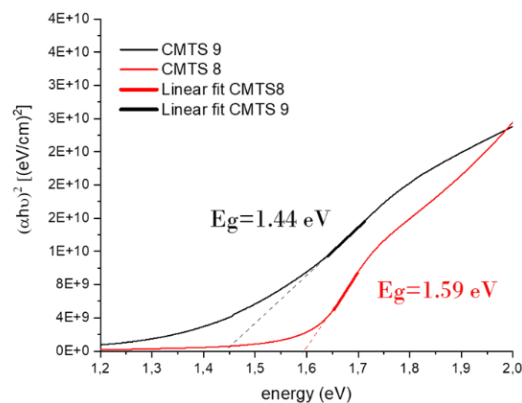


Figure 78: Comparison of Tauc plots of samples #8 and #9 to exemplify the two situations observed for all the other samples.

6.3.2.5. PL characterisation for Eg measures

To improve the study of the band gap of the material, PL measurements were carried out on the samples grown on bare SLG substrates. Two approaches were used to perform these measures: measures at RT to investigate band-to-band recombination and temperature-dependent measures to investigate lower-energy recombination involving defects. In Figure 79, the results of room-temperature PL measures of sample #8 are revealed as examples for every other sample, since the measures obtained are very similar. In Figure 80 are shown the temperature-dependent measures made from the same sample. From these measures, a few observations can be made:

- RT measures illustrate very **similar Eg values to transmittance measures**, with wide peaks centred on $\approx 1.6\text{eV}$; the wide shape of these peaks is due to the high temperature used for the measures. Moreover, the fact that we are observing band-to-band recombination is ensured by the laser's power (from the Raman device), which is much higher than the classical laser power used for low-temperature PL measures.

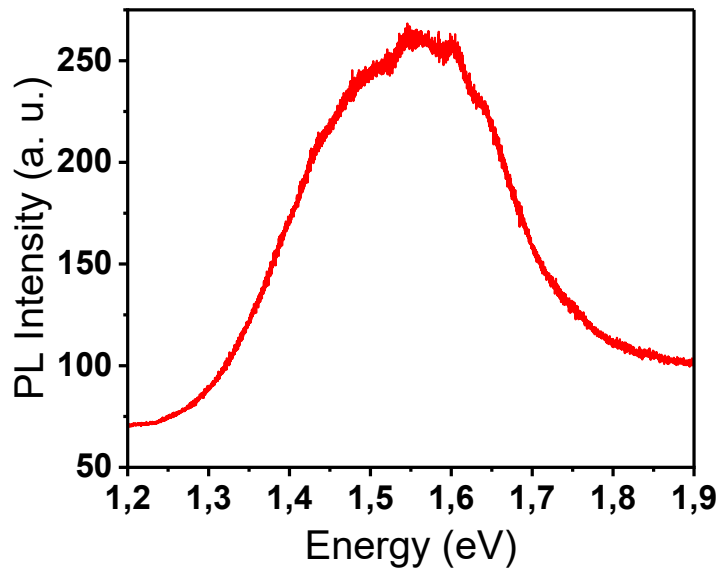


Figure 79: RT PL measure of sample #8 to exemplify other samples' results. A large PL band centred on 1.57eV is visible in accordance with the E_g value obtained from transmittance measures.

- Low-temperature measures demonstrate a very different situation: A high, sharp and asymmetric peak is observed around **1.3eV** (named D1 in Figure 80), and a group of low, large peaks can be seen for energy below **1.1eV** (named D2 in Figure 80). Similar behaviour has been observed from *Krustok et al.* [21] and can be explained by the presence of **two recombination paths**. The intensity of these peaks decreased with increasing temperature, depicting the intervention of a defect with different occupations with temperature. **The E_a calculated for this defect from the D1 measures is 55meV**, addressing the defect as shallow; this low E_a value can be associated with the value of the defect V_{Cu} , which conveys similar E_a values in CZTS. No fitting is reported for the D2 peak due to its low intensity, but we can speculate a lower E_a for this defect due to the lower temperature in which this peak system is still visible.
- The D1 peak demonstrates variations in peak position and intensity, also changing the laser power. As described by *Leitao et al.* [123], this behaviour has already been seen in other chalcogenide materials similar to CMTS, and *Tseberlidis et al.* [124] state that this behaviour is connected to donor–acceptor recombination. The peak position changes with a ratio of **6.1meV/decade**, which indicates a donor-to-acceptor transition, while the PL intensity increases with a ratio of 0.65, **indicating the involvement of defect states in the recombination**.

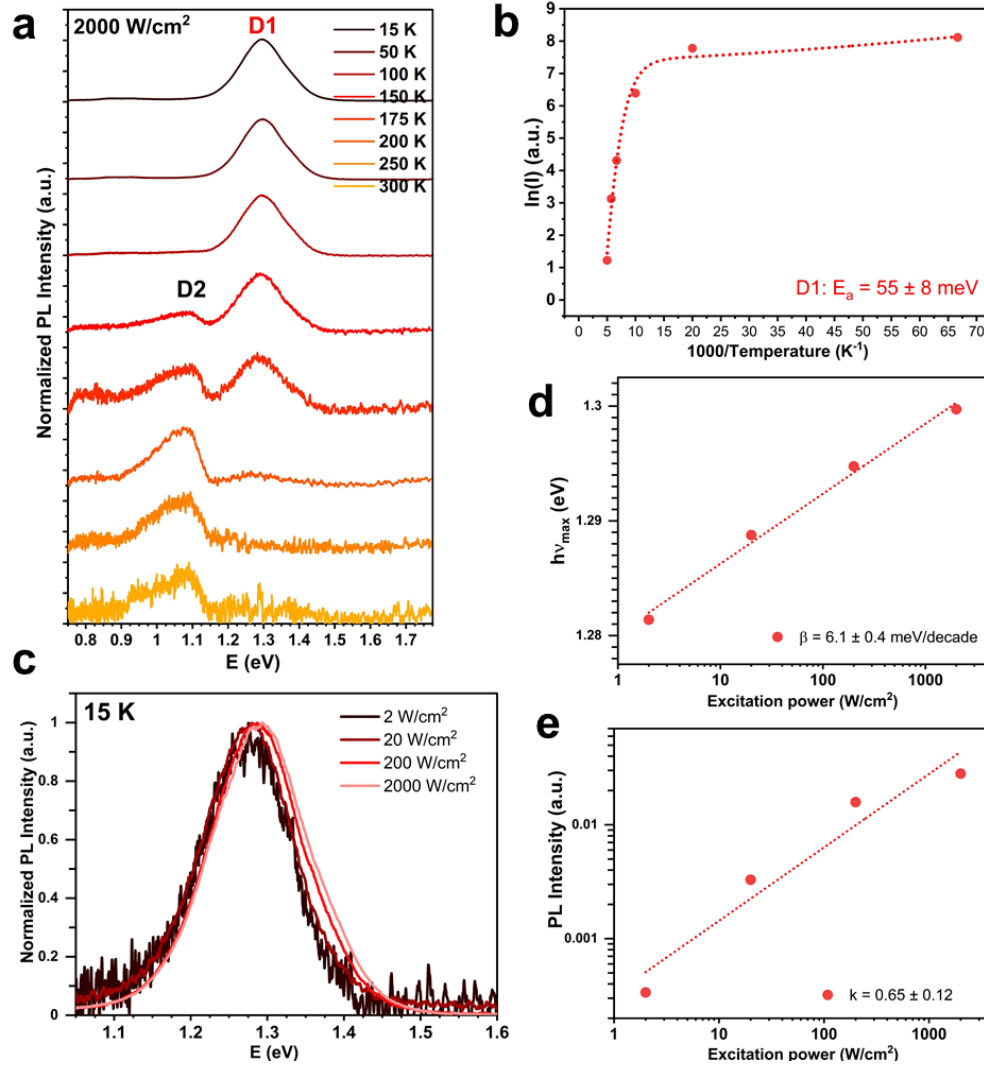


Figure 80: PL measures of sample #8 and their elaboration: a) PL spectra of sample #8 measured at different temperatures, presenting a main peak, D1, centred on 1.3eV and a secondary peak group, D2, under 1.1eV; b) dependence of the PL intensity of the peak centred on 1.3eV, showing the intervention of a defect with $E_a=55\pm 8\text{meV}$; the red shift of the D1 peak with laser power, showing the intervention of defect states in this recombination; d) dependence of the peak position on laser power, conveying a low β value for 6.1meV and d) dependence of PL intensity on laser power, showing a k value of 0.65.

From all these considerations, a model can be attained for recombination in CMTS samples. Following *Krustok et al.* [21], we can describe the system revealed in Figure 81: the good definition of the D1 peak permits us to build a good model, where the defect V_{Cu} placed at 55meV is coupled with a deep donor defect placed at 245meV. This E_a value can be attributed to one of the three metal interstitial defects (Cu_i , Mn_i or Sn_i), but it is impossible to define exactly which metal is effective. The model for D2 is less precise due to the absence of an exact identification for the acceptor defect, but we can assume that the donor defect E_a is higher than 500meV. Further characterisation should be used to correctly identify this recombination, but its low magnitude in PL measures illustrates the low impact that this recombination has on material properties. The defects will also be studied through impedance in Section 6.3.4.

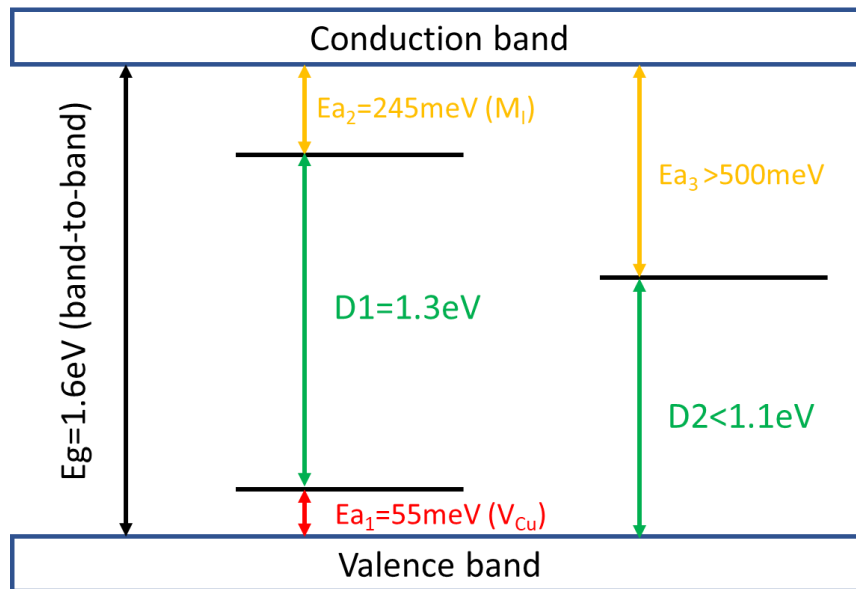


Figure 81: Scheme of the recombination mechanism built from temperature-dependent PL measures. The values for D2 are unclear, and the model must be observed qualitatively. From the D1 and E_{a1} values, we can extract the E_{a2} value, which results in 245 meV. This value can be connected to interstitial metal defects (Cu_i , Mn_i or Sn_i). The high value of E_{a3} is very difficult to assign, and more studies must be conducted.

6.3.2.6. XPS analysis

To determine the oxidation state of the elements in the CMTS TF, XPS measures were carried out. The objective of the study is to define the oxidation state of all the elements composing the material, especially Mn, which could assume many oxidation states' values, unlike Zn (the oxidation state of which is +2) in CZTS. The analysis was performed on TF realised on the SLG substrate, both on the surface as it is and after three *plasma etching sequences*, to clean the surface first and investigate the chemical nature of the elements in a deeper region of the TF, since XPS is a surface characterisation technique. In this case, this sequence is determined by the time of the process: 120s, 480s and 1,200s, respectively. For this study, the 120s step returns the best results, since we managed to discard inquinating compounds and elements and did not depict elements connected to the substrate.

Figure 82 (left) represents the results of XPS analysis on CMTS sample #7's surface after 120s of *plasma etching*. Figure 82 (right) shows that the regions of interest of Cu, Fe, Sn and S in the XPS spectrum are magnified, as reported by *Chen et al.* [125] and *Nie et al.* [126]. The spectra are compatible with the literature, presenting the correct oxidation states for Cu^{+1} , Sn^{+4} and S^{-2} , but very different for Mn. The profile observed for this element can be described as the sum of the various contributions of different Mn species. Observing the XPS results of the depths displayed in Figure 83, different contributions can be found at different depths, such as Mn peaks for Mn^{2+} related to sulphide materials [125, 126], Mn^{3+} related to Mn_2O_3 [127, 128] and Mn^{4+} related to MnO_2 [129, 130]. The presence of manganese oxides is also confirmed by peaks associated with O binding to Mn; these insulating compounds strongly affect conduction through the material, generally limiting PV performance.

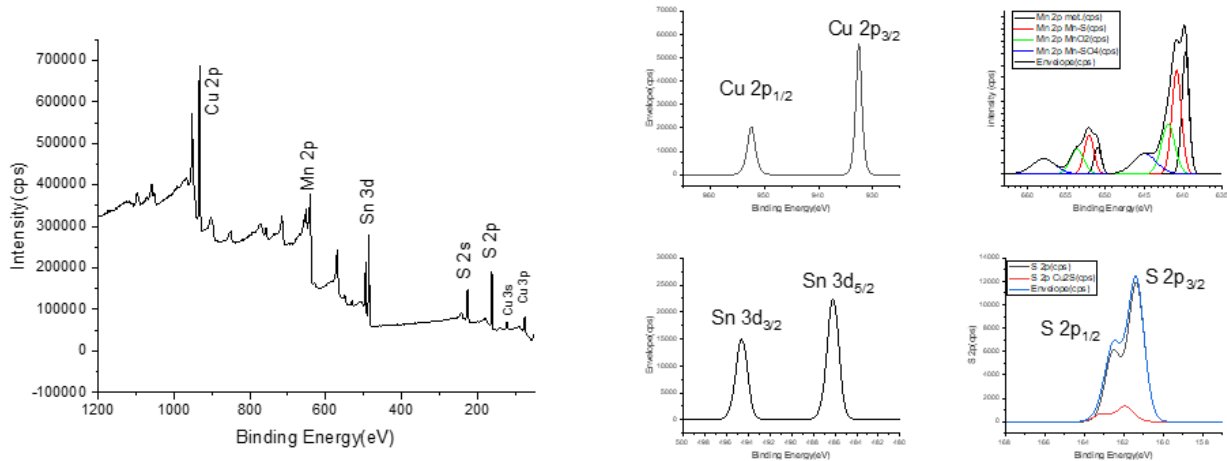


Figure 82: (Left) total XPS spectrum of CMTS sample #7 after a 120s plasma etch process, which conveys the peaks of every element contained in the TF; (right) regions of the spectra corresponding to the elements of interest for CMTS (Cu 2p, Mn 2p, Sn 3d and S 2p).

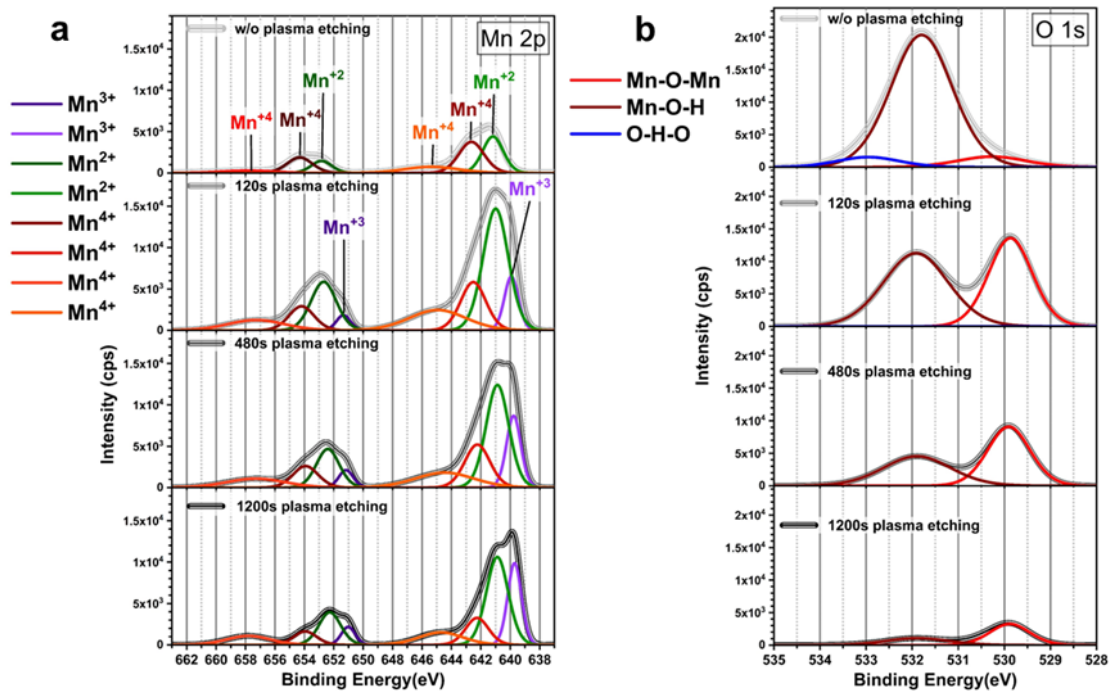


Figure 83: XPS spectra of Mn and O at different depths (defined by different durations of sputtering etching).

6.3.3. PV cell characterisation

Similar to our CZTS, CFTS and CMTS TF samples, we realised CMTS-based SC to test the application of this material as an absorber layer in TF SC applications. The manufacture of these devices followed the same procedure used for the other materials to obtain a final device with a SLG/Mo/CMTS/CdS/i-ZnO/AZO/Al grid. After the first test on the pristine samples, the application of the two PDT used for CZTS and CFTS were also tested.

6.3.3.1. PV device characterisation: J–V curves and EQE curves

Figure 84 reports a statistical study on the PV parameters of SC obtained with the second series' samples, the only ones that showed PV performance: It is represented by a box plot, which reports the median value (the line in the middle of the box), the mean value (the square marker inside the box) and the fifth (lower 'error' marker in the box), 25th (lower line of the box), 75th (higher line of the box) and 95th (higher 'error' marker) percentiles. The outliers are reported as full square markers. Figure 85 illustrates the effects of the PDT on the J–V curves and EQE curves of the final devices obtained from sample #8's replicas.

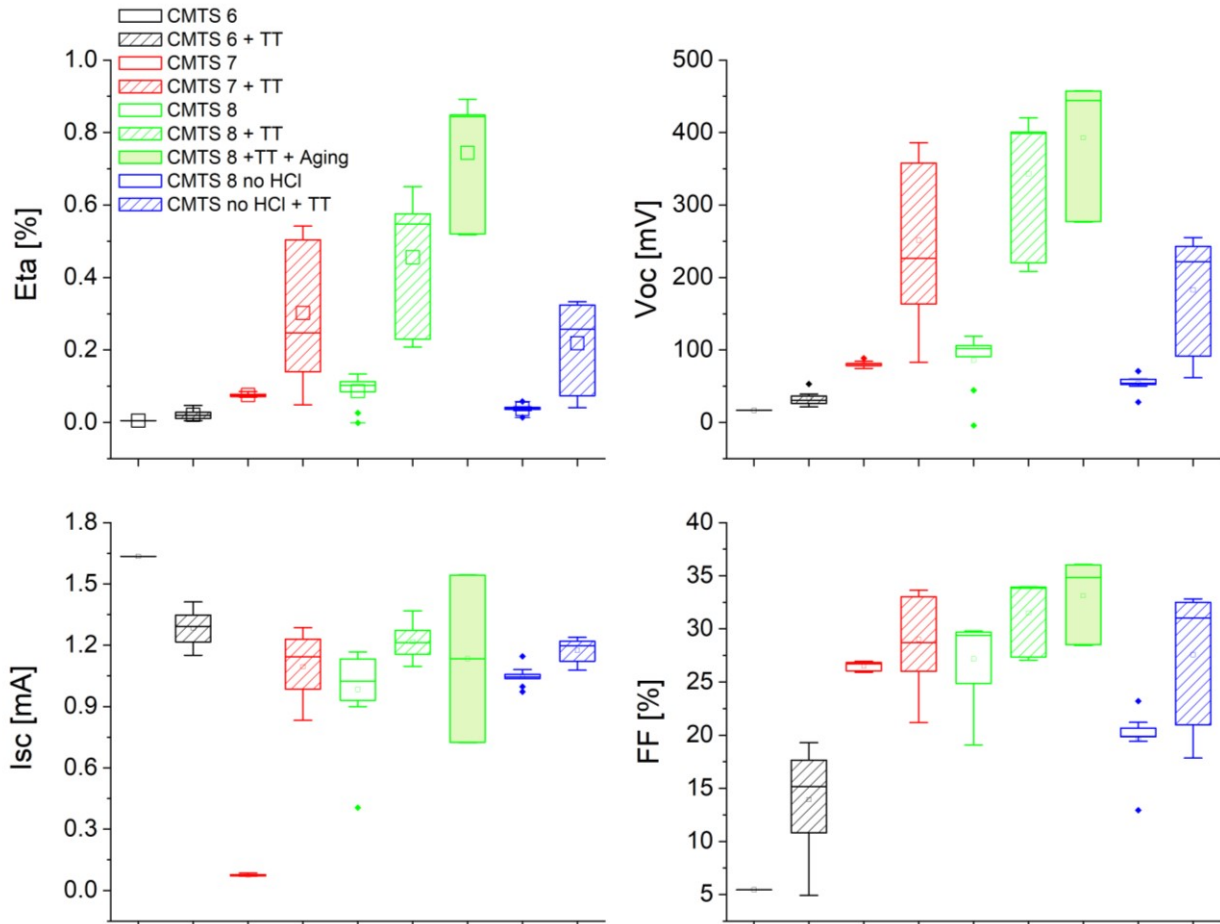


Figure 84: Statistical analysis of the main PV parameters of CMTS SC obtained from samples inside the second series of CMTS TF with the application of HCl treatment, with the data obtained on the same samples after the application of the thermal treatment described previously. The *box plots* demonstrate the median value (central line), the average value (square in the centre) and the following percentiles: 25th (lower line of the box), 75th (higher line in the box), 95th (vertical line above the box) and fifth (vertical line under the box). In addition, the two extreme values are marked with a \diamond . The parameters' distribution after the ageing effect and without the application of HCL treatment is also reported for Sample #8.

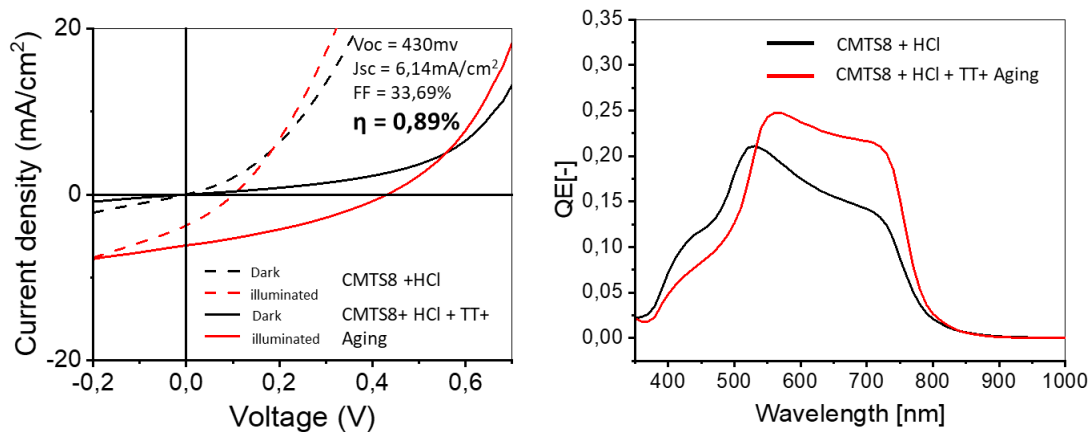


Figure 85: Comparison of the J–V curves (in dark and under 1SUN illumination) and the EQE curves of the record device of sample #8 before and after the application of the thermal treatment.

From the analysis of these data, we can affirm the following:

- We observed PV performances only in CMTS samples with precise compositional ratios, with **[Cu]/[Mn]+[Sn]≈0.9** and **[Mn]/[Sn] slightly higher than 1**. In every other case, with the presence of MnS or the excess presence of the thiospinel phase, no PV performance was observed.
- **The increase in the absorber layer thickness is associated with an increase in PV efficiencies**, mainly due to the increase of V_{oc} . No increase in J_{sc} demonstrates an effect on the charge carrier's photogeneration, usually connected to the increase in thickness, so the effect could be connected to an exceedingly low spatial charge region, which increases the charge separation.
- The EQE curves depict a **lower maximum value** ($\approx 25\%$) than the one for CZTS samples: It conveys the same feature observed for CZTS samples, with the high energy trend influenced by CdS adsorption and the lower energy slope that describes the CMTS E_g . **Eg evaluations derived from these measures show values similar to those derived from transmittance measures.**
- As for the CZTS samples and CMTS, the application of the two PDT presents an increase of PV performances altogether, unlike the CZTS case, where only the J_{sc} increased: As observed in morphological and XRD analysis, **the HCl treatment removes superficial secondary phases** and generally cleans the FRONT surface before CdS deposition. The effect of the thermal treatment seems quite complex, since no order–disorder transition seems to happen (confirmed by the two EQE measures, where the CMTS-related sharp edge does not change its inset, showing no difference in E_g values before and after the treatment). **A height increase in the absorber layer region is observed after treatment, which is usually** connected to decreased defect concentration in the absorber layer. More insights into this treatment effect will be discussed in the impedance section below.
- As for CZTS devices and CMTS-based SC, we observed a **positive ageing effect** for the record sample. This phenomenon's nature is still unclear in the literature, and more in-depth studies on this aspect are necessary to fully understand the limits of this class of materials as an absorber layer.

Accordingly, we now report a new record CMTS-based SC: The best device illustrates high PV parameters, with $\eta=0.89\%$, $V_{oc}=430\text{mV}$, $J_{sc}=6.14\text{mA/cm}^2$ and $FF=33.69\%$. These values validate the two-step production process tested before for CZTS and applied to a new material, achieving results similar to those of the research group [105, 121]. This result set a new milestone in CMTS SC applications. Even if it is not the highest result for this material, the 0.91% obtained by *Yu et al.* [108], we achieved a higher V_{oc} value (430mV vs. 310mV).

6.3.4. Defect mapping: Impedance measure and $V_{oc}(T)$

Similar to the CZTS TF samples, we performed preliminary impedance measures on specific CMTS samples. This kind of measure can be performed under different conditions, depending on the information desired. Two approaches were applied:

- RT measures: From these kinds of measures, we can understand which surface of the final device acts as a non-ohmic contact. By performing these measures at different bias voltages, we can build the so-called *loss maps* to understand the distribution of defects inside the device and their approximative activation energy (E_a). Finally, we used the Mott–Schottky approach to calculate the flat band potential (V_{FB}) and the concentration of acceptor states at the edge of the VB.
- Temperature-dependent measures: From these kinds of measures, we can build a different *loss map* to correlate the peak frequency of (dC/df) with the temperature and calculate the E_a from an Arrhenius plot.

6.3.4.1. RT measures: Loss maps vs. V

We used the impedance technique at RT to investigate the position of defect states in our devices: The variance of the capacitance versus bias voltage (V_{BIAS}) and frequency (f) represent the effect of nonlinearities in the device as resistances and defects [113]. Figure 86 reveals many loss maps obtained from various samples: (a) sample #4 without both PDTs, (b) sample #4 without HCl treatment but with thermal treatment and (d) the overall effect of both PDTs on sample #8. Figure 86-(c) demonstrates the *loss map* gleaned from the CIGS device studied by *Brammertz et al.* [113]. Figure 87 represents the Mott–Schottky elaborations calculated from the record device [114] to calculate the flat-band potential (V_{FB}) and the density of acceptor states (N_a).

From the loss maps in Figure 86, we can discuss the following:

- **The untreated sample depicts a busy loss map.** Several very high contributions are visible, making us believe that this sample conveys important nonlinearities, but this is only partially true: Figure 86-c illustrates a loss map of a CIGS device discussed by *Brammertz et al.* [113], presenting features at low frequencies that resemble the ones obtained on the untreated sample. In that work, these features are related to **high conduction throughout the p–n junction in the case of a low-performance device, a property** that our untreated samples also demonstrate. The other two contributions are quite similar to the ones observed before in CZTS samples, where defects with high activation energies are placed at the CMTS/CdS interface (vertical feature above 0V bias voltage) and a back contact barrier (horizontal feature at high frequency).

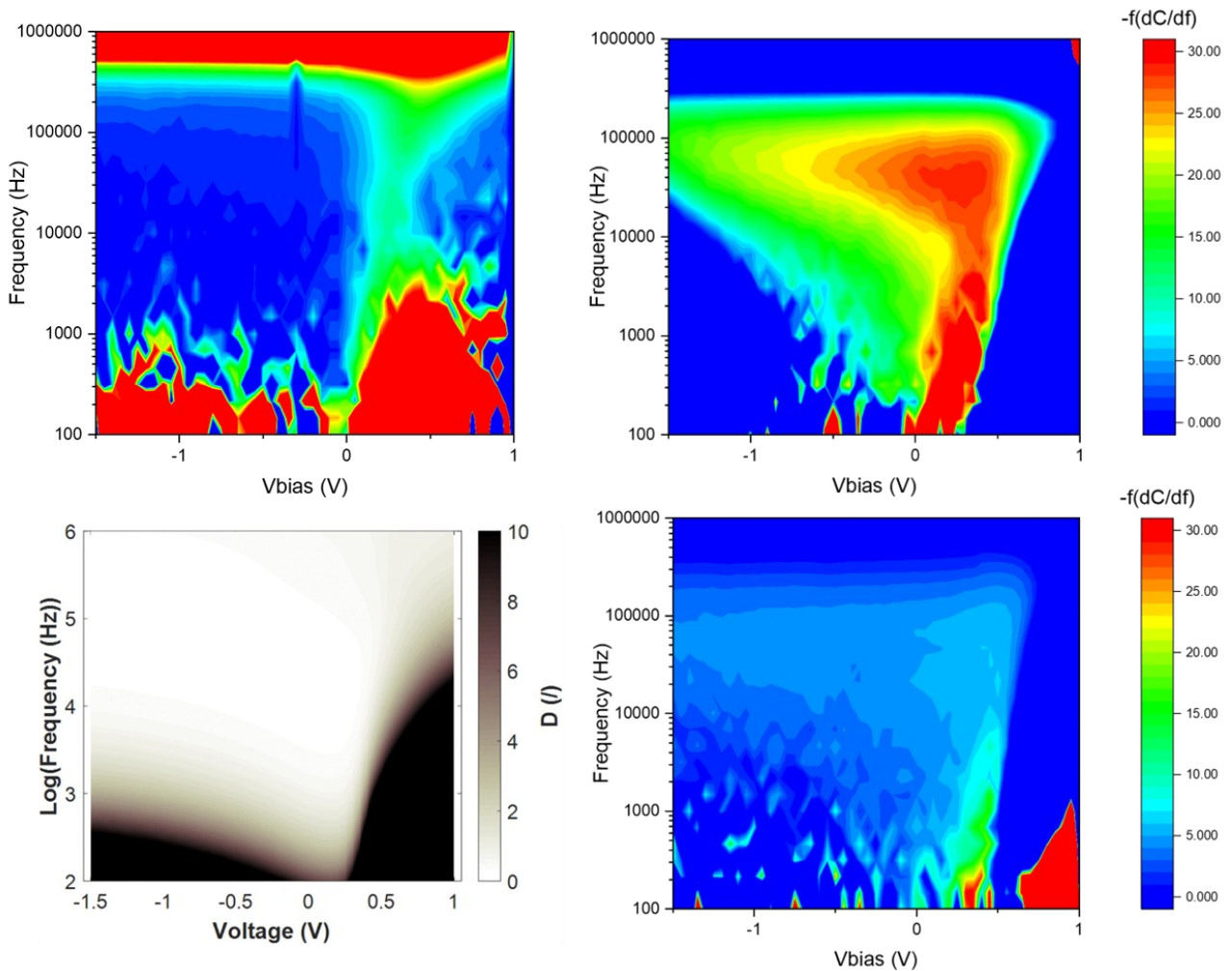


Figure 86: Loss maps of CMTS TF devices: (a) Loss map of a sample #4 device without HCl and thermal treatment; (b) Loss map of a sample #4 device without HCl but with thermal treatment; (c) Literature loss map, which displays features due to high conduction at low frequency, both at low and high bias voltage [113] and (d) Loss map of a sample #8 device with HCL and thermal treatment.

- The situation is clearer after the thermal treatment (differences between Figure 86-a and Figure 86-b): The contributions due to high conduction are reduced or removed, marking a better p–n junction. A large contribution appears in the centre of the loss map. From *Brammettz et al.*, this kind of feature can always be associated with a **bulk n-type defect**. This could be explained by the presence of a donor state related to the D1 PL band. Since the acceptor state is so low (V_{Cu}), the effect of the related donor state in the QDAP becomes stronger in the impedance measure. An interfacial defect between CMTS and CdS is still present, but its attribution is less clear.
- The application of HCl treatment (Figure 86-d) further cleans the loss map, reducing **every contribution visible**. The contributions due to CMTS/CdS interface defects and CMTS bulk defects remain but with a lower magnitude, similar to the CZTS case, where HCl treatment increases the quality of the material's surface.

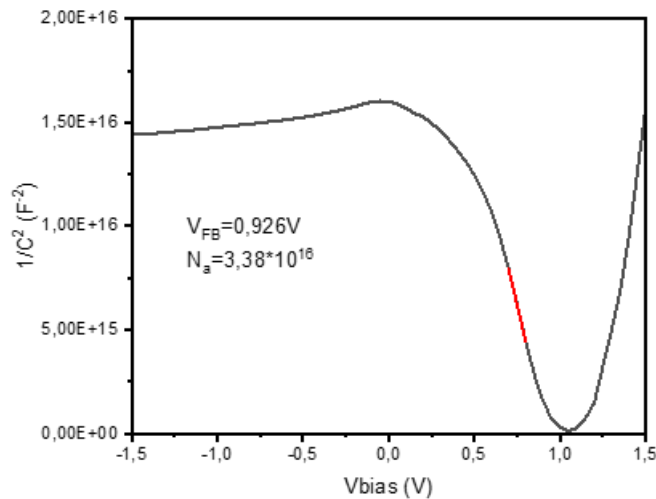


Figure 87: Mott–Schottky elaboration of the data obtained from the record CZTS SC and raw impedance data. The V_{FB} and N_a values are 0.926V and $3.38 \times 10^{16} \text{cm}^{-3}$.

From Figure 56, we can extract the following conclusions:

- The negative slope in the step region confirms the p-type behaviour of the CMTS semiconductor [115].
- The value of $V_{FB} = 0.926$ is higher than that obtained for CZTS ($V_{FB}=0.619\text{V}$): This value represents the maximum V_{OC} obtainable from the p–n junction, so the limit for this material is higher than that of CZTS.
- The value of $N_a=3.38 \times 10^{16} \text{cm}^{-3}$ for the CMTS obtained is in line with the acceptor density of high-performance CZTS SC, and it is the typical defect density of a doped semiconductor suitable for SC application.

6.3.4.2. Low-temperature measures: Loss maps vs. T and $V_{OC}(T)$

A very similar work to that made for the loss maps V vs. f can be made with a loss map f vs. T to investigate defects with lower activation energy (from 0.2V below). To do this, temperature-dependent impedance measures were performed on our CZTS record device using the same formulae employed in the previous section. Figure 88 reveals the loss map vs. T of the record CMTS-based device, together with the Arrhenius plot obtained from the loss map for the evaluation of the E_a of this defect.

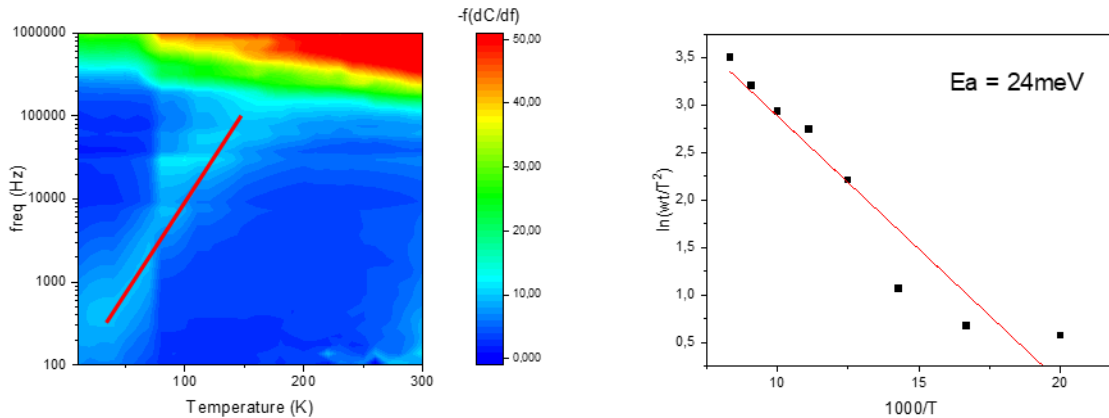


Figure 88: On the left, experimental loss map of record CMTS SC, where red marks the movement of the $-f(dC/df)$ function maximum vs. f and T , which is useful for calculating the Arrhenius plot of this defect. On the right, an Arrhenius plot of the defect is spotted on the loss map, which shows an E_a value of 24meV.

From this study, we can conclude the following:

- In our analysis, only **one peak is visible** on the loss map, which starts to appear at $T \approx 150\text{K}$ and drops in frequency to 10K. Another contribution could be present at a higher temperature (the red region of the loss map), but the very low variation in the position of this contribution and its appearance at such a high temperature make correct detection difficult.
- From the Arrhenius plot obtained from the loss map, we can extract an **E_a value of 24meV**: Even if lower than the value obtained from PL, this value is compatible with the presence of the V_{Cu} defect already spotted in the PL study. This also confirms the absence of the Cu_{Zn} defect usually present at $\approx 150\text{meV}$, demonstrating the absence of an order–disorder transition in this material (as intended for CZTS).

To complete the low-temperature characterisation, together with the temperature-dependent impedance measures, temperature-dependent I–V curves were also measured. This measure should provide information about energy losses due to temperature and insight into the behaviour of defects inside the CMTS layer. In Figure 89, the V_{OC} vs. T trend is shown with the interpolated value of $V_{OC}(0\text{K})$ and the slope of the linear fit. From this, we can confirm the assumptions made in previous sections:

- The value of V_{OC} at 0K describes the main recombination of photogenerated carrier pairs. The value reported is lower than the E_g calculated by transmittance measures. This means that the main recombination path in our device is **through an interface** [117]; this $V_{OC}(0\text{K})$ value corresponds with an E_g measure attained from PL measures, confirming the low-temperature recombination through defects (QDAP [118]).
- All these measures confirm the model constructed from the PL measures, with V_{Cu} as the main acceptor defect, coupled with a donor defect placed at 245meV below the CB.
- The slope in the case of CMTS SC is higher than that garnered for CZTS. This value strongly depends on the ideality factor n and the ratio I_{00}/I_L (with I_{00} being the reverse saturation current prefactor and I_L the photocurrent) [119], so the higher slope value is related to a higher n value, since the J–V curve of the device poorly follows the p–n junction law.

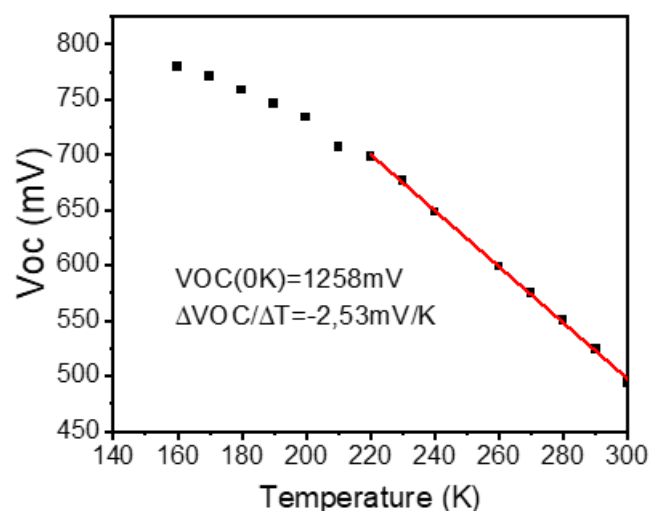


Figure 89: V_{oc} vs. T measure with the V_{oc} value at 0K obtained by interpolation.

6.3.5. Conclusion

We obtained CMTS TF samples, starting from the knowledge we developed in previous work about CZTS and CZTS TF samples and SC. We decided to follow the same approach we used for the CFTS work, testing a wider compositional range than that used for CZTS, since very little information about the correlation between the composition of the material and the insurgence of secondary phases is present in the literature. After preliminary experiments, we worked on three sets of samples that arrived at the following different objectives: a first set of samples with wide compositional variance, to study the correlation between composition and secondary phase formation; a second set of samples to investigate the effect of the absorber layer's thickness to test the uniformity of the material and the light collection properties; and a third set of samples where we studied the application of different metal deposition geometries, where we tested the co-sputtering approach. These samples were fully characterised using every technique already utilised for CZTS and CFTS, with the addition of new tools. We used SEM-EDX, XRD and Raman analysis to monitor the morphology and composition of the TF, correlating compositional ratios to the formation of secondary phases as thiospinel-, MnS- and Sn-rich phases. The influence of these phases on the final behaviour of the TF is not clear, but MnS is an insulating phase that should be avoided inside the film. Band gap measures were performed using UV-Vis measures: Most of the obtained CMTS TF illustrate a band gap around 1.6eV with the lower value of 1.44eV obtained on co-sputtered samples containing Sn phases. Quite high purity was realised with samples actualised using a composition near the CZTS values ($[Cu]/[Mn]+[Sn] \approx 0.9$, $[Mn]/[Sn] = 1.05$ and $[Cu]/[Sn] = 1.9$), with a phase purity up to 95% of the content of the pure CMTS phase. As for CFTS, we used XPS to monitor the oxidation state of the elements contained in the TF: While all the other elements depict an oxidation state equal to the nominal one (Cu^{1+} , Sn^{+4} , S^{-2}), the peaks observed in the Mn region convey the copresence of Mn^{2+} and Mn^{4+} , when there should only be Mn^{2+} . The low-temperature PL measures showed peaks at a lower value than the E_g obtained from the transmittance measures. The presence of QDAPs limits the effective E_g of the material, as observed for CZTS.

With all these TF samples, CMTS-based SC were obtained. Unlike CZTS devices, only high-purity CMTS devices represented PV performance – and only after the application of the thermal PDT studied for CZTS

devices. The PV efficiency increased with the absorber layer's thickness, with the V_{OC} that drove this increase. From EQE measures, we can say that thermal treatment decreases the defect concentration in the bulk of the material, as confirmed by the room-temperature loss maps from impedance measures. The temperature-dependent impedance and V_{OC} measures confirm what we discovered from PL measures on the bare material, with the presence of V_{Cu} as the main acceptor defect together with a deep donor defect to form the QDAP. No effect of the order–disorder transition is visible in this material, since no E_g or Raman spectra modification has been observed after the thermal treatment and no Cu_{Zn} -like defects (e.g. Cu_{Mn}) have been detected by PL and impedance measures. A record efficiency of $\eta=0.89\%$ was obtained with $V_{OC}=430mV$, $JSC=6.14mA/cm^2$ and $FF=33.69\%$. These values validate the two-step production process tested before for CZTS and applied to a new material, with results similar to those derived previously from the research group [105, 121]. This result sets a new milestone in CMTS SC development, and even if it is not the highest result obtained for this material, the 0.91% obtained by *Yu et al.* [108], we attained a higher V_{OC} value (430mV vs. 310mV).

7. CONCLUSION

The focus of this PhD thesis was the validation of a high-throughput production process for innovative chalcogenide TF-based SC technology. The synthesis made by a separated metal deposition (by magnetron sputtering) and sulphurisation (in an oven with elemental sulphur) returns chalcogenide TF with good compositional and thickness homogeneity on large, laboratory-scale samples (3.5x7.0cm²).

The work made on CZTS gave good results that are compatible with the literature: The optimisation of the chemical composition in the two series of samples permits us to limit the formation of secondary phases both quantitatively and spatially, presenting little ZnS formation on the FRONT surface of the material. Having arrived at the best stoichiometry for PV applications, the prototypal SC made with these TF resulted in PV performances in line with the literature, with a low deviation from $\eta \approx 3.5\%$. The application of two PDTs (thermal and chemical) further increases the PV performances of these devices (with a record device with $\eta = 4.5\%$, $J_{SC} = 15.1 \text{ mA/cm}^2$, $V_{OC} = 561 \text{ mV}$ and $FF = 54\%$). Studies of defects reveal the presence of the anti-site defect couple $\text{Cu}_{\text{Zn}} + \text{Zn}_{\text{Cu}}$, the distinctive mark of the order–disorder transition typical of this material and the main limit of the performances of CZTS-based SCs.

The work on CFTS started with CZTS information taken in previous work, but its nature was more explorative. A wide range of compositions were studied to investigate the appearance of secondary phases. Three compounds were observed in stoichiometric conditions: rhodostannite in Sn-rich samples, chalcopyrite in Fe-rich samples and $\text{Fe}_{0.87}\text{S}$ in intermediate conditions. The usage of a ‘constant current’ setting for the sputtering deposition gave back higher compositional homogeneity, demonstrating the strict correlation between deposition rates and currents. No effect of the order–disorder transition was observed, confirming the absence of this phenomenon for the stannite structure. No PV efficiencies have been observed on CFTS-based SC. The presence of both Fe^{2+} and Fe^{3+} inside the material, spotted with XPS, could be the main reason for this behaviour due to the contact between the metal stack and the atmosphere (especially O) before the sulphurisation process.

To overcome this problem, CFTS-based MG samples were synthesised: The powders obtained displayed different correlations between the initial element content and final powder composition, with the main phase of stoichiometric CFTS and different rhodostannite content depending on the initial powder composition. These first explorative tests depicted the potentiality of MGL technology application to attain O-free CFTS, but more tests should be performed to obtain the CFTS purity suitable for MGL-based SC with this material.

The work on CMTS also started with CZTS information, and it was an explorative study similar to that obtained for CFTS. Different secondary phases have been observed in different stoichiometric conditions: thiospinel in Mn-rich conditions and MnS in Mn-poor conditions. The application of the PDTs studied in the CZTS work was needed to obtain PV performance. Chemical PDT was needed to remove the MnS formations on the front surface, while thermal PDT improved the p–n junction quality, reducing the presence of detrimental point defects in the bulk of the material. PL and impedance measures showed a higher effective E_g than CZTS, depicting that the main p-type dopant of this material is V_{Cu} point defects. The absence of anti-site couples and a higher V_{OC} at 0K than CZTS demonstrate the high potential of CMTS for PV technologies, but the limited ideality of the final SC strongly limits the performances of these

prototypical devices, leading to a record device with $\eta=0.89\%$, $V_{oc}=430\text{mV}$, $J_{SC}=6.14\text{mA}/\text{cm}^2$ and $FF=33.69\%$.

8. PUBLICATIONS

- Trifiletti V., Frioni L., Tseberlidis G., Vitiello E., Danilson M., Grossberg M., Acciarri M., Binetti S., Marchionna S., Investigation of defect states in $\text{Cu}_2\text{MnSnS}_4$: an Earth-abundant Chalcogenide for Photovoltaic applications, *Solar Energy Materials and Solar Cells* (under revision)
- Tseberlidis G., Di Palma V., Trifiletti V., Frioni L., Valentini M., Malerba C., Mittiga A., Acciarri M., Binetti S., Titania as Buffer Layer for Cd-Free Kesterite Solar Cells, *ACS Materials Lett.* 2023, 5, 219–224
- Tseberlidis G., Trifiletti V., Vitiello E., Husien A. H., Frioni L., Da Lisca M., Alvarez J., Acciarri M., Binetti S., Band-Gap Tuning Induced by Germanium Introduction in Solution-Processed Kesterite Thin Films, *ACS Omega* 2022, 7, 23445–23456
- Tseberlidis G., Husien A. H., Riva S., Frioni L., Le Donne A., Acciarri M., Binetti S., Semi-transparent $\text{Cu}_2\text{ZnSnS}_4$ solar cells by drop-casting of sol-gel ink, *Solar Energy* 224 (2021) 134–141
- Tseberlidis G., Trifiletti, V., Le Donne A., Frioni L., Acciarri M., Binetti S., Kesterite solar-cells by drop-casting of inorganic sol-gel inks, *Solar Energy* 208 (2020) 532–538

9. REFERENCES

1. IEA. Available from: <https://www.iea.org/reports/electricity-information-overview/electricity-consumption>.
2. National Renewable Energy Laboratories (NREL), *Best Research-Cell Efficiency Chart*. 2022.
3. Nakamura, M., et al., *Cd-Free Cu(In,Ga)(Se,S)₂ Thin-Film Solar Cell With Record Efficiency of 23.35%*. IEEE Journal of Photovoltaics, 2019. **9**(6): p. 1863-1867.
4. European Commission, *Critical Raw Materials Resilience: Charting a Path towards greater Security and Sustainability*. 2020.
5. Wang, W., et al., *Device Characteristics of CZTSSe Thin-Film Solar Cells with 12.6% Efficiency*. Advanced Energy Materials, 2014. **4**(7): p. 1301465.
6. WebElements, <https://www.webelements.com>.
7. United States Geological Survey, N.M.I.C., *Commodity Statistics and Information*. 2022.
8. Hwang, S.K., et al., *Electrochemically Deposited CZTSSe Thin Films for Monolithic Perovskite Tandem Solar Cells with Efficiencies Over 17%*. ENERGY & ENVIRONMENTAL MATERIALS, 2022. **n/a**(n/a): p. e12489.
9. Chen, S., et al., *Intrinsic point defects and complexes in the quaternary kesterite semiconductor Cu₂ZnSnS₄*. Physical Review B, 2010. **81**(24): p. 245204.
10. Scragg, J.J.S., et al., *A low-temperature order-disorder transition in Cu₂ZnSnS₄ thin films*. Applied Physics Letters, 2014. **104**(4): p. 041911.
11. Scragg, J.J.S., et al., *Cu–Zn disorder and band gap fluctuations in Cu₂ZnSn(S,Se)₄: Theoretical and experimental investigations*. physica status solidi (b), 2016. **253**(2): p. 247-254.
12. Ford, G.M., et al., *Earth Abundant Element Cu₂Zn(Sn_{1-x}Ge_x)S₄ Nanocrystals for Tunable Band Gap Solar Cells: 6.8% Efficient Device Fabrication*. Chemistry of Materials, 2011. **23**(10): p. 2626-2629.
13. Siebentritt, S. and S. Schorr, *Kesterites - a challenging material for solar cells*. Progress in Photovoltaics: Research and Applications, 2012. **20**(5): p. 512-519.
14. Shockley, W. and H.J. Queisser, *Detailed Balance Limit of Efficiency of p-n Junction Solar Cells*. Journal of Applied Physics, 1961. **32**(3): p. 510-519.
15. Katagiri, H., et al., *Preparation and evaluation of Cu₂ZnSnS₄ thin films by sulfurization of E · B evaporated precursors*. Solar Energy Materials and Solar Cells, 1997. **49**(1): p. 407-414.
16. Mitzi, D.B., et al., *The path towards a high-performance solution-processed kesterite solar cell*. Solar Energy Materials and Solar Cells, 2011. **95**(6): p. 1421-1436.
17. Chen, S., et al., *Crystal and electronic band structure of Cu₂ZnSnX₄ (X=S and Se) photovoltaic absorbers: First-principles insights*. Applied Physics Letters, 2009. **94**(4): p. 041903.
18. Paier, J., et al., *Cu₂ZnSnS₄ as a potential photovoltaic material: A hybrid Hartree-Fock density functional theory study*. Physical Review B, 2009. **79**(11): p. 115126.
19. Persson, C., *Electronic and optical properties of Cu₂ZnSnS₄ and Cu₂ZnSnSe₄*. Journal of Applied Physics, 2010. **107**(5): p. 053710.
20. Botti, S., D. Kammerlander, and M.A.L. Marques, *Band structures of Cu₂ZnSnS₄ and Cu₂ZnSnSe₄ from many-body methods*. Applied Physics Letters, 2011. **98**(24): p. 241915.
21. Krustok, J., et al., *Photoluminescence study of deep donor- deep acceptor pairs in Cu₂ZnSnS₄*. Materials Science in Semiconductor Processing, 2018. **80**: p. 52-55.
22. Jiang, M. and X. Yan, *Cu₂ZnSnS₄ thin film solar cells: present status and future prospects*. Solar Cells—Research and Application Perspectives, 2013.
23. Gunawan, O., T. Gokmen, and D.B. Mitzi, *Suns-V_{OC} characteristics of high performance kesterite solar cells*. Journal of Applied Physics, 2014. **116**(8): p. 084504.
24. Luque, A. and S. Hegedus, *Handbook of photovoltaic science and engineering*. 2011: John Wiley & Sons.
25. Walsh, A., et al., *Kesterite Thin-Film Solar Cells: Advances in Materials Modelling of Cu₂ZnSnS₄*. Advanced Energy Materials, 2012. **2**(4): p. 400-409.

26. Olekseyuk, I.D., I.V. Dudchak, and L.V. Piskach, *Phase equilibria in the Cu₂S–ZnS–SnS₂ system*. Journal of Alloys and Compounds, 2004. **368**(1): p. 135-143.
27. Redinger, A., et al., *The Consequences of Kesterite Equilibria for Efficient Solar Cells*. Journal of the American Chemical Society, 2011. **133**(10): p. 3320-3323.
28. Huang, T.J., et al., *CZTS-based materials and interfaces and their effects on the performance of thin film solar cells*. physica status solidi (RRL) – Rapid Research Letters, 2014. **08**(09): p. 735-762.
29. Fairbrother, A., et al., *On the formation mechanisms of Zn-rich Cu₂ZnSnS₄ films prepared by sulfurization of metallic stacks*. Solar Energy Materials and Solar Cells, 2013. **112**: p. 97-105.
30. Khare, A., et al., *Calculation of the lattice dynamics and Raman spectra of copper zinc tin chalcogenides and comparison to experiments*. Journal of Applied Physics, 2012. **111**(8): p. 083707.
31. Katagiri, H., et al., *The Influence of the Composition Ratio on CZTS-based Thin Film Solar Cells*. MRS Proceedings, 2011. **1165**: p. 1165-M04-01.
32. Sugimoto, H., et al. *Lifetime Improvement for High Efficiency Cu₂ZnSnS₄ Submodules*. in *IEEE Photovoltaic Specialists Conference 2013*. Tampa (FL) USA.
33. Ito, K., *Copper Zinc Tin Sulfide-Based Thin-Film Solar Cells*. 2014.
34. Gokmen, T., et al., *Band tailing and efficiency limitation in kesterite solar cells*. Applied Physics Letters, 2013. **103**(10): p. 103506.
35. Yan, C., et al., *Beyond 11% Efficient Sulfide Kesterite Cu₂Zn_xCd_{1-x}SnS₄ Solar Cell: Effects of Cadmium Alloying*. ACS Energy Lett., 2017. **2**(4): p. 930-936.
36. Shin, D., et al., *Earth-Abundant Chalcogenide Photovoltaic Devices with over 5% Efficiency Based on a Cu₂BaSn(S,Se)₄ Absorber*. Advanced Materials, 2017. **29**(24): p. 1521-4095.
37. Mitzi, D.B., et al., *Prospects and performance limitations for Cu-Zn-Sn-S-Se photovoltaic technology*. Philos Trans A Math Phys Eng Sci, 2013. **371**(1996): p. 20110432.
38. Jackson, P., et al., *Effects of heavy alkali elements in Cu(In,Ga)Se₂ solar cells with efficiencies up to 22.6%*. Phys. Status Solidi RRL 2016. **10**: p. 583–586
39. Ratz, T., et al., *Physical routes for the synthesis of kesterite*. Journal of Physics-Energy, 2019. **1**(4): p. 042003.
40. Yan, C., et al., *Cu₂ZnSnS₄ solar cells with over 10% power conversion efficiency enabled by heterojunction heat treatment*. Nat Energy, 2018. **3**: p. 764–772.
41. S.Marchionna, et al., *Cu₂ZnSnS₄ solar cells grown by sulphurisation of sputtered metal precursors*. Thin Solid Films, 2013. **542**: p. 114-118.
42. Li, W., et al., *The effect of ZnS segregation on Zn-rich CZTS thin film solar cells*. Journal of Alloys and Compounds, 2015. **632**: p. 178-184.
43. Araki, H., et al., *Preparation of Cu₂ZnSnS₄ thin films by sulfurization of stacked metallic layers*. Thin Solid Films, 2008. **517**(4): p. 1457-1460.
44. Stolt, W.N.S.a.L., *Handbook of Photovoltaic Science and Engineering*. 2003: John Wiley & Sons, Ltd (Edited by A. Luque and S. Hegedus).
45. Platzer-Bjorkman, C., et al., *Back and front contacts in kesterite solar cells: state-of-the-art and open questions*. Journal of Physics-Energy, 2019. **1**(4): p. 044005.
46. Kessler, F. and D. Rudmann, *Technological aspects of flexible CIGS solar cells and modules*. Solar Energy, 2004. **77**(6): p. 685-695.
47. Scragg, J.J., et al., *Effects of Back Contact Instability on Cu₂ZnSnS₄ Devices and Processes*. Chemistry of Materials, 2013. **25**(15): p. 3162-3171.
48. Chopra, K.L., P.D. Paulson, and V. Dutta, *Thin-film solar cells: an overview*. Progress in Photovoltaics: Research and Applications, 2004. **12**(2-3): p. 69-92.
49. Minemoto, T., et al., *Theoretical analysis of the effect of conduction band offset of window/CIS layers on performance of CIS solar cells using device simulation*. Solar Energy Materials and Solar Cells, 2001. **67**(1): p. 83-88.
50. Haight, R., et al., *Band alignment at the Cu₂ZnSn(S_xSe_{1-x})₄/CdS interface*. Appl. Phys. Lett. **98**, (2011), 2011. **98**: p. 253502.
51. Li, J., et al., *The band offset at CdS/Cu₂ZnSnS₄ heterojunction interface*. Mater. Lett., 2012. **8**: p. 365–367.

52. Bar, M., et al., *Cliff-like conduction band offset and KCN-induced recombination barrier enhancement at the CdS/Cu₂ZnSnS₄ thin-film solar cell heterojunction*. Applied Physics Letters, 2011. **99**(22): p. 222105
53. Santoni, A., et al., *Valence band offset at the CdS/Cu₂ZnSnS₄ interface probed by x-ray photoelectron spectroscopy*. Journal of Physics D-Applied Physics, 2013. **46**(17): p. 175101.
54. Yan, C., et al., *Band alignments of different buffer layers (CdS, Zn(O,S), and In₂S₃) on Cu₂ZnSnS₄*. Applied Physics Letters, 2014. **104**(17): p. 173901.
55. Boistelle, R. and J.P. Astier, *Crystallization mechanisms in solution*. Journal of Crystal Growth, 1988. **90**(1): p. 14-30.
56. E. Mellikov*, J.H.a.M.A., *Powder materials and technologies for solar cells*. International Journal of Materials and Product Technology, 2007. **28**(3-4): p. 291-311.
57. Timmo, K., et al., *CuInSe₂ monograin growth in the liquid phase of potassium iodide*. Thin Solid Films, 2007. **515**(15): p. 5884-5886.
58. Altosaar, M., et al. *Cu₂ZnSnSe₄ Monograin Powders for Solar Cell Application*. in *2006 IEEE 4th World Conference on Photovoltaic Energy Conference*. 2006.
59. Altosaar, M., et al., *Cu₂Zn_{1-x}Cd_xSn(Se_{1-y}S_y)₄ solid solutions as absorber materials for solar cells*. physica status solidi (a), 2008. **205**(1): p. 167-170.
60. Leinemann, I., et al. *Comparison of copper zinc tin selenide formation in molten potassium iodide and sodium iodide as flux materials*. in *Conference of Young Scientists on Energy Issues Kaunas (CD pub)*. 2011.
61. Nkwusi, G., et al. *Formation of copper zinc tin sulfide in cadmium iodide for monograin membrane solar cells*. in *Conf. of Young Scientists on Energy Issues, Kaunas*. 2012.
62. Mellikov, E., et al., *Growth of CZTS-Based Monograins and Their Application to Membrane Solar Cells*, in *Copper Zinc Tin Sulfide-Based Thin-Film Solar Cells*. 2014. p. 289-309.
63. Muska, K., et al., *Synthesis of Cu₂ZnSnS₄ monograin powders with different compositions*. Energy Procedia, 2011. **10**: p. 203-207.
64. Timmo, K., et al. *Chemical etching of Cu₂ZnSn(S,Se)₄ monograin powder*. in *2010 35th IEEE Photovoltaic Specialists Conference*. 2010.
65. Kauk, M., et al., *Effects of sulphur and tin disulphide vapour treatments of Cu₂ZnSnS(Se)₄ absorber materials for monograin solar cells*. Energy Procedia, 2011. **10**: p. 197-202.
66. Di Benedetto, F., et al., *⁵⁷Fe- and ¹¹⁹Sn- Mössbauer study on stannite (Cu₂FeSnS₄)-kesterite (Cu₂ZnSnS₄) solid solution*. Physics and Chemistry of Minerals, 2005. **31**(10): p. 683-690.
67. Evstigneeva, T.L. and Y.K. Kabalov, *Crystal structure of the cubic modification of Cu₂FeSnS₄*. Crystallography Reports, 2001. **46**(3): p. 368-372.
68. OHTSUKI, T., *Synthetic minerals with quaternary components in the system Cu-Fe-Sn-S-synthetic sulfide minerals (X)*. 1980.
69. Bonazzi, P., et al., *A model for the mechanism of incorporation of Cu, Fe and Zn in the stannite – kesterite series, Cu₂FeSnS₄ – Cu₂ZnSnS₄*. The Canadian Mineralogist, 2003. **41**(3): p. 639-647.
70. Cabri, L.J., *New data on Phase Relations in the Cu-Fe-S System*. Economic Geology, 1973. **68**(4): p. 443-454.
71. Meng, X., et al., *Synthesis, structure, optics and electrical properties of Cu₂FeSnS₄ thin film by sputtering metallic precursor combined with rapid thermal annealing sulfurization process*. Materials Letters, 2015. **151**: p. 61-63.
72. Meng, X., et al., *Sulfurization temperature dependence of the structural transition in Cu₂FeSnS₄-based thin films*. Materials Letters, 2015. **161**: p. 427-430.
73. Meng, X., et al., *Investigate the growth mechanism of Cu₂FeSnS₄ thin films by sulfurization of metallic precursor*. Materials Letters, 2017. **186**: p. 138-141.
74. Chatterjee, S. and A.J. Pal, *A solution approach to p-type Cu₂FeSnS₄ thin-films and pn-junction solar cells: Role of electron selective materials on their performance*. Solar Energy Materials and Solar Cells, 2017. **160**: p. 233-240.
75. Podsiadlo, S., et al., *Synthesis of magnetic doped kesterite single crystals*. Crystal Research and Technology, 2015. **50**(9-10): p. 690-694.

76. Fontané, X., et al., *Vibrational properties of stannite and kesterite type compounds: Raman scattering analysis of $Cu_2(Fe,Zn)SnS_4$* . Journal of Alloys and Compounds, 2012. **539**: p. 190-194.
77. Tobbens, D.M., et al., *Cation distribution in $Cu_2ZnSnSe_4$, Cu_2FeSnS_4 and $Cu_2ZnSiSe_4$ by multiple-edge anomalous diffraction*. Acta Crystallographica Section B, 2020. **76**(6): p. 1027-1035.
78. Guan, H., et al., *Structural and optical properties of Cu_2FeSnS_4 thin film synthesized via a simple chemical method*. Materials Science in Semiconductor Processing, 2014. **25**: p. 159-162.
79. Ghosh, A., et al., *Photo-electrochemical properties and electronic band structure of kesterite copper chalcogenide $Cu_2-II-Sn-S_4$ ($II = Fe, Co, Ni$) thin films*. RSC Advances, 2016. **6**(98): p. 96025-96034.
80. Vanalakar, S.A., P.S. Patil, and J.H. Kim, *Recent advances in synthesis of Cu_2FeSnS_4 materials for solar cell applications: A review*. Solar Energy Materials and Solar Cells, 2018. **182**: p. 204-219.
81. Lennie, A.R. and D.J. Vaughan, *Spectroscopic studies of iron sulfide formation and phase relations at low temperatures*. Vol. 5. 1996: The Geochemical Society Houston, TX.
82. Descostes, M., et al., *Use of XPS in the determination of chemical environment and oxidation state of iron and sulfur samples: constitution of a data basis in binding energies for Fe and S reference compounds and applications to the evidence of surface species of an oxidized pyrite in a carbonate medium*. Applied Surface Science, 2000. **165**(4): p. 288-302.
83. Trifiletti, V., et al., *Growth and Characterization of $Cu_2Zn_{1-x}Fe_xSnS_4$ Thin Films for Photovoltaic Applications*. Materials, 2020. **13**(6): p. 1471.
84. Madhusudanan, S.P., et al., *Photoactive Cu_2FeSnS_4 thin films: Influence of stabilizers*. Applied Surface Science, 2021. **535**: p. 147600.
85. Zhou, J., et al., *Preparation and characterization of Cu_2FeSnS_4 thin films for solar cells via a co-electrodeposition method*. Current Applied Physics, 2019. **19**(2): p. 67-71.
86. Orletskiy, I., et al., *Optical properties and kinetic parameters in Cu_2FeSnS_4 thin films prepared by spray pyrolysis*. Fourteenth International Conference on Correlation Optics. Vol. 11369. 2020: SPIE.
87. Mokurala, K. and S. Mallick, *Effect of annealing atmosphere on quaternary chalcogenide-based counter electrodes in dye-sensitized solar cell performance: synthesis of Cu_2FeSnS_4 and Cu_2CdSnS_4 nanoparticles by thermal decomposition process*. RSC Advances, 2017. **7**(25): p. 15139-15148.
88. Prabhakar, R.R., et al., *Facile Water-based Spray Pyrolysis of Earth-Abundant Cu_2FeSnS_4 Thin Films as an Efficient Counter Electrode in Dye-Sensitized Solar Cells*. ACS Applied Materials & Interfaces, 2014. **6**(20): p. 17661-17667.
89. Gonce, M.K., et al., *Dye-Sensitized Cu_2XSnS_4 ($X=Zn, Ni, Fe, Co, \text{ and } Mn$) Nanofibers for Efficient Photocatalytic Hydrogen Evolution*. ChemSusChem, 2016. **9**(6): p. 600-605.
90. Li, X., et al., *Efficient Optimization of the Performance of Mn^{2+} -Doped Kesterite Solar Cell: Machine Learning Aided Synthesis of High Efficient $Cu_2(Mn,Zn)Sn(S,Se)_4$ Solar Cells*. Solar RRL, 2018. **2**(12): p. 1800198.
91. Thompson, M.J., et al., *Cu_2ZnSnS_4 Nanorods Doped with Tetrahedral, High Spin Transition Metal Ions: Mn^{2+} , Co^{2+} , and Ni^{2+}* . Chemistry of Materials, 2016. **28**(6): p. 1668-1677.
92. Fries, T., et al., *Magnetic ordering of the antiferromagnet Cu_2MnSnS_4 from magnetization and neutron-scattering measurements*. Physical Review B, 1997. **56**: p. 5424-5431.
93. Prabhakar, R.R., et al., *Photovoltaic effect in earth abundant solution processed Cu_2MnSnS_4 and $Cu_2MnSn(S,Se)_4$ thin films*. Solar Energy Materials and Solar Cells, 2016. **157**: p. 867-873.
94. Chen, L.L., et al., *Structural and Optical Properties of Cu_2MnSnS_4 Thin Film Fabricated by Sol-Gel Technique*. 2015. p. 39-39-43.
95. López-Vergara, F., et al., *$Cu_2Mn_{1-x}Co_xSnS_4$: Novel kesterite type solid solutions*. Journal of Solid State Chemistry, 2013. **198**: p. 386-391.
96. Rudisch, K., et al., *Structural and Electronic Properties of Cu_2MnSnS_4 from Experiment and First-Principles Calculations*. physica status solidi (b), 2019. **256**(7): p. 1800743.
97. Cui, Y., et al., *A general strategy for synthesis of quaternary semiconductor Cu_2MSnS_4 ($M = Co^{2+}, Fe^{2+}, Ni^{2+}, Mn^{2+}$) nanocrystals*. Journal of Materials Chemistry, 2012. **22**(43): p. 23136-23140.
98. Garg, G., S. Bobev, and A.K. Ganguli, *Single crystal structures of two new cation-deficient thiospinels: $Cu_{7.38(11)}Mn_4Sn_{12}S_{32}$ and $Cu_{7.07(6)}Ni_4Sn_{12}S_{32}$* . Solid State Ionics, 2002. **146**(1): p. 195-198.

99. Harada, S., *Some new sulfo-spinels containing iron-group transition metals*. Materials Research Bulletin, 1973. **8**(12): p. 1361-1369.
100. Xu, Y. and M.A.A. Schoonen, *The absolute energy positions of conduction and valence bands of selected semiconducting minerals*. American Mineralogist, 2000. **85**(3-4): p. 543-556.
101. Partik, M., et al., *Strukturverfeinerung und magnetische Messungen an Mn_2SnS_4* . Zeitschrift für anorganische und allgemeine Chemie, 1995. **621**(9): p. 1600-1604.
102. Pogue, E.A. and A.A. Rockett. *Phase stability of Cu_2ZnSnS_4 - SnS_2 interfaces: $Cu_2ZnSn_3S_8$* . in 2016 IEEE 43rd Photovoltaic Specialists Conference (PVSC). 2016.
103. Tauc, J., R. Grigorovici, and A. Vancu, *Optical Properties and Electronic Structure of Amorphous Germanium*. physica status solidi (b), 1966. **15**(2): p. 627-637.
104. Chen, L., et al., *Influence of annealing temperature on structural and optical properties of Cu_2MnSnS_4 thin films fabricated by sol-gel technique*. Journal of Alloys and Compounds, 2015. **640**: p. 23-28.
105. Marchionna, S., et al., *Growth of Cu_2MnSnS_4 PV absorbers by sulfurization of evaporated precursors*. Journal of Alloys and Compounds, 2017. **693**: p. 95-102.
106. Liang, X., et al., *Dilute magnetic semiconductor Cu_2MnSnS_4 nanocrystals with a novel zincblende and wurtzite structure*. RSC Advances, 2012. **2**(12): p. 5044-5046.
107. Kumar, M.S., S.P. Madhusudanan, and S.K. Batabyal, *Substitution of Zn in Earth-Abundant $Cu_2ZnSn(S,Se)_4$ based thin film solar cells – A status review*. Solar Energy Materials and Solar Cells, 2018. **185**: p. 287-299.
108. Yu, J., et al., *The role of sulfurization temperature on the morphological, structural and optical properties of electroplated Cu_2MnSnS_4 absorbers for photovoltaics*. Materials Letters, 2018. **233**: p. 111-114.
109. Le Donne, A., et al., *Effects of CdS Buffer Layers on Photoluminescence Properties of Cu_2ZnSnS_4 Solar Cells*. International Journal of Photoenergy, 2015. **2015**: p. 583058.
110. Calixto, M.E., et al. *Chemical Bath Deposited CdS for CdTe and $Cu(In,Ga)Se_2$ Thin Film Solar Cells Processing*. 2011.
111. *Cu_2ZnSnS_4 solar cells with over 10% power conversion efficiency enabled by heterojunction heat treatment*. Nat Energy, 2018. **3**: p. 764–772.
112. Malerba, C., M. Valentini, and A. Mittiga, *Cation Disorder in Cu_2ZnSnS_4 Thin Films: Effect on Solar Cell Performances*. Solar Rrl, 2017. **1**(9): p. 1700101.
113. Brammertz, G., et al., *Bias-Dependent Admittance Spectroscopy of Thin-Film Solar Cells: Experiment and Simulation*. IEEE Journal of Photovoltaics, 2020. **10**(4): p. 1102-1111.
114. Kauk-Kuusik, M., et al., *Detailed Insight into the CZTS/CdS Interface Modification by Air Annealing in Monocrystalline Layer Solar Cells*. ACS Applied Energy Materials, 2021. **4**(11): p. 12374-12382.
115. Ghisani, F., et al., *Photoelectrochemical properties and band positions of Cd-substituted tetrahedrite $Cu_{10}Cd_2Sb_4S_{13}$ monocrystalline materials grown in molten CdI_2 and LiI* . Thin Solid Films, 2022. **741**: p. 139030.
116. Grossberg, M., et al., *The electrical and optical properties of kesterites*. Journal of Physics: Energy, 2019. **1**(4): p. 044002.
117. Danilson, M., et al., *Temperature dependent current transport properties in Cu_2ZnSnS_4 solar cells*. Thin Solid Films, 2015. **582**: p. 162-165.
118. Tiwari, D., et al., *Mapping the Energetics of Defect States in Cu_2ZnSnS_4 films and the Impact of Sb Doping*. ACS Applied Energy Materials, 2022. **5**(4): p. 3933-3940.
119. Krustok, J., et al., *Temperature dependence of $Cu_2ZnSn(Se_xS_{1-x})_4$ monocrystalline solar cells*. Solar Energy, 2010. **84**(3): p. 379-383.
120. Li, Y., et al., *Comparison study of crystal and electronic structures for chalcopyrite ($CuFeS_2$) and pyrite (FeS_2)*. Physicochemical Problems of Mineral Processing, 2021. **57**.
121. Le Donne, A., et al., *Relevant efficiency enhancement of emerging Cu_2MnSnS_4 thin film solar cells by low temperature annealing*. Solar Energy, 2017. **149**: p. 125-131.
122. Fernandes, P.A., P.M.P. Salomé, and A.F. da Cunha, *Study of polycrystalline Cu_2ZnSnS_4 films by Raman scattering*. Journal of Alloys and Compounds, 2011. **509**(28): p. 7600-7606.

123. Leitão, J.P., et al., *Photoluminescence and electrical study of fluctuating potentials in Cu₂ZnSnS₄-based thin films*. Physical Review B, 2011. **84**(2): p. 024120.
124. Tseberlidis, G., et al., *Kesterite solar-cells by drop-casting of inorganic sol–gel inks*. Solar Energy, 2020. **208**: p. 532-538.
125. Chen, L., et al., *Strategic improvement of Cu₂MnSnS₄ films by two distinct post-annealing processes for constructing thin film solar cells*. Acta Materialia, 2016. **109**: p. 1-7.
126. Nie, L., et al., *Effect of substrate temperature on growth and properties of Cu₂MnSnS₄ thin films prepared by chemical spray pyrolysis*. Journal of Materials Science: Materials in Electronics, 2019. **30**(4): p. 3760-3766.
127. Zakaria, M.B., et al., *Nanoporous Mn-based electrocatalysts through thermal conversion of cyano-bridged coordination polymers toward ultra-high efficiency hydrogen peroxide production*. Journal of Materials Chemistry A, 2016. **4**(23): p. 9266-9274.
128. Zheng, X., et al., *Three-dimensional radial α-MnO₂ synthesized from different redox potential for bifunctional oxygen electrocatalytic activities*. Journal of Power Sources, 2017. **362**: p. 332-341.
129. Davoglio, R.A., et al., *Synthesis and characterization of α-MnO₂ nanoneedles for electrochemical supercapacitors*. Electrochimica Acta, 2018. **261**: p. 428-435.
130. Ilton, E.S., et al., *XPS determination of Mn oxidation states in Mn (hydr)oxides*. Applied Surface Science, 2016. **366**: p. 475-485.

10. ACKNOWLEDGEMENTS

First, I thank Prof Simona Olga Binetti for her supervision of this work and with her all the staff of the MIBSolar laboratory: Prof Maurizio Acciarri, Dr Vanira Trifiletti and Dr Giorgio Tseberlidis for all the support and help they gave me throughout these years. A warm thanks goes out to all the people of our 'enlarged' research group and all the students that passed through our academic life. Being surrounded by so many great people has been fantastic.

A big thanks goes to Dr Stefano Marchionna for his wonderful contribution to practical activity and technical supervision. I also thank every member of TGM Laboratory in RSE S.p.a. Your different perspectives helped me to ask myself new questions.

I also would like to specially mention Prof Maarja Grossberg and every member of the Laboratory of Photovoltaic Materials of Tallinn University of Technology for their support during my time abroad. Your kindness helped me through this incredible adventure.

Last, of course, I thank everyone I have not mentioned, because everyone whose paths crossed mine left a mark that will be there forever.

Thank you all!